# UNIVERSITAT DE BARCELONA

# Effective Dynamics of Black Hole Horizons

David Licht

PhD Thesis

# Effective Dynamics of Black Hole Horizons

DAVID LICHT

UNIVERSITAT DE
BARCELONA

# Effective Dynamics of Black Hole Horizons

Programa de doctorado en física

Autor: David Licht
Director: Roberto Emparan García de Salazar
Tutor: Doménec Espriu Climent

UNIVERSITAT DE BARCELONA

# Acknowledgments

First and foremost I would like to thank my supervisor Roberto Emparan. Thank you for guiding me through this PhD, thank you for constantly providing useful advice and taking so much of your time for your students while also having the trust to allow us a great deal of liberty and let us try things our own way. It has been an amazing experience to work with you and to get inspired by your profound insights into physics and your tremendous experience in so many fields.

Secondly I would like to thank all my other collaborators whose work appears here in this thesis: I would like to thank Tomàs Andrade for always pushing new ideas and his essential contributions to most papers presented here, Raimon Luna for the uncountable discussions we had and more generally for being one of the most helpful people here during my PhD, Ryotaku Suzuki for his impressive contributions in terms of analytical calculations and of course more generally for developing the large $D$ theory yielding the playground of this thesis, finally I also want to thank Aron Jansen for his helpful contributions and discussions to the last paper presented in this thesis. All in all it has been a great pleasure to discuss and work with all of you.

Also I would like to thank all the other postdocs that have been in Barcelona during my PhD. I would like to thank Jorge Rocha, Benson Way, Jakob Salzer, Antonia Micol Frassino, Chris Rosen, Helvi Witek. It has been a pleasure to discuss a lot of ideas about physics with you and I thank you all for many insightful comments. Also it has always been exciting to talk to you guys about more mundane things.

I would like to thank all the other PhD students that I met and spent time here in Barcelona during my PhD. I would like to thank Marija Tomašević, Miquel Triana, Marina Martinez Montero, David Pravos, and Mikel Sanchez for making the time during my PhD a lot more pleasant and for always supporting each other.

Most importantly I want to thank here my parents and my whole family. Danke dafür dass ihr immer für mich da ward, danke an meine Eltern dafür, dass ihr großartige Eltern seid und mich in Allem unterstützt habt, dem ich mich gerne widmen wollte. Danke dafür in mir die Begeisterung zu entfachen neue Dinge zu lernen.

Thanks also to all the good friends I made over the years, be it in Germany or in Barcelona, thank you all for enriching my life.

Lastly I should mention that funding throughout my hole PhD was provided through ERC Advanced Grant GravBHs-692951.

# Contents

# Introduction

Albert Einstein might not have expected to its full extent the importance of the theory of General Relativity (GR) to our current understanding of physics. Of course, much of the importance we attribute to it nowadays stems from the excellent agreement of its predictions (which partially were made by Einstein himself) with experiment. It is often stated that this agreement is especially remarkable since GR shows a huge range of applicability. GR has given predictions that have shown to be consistent with experiment for the whole universe as an integral part of the standard model of cosmology, the large scale structure of the universe, for black holes [1, 2, 3], for gravitational waves [4, 5], gravitational lensing [6], orbital mechanics (e.g. the famous precession of Mercury), the bending of light [7] and gravitational redshifts [8].

The maybe less expected part about the development of GR is the essential role it takes in modern day theoretical physics as a tool to understand other theories. The language and concepts of GR are vitally important for the formulation of string theory and even in the description of physical systems that do not contain any gravity at all. The formalism of general relativity can be used to make predictions through dualities commonly known as the gauge/gravity-duality or holography. This aspect of GR seems unlikely to be foreseen in the earlier days of the theory.[1]

Both of these developments, string theory and holography, go hand in hand with the concept of extra-dimensions, *i.e.,* the consideration that physical laws can also be formulated in more than $3 + 1$ dimensions. Or more generally speaking, these theories fostered the perspective to view the number of spacetime dimensions $D$ as a parameter in the formulation of our theories, to adapt to different physical situations. Furthermore these developments have increased interest to understand better the behavior of spacetimes in higher dimensions.

In many (or even the most) cases of interest, these spacetimes contain horizons often as a part of black holes, the most extreme objects of GR. In higher dimensional spacetimes the dynamics of black holes is considerably richer than in $D = 4$ spacetime dimensions: Black hole horizons can appear in different topologies [9, 10], the uniqueness theorems valid in $D = 4$ do not apply, and many black hole solutions exhibit instabilities suggesting

---

[1]Of course Einstein himself tried in his later life to integrate the at that time known forces into a unified theory using a geometrized formulation akin to that of GR, and accordingly he had some high expectations for his theory and its new way of formulating laws of physics. We also do not want to make any historically accurate claims here and just want to point out that the maturation of GR has taken some interesting turns in its roughly 100 years of existence.

that there exist transitions between the different solutions.

The study of the mentioned processes, poses a challenging task, because they are inherently connected to the non-linear equations of GR, often in the case of little symmetry. And one is typically left with the difficult problem of solving non-linear coupled partial differential equations. This can be addressed by resorting to numerical approaches, which in many cases are very resource intensive.

A different approach is to come up with effective descriptions that simplify the equations at the cost of having a more limited range of applicability. These simplified effective theories often have the advantage of yielding more analytical control than the original theory and also can be used to ease the cost of solving the equations numerically.

One such approach that we are going to consider in this thesis is the so-called large $D$ effective theory for GR, where the number of spacetime dimensions is taken as an expansion parameter to simplify the theory. We are going to explain the main idea in chapter 1. The equations of the large $D$ effective theory can take different forms depending on the black hole under study and depending on which quantities are taken to be fixed while the limit is taken. The maybe most tractable and best understood form of the effective theory is the hydro-elastic formulation of the equations [11] in the case of asymptotically flat and asymptotically AdS black branes, where the equations take a non-relativistic hydrodynamic form.

Interestingly this effective theory contains, apart from the black branes and its non-uniform counterparts, further 'blob'-like solutions that, as we will argue should be interpreted as solutions with a spherical topology rather than a planar one of the former solutions. This type of solution is the main subject studied in the publications [12, 13, 14, 15, 16, 17] that are presented in this thesis.

We are going to introduce the general idea of describing localized black holes as blobs on a membrane in chapter 2 and will introduce the general idea of describing localized black holes as blobs on a membrane. We are going to describe further new types of solutions in chapter 3 where we show how this approach easily provides solutions for charged rotating black holes and chapter 4 will present additional non-uniform counterparts of these blobs.

The last chapters are going to describe further applications that can be investigated with the insight into these types of solutions: Chapter 5 studies the collisions of black holes and how the effective equations can be used to study the evolution of ultra-spinning instabilities. Chapter 6 describes how we can associate an entropy current to the theory and how entropy growth occurs in these processes. All the above mentioned chapters contain a first section that summarizes the main idea and contents of the chapter. The final two chapters 7 and 8 provide rather short summaries of the results in English and Spanish respectively.

# Chapter 1

# The large D expansion of General Relativity

## 1.1 The idea

General relativity when not coupled to any matter does not contain any (naive) parameter that can be used to treat the theory perturbatively. This is directly apparent in the Lagrangian formulation of GR or in its equation of motion in vacuum

$$\mathcal{L}_{GR} = \sqrt{g}R, \quad \rightarrow \quad G_{\mu\nu} = 0. \tag{1.1}$$

One is confronted with a similar situation in the study of the non-linear equations of self-interacting, non-abelian Yang-Mills theories. In this case it has been know for years that the theory can be expanded in the inverse of the rank $N$ of the gauge group $SU(N)$ [18], which makes it possible to reorganize the theory in a genus expansion and ultimately helped to reformulate the theory as a theory of strings and quantum gravity through holography [19, 20].

With this backdrop one might come up with the idea to consider the number of space-time dimensions $D$ as a parameter for a similar expansion of GR. However up to now a treatment that mimics the approach of the large t'Hooft-expansion for a semi-classical quantum theory of gravity has not been found. Nevertheless there has been great progress in using $1/D$ as a expansion parameter for the classical theory of gravity mostly in the case when black holes are present. (See also [21] for more discussion on this specifically and more generally as a well-written and extensive review of the large $D$ expansion and its applications.)

The relevant physics that occur when taking the limit of a large number of dimensions for the classical theory can be understood rather easily: For this consider an asymptotically flat $p$-brane in $D$ dimensions in

$$ds^2 = 2dtdr - \left(1 - \frac{r_0^n}{r^n}\right)dt^2 + \delta_{ij}d\sigma^i d\sigma^j + r^2 d\Omega_{n+1}.$$

This solution gives rise to the gravitational potential $\Phi$ on its outside

$$\Phi \propto \left(\frac{r_0}{r}\right)^{D-p-3}.$$

Now, as the dimensionality of the spacetime increases the gravitational potential steepens and gets more and more localized close to the horizon at $r_0$. More precisely the gravitational potential gets confined to a *near-horizon zone* of extent $r - r_0 \lesssim \mathcal{O}\left(D^{-1}\right)$, while the *far zone* further outside is left without a potential and effectively becomes flat Minkowski space.

Furthermore it was found in [22, 23] that linear perturbations of large classes of black holes show a decoupling phenomenon of different modes at large $D$. The modes separate into *non-decoupled modes* with high frequency $\omega \sim \frac{D}{r_0}$ and *decoupled modes* of lower frequency $\omega \sim \frac{1}{r_0}$. The decoupled modes are mostly supported in the near-horizon region and thereby decouple from the far zone. They encode physics particular to the black hole under consideration, whereas the non-decoupled modes are largely localized in the far zone and are independent of the features of the black hole apart from its horizon radius and shape.

This geometrical picture of localization and the separation of scales in the quasi-normal mode spectrum at large $D$ suggest that there should be an effective theory that captures the physics of the black hole in terms of a membrane embedded in an exterior spacetime and its fluctuations. Indeed, formulations of a full non-linear effective theory were first given in partially different formulations in [24, 25, 26, 27, 28, 29].

The effective theory can be considered for different black holes and in different regimes. In some instances the effective equations are more manageable than in others. They are particularly simple for black branes, either asymptotically flat or asymptotically AdS [27, 30, 31].

In this thesis we are going to focus mostly on the equations for asymptotically flat black holes, which trivially can be solved to describe black branes and to study the main dynamical feature of these objects: the linearized instability discovered by Gregory and Laflamme (GL) [32], as well as its subsequent non-linear evolution. We are going to describe the derivation of these equations and the aforementioned application in the subsequent chapters.

## 1.2    Effective black brane equations

We begin with an extensive review of the effective theory of large-$D$ black branes as derived in [27] and further developed in [31].

We write the metric for a dynamical, neutral, vacuum black $p$-brane to leading order at large-$D$ in Eddington-Finkelstein coordinates as

$$ds^2 = 2dtd\rho - Adt^2 - \frac{2}{n}C_i d\sigma^i dt + \frac{1}{n}G_{ij}d\sigma^i d\sigma^j + \rho^2 d\Omega_{n+1}\,, \tag{1.2}$$

with $n = D - 3 - p$. The radial coordinate orthogonal to the brane is $\rho$, and $\sigma^i$, $i = 1, \ldots, p$, are spatial coordinates along the brane. The lengths along these directions have been rescaled by a factor $1/\sqrt{n}$. The coordinate $t$ is null in (1.2) but it will play the role of time in the effective membrane theory, which can be regarded as living on a surface at a distance in $\rho$ of order $1/n$ away from the horizon. Note also that the time scales we

consider are order one in $n$ (*i.e.*, $\mathcal{O}\left(n^0\right)$), and thus are slow compared to the short time scales $\mathcal{O}\left(1/n\right)$ of the fast quasinormal frequencies that are integrated out in the effective theory.

The radial dependence in the Einstein equations can be solved to determine that the metric functions are

$$A = 1 - \frac{m(t,\sigma)}{\mathsf{R}}\,, \tag{1.3}$$

$$C_i = \frac{p_i(t,\sigma)}{\mathsf{R}}\,, \tag{1.4}$$

$$G_{ij} = \delta_{ij} + \frac{1}{n}\frac{p_i(t,\sigma)p_j(t,\sigma)}{m(t,\sigma)\mathsf{R}}\,, \tag{1.5}$$

where we have introduced the near-horizon radial coordinate $\mathsf{R} = \rho^n$. Then, the remaining Einstein equations reduce to a set of effective equations for the functions $m(t,\sigma)$ and $p_i(t,\sigma)$, namely

$$\partial_t m - \nabla^2 m = -\nabla_i p^i\,, \tag{1.6}$$

$$\partial_t p_i - \nabla^2 p_i = \nabla_i m - \nabla_j\left(\frac{p_i p^j}{m}\right)\,, \tag{1.7}$$

where the derivatives are taken in the flat spatial geometry $\delta_{ij}d\sigma^i d\sigma^j$.[1]

These equations encode the effective non-linear dynamics of a black brane at large $D$ and we will use them to investigate the properties of black holes in this limit. As we explained in the introduction, our approach is based on the fact that the uniform black branes (the solutions with $m = 1$, $p_i = 0$) are unstable and tend to localize into black-hole-like lumps.

We have written the effective equations as resembling diffusion equations, but they can also be recast in other forms. For instance, they take on a hydrodynamical aspect if instead of $p_i$ we use the velocity $v_i$, such that

$$p_i = \nabla_i m + mv_i\,. \tag{1.8}$$

Then the equations (1.6), (1.7) are those of mass continuity

$$\partial_t m + \nabla_i(mv^i) = 0\,, \tag{1.9}$$

and momentum continuity

$$\partial_t(mv_i) + \nabla^j\left(mv_i v_j + \tau_{ij}\right) = 0\,, \tag{1.10}$$

with effective stress tensor

$$\tau_{ij} = -m\delta_{ij} - 2m\nabla_{(i}v_{j)} - m\nabla_j\nabla_i \ln m\,. \tag{1.11}$$

The function $m(t,\sigma)$ is (up to constant factors) the effective mass density of the black brane. Since the horizon is at $\mathsf{R} = m$, we see that (to leading order in $1/D$) $m$ is also equal to the area density. The radius of the horizon is then

$$\rho_H = 1 + \frac{\mathcal{R}(t,\sigma)}{n} + \mathcal{O}\left(1/n^2\right)\,, \tag{1.12}$$

---

[1]The generalization to curved membrane geometries has been given in [33].

where we have introduced the field

$$\mathcal{R}(t,\sigma) = \ln m(t,\sigma)\,, \tag{1.13}$$

as a convenient measure of the area-radius. This radius variable is useful for another, more geometric interpretation of the effective equations and their solutions: the elastic 'soap bubble' viewpoint discussed in sec. 1.3.2.

The effective equations have two important symmetries. First, if we perform a Galilean boost

$$\sigma_i \to \sigma_i - u_i t\,, \tag{1.14}$$

then the velocity gets shifted accordingly,

$$v_i \to v_i + u_i\,. \tag{1.15}$$

The symmetry is Galilean rather than relativistic since when $D$ is large the effective speed of sound on the black brane decreases as $\sim 1/\sqrt{D}$. In (1.2) we rescale the lengths so as to maintain this speed finite.

Second, the equations are invariant under constant rescalings $m \to \lambda m$, $p_i \to \lambda p_i$. This symmetry corresponds to the scaling invariance of the vacuum Einstein equations, and allows to fix a reference scale arbitrarily, *e.g.,* to fix the mass of the solutions.

The spatial integrals of $m$, $p_i$, and $mv_i$ are conserved in time when spatially periodic boundary conditions are imposed, or when these fields vanish at infinity. These are the conservation laws of mass and momenta. The conserved quantities in the effective field theory are given by

$$J_{ij} = \int d^p\sigma\, m(\sigma_i v_j - \sigma_j v_i) = \int d^p\sigma\, (\sigma_i p_j - \sigma_j p_i)\,, \tag{1.16}$$

$$M = \int d^p\sigma\, m\,. \tag{1.17}$$

## 1.3   Stationary configurations

### 1.3.1   Master equation

We define stationary configurations as those that are invariant under the action of a vector

$$k = \partial_t + v^i \partial_i\,. \tag{1.18}$$

Observe that we do not require that the solution be time-independent. Nevertheless, $k(m) = 0$ determines that

$$\partial_t m = -v^i \partial_i m\,. \tag{1.19}$$

Then the mass continuity equation (1.9) becomes the condition that the expansion vanishes

$$\nabla_i v^i = 0\,. \tag{1.20}$$

If in addition we require that $k$ is a Killing vector, $\nabla_{(\mu}k_{\nu)} = 0$, then we obtain that the velocity flow is also time-independent and shear-free,

$$\partial_t v^i = 0, \qquad \nabla_{(i}v_{j)} = 0. \tag{1.21}$$

It may not be obvious that one should require that $k$ be a Killing vector, but this can be proved from the requirement of absence of shear and expansion [34], since otherwise viscosity (both shear and bulk) would generate dissipation in the system. The velocity flow may still have vorticity.

Under these conditions we can follow the steps in [31] and show that, using the membrane radius $\mathcal{R}$ (1.13), we can write

$$\partial_t(mv_i) + \nabla^j(mv_iv_j) = -\frac{1}{2}e^{\mathcal{R}}\nabla_i(v^2) \tag{1.22}$$

and

$$\nabla^j \tau_{ij} = -e^{\mathcal{R}}\nabla_i\left(\mathcal{R} + \nabla^2\mathcal{R} + \frac{1}{2}(\nabla\mathcal{R})^2\right). \tag{1.23}$$

This reduces the momentum continuity equations (1.10) to a single equation for $\mathcal{R}$,

$$\nabla^2\mathcal{R} + \frac{1}{2}(\nabla\mathcal{R})^2 + \mathcal{R} + \frac{v^2}{2} = 0, \tag{1.24}$$

where we have absorbed an integration constant by appropriately shifting the value of $\mathcal{R}$.

Eq. (1.24) is the master equation that governs the stationary sector of solutions. The derivation of this equation in [31] made the assumption that $\partial_t m = 0$. We now see that it also applies to more general stationary configurations in which (1.19) holds instead.

### 1.3.2   Elastic viewpoint

The master equation (1.24) admits an interpretation as an elasticity equation for a soap bubble [24, 26, 31]. To see this, consider embedding the surface

$$\rho = 1 + \frac{\mathcal{R}(\sigma)}{n} \tag{1.25}$$

in a constant-time section of the Minkowski geometry that appears at large $\mathsf{R}$ in (1.2), (1.3),

$$ds^2 = -d\hat{t}^2 + d\rho^2 + \frac{1}{n}\delta_{ij}d\sigma^i d\sigma^j + \rho^2 d\Omega_{n+1} \tag{1.26}$$

(we have changed from the Eddington-Finkelstein null coordinate $t$ in (1.2) to Minkowski time $\hat{t}$). The trace of the extrinsic curvature of this surface is

$$K = n + 1 - \left(\mathcal{R} + \nabla^2\mathcal{R} + \frac{1}{2}(\nabla\mathcal{R})^2\right) + \mathcal{O}\left(1/n\right). \tag{1.27}$$

Then eq. (1.24) can be written, up to next-to-leading order in $1/n$, as

$$\sqrt{1 - \mathbf{v}^2}K = \text{constant}, \tag{1.28}$$

where $\mathbf{v} = v/\sqrt{n}$ is the physical velocity along the brane, since the lengths in (1.26) are rescaled by a factor $1/\sqrt{n}$. The Young-Laplace equation $K = \text{constant}$ famously describes

the shape of soap bubbles (more generally, interfaces between fluids). Eq. (1.28), which was first derived for large-$D$ black holes in [26], includes a Lorentz-redshift factor that accounts for the possible rotation of the bubble (or any motion along its surface).

This elastic interpretation of the effective theory allows to make sense of some features of the effective equations that remain obscure in the hydrodynamic version. In the latter, the constitutive relations (1.11) contain only one term at next-to-viscous order, and none at higher gradient order. But the large-$D$ expansion is not an expansion in worldvolume gradients. Why should the effective theory involve only a finite number of them? The mystery dissipates (at least for stationary solutions) in the elastic interpretation, which leaves no room for any other form of $\tau_{ij}$ than precisely (1.11), since this is the one that completes the expression for $K$ in (1.27).

Furthermore, the elastic viewpoint, in which a membrane with positive tension forms soap bubbles, may look more natural than a hydrodynamic view where an unstable fluid with negative pressure (as in (1.11)) clumps into blobs of fluid.[2],[3]

## 1.4   Charged equations

The above equations can be generalized in several directions: They can be formulated for branes with electric charge and $p$-brane charge, and external electric field [31], for curved background geometries (deformed boundary metrics) [33], for higher-curvature theories [36, 37, 38], for different classes of deformations of AdS black branes [39]. They can also be generalized to include higher orders in $1/D$ [40, 41, 11], and also exist as similar theories for finite black holes [28, 42, 43, 44, 45, 38].

In this section we are going to focus only on the charged generalization of the equations, which will serve us a s a useful tool in chapter 3. For this we study electrically charged black holes of the Einstein-Maxwell theory

$$I = \int d^D x \sqrt{-g} \left( R - \frac{1}{4} F^2 \right) , \tag{1.29}$$

in the limit of large $D$, following ref. [31] and using the same notation as in the previous section we again consider fluctuations of a $p$-brane,

$$ds^2 = 2dtdr - Adt^2 - \frac{2}{n} C_i d\sigma^i dt + \frac{1}{n} G_{ij} d\sigma^i d\sigma^j + r^2 d\Omega_{n+1} , \tag{1.30}$$

but now allow for a new degree of freedom $q(t,\sigma)$ that will appear in the effective theory

$$A = 1 - \frac{m(t,\sigma)}{\mathsf{R}} + \frac{q(t,\sigma)^2}{2\mathsf{R}^2} , \qquad C_i = \left( 1 - \frac{q(t,\sigma)^2}{2m(t,\sigma)\mathsf{R}} \right) \frac{p_i(t,\sigma)}{\mathsf{R}} , \tag{1.31}$$

---

[2]For a black brane in AdS the hydrodynamic interpretation is apt since the large-$D$ effective fluid has positive pressure and is stable. Curiously, the effective elastic equation is one with positive tension, but the membrane is subject to a gravitational potential from the AdS geometry.

[3]Note the contrast with the blackfold approach of [35] (which is another effective theory of black brane dynamics): in the latter some collective degrees of freedom are elastic and others are hydrodynamic, whereas in the large-$D$ effective theory the same degrees of freedom admit one or the other interpretation.

$$G_{ij} = \delta_{ij} + \frac{1}{n} \left\{ \left( 1 - \frac{q(t,\sigma)^2}{2m(t,\sigma)\mathsf{R}} \right) \frac{p_i(t,\sigma)p_j(t,\sigma)}{m(t,\sigma)\mathsf{R}} \right.$$
$$\left. - \ln \left( 1 - \frac{m_-(t,\sigma)}{\mathsf{R}} \right) \left[ 2\delta_{ij} + \nabla_i \frac{p_j(t,\sigma)}{m(t,\sigma)} + \nabla_j \frac{p_i(t,\sigma)}{m(t,\sigma)} \right] \right\}. \tag{1.32}$$

The electric potential is

$$A_t = -\frac{q(t,\sigma)}{\mathsf{R}}. \tag{1.33}$$

The worldvolume collective fields $m(t,\sigma)$, $q(t,\sigma)$ are the mass and charge density of the black brane. It is convenient to define

$$m_\pm = \frac{1}{2} \left( m \pm \sqrt{m^2 - 2q^2} \right). \tag{1.34}$$

The Einstein-Maxwell equations are solved to $\mathcal{O}(1/D)$ if and only if these collective fields satisfy the effective equations for mass continuity (using the definition of velocity fields according to (1.8) as before),

$$\partial_t m + \nabla_i(mv^i) = 0, \tag{1.35}$$

the equations for momentum continuity,

$$\partial_t(mv^i) + \nabla_j(mv^i v^j + \tau^{ij}) = 0 \tag{1.36}$$

with stress tensor

$$\tau_{ij} = -(m_+ - m_-)\delta_{ij} - 2m_+ \nabla_{(i}v_{j)} - (m_+ - m_-)\nabla_i\nabla_j \ln m, \tag{1.37}$$

and for charge continuity,

$$\partial_t q + \nabla_i j^i = 0 \tag{1.38}$$

with current

$$j_i = qv_i - m\nabla_i \left( \frac{q}{m} \right). \tag{1.39}$$

In addition to the conserved quantities of the uncharged theory (1.16), we can define the conserved $U(1)$-charge of these theories

$$Q = \int d^p \sigma \, q. \tag{1.40}$$

Note that the one-derivative terms in $\tau_{ij}$ and $j_i$ can be interpreted as viscous stresses and charge diffusivities. It has been proven in [31] that, with these equations, charge diffusion leads to entropy production at leading order but viscosity does not. See chapter 6 for further discussion on this.

The solutions have an outer event horizon at $\mathsf{R} = m_+(t,\sigma)$ wherever and whenever $m(t,\sigma) > \sqrt{2}q(t,\sigma)$. In principle the extremal limit $m = \sqrt{2}q$ lies outside the range of validity of the approximations made in the derivation. Taking the extremal limit requires separate study, and therefore we will always remain strictly away from it here.

### 1.4.1   Stationary configurations

Following section 1.3 (and with that [12]), we investigate stationary configurations where the mass and charge density are Lie-dragged with velocity $v^i$,

$$(\partial_t + v^i \partial_i)m = 0\,, \qquad (\partial_t + v^i \partial_i)q = 0\,, \tag{1.41}$$

but without acceleration, $\partial_t v^i = 0$. In addition we require that dissipative effects are absent, be they viscous shear and expansion or charge diffusion, so that

$$\nabla_{(i} v_{j)} = 0 \tag{1.42}$$

and

$$\nabla_i \left( \frac{q}{m} \right) = 0\,. \tag{1.43}$$

The latter implies that

$$\mathfrak{q} \equiv \frac{q}{m} \tag{1.44}$$

is a constant, so that the charge density must proportionally track the mass density exactly. This property of the charge distribution in stationary configurations provides the crucial simplification that will allow us to easily obtain charged rotating black hole solutions from neutral ones.

In order to see how this occurs, we derive a single master equation for stationary configurations in terms of the area-radius variable

$$\mathcal{R} = \ln m\,. \tag{1.45}$$

The derivation piggybacks on [31] and [12] to arrive at

$$\nabla_i \left( \frac{v^2}{2} + \frac{m_+ - m_-}{m} \left( \mathcal{R} + \nabla_j \nabla^j \mathcal{R} + \frac{1}{2} \nabla^j \mathcal{R} \nabla_j \mathcal{R} \right) \right) = 0\,. \tag{1.46}$$

Noting that (1.44) implies that $m_\pm/m$ are constants, we define a 'charge-rescaled velocity'

$$v_q^i = \sqrt{\frac{m}{m_+ - m_-}}\, v^i = \frac{v^i}{(1 - 2\mathfrak{q}^2)^{1/4}}\,. \tag{1.47}$$

Then, after absorbing an integration constant by shifting $\mathcal{R}$ (which is simply a rescaling of the mass), the master equation takes the form

$$\frac{v_q^2}{2} + \mathcal{R} + \nabla_j \nabla^j \mathcal{R} + \frac{1}{2} \nabla^j \mathcal{R} \nabla_j \mathcal{R} = 0\,. \tag{1.48}$$

All of the dependence on the charge in this equation is encoded in $v_q$. Therefore, given a neutral stationary solution for $\mathcal{R}$ with velocity $v$, we can immediately construct a charged stationary solution by substituting $v \to v_q$. Note that this substitution must not be applied when $v$ appears through the comoving dependence on $\sigma^i - v^i t$, since this is fixed by the stationarity condition of invariance under $\partial_t + v^i \partial_i$.

After obtaining in this manner the mass density $m = \exp \mathcal{R}$ for the new charged solution in terms of $v_q$, the actual velocity of the flow, $v$, will be given in terms of $v_q$ through (1.47), and the charge density will be proportional to $m$ as in (1.44).

Observe that this mapping from neutral to charged solutions implies that two black holes can have the same profile for $m$ even if their charges and rotations are very different. In particular, an almost static (small $v$) but highly charged black hole ($\mathfrak{q}$ slightly below $1/\sqrt{2}$), can have the same shape as a neutral black hole with large velocity if the two solutions have the same value of $v_q$.

## 1.5 Black branes and the GL instability

In this section we are going to explore the brane-like solutions as the first class of solutions that were found for this theory. We will present how the effective theory is capable of capturing the most prominent feature of the dynamics of these objects: thin enough black branes are unstable [32, 46].

### 1.5.1 Quasinormal modes

To see this we consider perturbations of the uniform equilibrium solution for a charged black brane with mass and charge density given by the constants $m_0, q_0$:

$$m = m_0 + \delta m\, e^{-i\omega t + i k_j \sigma^j}\,, \tag{1.49}$$

$$q = q_0 + \delta q\, e^{-i\omega t + i k_j \sigma^j}\,, \tag{1.50}$$

$$v^i = \delta v^i\, e^{-i\omega t + i k_j \sigma^j}\,. \tag{1.51}$$

Solving the perturbation equations resulting from this ansatz in the equations of motion (1.35,1.36), the authors of ref. [31] found the following modes.

**Charge diffusion mode** which has $\delta q/\delta m \neq q_0/m_0$ and is purely dissipative

$$\omega = -ik^2\,. \tag{1.52}$$

**Shear mode** which is also dissipative

$$\omega = -ia_+ k^2\,, \tag{1.53}$$

where we introduced

$$a_\pm = \left(\frac{m_\pm}{m}\right)_0 = \frac{1}{2}\left(1 \pm \sqrt{1 - \frac{2q_0^2}{m_0^2}}\right) \leq 1\,. \tag{1.54}$$

**Sound mode** which satisfies $\delta q/\delta m = q_0/m_0$ and has frequencies

$$\omega_\pm = \pm ik\sqrt{a_+ - a_- + k^2 a_-^2} - ia_+ k^2\,. \tag{1.55}$$

The +-mode is unstable for all wavelengths $k < k_{GL} = 1$ and has the positive growth rate

$$\Omega = -i\omega_+ = k\sqrt{a_+ - a_- + k^2 a_-^2} - a_+ k^2\,. \tag{1.56}$$

This instability exists for all charges captured in the effective theory but becomes weaker for larger charges.

The marginal mode with $k_{GL}$ at threshold of the instability was computed also to higher orders in $1/n$ and found to be [47, 48]

$$k_{GL} = 1 - \frac{1}{2n} + \frac{7}{8n^2} + \frac{-\frac{25}{16} + 2\zeta(3)}{n^3} + \frac{\frac{363}{128} - 5\zeta(3)}{n^4} + \mathcal{O}\left(n^{-5}\right). \qquad (1.57)$$

This analytic result reproduces numerical calculations down to $D = 6$ up to an accuracy of 2.4%.

## 1.5.2   Static solutions

To find static stringlike solutions that are admitted in the effective theory we solve eq. (1.48) in one effective variable $z$ in which the solution should satisfy periodic boundary conditions and set $v_q = 0$ [24]. The resulting equation

$$\partial_z^2 \mathcal{R} + \frac{1}{2}\left(\partial_z \mathcal{R}\right)^2 + \mathcal{R} = 0, \qquad (1.58)$$

can be integrated to obtain

$$\frac{1}{2}\mathcal{R}'^2 + U(\mathcal{R}) = 1, \qquad (1.59)$$

with

$$U(\mathcal{R}) = \mathcal{R} + \tau e^{-\mathcal{R}}, \qquad (1.60)$$

where $\tau$ is the constant of integration, and corresponds to the tension of the string. In this form the static equation can be interpreted as an equation of motion for a classical particle in one dimension, *i.e.,* we could view $\mathcal{R}$ as the position of a particle, $z$ as the time variable and $E = 1$ as the (fixed) energy of the particle in the potential $U$.

When $\tau > 0$ this potential has a minimum and allows for bound states. The uniform string is obtained when the particle sits still at the minimum of the potential at $U = 1 + \log\tau$, *i.e.,* when $\tau = 1$. Bound states above the minimum correspond to non-uniform black strings (since they satisfy periodic boundary conditions), and are possible for $0 < \tau < 1$. These solutions can not be obtained analytically but they were constructed numerically in [24].

It is however possible and interesting to consider approximate solutions to these equations at a fixed positive, small $\tau$. In the particle picture we can see that the potential $U$ has a steeper side for negative $\mathcal{R}$ and the particle will spend less time there. That is this solution will only extend over a short extent of $z$. While for large (positive) $\mathcal{R}$ we see that $U \simeq \mathcal{R}$, that is the potential is flatter on this side and the particle will spend more time in the $\mathcal{R} > 0$ region. In this case we can find the approximate solution

$$\mathcal{R} \simeq \mathcal{R}_0 - \frac{1}{2}z^2. \qquad (1.61)$$

The solutions thus have the form of long extended bulges that are approximately Gaussian when expressed in $m = \exp(\mathcal{R})$ and these bulges are connected by thin short necks.
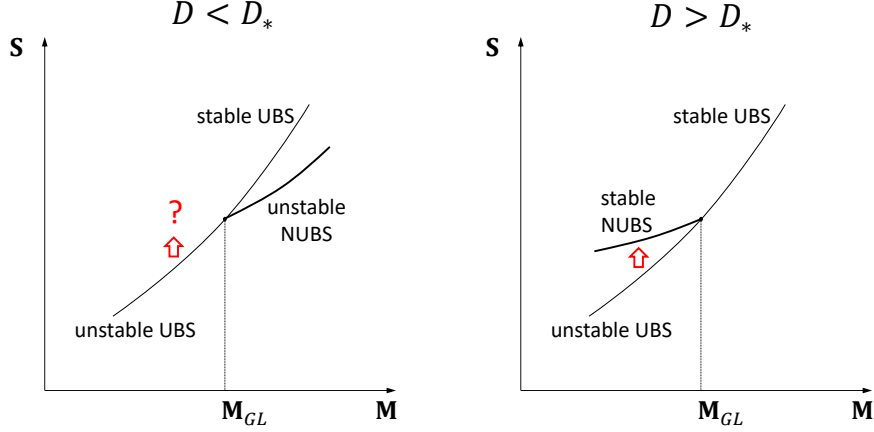
Figure 1.1: Mass and entropy for the stable and unstable uniform black string branches (UBS) and for non-uniform black strings (NUBS). The right panel shows the case above the critical dimension $D_\star$ where unstable UBS can transition into NUBS via a second order phase transition, while below the critical dimension shown in the left panel there is no NUBS that the unstable UBS can transition into. (Figure taken from [11])

Ref. [11] studied further these non-uniform black strings (NUBS). The authors constructed NUBS analytically to higher orders in non-uniformity $\delta m$ and to higher orders in $1/n$ and calculated their thermodynamic properties, they calculated their mass $\mathbf{M}$ and entropy $\mathbf{S}$ (normalized to the critical string)

$$\mathbf{M} = 1 + n\,\delta m^2 \left( -\frac{1}{24} + \frac{1}{3n} + \frac{7}{12n^2} + \mathcal{O}\left(n^{-3}\right) \right) + \mathcal{O}\left(\delta m^4\right), \tag{1.62}$$

$$\mathbf{S} = 1 + n\,\delta m^2 \left( -\frac{1}{24} + \frac{11}{12n} + \frac{7}{24n^2} + \mathcal{O}\left(n^{-3}\right) \right) + \mathcal{O}\left(\delta m^4\right). \tag{1.63}$$

Crucially it can be seen that the $\mathcal{O}\left(n\,\delta m^2\right)$-correction to the mass undergoes a sign change at $n_* = 9.48$ which is equivalent to the dimension

$$D_* = 13.48. \tag{1.64}$$

The behavior of the solutions is depicted in figure 1.1, it can be seen that below $D_*$ there is no weakly non-uniform black string that the dynamically instable UBS can decay into, while in dimensions above $D_*$ it can be seen that there exist NUBS that the dynamically instable UBS can decay into via a second order phase transition. This critical behavior of the black string was first described in [49].
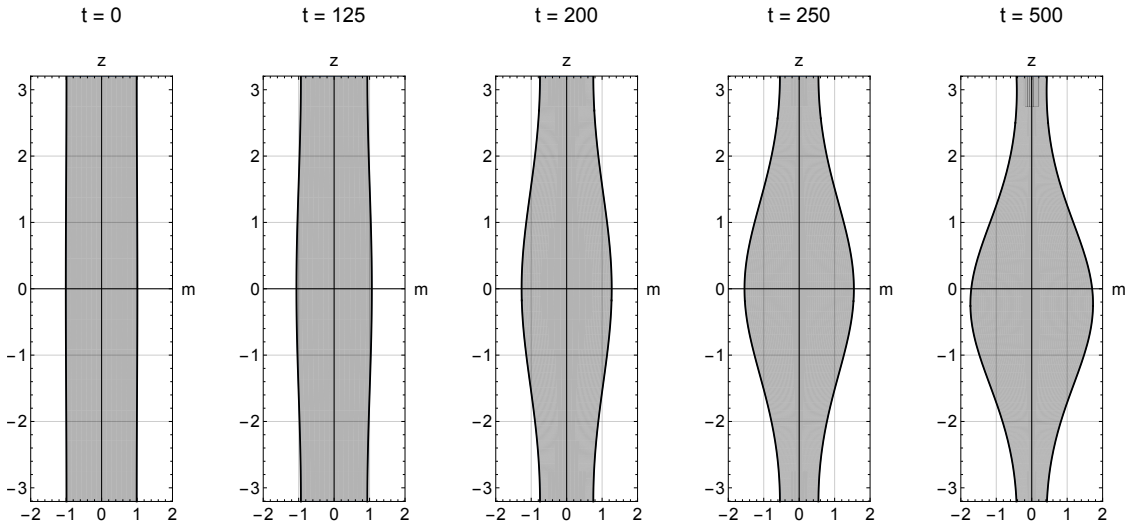
Figure 1.2: Evolution of a perturbed UBS with $k_L = 0.98$. The final shape is only weakly non-uniform and approximately sinusoidal.

### 1.5.3   Non-linear evolution

Apart from the static thermodynamic analysis the effective large $D$ equations also allow to perform direct evolutions of the GL-instability [27, 50, 41].

Ref. [27] evolved the effective dynamical equations (1.6, 1.7) with a perturbed uniform black string $m(0, z) = 1 + \delta m_0(z)$, $\delta p(0, z) = \delta p_0(z)$, where the coordinate along the string is taken to be periodic on an compactification length $L$. With these boundary conditions the smallest wavenumber the perturbation can have is

$$k_L = \frac{2\pi}{L} \,. \tag{1.65}$$

As expected from the linear analysis, it was found there that for strings with $k_L > k_{GL} = 1$ the perturbations quickly disappear and the dynamics is purely dissipative. Also in accordance with the perturbative analysis, thinner strings with $k_L < 1$ evolve initially at an approximately exponential rate but ultimately settles down at a stable configuration that resembles strongly the NUBS found in the linear analysis. Figures 1.2 and 1.3 show to examples of such evolutions at different compactification lengths.
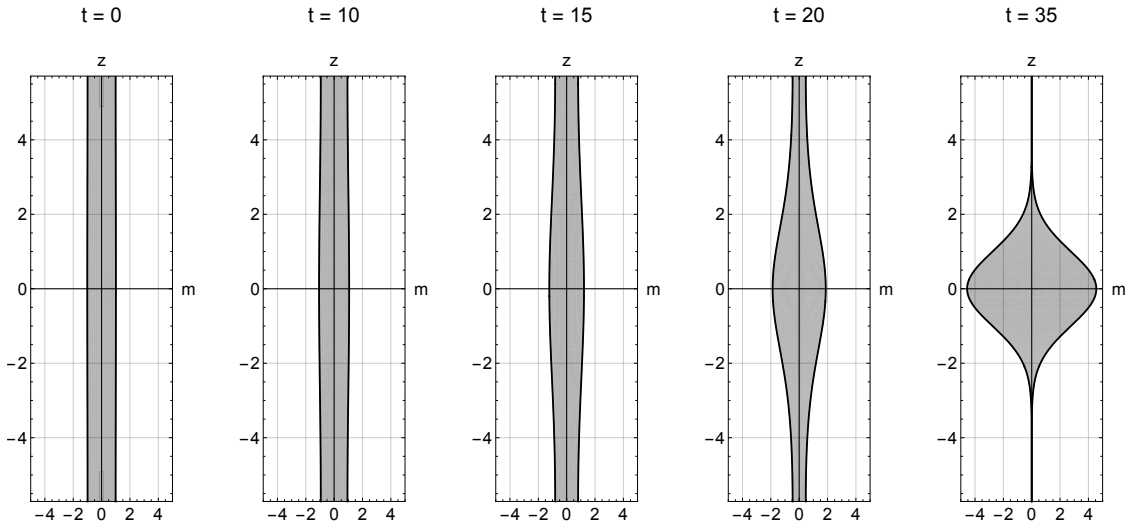
Figure 1.3: Evolution of a perturbed UBS with $k_L = 0.55$. The final shape is only strongly non-uniform and approximately a gaussian.

The very non-uniform endpoints of the evolution are very approximately gaussian, with profile

$$m(z) \simeq \frac{L}{\sqrt{2\pi}} e^{-z^2/2} \, . \tag{1.66}$$

In the following chapters we are going to describe that the effective theory actually contain a solution that is proportional to this expression and we are going to see that these blobs capture a lot of physics of topologically spherical black holes.

# Chapter 2

# Black holes as blobs on a membrane

## 2.1 Main idea

Consider the simplest case of a black string compactified on a long circle. As described in the previous chapter the perturbed string becomes increasingly inhomogeneous driven by the GL instability and develops lumps along its length. The endpoint of the instability depends on the number of spacetime dimensions [49, 51, 52, 11], but for a thin initial string and at large enough $D$, the system stabilizes on a configuration with large blobs that approach the shape of a Schwarzschild black hole, and which are connected by thin tubes of black string [27]. For a black brane the end result is similar: black-hole-like bulges on a thin membrane (see fig. 2.1). We will show that there is a simple, exact solution of the effective black brane equations that describes a bulge with many of the physical properties of a Schwarzschild black hole. It can be boosted to move at constant velocity like a black hole would, and it also generalizes to a solution that rotates around its axis like a MP black hole.

In the large-$D$ approximation, the bulge on the brane is a good approximation for only a 'cap' of the Schwarzschild (or Myers-Perry) black hole horizon. It may then be surprising that, even though the angular extent of this cap is small, $\sim 1/\sqrt{D}$, it is nevertheless large enough to accurately account for much of the physics of the black hole when $D \gg 1$.

In order to illustrate how this is possible, let us take a sphere $S^D$, built as a fibration of spheres $S^{D-2}$ over a hemisphere (a topological disk) parametrized by $\theta \in [0, \pi/2]$, $\phi \in [0, 2\pi)$, such that its metric is

$$d\Omega_D = d\theta^2 + \sin^2\theta \, d\phi^2 + \cos^2\theta \, d\Omega_{D-2} \,. \tag{2.1}$$

The area of this sphere can be computed in an exact, recursive manner as

$$\Omega_D = \Omega_{D-2} \, 2\pi \int_0^{\pi/2} d\theta \, \sin\theta \, (\cos\theta)^{D-2}$$

$$= \frac{2\pi}{D-1} \Omega_{D-2} \,. \tag{2.2}$$
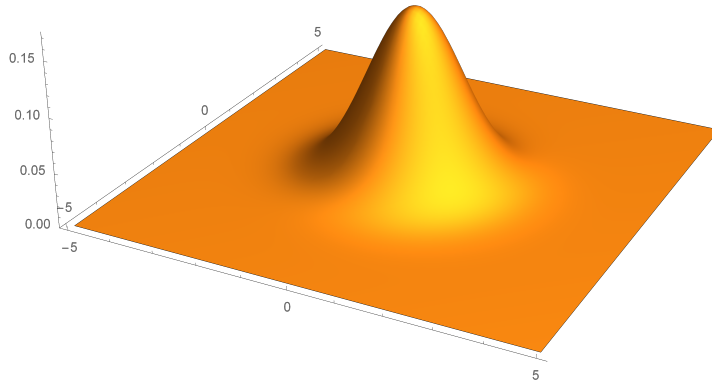
Figure 2.1: Black holes as gaussian lumps.  Driven by the GL instability, a black membrane develops a bulge where most of its area and mass are concentrated with a profile that, when $D \to \infty$, is a gaussian, as shown in the figure.  Representing Schwarzschild and Myers-Perry black holes in this manner accurately captures much of their physics, including their quasinormal vibrations.

However, for us it is more interesting to observe that when $D$ is very large the above integrand is strongly peaked around the center of the hemisphere, $\theta \approx 0$. We can then estimate the integral using a saddle-point approximation. If we make

$$\theta = \frac{r}{\sqrt{D}} \,, \tag{2.3}$$

so that $\cos\theta \approx 1 - r^2/(2D)$, then the 'density of $S^{D-2}$-area' on the plane $(r, \phi)$ becomes

$$a(r) = (\cos\theta)^{D-2} \approx e^{-r^2/2} \,, \tag{2.4}$$

and we compute

$$\Omega_D \approx \frac{2\pi}{D} \Omega_{D-2} \int_0^\infty dr\, r\, e^{-r^2/2} = \frac{2\pi}{D}\, \Omega_{D-2} \,, \tag{2.5}$$

which is indeed the leading order approximation to the exact result (2.2) when $D \gg 1$. The upshot is that almost all of the area of the sphere is concentrated with a gaussian profile in a section of small angular extent $\Delta\theta \sim 1/\sqrt{D}$.

When the sphere is that of a large-$D$ black hole, essentially the same argument reveals that not only its area, but also the mass and other extensive quantities, as well as the far-zone gravitational potential $1/r^{D-3}$ of the black hole, can be recovered from a small cap, which can be alternatively viewed as a gaussian bulge on a black brane [53, 24]. More generally, if we view the $S^D$ as a fibration of $S^{D-p}$ over a ball $B_p$ (with $p \geq 1$ finite as $D \to \infty$), then the black hole is very well approximated by a gaussian bulge of width $\sim 1/\sqrt{D}$ on a black $p$-brane.

This observation had essentially been made already in [24] and [53]. What we have discovered, and will demonstrate here, is that this small cap of the horizon is sufficient to capture not only static, integrated magnitudes of the black hole: it also contains dynamical

information such as the spectrum and profiles of its quasinormal excitations. Moreover, the simplicity of the equations has allowed us to identify a new kind of black hole, namely a rotating black bar, which is stationary when $D \to \infty$ but should be slowly radiating and long-lived for large but finite $D$. The instability of rotating black holes that is associated to this new branch of solutions is captured by our leading large-$D$ calculation at per-cent level accuracy when compared to earlier numerical results [54, 23].

Our study can be usefully related and compared with the effective theory of stationary black holes at large $D$ that was derived and solved in [26]. In that theory, the singly-spinning MP black hole is represented as an spheroidal elastic membrane rotating in a flat background. The theory also yields the quasinormal spectrum of the MP black hole. In our approach, the bulges of the membrane match the spheroidal membrane around the symmetry axis on a region of angular size $\sim 1/\sqrt{D}$. The two descriptions complement each other well: the equations of [26] capture all of the horizon, but ours have finer resolution in the region near the symmetry axis, as we will argue. When the two approaches overlap we find perfect agreement; in particular, the quasinormal spectra coincide exactly.

Very recently, the elegant formulation of the large-$D$ effective theory by Bhattacharyya, Minwalla and collaborators [25, 29] has been applied in [55] to describe the simplest stationary black holes, namely, MP black holes and black rings, in good agreement with the construction of [26, 28]. It should be interesting to also investigate our approach within this framework.

## 2.2 Effective 2+1 membrane equations

For the case of singly spinning solutions it is useful to use the effective theory in the case $p = 2$, *i.e.,* we will consider membranes (2-branes), for which we write the spatial geometry as

$$ds^2 = dr^2 + r^2 d\phi^2 \tag{2.6}$$

and set

$$p = p_r dr + p_\phi d\phi \,. \tag{2.7}$$

The effective equations of motion (1.6,1.7) in these coordinates take the form

$$\partial_t m = \partial_r^2 m + \frac{\partial_r m}{r} + \frac{\partial_\phi^2 m}{r^2} - \partial_r p_r - \frac{p_r}{r} - \frac{\partial_\phi p_\phi}{r^2} \,, \tag{2.8}$$

$$\partial_t p_r = \partial_r m + \partial_r^2 p_r + \frac{\partial_r p_r}{r} - \frac{p_r}{r^2} + \frac{\partial_\phi^2 p_r}{r^2} - \frac{2\partial_\phi p_\phi}{r^3}$$
$$- \partial_r \left( \frac{p_r^2}{m} \right) - \frac{p_r^2}{rm} - \frac{1}{r^2} \partial_\phi \left( \frac{p_r p_\phi}{m} \right) + \frac{p_\phi^2}{r^3 m} \,, \tag{2.9}$$

$$\partial_t p_\phi = \partial_\phi m + \frac{\partial_\phi^2 p_\phi}{r^2} - \frac{\partial_r p_\phi}{r} + \partial_r^2 p_\phi + \frac{2}{r} \partial_\phi p_r$$
$$- \frac{1}{r^2} \partial_\phi^2 \left( \frac{p_\phi^2}{m} \right) - \partial_r \left( \frac{p_r p_\phi}{m} \right) - \frac{p_r p_\phi}{rm} \,. \tag{2.10}$$

### 2.2.1    Time-independent axisymmetric configurations

For configurations that are independent of $t$ and $\phi$, eq. (2.8) is solved by

$$p_r = \partial_r m \,, \tag{2.11}$$

i.e., $v_r = 0$. Using this, eq. (2.10) can be rewritten as

$$\partial_r \left( m r^3 \partial_r \frac{p^\phi}{m} \right) = 0 \,, \tag{2.12}$$

where $p^\phi = g^{\phi\phi} p_\phi = p_\phi / r^2$. If we require that $m$ and $p^\phi$ asymptote to finite values at $r \to \infty$, then we can integrate this equation to conclude that

$$\frac{p^\phi}{m} = \Omega \tag{2.13}$$

is a constant, equal to the angular velocity of the horizon. That is,

$$p_\phi = m r^2 \Omega \,. \tag{2.14}$$

Hence we have proven that the rotation velocity $v^\phi = \Omega$ is a constant, which in sec. 1.3 we had assumed. Thus we have given the large-$D$ proof of the black hole rigidity theorem.

The remaining equation (2.9), in terms of $\mathcal{R}(r) = \ln m(r)$, is indeed a particular case of the master stationary equation (1.24), namely,

$$\mathcal{R}'' + \frac{\mathcal{R}'}{r} + \frac{1}{2}\mathcal{R}'^2 + \mathcal{R} + \frac{\Omega^2 r^2}{2} = 0 \,. \tag{2.15}$$

### 2.2.2    Stationary membrane master equation

Consider a configuration that is stationary but not necessarily axisymmetric nor time-independent, and take a purely rotational velocity field,

$$v^\phi = \Omega \,. \tag{2.16}$$

In this case the master equation (1.24) for

$$\mathcal{R} = \mathcal{R}(r, \phi - \Omega t) \tag{2.17}$$

takes the form

$$\partial_r^2 \mathcal{R} + \frac{\partial_r \mathcal{R}}{r} + \frac{\partial_\phi^2 \mathcal{R}}{r^2} + \frac{1}{2}\left( (\partial_r \mathcal{R})^2 + \frac{(\partial_\phi \mathcal{R})^2}{r^2} \right) + \mathcal{R} + \frac{\Omega^2 r^2}{2} = 0 \,. \tag{2.18}$$

In our subsequent analysis we will make extensive use of this equation and of (2.15), to which (2.18) reduces for axisymmetric profiles.

The mass density is

$$m(r, \phi - \Omega t) = e^{\mathcal{R}(r, \phi - \Omega t)} \tag{2.19}$$

and the $p_i$ are

$$p_r = \partial_r m \,, \tag{2.20}$$

$$p_\phi = \partial_\phi m + \Omega \, r^2 m \,. \tag{2.21}$$

## 2.3  Axisymmetric black holes

In ref. [27] the numerical evolution of thin unstable black branes was found to stabilize at very approximately gaussian profiles $m(r) \sim e^{-r^2/2}$. It was noticed in [24, 53] that these reproduce well the features of a Schwarzschild black hole. This is the main intuition that leads us to seek new solutions to the effective equations (1.6), (1.7) that capture the physical properties of localized black holes —even if, as we will see later, some of these are not always stable themselves.

When looking for stationary axisymmetric configurations we only need to solve the master equation (2.15). The rotation term $\sim \Omega^2 r^2$ suggests that we try an ansatz where $\mathcal{R}$ is quadratic in $r$. This yields easily the solution

$$\mathcal{R}(r) = \mathcal{R}_0 - \frac{r^2}{2(1+a^2)} \,, \tag{2.22}$$

with

$$\Omega = \frac{a}{1+a^2} \,. \tag{2.23}$$

The constant $\mathcal{R}_0$ can be chosen arbitrarily, but our specific choices in (2.15) require that $\mathcal{R}_0 = 2/(1+a^2)$, and then

$$\mathcal{R}(r) = \frac{2}{1+a^2} \left( 1 - \frac{r^2}{4} \right) \,. \tag{2.24}$$

The solution for the mass and area density has gaussian profile

$$m(r) = m_0 \exp\left( -\frac{r^2}{2(1+a^2)} \right) \,, \tag{2.25}$$

with $m_0 = e^{\mathcal{R}_0}$, and

$$p_r = \partial_r m = -m_0 \frac{r}{1+a^2} \exp\left( -\frac{r^2}{2(1+a^2)} \right) \,, \tag{2.26}$$

$$p_\phi = mr^2\Omega = m_0 \frac{ar^2}{1+a^2} \exp\left( -\frac{r^2}{2(1+a^2)} \right) \,. \tag{2.27}$$

The angular momentum per unit mass is

$$\frac{J}{M} = \frac{\int_0^\infty dr\, r\, p_\phi(r)}{\int_0^\infty dr\, r\, m(r)} = 2a \,. \tag{2.28}$$

This reproduces correctly the large-$D$ value for MP black holes [56], once we take into account that lengths on the membrane are rescaled by a factor of $1/\sqrt{D}$. so the physical value is actually $J/(MD) = 2a/D$.

Note that $\Omega \in [0, 1/2]$. The maximum $\Omega = 1/2$ is achieved for $a = 1$. On the other hand, the value $\Omega \to 0$ is reached both when $a \to 0$ and when $a \to \infty$. The former is the static limit, whereas the latter is the ultraspinning limit where $J/M \to \infty$. If we keep the mass fixed and increase the spin, the brane profile $m(r)$ flattens as it spreads over an area $\propto a^2$, see fig. 2.2. The rotation parameter in terms of $\Omega$ is

$$a = \frac{1 \pm \sqrt{1 - 4\Omega^2}}{2\Omega} \,, \tag{2.29}$$

and the $+$ sign gives the ultraspinning branch.
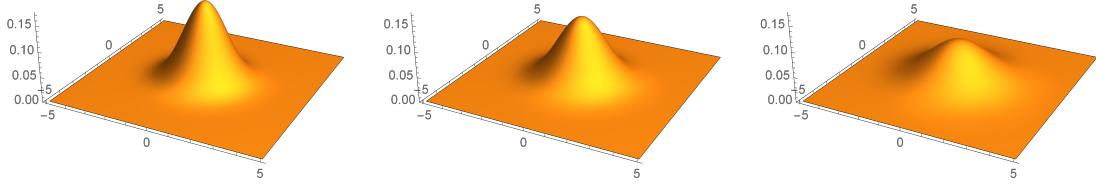
Figure 2.2: Mass density profiles $m(r)$ for black holes with $J/M = 0$ (left), $J/M = 1$ (middle), $J/M = 2$ (right).

### 2.3.1   Traveling rotating black holes

The boost symmetry (1.14) can be used to generate solutions that travel at constant speed $u_i$. Changing to Cartesian coordinates $(x^1, x^2)$, the traveling rotating black hole is described by

$$m(t, x) = m_0 \exp\left(-\frac{(x_i - u_i t)(x^i - u^i t)}{2(1 + a^2)}\right),\tag{2.30}$$

$$v_i = u_i + \frac{a}{1 + a^2}\varepsilon_{ij}(x^j - u^j t).\tag{2.31}$$

## 2.4   Relation to finite D black holes

Here we are going to show that these solutions can be recovered if we start with the known Schwarzschild-Tangherlini and Myers-Perry black holes, and take their limit when $D \to \infty$ in an appropriate manner. Thus, in the following we will refer to the solution (3.1), (2.25) as the MP black hole. This derivation can also guide us how to relate the quantities in the effective theory to physical quantities. The corresponding quantities will be provided in section 2.4.2.

### 2.4.1   Blobs as the limit of large D black holes

The Schwarzschild-Tangherlini and Myers-Perry black holes admit large-$D$ limits s.t. they can be taken as instances of the metric (1.2), (1.3) with arbitrary $p$. We will illustrate this by casting them as gaussian bulges on strings and as bulges on 2-branes.

**Gaussian string**

Begin with the Schwarzschild-Tangherlini solution,

$$ds^2 = -\left(1 - \frac{1}{\hat{r}^n}\right)d\hat{t}^2 + \frac{d\hat{r}^2}{1 - \hat{r}^{-n}} + \hat{r}^2 d\theta^2 + \hat{r}^2 \cos^2\theta d\Omega_n,\tag{2.32}$$

where we have set the horizon radius to one. In analogy to our discussion in the introduction, the sphere $S^{n+1}$ is built here as a fibration of spheres $S^n$ over the interval $\theta \in [-\pi/2, \pi/2]$, with the equator at $\theta = 0$.

In order to take the large-$D$ limit, change $(\hat{r}, \theta) \to (\rho, z)$ as

$$\rho = \hat{r} \cos \theta , \qquad z = \sqrt{n} \, \hat{r} \sin \theta , \tag{2.33}$$

and let $n \to \infty$ while keeping $z$ finite. In this limit we are focusing on a small region around

$$\theta = \mathcal{O}\left(\frac{1}{\sqrt{n}}\right) . \tag{2.34}$$

Introduce

$$\mathsf{R} = \rho^n . \tag{2.35}$$

Then, since

$$\hat{r}^2 = \rho^2 + \frac{z^2}{n} , \tag{2.36}$$

we have, at large $n$,

$$\hat{r}^n = \mathsf{R} \, e^{z^2/2} . \tag{2.37}$$

We are viewing $\rho$ (and $\mathsf{R}$) as the coordinate orthogonal to the brane, and $z$ as the coordinate along the brane. Since the horizon is actually at constant $\hat{r}$, this means that we regard it as a brane that is bent along the $z$ direction.

In these coordinates, and in the limit of large $n$, the solution (2.32) becomes

$$ds^2 \simeq -A d\hat{t}^2 + \frac{1}{n^2} \frac{d\mathsf{R}^2}{A\mathsf{R}^2} + \frac{1}{n}\left(1 + \frac{1}{n} \frac{z^2 e^{-z^2/2}}{A\mathsf{R}}\right) dz^2 + \rho^2 d\Omega_n , \tag{2.38}$$

with

$$A = 1 - \frac{e^{-z^2/2}}{\mathsf{R}} . \tag{2.39}$$

Change to the Eddington-Finkelstein time $t$,

$$t = \hat{t} - \frac{1}{n} \ln(A\mathsf{R}) = \hat{t} - \frac{1}{n} \ln\left(\mathsf{R} - e^{-z^2/2}\right) . \tag{2.40}$$

The solution now takes the form of (1.2) with

$$m(z) = e^{-z^2/2} , \qquad p(z) = z \, e^{-z^2/2} . \tag{2.41}$$

This limit had also been obtained (though in a different gauge) in [53].

## Gaussian singly-rotating membrane

If we extend now the previous limit to involve two directions on the $S^{D-2}$, we can incorporate the effects of rotation on the plane of these directions.

Consider then the Myers-Perry black hole with a single spin in $D = n + 5$ [57],

$$ds^2 = -\left(1 - \frac{1}{\hat{r}^n \Sigma}\right) d\hat{t}^2 + \frac{2a \sin^2 \theta}{\hat{r}^n \Sigma} d\hat{t} d\hat{\phi} + \left(\hat{r}^2 + a^2 + \frac{a^2 \sin^2 \theta}{\hat{r}^n \Sigma}\right) \sin^2 \theta \, d\hat{\phi}^2$$
$$+ \frac{\Sigma}{\Delta} d\hat{r}^2 + \Sigma d\theta^2 + \hat{r}^2 \cos^2 \theta d\Omega_{n+1} \tag{2.42}$$

where

$$\Sigma = \hat{r}^2 + a^2 \cos^2 \theta \,, \qquad \Delta = \hat{r}^2 + a^2 - \frac{1}{\hat{r}^n} \,, \tag{2.43}$$

and $\theta \in [0, \pi/2]$.

The horizon is at $\hat{r} = r_H$, where $\Delta(r_H) = 0$. Then it satisfies

$$r_H = \left( 1 + \frac{a^2}{r_H^2} \right)^{-\frac{1}{n+2}} \,. \tag{2.44}$$

When $n \to \infty$ we have

$$r_H \to 1 \,, \qquad r_H^n \to \frac{1}{1+a^2} \,. \tag{2.45}$$

Now change $(\hat{r}, \theta) \to (\rho, r)$, with

$$\rho = \hat{r} \cos \theta \,, \qquad r = \sqrt{n(\hat{r}^2 + a^2)} \sin \theta \,. \tag{2.46}$$

It is useful to note that

$$\Sigma \left( \frac{d\hat{r}^2}{\hat{r}^2 + a^2} + d\theta^2 \right) + \left( \hat{r}^2 + a^2 \right) \sin^2 \theta \, d\hat{\phi}^2 + \hat{r}^2 \cos^2 \theta d\Omega_{n+1} = d\rho^2 + \frac{dr^2 + r^2 d\hat{\phi}^2}{n} + \rho^2 d\Omega_{n+1} \,. \tag{2.47}$$

$\rho$ is the coordinate orthogonal to the membrane. The membrane worldvolume is described in polar coordinates in which $r$ is the radius and $\hat{\phi}$ the polar angle.

We introduce

$$\mathsf{R} = (1 + a^2)\rho^n \,. \tag{2.48}$$

Then

$$\hat{r}^n = \frac{\mathsf{R}}{1 + a^2} e^{\frac{r^2}{2(1+a^2)}} \,. \tag{2.49}$$

In the new coordinates, expanding in $1/n$, the metric becomes

$$ds^2 \simeq -A d\hat{t}^2 + \frac{1}{n} \frac{2a}{1+a^2} \frac{r^2 e^{-\frac{r^2}{2(1+a^2)}}}{\mathsf{R}} d\hat{t} \, d\hat{\phi} + \frac{r^2}{n} \left( 1 + \frac{r^2}{n} \frac{a^2}{(1+a^2)^2} \frac{e^{-\frac{r^2}{2(1+a^2)}}}{\mathsf{R}} \right) d\hat{\phi}^2$$

$$+ \frac{1}{n^2} \frac{d\mathsf{R}^2}{A\mathsf{R}^2} + \frac{1}{n} \left( 1 + \frac{r^2}{n(1+a^2)^2} \frac{e^{-\frac{r^2}{2(1+a^2)}}}{A\mathsf{R}} \right) dr^2 + \rho^2 d\Omega_{n+1} \,, \tag{2.50}$$

with

$$A = 1 - \frac{e^{-\frac{r^2}{2(1+a^2)}}}{\mathsf{R}} \,. \tag{2.51}$$

In order to go to Eddington-Finkelstein coordinates, change

$$\hat{t} = t + \frac{1}{n} \ln(A\mathsf{R}) \,, \qquad \hat{\phi} = \phi - \frac{1}{n} \frac{a}{1+a^2} \ln(A\mathsf{R}) \,. \tag{2.52}$$

The metric is now of the form of (1.2) with

$$m(r) = e^{-\frac{r^2}{2(1+a^2)}} \,,$$

$$p_r(r) = -\frac{r}{1+a^2} e^{-\frac{r^2}{2(1+a^2)}} \,, \tag{2.53}$$

$$p_\phi(r) = \frac{ar^2}{1+a^2} e^{-\frac{r^2}{2(1+a^2)}} \,.$$

This is the same as we found in (2.25), (2.26), (2.27) (here with $\mathcal{R}_0 = 0$) by direct solution of the large-$D$ effective membrane equations. Therefore the MP black hole is represented as a gaussian blob on the membrane, whose width expands as $a$ grows.

More generally one can show that a MP-solution can be cast as a Gaussian bulge on a $2p$-brane.

### 2.4.2 Physical quantities

A careful study of the matching of the solutions of the effective theory (1.2) with (1.3) to the geometry of an asymptotically flat black hole yields the physical mass, area, spin, angular velocity and surface gravity of the configurations (denoted in boldface), in terms of the effective theory magnitudes defined in equations 1.16, as

$$\mathbf{M} = \frac{\Omega_{n+3}}{16\pi G} r_+^{n+2} \frac{n+3}{2\pi m_0} M \,, \tag{2.54}$$

$$\mathbf{A} = \Omega_{n+3} r_+^{n+3} \frac{1}{2\pi m_0} M \,, \tag{2.55}$$

$$\mathbf{J} = \frac{\Omega_{n+3}}{16\pi G} r_+^{n+3} \frac{1}{2\pi m_0} J \,, \tag{2.56}$$

$$\mathbf{\Omega} = \frac{1}{r_+} \Omega \,, \tag{2.57}$$

$$\boldsymbol{\kappa} = \frac{n}{2r_+} + \frac{1}{2r_+} \ln m_0 \,. \tag{2.58}$$

Here $n = D - 5$, and $r_+$ is a length scale (necessary, since in the effective theory all quantities are dimensionless) that corresponds to the radius of the transverse sphere $S^{n+1}$, with unit volume $\Omega_{n+1}$, at the rotation axis. It can be eliminated in favor of $\boldsymbol{\kappa}$ in the expressions for the other physical quantities. A useful, equivalent form of (2.58) is

$$m_0 = \left( \frac{2\boldsymbol{\kappa} r_+}{n} \right)^n \,. \tag{2.59}$$

Observe that we have distinguished $r_+^{n+2}$ in the mass from $r_+^{n+3}$ in the area and spin, even though they become the same as $n \to \infty$; we do this in order to maintain the correct dimensionality of these magnitudes. Other apparently subleading dependences at large $n$ have also been fixed through matching to known exact solutions—not a necessity but a convenience. The first correction to the surface gravity (and temperature)—which, as we mentioned earlier, is constant at leading large $n$ order—can be consistently determined from the geometry (1.2,1.3).

A convenient parameter to characterize the configurations is the spin per unit mass $J/M$. The corresponding dimensionless physical magnitude is

$$\frac{J}{M} = \frac{D-2}{r_+} \frac{\mathbf{J}}{\mathbf{M}} \,, \tag{2.60}$$

where the horizon radius $r_+$ was invariantly defined above. This allows to translate in a simple manner the parameter $J/M$ of our colliding black hole simulations to the physical magnitudes in a collision at finite $D$. Again, the factor $D - 2$, instead of simply $D$, is chosen to better match known exact solutions, but it need not be accurate for generic configurations.

## 2.5   Rotating black bars

Remarkably, it is also possible to find explicitly a class of stationary but time-dependent, non-axisymmetric exact solutions.

### 2.5.1   Solution

Assume again that $\mathcal{R}$ depends quadratically on $r$, but now allow an angle-dependent stationary profile[1]

$$\mathcal{R} = \mathcal{R}_0 - r^2 F(\phi - \Omega t) \,. \tag{2.61}$$

Plugging this ansatz into (2.18), and setting for convenience $\mathcal{R}_0 = 1$, we get an $r$-dependent equation for $F$. If we consider it at $r = 0$ we get the equation

$$F'' + 4F - 1 = 0 \,, \tag{2.62}$$

which, up to an arbitrary initial value of the phase, is solved by

$$F = \frac{1}{4} + C \cos\left(2(\phi - \Omega t)\right) \tag{2.63}$$

with constant $C$. Inserting this again in eq. (2.18), but considering $r \neq 0$, we find an algebraic equation that is solved for

$$C = \pm \frac{\sqrt{1 - 4\Omega^2}}{4} \,. \tag{2.64}$$

The sign choice here can be absorbed by a phase shift, so the solution we finally obtain is

$$\mathcal{R}(t, r, \phi) = 1 - \frac{r^2}{4}\left(1 + \sqrt{1 - 4\Omega^2} \cos\left(2(\phi - \Omega t)\right)\right) \,. \tag{2.65}$$

The corresponding mass density is

$$m(t, r, \phi) = \exp\left(1 - \frac{r^2}{4}\left(1 + \sqrt{1 - 4\Omega^2} \cos\left(2(\phi - \Omega t)\right)\right)\right) \,, \tag{2.66}$$

and the $p_i$ are given by (2.20).

This mass profile (2.66) has a dipolar dependence on the angle, and thus can be regarded as describing a 'rotating bar', which extends along the angular directions

$$\phi = \Omega t \pm \frac{\pi}{2} \,. \tag{2.67}$$

It is also useful to present the solution in rotating Cartesian coordinates

$$\begin{aligned}
x &= x^1 \cos\Omega t + x^2 \sin\Omega t = r\cos(\phi - \Omega t) \,, \\
y &= x^2 \cos\Omega t - x^2 \sin\Omega t = r\sin(\phi - \Omega t) \,,
\end{aligned} \tag{2.68}$$

---

[1]Regularity at the rotation axis $r = 0$ requires that $\mathcal{R}_0$ be $\phi$-independent.
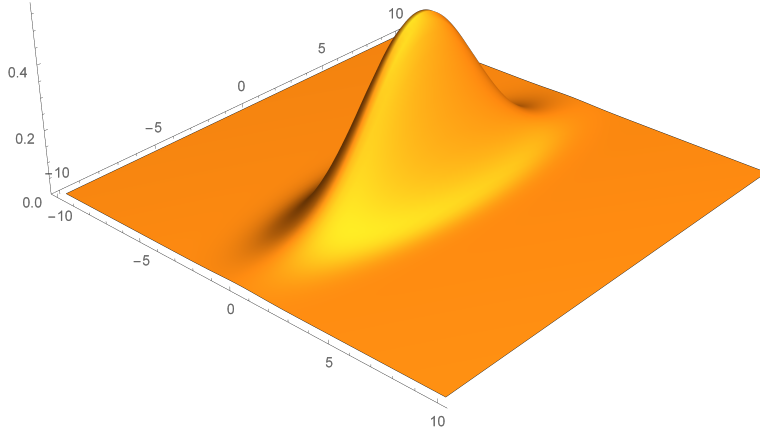
Figure 2.3: Mass density profile $m$ for the black bar with $\Omega = 0.3$.

such that $x$ and $y$ are corotating directions transverse to the bar and along the bar, respectively. If we introduce the length $\ell_\parallel$ and width $\ell_\perp$ of the bar,

$$\ell_\parallel^2 = \frac{2}{1 - \sqrt{1 - 4\Omega^2}} \,,$$
$$\ell_\perp^2 = \frac{2}{1 + \sqrt{1 - 4\Omega^2}} \,, \tag{2.69}$$

then the solution (3.14) reads

$$\mathcal{R}(x, y) = 1 - \frac{x^2}{2\ell_\perp^2} - \frac{y^2}{2\ell_\parallel^2} \,. \tag{2.70}$$

### 2.5.2 Physical properties

The spin per unit mass of this solution is[2]

$$\frac{J}{M} = \frac{1}{\Omega} \,. \tag{2.71}$$

The angular velocity in (3.14) is restricted to $0 \leq \Omega \leq 1/2$. When $\Omega = 1/2$ we recover a rotating MP black hole (2.22) with $a = 1$. Starting from this solution and decreasing $\Omega$ the profile (2.66) develops an increasingly longer and narrower shape (see fig. 2.3), with longitudinal extent $\ell_\parallel$ and transverse thickness $\ell_\perp$. If we keep the mass fixed, the height $m_0$ of the bar decreases in proportion to $\Omega$. In the limit $\Omega \to 0$ we have

$$\ell_\parallel \to \infty \,, \qquad \ell_\perp \to 1 \,, \tag{2.72}$$

and thus we recover an infinite, static black string.

At $\Omega = 1/2$ we have a bifurcation into MP black holes and black bars, see fig. 2.4. In

---

[2]Henceforth we assume $\Omega \geq 0$ without loss of generality.
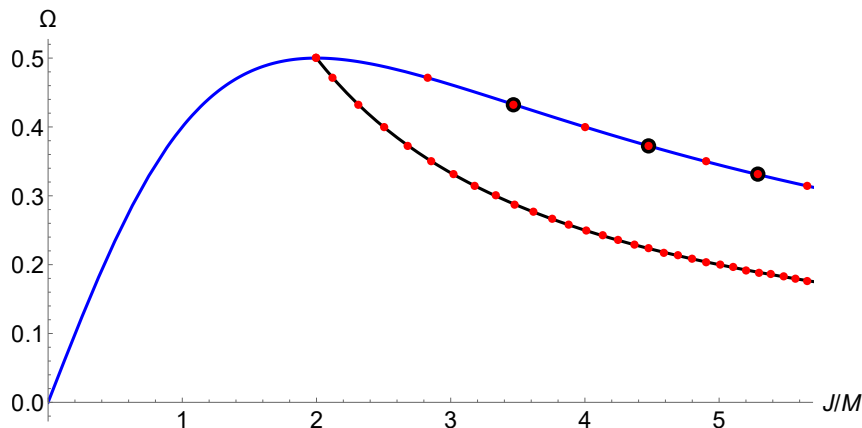
Figure 2.4: Phases of Myers-Perry black holes (blue line) and black bars (black line) in the plane $(J/M, \Omega)$. The red dots indicate the presence of non-axisymmetric corotating zero modes for MP black holes (2.88) and for black bars (2.143). The ones in the MP branch encircled by a black dot indicate also axisymmetric zero modes (2.87). New families of solutions branch off all these points and are explored in 4.

both the MP black hole and the black bar the angular velocity decreases from that point on, but for the same spin and mass, the bar rotates more slowly than the MP black hole. That is, it has a larger moment of inertia. The solutions with the same mass also have the same area, so we cannot predict on thermodynamic grounds which of the two solutions is preferred for given $M$ and $J$. This requires a computation to a higher order in the $1/D$ expansion. Nevertheless, since as we will see the MP black holes become unstable for $J/M > 2$, and the black bars resemble black strings of finite length, we expect that the black bar is dynamically stable after the bifurcation[3] and also thermodynamically preferred over the MP black hole.

When $\Omega$ is small the length of the bar is $\ell_\parallel \sim 1/\Omega$ and we can easily see that $J$ and $M$ behave like in a rigidly rotating solid,

$$J \sim M \ell_\parallel^2 \Omega \,. \tag{2.73}$$

A similar relation has been known since long ago to also hold for the ultraspinning MP black hole, with $\ell_\parallel \sim a$ [58] and also for black rings.

### 2.5.3   Stationarity of black bars

It may seem surprising that a rotating black bar exists as a stationary configuration: should it not be radiating gravitational waves?

The reason it does not is that in the large-$D$ limit the gravitational radiation decouples from the effective membrane [22, 24, 59]. The decoupling actually holds to all perturbative orders in the $1/D$ expansion.[4] In other words, the decay rate of a black bar that is radiating gravitational waves must be non-perturbatively small in $1/D$.

---

[3]But only until the appearance of an instability of the black bar at $J/M = 3/\sqrt{2} \approx 2.12$, see sec. 2.7.

[4]The rotating black bar would cease to be stationary, without still radiating, if the effective theory at higher perturbation orders in $1/D$ gave rise to dissipation from squared vorticity terms.

We can easily estimate this rate. The bar has length $\sim \Omega^{-1}$, and when it rotates it emits waves with frequency $\Omega$. The radiating power is then

$$P \sim GM^2\Omega^{D-2} \,. \tag{2.74}$$

Since $\Omega < 1$, this implies that the decay rate

$$\frac{\dot{M}}{M} = \frac{P}{M} \sim GM\,\Omega^{D-2} \tag{2.75}$$

is small exponentially in $D$.

Bar deformations of rotating black holes in $D = 6, 7$ have been observed in full numerical simulations in [54]. These black bars spin down to a stable configuration through the emission of gravitational waves. The relaxation timescale in $D = 6$ is found to be $\sim 100r_0$, and in $D = 7$ even larger than this. So indeed the black bars are long-lived, in agreement with our arguments.

## 2.6 Quasinormal modes and stability of MP black holes

Now we analyze the small, linearized perturbations of the previous solutions.

We begin by studying zero modes of the MP black holes, which leave the solution stationary. Their computation is simpler than the generic non-zero frequency quasinormal modes, and they are particularly important since they indicate the onset of instabilities and new branches of stationary solutions. When we solve afterwards for the modes with finite frequency, we will recover the zero modes as special cases.

### 2.6.1 Corotating zero modes

We perturb the rotating MP solution (3.1), while remaining in the stationary sector, by making

$$\mathcal{R}(r) = \frac{2}{1+a^2}\left(1 - \frac{r^2}{4}\right) + \epsilon\,\delta\mathcal{R}(r)e^{im_\phi(\phi-\Omega t)}\,, \tag{2.76}$$

with

$$\Omega = \frac{a}{1+a^2}\,, \tag{2.77}$$

and integer $m_\phi$. When $m_\phi = 0$ these are axisymmetric, time-independent perturbations, and therefore are properly zero modes. When $m_\phi \neq 0$ their frequency

$$\omega = m_\phi\Omega \tag{2.78}$$

is real and such that the perturbation corotates with the unperturbed black hole. Therefore we also regard them as zero modes. We can still use eq. (2.18) to study them. Note that corotating modes satisfying (2.78) are at the threshold for superradiance. Below we will comment further on this point.

We adjust $\delta\mathcal{R}$ by an additive constant so as to maintain $\mathcal{R}_0$ fixed. Then we find the equation

$$\delta\mathcal{R}'' + \left(\frac{1}{r} - \frac{r}{1+a^2}\right)\delta\mathcal{R}' + \left(1 - \frac{m_\phi^2}{r^2}\right)\delta\mathcal{R} = 0\,. \tag{2.79}$$

It can be shown that this is precisely the equation for spheroidal harmonics on $S^{D-2}$, in the limit $n \to \infty$, when we focus on small polar angles $\theta \sim r/\sqrt{n}$. The appearance of this equation in this problem is a remarkable illustration of the extent to which the black brane equations (1.6), (1.7), manage to capture the dynamics of localized black holes. Even though eqns. (1.6) and (1.7) should seemingly only know about fluctuations of planar black branes, they also describe accurately the vibrations of a spheroidal, large-$D$ MP black hole. This explains why in our subsequent analyses we will repeatedly encounter this equation.

Eq. (2.79) has a regular singular point at $r = 0$ and an irregular point at $r = \infty$, and it can be transformed into a confluent hypergeometric equation. The solutions that are regular at $r = 0$ and which avoid non-analytic behavior $\sim e^{r^2}$ at $r \to \infty$ are expressed in terms of associated Laguerre polynomials $L_k^{|m_\phi|}(x)$, in the form

$$\delta\mathcal{R}(r) = r^{|m_\phi|} L_k^{|m_\phi|}\left(\frac{r^2}{2(1+a^2)}\right) , \tag{2.80}$$

with non-negative integer index

$$k = \frac{a^2 + 1 - |m_\phi|}{2} . \tag{2.81}$$

Then, MP black holes admit corotating zero mode perturbations only when the rotation parameter has the critical value

$$a_c^2 = |m_\phi| + 2k - 1 , \qquad k = 0, 1, 2, \ldots \tag{2.82}$$

The index $k$ has the interpretation of a 'radial overtone' number, such that, for a given value of $m_\phi$, the number of oscillations along $r$ increases with $k$. It is convenient to introduce the angular momentum number $\ell$

$$\ell = 2k + |m_\phi| \tag{2.83}$$

for the spherical harmonics of $S^{D-2}$ (see sec. 2.6.3), in terms of which the critical values of the rotation are

$$a_c^2 = \ell - 1 . \tag{2.84}$$

These values are the same as found in [26]. The behavior of (3.25) at large $r$, $\mathcal{R} \sim r^\ell$, also matches the dependence $\sim \theta^\ell$ at small $\theta$ of the mode solutions in [26].

We analyze now these solutions in more detail. Note that the solution for $|m_\phi| = 1$ and $k = 0$ corresponds to a shift of the center of the Schwarzschild solution away from $r = 0$, so it is pure gauge.

**Axisymmetric, time-independent zero modes**

These are obtained when $m_\phi = 0$. In this case the solutions are Laguerre polynomials,

$$\delta\mathcal{R}(r) = L_k\left(\frac{r^2}{4k}\right) , \tag{2.85}$$

for $k = 1, 2, \ldots$

When $k = 1$ and therefore $a = 1$, we have

$$\delta\mathcal{R}(r) = 1 - \frac{r^2}{4}, \tag{2.86}$$

which does not yield any new solution: it is a perturbation that varies $a$, adding angular momentum to the MP black hole while remaining in the same family of solutions. It has been known for some time that these zero mode deformations of MP black holes exist at the maximum of $\Omega$ in any $D \geq 6$ [60].

The modes for $k = 2, 3, \ldots$, which appear at

$$a = \sqrt{3}, \sqrt{5}, \sqrt{7}, \ldots, \qquad \Omega = \frac{\sqrt{3}}{4}, \frac{\sqrt{5}}{6}, \frac{\sqrt{6}}{7}, \ldots \tag{2.87}$$

are deformations that should lead to new branches of stationary axisymmetric 'bumpy black holes' (in this context also called black ripples see chapter 4). These had been first conjectured to exist in $D \geq 6$ in [58]. The zero modes were explicitly constructed numerically in $D = 6, 7, 8$ in [60], and their non-linear extension in [61, 62].

**Non-axisymmetric, corotating zero modes**

When we consider $|m_\phi| > 0$ there are zero modes for

$$a = 1, \sqrt{2}, \sqrt{3}, 2, \ldots, \qquad \Omega = \frac{1}{2}, \frac{\sqrt{2}}{3}, \frac{\sqrt{3}}{4}, \frac{2}{5}, \ldots. \tag{2.88}$$

Observe that when different values of $m_\phi$ and $k$ combine to give the same value of $|m_\phi| + 2k$, then the same solution admits several zero modes.

The 'fundamental' modes with $k = 0$ have a simple radial profile,

$$\delta\mathcal{R}(r) = r^{|m_\phi|}. \tag{2.89}$$

Of these modes, the first non-trivial one, with $|m_\phi| = 2$, corresponds to the black bar in a perturbative expansion around $a = 1$, namely (taking a real perturbation)

$$\mathcal{R}(r) = 1 - \frac{r^2}{4} + \epsilon\, r^2 \cos(2\phi - t). \tag{2.90}$$

Higher values of $|m_\phi|$ signal new branches of solutions with higher multipole-bar deformations. Solutions with $k > 0$ involve additional, higher powers of $r$, so they have more radial oscillations and can be regarded as 'bumpy $m_\phi$-bar modes'. We discuss the corresponding non-linear solution in chapter 4, where they are dubbed as 'black flowers'.

### 2.6.2 Quasinormal modes

In order to study the spectrum of QNMs at arbitrary finite frequency, we need to turn to the full equations (2.8) (2.9), (2.10). We perturb around the MP black hole, taking

$$m = \bar{m}(r) + \epsilon\, e^{-i\omega t + im_\phi\phi}\, \delta m(r), \tag{2.91}$$

$$p_r = \bar{p}_r(r) + \epsilon\, e^{-i\omega t + im_\phi\phi}\, \delta p_r(r), \tag{2.92}$$

$$p_\phi = \bar{p}_\phi(r) + \epsilon\, e^{-i\omega t + im_\phi\phi}\, \delta p_\phi(r), \tag{2.93}$$

with the background $\bar{m}$, $\bar{p}_r$, $\bar{p}_\phi$ given by (2.25), (2.26), (2.27), and working to linear order in $\epsilon$. By doing so, we obtain three coupled ODEs for the radial profiles. Quite remarkably, the spectrum of QNM can be found analytically. To do so, we first find a decoupled sixth order equation for $\delta m$, which can be easily obtained by taking linear combinations of the fluctuation equations. This equation takes the form

$$\mathcal{L}_1 \mathcal{L}_2 \mathcal{L}_3 \delta \mathcal{R}(r) = 0 \,, \tag{2.94}$$

where (up to irrelevant constant factors)

$$\delta \mathcal{R}(r) = \frac{\delta m(r)}{\bar{m}(r)} = \exp\left(\frac{r^2}{2(1+a^2)}\right) \delta m(r) \,, \tag{2.95}$$

and $\mathcal{L}_i$ are three second order, linear differential operators of the form

$$\mathcal{L}_i = \frac{d^2}{dr^2} + \left(\frac{1}{r} - \frac{r}{1+a^2}\right)\frac{d}{dr} + \frac{m_\phi + 2k_i}{1+a^2} - \frac{m_\phi^2}{r^2} \,. \tag{2.96}$$

Here we recognize again the confluent hypergeometric operators of sec. 2.6.3, whose eigenfunctions are spheroidal harmonics of the $S^{D-2}$ at large $D$.

The constants $k_i$ are the three roots of the cubic equation

$$0 = k^3 - \frac{\gamma_\omega}{2}k^2 + \frac{\gamma_\omega\left(1 - a^2 + \gamma_\omega\right) + 2\left(a^2 - 3\right) - 3(a-i)^2 m_\phi}{12}k \tag{2.97}$$
$$+ \frac{\left(a^2 + 6ia - \gamma_\omega - 3\right)\left(a^4 - 6ia^3 - 2(a-3i)a\gamma_\omega - 9(a-i)^2 m_\phi - 18ia + \gamma_\omega^2 - 9\right)}{216} \,,$$

where we have introduced

$$\gamma_\omega = 3i\left(a^2 + 1\right)\omega + a^2 - 3iam_\phi - 3m_\phi + 3 \,. \tag{2.98}$$

For any $k_i$ the operators (2.96) commute. Thus, the profiles correspond to the solutions of $\mathcal{L}_i \delta \mathcal{R} = 0$, for $i = 1, 2, 3$. Since the $k_i$ are all roots of the same polynomial, the three equations are equivalent. The solutions that are regular at $r = 0$ and at infinity are given by the associated Laguerre polynomials (3.25) with

$$k = 0, 1, 2, 3 \ldots \tag{2.99}$$

This imposes a quantization condition on the frequencies that appear in (2.97), which is itself a cubic equation in $\omega$. In order to write it more manifestly as such, it is convenient to use, instead of $k$, the angular momentum parameter $\ell$ of (2.83). Using it, (2.97) can be rewritten as[5]

$$0 = \omega^3 - \frac{\omega^2\left(3(a|m_\phi| - i\ell) + 4i\right)}{a^2 + 1}$$
$$+ \frac{\omega\left(a^2\left(3|m_\phi|^2 + \ell - 4\right) - 6ia|m_\phi|(\ell - 1) - (\ell - 1)(3\ell - 4)\right)}{\left(a^2 + 1\right)^2}$$
$$- \frac{(a|m_\phi| - i\ell)\left(a^2\left(|m_\phi|^2 + \ell - 2\right) - 2ia|m_\phi|(\ell - 1) - (\ell - 2)(\ell - 1)\right)}{\left(a^2 + 1\right)^3} \,. \tag{2.100}$$

---

[5]This agrees with the result of [26], after correcting typos in their eq. (4.20).

For a given solution of this equation, eqs. (3.25) and (2.95) yield the profile of $\delta m(r)$ as

$$\delta m = e^{-\frac{r^2}{2(1+a^2)}} r^{|m_\phi|} L_k^{|m_\phi|}\left(\frac{r^2}{2(1+a^2)}\right). \tag{2.101}$$

Using this in the linearized perturbation equations we can obtain $\delta p_r$ and $\delta p_\phi$, which are uniquely determined once regularity at infinity is imposed. They are finite polynomials but their general expressions are cumbersome, so we do not give them explicitly. Nevertheless, one can readily obtain the coefficients of the polynomials in particular cases by inserting the specific polynomial (2.101) in the linearized equations of motion and solving the resulting algebraic equations for the coefficients.

The solution to the cubic (2.100) for $\omega$ can be given explicitly for generic values of $\ell$ and $m_\phi$, but it is rather unilluminating. Instead, we will discuss generic features of axisymmetric and non-axisymmetric modes, and then consider certain special modes.

**Axisymmetric modes: $m_\phi = 0$**

- $k = 0$, $\ell = 0$. There are no non-trivial regular modes. Besides the trivial constant mode with $\omega = 0$ we find

$$\omega = \frac{2}{1 + a^2}(i \pm a), \tag{2.102}$$

which appear to be unstable modes, but their profiles for $p_\phi$ approach a constant at infinity, which results in unphysical infinite angular momentum.

- $k \geq 1$, $\ell = 2, 4, 6, \ldots$. All the solutions to (2.100) yield regular profiles of the form

$$\delta p_r = e^{-\frac{r^2}{2(1+a^2)}} r \sum_{i=0}^{k} \delta p_r^{(i)} r^{2i}, \tag{2.103}$$

$$\delta p_\phi = e^{-\frac{r^2}{2(1+a^2)}} r^2 \sum_{i=0}^{k} \delta p_\phi^{(i)} r^{2i}. \tag{2.104}$$

**Non-axisymmetric modes: $|m_\phi| \geq 1$**

- $k = 0$, $\ell = |m_\phi|$. The frequencies of these fundamental quasinormal 'bar-modes' obtained from (2.100) are

$$\omega_0 = \frac{(|m_\phi| + 2)a - i(|m_\phi| - 2)}{1 + a^2}, \tag{2.105}$$

$$\omega_\pm = \frac{\sqrt{|m_\phi| - 1}}{1 + a^2}\left(a\sqrt{|m_\phi| - 1} \pm 1 - i\left(\sqrt{|m_\phi| - 1} \mp a\right)\right). \tag{2.106}$$

Modes with $\omega = \omega_0$ have momenta which are regular for $|m_\phi| > 2$, and they are stable. For $|m_\phi| = 1, 2$ they are singular, *i.e.,* unphysical.

Modes with $\omega = \omega_\pm$ are regular for $|m_\phi| \geq 1$ and have profiles of the form

$$\delta p_r = e^{-\frac{r^2}{2(1+a^2)}} r^{|m_\phi|+1} \delta p_r^{(1)}, \tag{2.107}$$

$$\delta p_\phi = e^{-\frac{r^2}{2(1+a^2)}} r^{|m_\phi|+2} \delta p_\phi^{(1)}. \tag{2.108}$$

The mode $\omega_+$ with $|m_\phi| = 2$ and $a = 1$ is the corotating black bar mode (2.90). More generally, the modes $\omega_+$ with $|m_\phi| \geq 2$ and $\omega_+ = a = \sqrt{|m_\phi| - 1}$ are purely real and correspond to the non-axisymmetric corotating zero-modes in (2.88).

- $k \geq 1$. All profiles are regular, with momenta of the form

$$\delta p_r = e^{-\frac{r^2}{2(1+a^2)}} r^{|m_\phi|-1} \sum_{i=0}^{k+1} \delta p_r^{(i)} r^{2i} \,, \tag{2.109}$$

$$\delta p_\phi = e^{-\frac{r^2}{2(1+a^2)}} r^{|m_\phi|} \sum_{i=0}^{k+1} \delta p_\phi^{(i)} r^{2i} \,. \tag{2.110}$$

When written in Cartesian coordinates these modes are manifestly regular at the origin, even when $|m_\phi| = 1$, for which the radial profiles behave as $p_r \sim 1$, $p_\phi \sim r$ near $r = 0$. The contribution from the angular part $e^{im_\phi\phi}$ plays a crucial role for regularity.

These modes can become unstable for sufficiently large values of $a$, as we discuss below.

**Schwarzschild modes**

When $a = 0$ the solutions to (2.100) are

$$\omega_\pm^{Sch} = \pm\sqrt{\ell - 1} - i(\ell - 1), \qquad \omega_0^{Sch} = -i(\ell - 2) \,. \tag{2.111}$$

Modes with frequencies $\omega_\pm^{Sch}$ are physical (have finite total angular momentum) for $\ell > 1$. This matches the earlier result of [22] for the quasinormal frequencies that are scalars of $S^{D-2}$ for the Schwarzschild solution at large $D$.

Modes with frequency $\omega_0^{Sch}$ are regular only for $\ell > 2$. They can be seen to have constant $\delta\mathcal{R}$, which identifies them as vector deformations of the $S^{D-2}$. The calculation of [22] gave the vector frequency as $\omega_0 = -i(\ell - 1)$. The difference with (2.111) is simply due to the fact that as shown in sec. 2.6.3 $\ell$ can be identified using the scalar spherical harmonics, while for the vector harmonics $\ell$ is shifted by 1.

All the allowed modes in (2.111) are stable, in agreement with the proven mode stability of the Schwarzschild-Tangherlini solution in all $D$ [63].

**Near-critical unstable modes**

For

$$a = a_c \equiv \sqrt{\ell - 1} \,, \qquad \omega = |m_\phi| \frac{a}{1 + a^2} \,, \qquad \ell \geq 2 \,, \tag{2.112}$$

we recover the corotating zero modes discussed in section 2.6.1. These modes have purely real frequency, but they mark the appearance of unstable modes as $a$ increases past each critical value $a_c$. We can verify this by moving slightly away from the critical points, by setting

$$\omega = |m_\phi| \frac{a_c}{1 + a_c^2} + \delta\omega \,, \qquad a = a_c + \delta a \,. \tag{2.113}$$

Linearizing (2.100) in $\delta\omega$ and $\delta a$ we find that the frequency develops an imaginary part,

$$\text{Im}\,\omega = \delta a\,\frac{a_c}{a_c^2(1+a_c^2)^2+m_\phi^2}\left(\frac{2m_\phi^2}{1+a_c^2}+a_c^4-1\right).\tag{2.114}$$

Since $a_c \geq 1$, we see that $\text{Im}\,\omega > 0$ whenever $\delta a > 0$, so the mode is unstable, while if $\delta a < 0$ the mode has $\text{Im}\,\omega < 0$ and therefore is stable. Hence, as the rotation increases crossing each of the critical values, a new unstable mode is added to the MP black hole.

Eq. (2.114) gives the growth rate of the bar-mode instability near the threshold ($a_c = 1$ and $m_\phi = 2$) as

$$\text{Im}\,\omega = \frac{1}{2}\delta a\,.\tag{2.115}$$

Interestingly, this unstable growth rate of bar modes has been computed numerically in $D = 6, 7$ in [54] and [23], who find (in units where $r_0 = 1$)

$$\text{Im}\,\omega \sim C_\tau \delta a\tag{2.116}$$

with

$$C_\tau \sim 0.51 \quad (D = 6) \qquad C_\tau \sim 0.54 \quad (D = 7) \qquad [54]\,,\tag{2.117}$$

$$C_\tau \sim 0.521 \quad (D = 6, 7) \qquad [23]\,.\tag{2.118}$$

The leading-order large-$D$ result from (2.115),

$$C_\tau = 1/2\tag{2.119}$$

is in agreement with the numerical calculations to a few percent level. More generally one can readily verify that the plots of quasinormal frequencies, both real and imaginary, obtained from (2.100) as a function of $a$ agree very well with the results presented in [23].

**Bar modes and the CFS instability**
The real part of the frequency of the bar mode near the critical point is

$$\text{Re}\,\omega = |m_\phi|\Omega - \frac{1}{4}\delta a\,|m_\phi|\,,\tag{2.120}$$

so we see that as the rotation increases, the stable mode before the critical rotation (with $\delta a < 0$), rotates faster than the black hole, whereas the unstable mode (with $\delta a > 0$) rotates more slowly than the black hole. The superradiant limit $\omega = |m_\phi|\Omega$ corresponds of course to exact corotation.

This behavior is strongly reminiscent of the Chandrasekhar-Friedman-Schutz (CFS) instability in neutron stars [64, 65]: unstable modes are present only for perturbations that rotate in the same sense that the star but more slowly than it. This is because when the perturbation moves backwards relative to the star, but forwards relative to inertial observers, it excites the emission of gravitational waves that remove positive angular momentum from the mode, driving the deformation even slower. In our set up the emission of gravitational waves is suppressed, so the details of the instability mechanism are not the same, but it seems plausible that the two phenomena are related.

### 2.6.3   Spheroidal harmonics at large $D$

Here we analyze scalar spheroidal harmonics at large $D$ and relate them to our study of quasinormal perturbations of gaussian black-hole lumps in sec. 2.6. Initially we follow appendix C of [26], but then we depart from it so as to highlight the differences and connections between their approach and ours.[6]

As in [26], we study the massless scalar field equation

$$\Box \Psi = 0 \tag{2.121}$$

in $D = n + 5$ dimensions, written in spheroidal coordinates,

$$ds^2 = -dt^2 + (\hat{r}^2 + a^2 \cos^2 \theta) \left( \frac{d\hat{r}^2}{\hat{r}^2 + a^2} + d\theta^2 \right)$$
$$+ (\hat{r}^2 + a^2) \sin^2 \theta \, d\phi^2 + \hat{r}^2 \cos^2 \theta \, d\Omega_{n+1} \tag{2.122}$$

(appropriate for embedding a rotating, MP-type, large-$D$ membrane).

We separate variables as

$$\Psi = e^{-i\omega t} e^{im_\phi \phi} \psi(\hat{r}) S(\theta) \,, \tag{2.123}$$

where, in order to avoid inessential details, we are assuming no dependence on the angles of the sphere $S^{n+1}$. Introducing a separation constant $\Lambda$, we obtain the equations[7]

$$\left( \frac{1}{\hat{r}^{n+1}} \frac{d}{d\hat{r}} (\hat{r}^2 + a^2) \hat{r}^{n+1} \frac{d}{d\hat{r}} + \frac{m_\phi^2 a^2}{\hat{r}^2 + a^2} + \omega^2 \hat{r}^2 - \Lambda \right) \psi(\hat{r}) = 0 \tag{2.124}$$

and

$$\left( \frac{d^2}{d\theta^2} + (\cot \theta - (n+1) \tan \theta) \frac{d}{d\theta} - \frac{m_\phi^2}{\sin^2 \theta} + \omega^2 a^2 \cos^2 \theta + \Lambda \right) S(\theta) = 0 \,. \tag{2.125}$$

When $a = 0$ we get the usual scalar spherical harmonics, with the separation constant quantized as

$$\Lambda = \ell(\ell + n + 2) \,, \tag{2.126}$$

where $\ell$ is a non-negative integer. This result indicates that if we consider $\ell = \mathcal{O}(1)$, then we must have $\Lambda = \mathcal{O}(n)$. The authors of [26] argue that it is appropriate to extend this behavior to $a \neq 0$ and set

$$\Lambda = n\ell + \mathcal{O}(1) \,. \tag{2.127}$$

They then proceed to take the the limit $n \to \infty$ in (2.125) while keeping $\theta = \mathcal{O}(1)$. This yields, to leading order,

$$\frac{dS(\theta)}{d\theta} = \frac{\ell}{\tan \theta} S(\theta) \,, \tag{2.128}$$

---

[6]Related aspects have been analyzed by K. Tanabe, to whom we are indebted for private communications.

[7]The differences with [26] are a shift in the definition of $\Lambda$ and a corrected typo in their radial equation, both inconsequential to the rest of the analysis.

which is solved by

$$S_\ell(\theta) = \sin^\ell \theta\,. \tag{2.129}$$

Crucially, note that in the limit from (2.125) to (2.128) the latter has become a first order equation —so the condition of regularity at $\theta = \pi/2$, which leads to the quantization of $\ell$, is mysteriously absent—, and its solutions $S_\ell(\theta)$ have lost all the characteristic structure of the spherical harmonics with nodes in the angular direction. These two features are intimately related, and point to the fact that when $n$ is large, the angular structure of the spherical harmonics is hidden within a small region $\theta = \mathcal{O}\left(1/\sqrt{n}\right)$, which is invisible when we consider $\theta = \mathcal{O}\left(1\right)$.

In order to reveal this fine structure, we first rescale the angle in the by now familiar manner (cf. (2.46)),

$$\theta = \frac{r}{\sqrt{n(1 + a^2)}}\,, \tag{2.130}$$

so that, when we now take $n \to \infty$, (2.125) becomes

$$\left(\frac{d^2}{dr^2} + \left(\frac{1}{r} - \frac{r}{1 + a^2}\right)\frac{d}{dr} + \frac{\ell}{1 + a^2} - \frac{m_\phi^2}{r^2}\right)S(r) = 0\,. \tag{2.131}$$

This is a second-order equation, exactly the kind of confluent hypergeometric equation that we encounter when we study perturbations of the gaussian MP black holes in sec. 2.6. Requiring regularity at both $r = 0$ and $r \to \infty$, its solutions are given in terms of associated Laguerre polynomials,

$$S(r) = r^{|m_\phi|} L_k^{|m_\phi|}\left(\frac{r^2}{2(1 + a^2)}\right)\,, \tag{2.132}$$

where the non-negative integer index $k$ specifies the quantization condition on $\ell$ through the relation (2.83).

Now the eigenfunctions (2.132) have the expected $k$ nodes away from $r = 0$. Moreover, since the $L_k^{|m_\phi|}$ are polynomials of $k$-th order, then at large values of $r$ we have

$$S(r) \sim r^\ell\,, \tag{2.133}$$

which correctly matches the behavior of (2.129) at small $\theta$.

We conclude that our approach to localized black holes based on the effective black brane equations is able to accurately capture the detailed structure of linear perturbations of a black hole, and in particular its quasinormal modes —not only the frequency spectrum, but also their waveforms. It can be smoothly continued into the approach of [26] at larger angles $\theta = \mathcal{O}\left(1\right)$, by asymptotic matching over a common region where $1 \ll r \ll \sqrt{n}$, i.e., $1/\sqrt{n} \ll \theta \ll 1$.

## 2.7 Corotating perturbations of black bars

Black bars approach black strings as $\Omega \to 0$, so it is natural to expect that at sufficiently small $\Omega$ they develop instabilities similar to the Gregory-Laflamme instability of black

strings. This argument, however, does not determine at what values of $\Omega$ the instabilities set in. This requires a perturbative analysis of finite black bars with non-zero $\Omega$.

The generic linearized perturbations of black bars with $0 < \Omega < 1/2$ are rather more complicated than those of either the black strings or the MP black holes. Nevertheless, using (2.18) we have been able to explicitly obtain corotating, zero mode perturbations. These appear at discrete values of $\Omega$, and approach the GL zero modes of a black string as $\Omega \to 0$. As with the MP black holes, we expect that these zero modes mark the addition of new unstable modes, as well as indicate new branches of stationary, 'bumpy black bar' solutions.

Using the Cartesian coordinates of (3.15), the equation for corotating linear perturbations $\delta\mathcal{R}$ is

$$\nabla^2 \delta\mathcal{R} - \left( \frac{x}{\ell_\perp^2} \partial_x + \frac{y}{\ell_\parallel^2} \partial_y \right) \delta\mathcal{R} + \delta\mathcal{R} = 0 \,. \tag{2.134}$$

We look for factorized solutions

$$\delta\mathcal{R} = f_x(x) f_y(y) \,. \tag{2.135}$$

These must satisfy

$$\left( \partial_x^2 - \frac{x}{\ell_\perp^2} \partial_x + 1 \right) f_x \; = \frac{n_y}{\ell_\parallel^2} f_x \,, \tag{2.136}$$

$$\left( \partial_y^2 - \frac{y}{\ell_\parallel^2} \partial_y \right) f_y \; = -\frac{n_y}{\ell_\parallel^2} f_y \,, \tag{2.137}$$

where, for later convenience, we have written the separation constant as $\frac{n_y}{\ell_\parallel^2}$.

These equations are again of confluent hypergeometric type. If we demand regular, algebraically-bounded behavior at the irregular point at infinity, the solutions are Hermite polynomials

$$f_x(x) = H_{n_x} \left( \frac{x}{\sqrt{2}\ell_\perp} \right) \,, \qquad f_y(y) = H_{n_y} \left( \frac{y}{\sqrt{2}\ell_\parallel} \right) \,, \tag{2.138}$$

where $n_x$ is another constant given in terms of $n_y$ and $\Omega$ by

$$n_x = \ell_\perp^2 - \frac{\ell_\perp^2}{\ell_\parallel^2} n_y \,. \tag{2.139}$$

The solutions are finite polynomials only if $n_x$ and $n_y$ take non-negative integer values. Therefore, co-rotating zero modes exist for a discrete set of values of $\Omega$ determined by solving (2.139). This gives

$$\Omega = \frac{\sqrt{1 - n_x}\sqrt{n_y - 1}}{|n_y - n_x|} \tag{2.140}$$

(recall we only consider $\Omega \geq 0$).

When $\Omega = 0$, which is a static, infinite black string and is obtained for either $n_x = 1$ or $n_y = 1$, we do not obtain anything new. The perturbation with $n_x = 1$ is simply a translation of the black string in the orthogonal direction $x$, while $n_y = 1$ are sinusoidal deformations along $y$ corresponding to the GL zero modes of a black string.
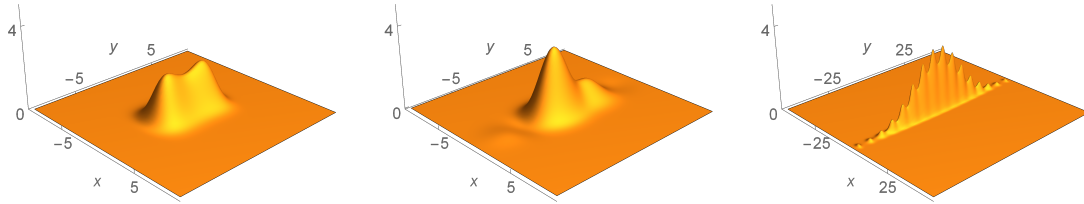
Figure 2.5: Mass density profile $m(x, y) = \exp(\mathcal{R} + \epsilon \, \delta\mathcal{R})$ for black bars perturbed by zero modes. From left to right: perturbations with $n_y = 4, 5, 200$.

There is only one mode that is not constant along the orthogonal direction $x$, *i.e.*, with $n_x \neq 0$, namely, $n_x = 2$ and $n_y = 0$. However, this is the bar-mode along $x$ of the $\Omega = 1/2$ MP black hole (*i.e.*, (2.90)), so again we do not get any new physical solution.

The remaining modes all have $n_x = 0$ and thus are uniform along $x$. They have

$$\Omega = \frac{\sqrt{n_y - 1}}{n_y} \, , \qquad \ell_{\parallel}^2 = n_y \, , \qquad \ell_{\perp}^2 = \frac{n_y}{n_y - 1} \, , \tag{2.141}$$

and

$$\delta\mathcal{R} = H_{n_y}\left(\frac{y}{\sqrt{2n_y}}\right) \, . \tag{2.142}$$

For $n_y = 2$ this is again a bar-mode of the $\Omega = 1/2$ MP black hole, so we disregard it. However, for

$$n_y = 3, 4, 5, \dots, \qquad \Omega = \frac{\sqrt{2}}{3}, \frac{\sqrt{3}}{4}, \frac{2}{5} \, \dots \tag{2.143}$$

we find genuinely new zero modes, which extend all the way down to $\Omega = 0$ as $n_y \to \infty$. Remarkably, these are the same values (2.88) of $\Omega$ for which the MP black holes admit zero modes (the one at $\Omega = 1/2$ gives the black bar itself), even if the spins of the corresponding solutions are different (see fig. 2.4).

These perturbations create bumps along the length of the black bars, as shown in figure 2.5. The first non-trivial mode, with

$$n_y = 3 \, , \qquad \Omega = \frac{\sqrt{2}}{3} \approx 0.47 \, , \tag{2.144}$$

has the profile

$$\delta\mathcal{R} = -\left(\frac{2}{3}\right)^{3/2} y \left(9 - y^2\right) \, , \tag{2.145}$$

which is odd in $y$. We are not representing it in fig. 2.5 since its skewed gaussian shape is not very illustrative. The next mode, with

$$n_y = 4 \, , \qquad \Omega = \frac{\sqrt{3}}{4} \approx 0.43 \, , \tag{2.146}$$

has the profile

$$\delta\mathcal{R} = 12 - 6y^2 + \frac{y^4}{4} \, , \tag{2.147}$$

and is shown in fig. 2.5 (left).

When continued into the non-linear regime, both the even and the odd modes give rise to branches of bumpy black bars. However, the even modes can be added or subtracted from the initial black bar, creating a dip or a rise at its center. These two possibilities will lead to two different branches of bumpy black bars, analogous to what happens for bumpy black holes [61, 62]. In contrast, the odd modes will give only one branch of skewed bumpy black bars. See also the complete non-linear analysis in chapter 4.

Modes with high $n_y$, *i.e.*, $\Omega \ll 1$, give a perturbation of the mass density that is asymptotically of the form

$$\delta m(x,y) = e^{\mathcal{R}_{\text{bar}}(x,y)} H_{n_y}\left(\frac{y}{\sqrt{2n_y}}\right) \to e^{1-\frac{x^2}{2}-\frac{y^2}{4n_y}} \cos\left(y - \frac{n_y\pi}{2}\right) . \tag{2.148}$$

Therefore, very long black bars have zero modes that, away from the edges of the bar, where $|y| \ll \ell_\parallel = \sqrt{n_y}$, approach the sinusoidal oscillations of the GL modes of a black string, as we anticipated. We see that the modes with even $n_y$ converge to $\cos y$, whereas the modes with odd $n_y$ converge to $\sin y$. In this limit, odd and even modes are equivalent as they are simply shifted in $y$ by $\pi/2$. However, for non-zero values of $\Omega$ the even and odd modes are physically distinct from each other.

The linear stability of black bars requires the investigation of non-corotating perturbations, which we have not done, but we can expect that unstable modes are added after each new zero mode appears. Given the similarities to the GL phenomenon, we find it natural to conjecture that black bars in the limit $D \to \infty$ are linearly stable when they are short enough, more precisely when

$$\frac{\sqrt{2}}{3} < \Omega < \frac{1}{2} , \tag{2.149}$$

and then only in this rather narrow range. Then, as $\Omega$ decreases below each of the critical rotation values (2.143), the black bar will successively acquire new unstable modes. See also chapter 6 for additional discussion on this.

# Chapter 3

# Charged rotating black holes

## 3.1  Overview

Rotation and charge often have similar effects on a black hole, both of them opposing the gravitational field attraction. The Kerr-Newman solution indeed shows that, for a given mass, the black hole reduces its size as either charge or rotation are added [66].

In higher dimension $D \geq 5$ one expects that these behaviors not only persist but become more varied, since the gravitational effects of rotation and charge have different fall-off with distance. It is natural to anticipate a rich spectrum of black hole physics as charge and rotation are increased, extending what is already known when only rotation is present [10]. However, the investigation of this problem has been hampered by the striking fact that, long after Tangherlini extended the Reissner-Nordström solution to any $D \geq 5$ [67], and Myers and Perry did likewise for the Kerr solution [57], the only charged and rotating black hole solution of the Einstein-Maxwell equations known exactly in any $D \geq 4$ remains the Kerr-Newman solution[1].

Although approximate solutions have been obtained through a variety of methods[2], large regions in parameter space remain poorly explored where unusual features of black holes may be revealed. We find particularly appealing the discovery in [75] of near-extremal charged black holes in all $D \geq 6$ which have arbitrarily small spin but are nevertheless very far from the extremal Reissner-Nordström black hole. Their horizons are not approximately round but are instead highly pancaked along the rotation plane, even though their angular momentum and angular velocity are small. In the extremal limit they approach a static, singular disk of charged dust. Little else is known about these black holes. The methods of [75] only yield access to certain limits of parameter space and do not allow, *e.g.,* to connect between the Reissner-Nordström solution and these pancaked near-extremal black holes. Interestingly, although the latter are arbitrarily close to extremality, they were conjectured in [75] to be dynamically unstable due to an

---

[1]Here we only consider asymptotically flat black hole solutions of the pure Einstein-Maxwell theory, without any Chern-Simons terms nor additional scalar fields.

[2]These include: perturbatively small charge [68, 69, 70, 71] or slow rotation [72, 73, 74, 44]; charged rotating black holes with two widely separate horizon length scales [75, 76, 77]; charged black holes in large odd $D$ [78] or at large $D$ with either small charge or rotation [55, 79].

undamped quasinormal mode. Unfortunately, the quasinormal spectra of black holes with both charge and rotation are almost unknown[3].

In this chapter we show that many of these limitations can be overcome through the use of the large-$D$ effective theory of black holes [47, 56, 22, 24, 31, 25, 29], and more specifically its recent efficient implementation in [12]. As we will see, these methods allow to analytically investigate black hole phases with arbitrary values of the charge and of the angular momentum (in a single plane), as well as to obtain their quasinormal spectrum at low frequencies, $\omega = \mathcal{O}\left(D^0\right)$. Rotations in any finite number of planes are straightforward to add, but we will not pursue this here.

We expect that our results are not only qualitatively but also quantitatively good in any $D \geq 6$. This is a reasonable prospect given the remarkable accuracy that the large-$D$ methods have obtained for the features, including instability onsets and unstable growth rates, of neutral rotating black holes in this range of dimensions [12, 26]. In contrast, rotating black holes in $D = 5$ typically exhibit qualitative differences compared to $D = 4$ and $D \geq 6$; it would not be surprising if the non-perturbative corrections to the $1/D$ expansion became large in $D = 5$.

The approach started in [12] for the investigation of black holes succeeds by focusing on the region of the horizon where, when $D$ is large, most of the physics of the black hole concentrates: a small cap of polar-angular extent $\Delta\theta = \mathcal{O}\left(1/\sqrt{D}\right)$ around the rotation axis. Here the horizon is well approximated by a gaussian bulge on a black membrane. That is, we study lumps on a black brane that share the main properties of a localized black hole. The study of this bulge accurately reproduces properties of the black hole such as its shape, area, mass, and angular momentum. Moreover, its linear perturbations can be solved to obtain the waveforms and frequencies of the least-damped quasinormal modes. In addition, this approach has revealed the existence of 'black bar' configurations: elongated, bar-shaped rotating black holes whose emission of gravitational radiation vanishes to all perturbative orders in $1/D$ and therefore evolve very slowly at finite but large $D$.

We will see that the methods of [12] readily extend to black holes with charge in addition to rotation —surprisingly easily, given the difficulties in doing so at any finite $D$. Although technically the extension is straightforward, the resulting parameter space becomes richer with the inclusion of charge. In particular, we will be able to interpolate between the static, spherical Reissner-Nordström black hole, and the near-extremally charged, small-spin pancaked black holes of [75]. Along the way, we will identify the quasinormal modes that trigger the instability of the latter. We will also construct a new family of charged black bars, which remain stationary since their radiation into photons and gravitons is exponentially suppressed in the $1/D$ expansion.

Figure 3.1 summarizes our main findings concerning the space of solutions of charged rotating black holes. We refer to the axisymmetric charged rotating solutions as "the large-$D$ limit of the higher-dimensional Kerr-Newman black hole". This is justified since these solutions correctly reproduce the limit $D \to \infty$ of the Reissner-Nordström-Tangherlini

---

[3]All the studies that we know of use the large $D$ expansion: [44, 79] for small charge or rotation, and [78] for black holes with all rotations turned on in odd $D$.
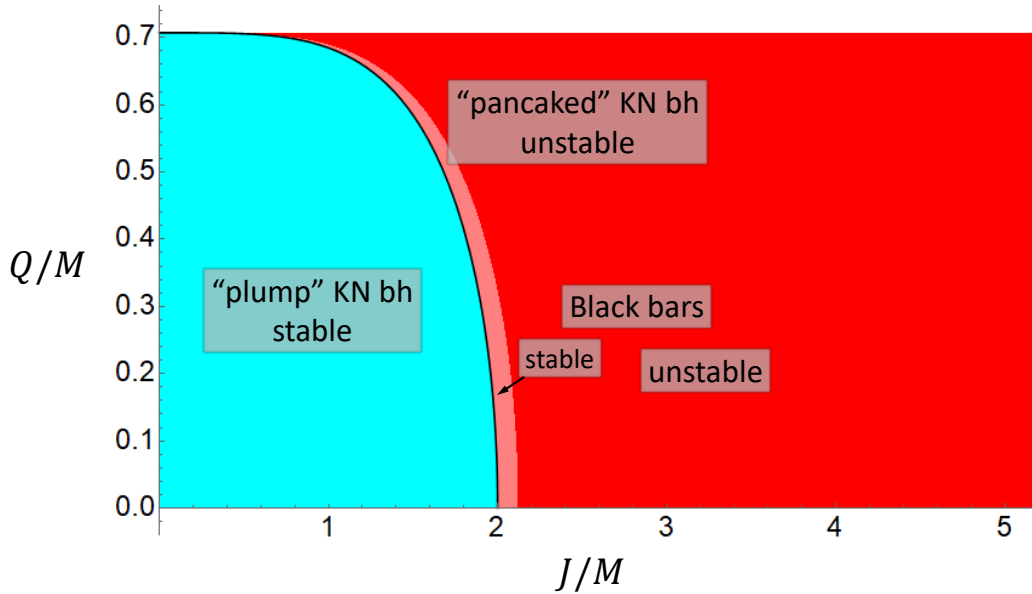
Figure 3.1: Phases of the charged rotating black holes constructed to leading order in the $1/D$ expansion. We label them by their angular momentum $J$ and charge $Q$ for fixed mass $M$. The charge is bounded above, $Q \leq M/\sqrt{2}$, but the upper, extremal limit lies outside the strict range of validity of our construction. Kerr-Newman-like (KN) black holes exist for all $J/M$. The black line $J/M = 2\left(1 - 2(Q/M)^2\right)^{1/4}$ separates the region (blue) where they are stable and round-shaped ("plump"), from the region (red, light and dark) where they are unstable and pancake-shaped (eq. (3.29)). Charged black bars exist in the red regions (sec. 3.3.1), but are stable (and only to leading order in $1/D$) only in the light-red area with outer boundary $J/M = (3/\sqrt{2})\left(1 - 2(Q/M)^2\right)^{1/4}$ (eq. (3.31)). In the upper-left corner there exist near-extremal black holes with arbitrarily small spin (sec. 3.2.3): below the black line they are close to the Reissner-Nordström solution, approximately spherical and stable; above the black line they are unstable and highly pancaked.

black hole when $J = 0$, and of the Myers-Perry black hole when $Q = 0$.

This chapter is structured as follows sec. 3.2 we construct and study the solutions that correspond to the limit $D \to \infty$ of the Kerr-Newman black hole. Sec. 3.3 describes charged black bars. Sec. 3.4 computes the quasinormal modes and stability properties of the solutions of the previous sections.

## 3.2 Charged rotating black holes: Kerr-Newman at $D \to \infty$

The solutions of (1.48) for stationary axially symmetric charged lumps on a 2-brane that we construct in this section correspond to the large-$D$ limit of the elusive higher-dimensional generalization of the Kerr-Newman black hole.

### 3.2.1   Solution

We employ polar coordinates $(r, \phi)$ on the 2-brane. Ref. [12] found the neutral solution that describes the Myers-Perry rotating black hole, with area-radius profile

$$\mathcal{R}(r) = \frac{2}{1 + a^2} \left(1 - \frac{r^2}{4}\right), \tag{3.1}$$

and angular velocity

$$v^\phi = \Omega = \frac{a}{1 + a^2}. \tag{3.2}$$

When we fix the overall scale, *e.g.,* by fixing the mass, this is a one-parameter family of solutions with the rotation parameter $a$ varying in $[0, \infty)$. We restrict to non-negative angular velocities without loss of generality. Observe that $\Omega$ varies between 0 and 1/2, the latter maximum being reached when $a = 1$.

Applying the procedure described at the end of the previous section we obtain a charged rotating solution, with

$$\mathcal{R}(r) = \frac{2}{1 + a_q^2} \left(1 - \frac{r^2}{4}\right). \tag{3.3}$$

The constant $a_q$ is not the rotation parameter anymore, but can be regarded as characterizing the spread of the gaussian for $m(r) = \exp\left(\mathcal{R}(r)\right)$. Now we have a family of solutions with two parameters, $a_q$ and $\mathfrak{q}$, whose range is

$$0 \le a_q < \infty, \qquad 0 \le \mathfrak{q} < \frac{1}{\sqrt{2}}. \tag{3.4}$$

The angular velocity is determined by (1.47) as

$$\Omega = \left(1 - 2\mathfrak{q}^2\right)^{1/4} \frac{a_q}{1 + a_q^2}, \tag{3.5}$$

and the angular momentum, charge and horizon entropy for a given mass are

$$J = 2a_q \left(1 - 2\mathfrak{q}^2\right)^{1/4} M, \tag{3.6}$$

$$Q = \mathfrak{q}M, \tag{3.7}$$

$$S = 2\pi \left(1 + \sqrt{1 - 2\mathfrak{q}^2}\right) M. \tag{3.8}$$

In addition, the temperature and electric potential are[4]

$$T = \frac{\sqrt{1 - 2\mathfrak{q}^2}}{2\pi \left(1 + \sqrt{1 - 2\mathfrak{q}^2}\right)}, \tag{3.9}$$

and

$$\Phi = \frac{2\mathfrak{q}}{1 + \sqrt{1 - 2\mathfrak{q}^2}}. \tag{3.10}$$

---

[4]The dimensionally correct area is actually not proportional to $M$ but to $M^{1+1/(n+2)}$, and $\Omega$ and $T$ are proportional to $M^{-1/(n+2)}$, but we neglect these differences in the limit $n \to \infty$. Moreover, at large $D$ the actual physical values of $J/M$ and $A_H/M$ are $1/D$ times those in (3.6) and (3.8), and $T$ is $D$ times (3.9); here they have all been rescaled to render them finite [31]. Finally, we use units where $16\pi G = 1$.

These satisfy

$$M = TS + \Phi Q \, . \tag{3.11}$$

Observe that the rotation term $\Omega J$ does not appear in this relation: at large $D$ it only enters at next to leading order [56] since the velocities and momenta along the effective membrane are $\mathcal{O}\left(1/\sqrt{D}\right)$. Since (3.7)–(3.10) are fixed by the properties of the charged membrane and therefore are common to all stationary solutions of the effective equations, in order to distinguish different phases we need to consider their rotational properties.

It can be shown that the solution with $a_q = 0$, $\Omega = 0$ corresponds to the large-$D$ limit of the static Reissner-Nordström black hole. See appendix of [13] for this.

### 3.2.2 Uniqueness

An immediate consequence of our construction is the uniqueness of the solutions: given $J$ and $Q$ for fixed mass $M$, the parameters $a_q$ and $\mathfrak{q}$ are uniquely determined and therefore so is the solution too.

This result is perhaps not unexpected, but given the previous lack of knowledge about these black holes when neither $J$ nor $Q$ are infinitesimally small, it was not obviously foreordained. The uniqueness only holds, though, within the Kerr-Newman class: it will be violated by the charged black bars of the next section (but only at $D \to \infty$) and by other classes of charged black holes, such as charged black rings and bumpy black holes (in all $D \geq 6$).

### 3.2.3 Effects of charge and rotation

Let us now use (3.7) to rewrite (3.6) as

$$a_q = \frac{J}{2M} \frac{1}{\left(1 - 2\left(\frac{Q}{M}\right)^2\right)^{1/4}} \, . \tag{3.12}$$

This equation serves to illustrate the effect that angular momentum and charge have on the shape of a black hole of a given mass. Increasing the spin $J$ results in a proportionately larger spread of the black hole $a_q$, as is already familiar for rotating black holes in any $D \geq 6$ [58]. If we then add charge, we see that the rotational spreading is enhanced. This effect, which, again, we expect to happen in every $D \geq 6$, is naturally attributed to electrostatic repulsion: intuitively, the horizon becomes less gravitationally tight.

We can also see in (3.8) how the charge reduces the horizon area for a given black hole mass, which is a generic phenomenon in all $D \geq 4$. Observe, however, that the presence of rotation does not change the horizon area. As discussed above, this is a leading large-$D$ effect, which can be explicitly observed for Myers-Perry black holes. Relatedly, note that the extremal limit (which, as we said, strictly lies outside the scope of our analysis) depends only on $Q/M$ but not on $J/M$. This is in contrast to the properties of the four-dimensional Kerr-Newman solution, but on the other hand is in consonance with the absence of an extremal rotating limit for singly-spinning black holes in $D \geq 6$.

Consider now solutions with fixed charge-to-mass ratio $\mathfrak{q}$. Eq. (3.5) implies that the maximum rotation velocity in this case is

$$\Omega_{\max} = \frac{1}{2} \left(1 - 2\mathfrak{q}^2\right)^{1/4} . \tag{3.13}$$

For any other value of the rotation, $\Omega$ in (3.5) is a two-valued function of $a_q$, so there are two possible black holes with the same charge and angular velocity: a 'plump' one with $a_q < 1$ and a corresponding 'pancaked' one with $a_q > 1$. In particular, close to the extremal charge limit, for any given small angular velocity we can find two distinct black hole solutions: an almost round one with $a_q \ll 1$, which is very close to the extremal Reissner-Nordström black hole, and a highly pancaked one with $a_q \gg 1$. Note, however, that these two black holes have very different spins, since the angular momentum $J$ for fixed charge grows monotonically as the gaussian profile broadens with increasing $a_q$.

Eq. (3.12) shows that it is possible to have highly pancaked black holes (with large $a_q$) whose angular momentum is small if the charge is sufficiently close (but still not equal) to the maximum value, namely $1/\sqrt{2} - \mathfrak{q} \ll 2\sqrt{2}/a_q^4$. The existence of these black holes with near-extremal charge and small spin whose horizons are pancaked along the rotation plane was first identified in [75] in any dimension $D \geq 6$. Their extremal limit corresponds to singular solutions of disks of extremal charged dust. In contrast to the method used in [75], which only works in the highly-pancaked limit (charged or not), our construction allows to cover the entire phase space of charges (above extremality) and rotations, and thus interpolate continuouly between plump and pancaked solutions.

## 3.3   Charged rotating black bars

We can similarly apply the procedure described in sec. 1.4.1 to the neutral black bar solution of [12], and thereby generate charged rotating black bars, with area-radius profile

$$\mathcal{R}(t, r, \phi) = 1 - \frac{r^2}{4} \left(1 + \sqrt{1 - \frac{4\Omega^2}{\sqrt{1 - 2\mathfrak{q}^2}}} \cos\left(2(\phi - \Omega t)\right)\right) . \tag{3.14}$$

If we employ corotating coordinates

$$x_t = r \cos(\phi - \Omega t) , \qquad y_t = r \sin(\phi - \Omega t) , \tag{3.15}$$

then the solution (3.14) reads

$$\mathcal{R}(x_t, y_t) = 1 - \frac{x_t^2}{2\ell_\perp^2} - \frac{y_t^2}{2\ell_\parallel^2} , \tag{3.16}$$

where the lengths parallel to the bar and transverse to it are

$$\ell_\parallel^2 = \frac{2}{1 - \sqrt{1 - \frac{4\Omega^2}{\sqrt{1 - 2\mathfrak{q}^2}}}} ,$$

$$\ell_\perp^2 = \frac{2}{1 + \sqrt{1 - \frac{4\Omega^2}{\sqrt{1 - 2\mathfrak{q}^2}}}} . \tag{3.17}$$

The effect of adding charge to a bar of a given mass and angular velocity is to reduce its length $\ell_\parallel$ and increase its thickness $\ell_\perp$.

### 3.3.1 Physical properties and non-uniqueness

For these solutions the angular momentum is

$$J = \frac{\sqrt{1 - 2\mathfrak{q}^2}}{\Omega} M \,, \tag{3.18}$$

while the charge, entropy, temperature and potential are given by the same expressions as (3.7)–(3.10).

The angular velocity $\Omega$ varies between 0 and a maximum $\Omega_{\max}$ which is the same as in (3.13). Therefore the angular momentum of the black bars is bounded below, satisfying

$$\frac{J}{M} \geq 2 \left( 1 - 2 \left( \frac{Q}{M} \right)^2 \right)^{1/4} \,. \tag{3.19}$$

This is the region marked in red in fig. 3.1.

Unlike the solutions of the previous section, there is only one black bar for given $\Omega$ and $Q/M$. The limit $\Omega \to 0$ yields an infinite, static charged black string. As in the neutral case, long charged bars behave like rigidly rotating solids with $J \sim M\ell_\parallel^2\Omega$.

When $\Omega = \Omega_{\max}$ the solution becomes axisymmetric, with $\ell_\parallel = \ell_\perp$; actually, we recover the same maximally-rotating charged black hole of sec. 3.2 with $a_q = 1$. Thus this solution sits at a bifurcation point in solution space—actually it is a line of bifurcation points, parametrized by $\mathfrak{q}$. We will see later that this family is indeed marked by the appearance of a zero mode at the threshold of a bar-mode instability of the axisymmetric charged black holes.

For $M$, $Q$ and $J$ that satisfy (3.19) we can always find a Kerr-Newman black hole and a black bar with the same values of these conserved charges. In this range, therefore, black hole uniqueness does not hold. These solutions also have the same entropy (to leading order at large $D$), but even if they are thermodynamically equally preferred, they can differ in their dynamical stability. Indeed, we will see that near the saturation of the bound (3.19) the Kerr-Newman black hole is linearly unstable while the black bar is (most likely) stable.

### 3.3.2 Radiation from charged black bars

In any finite number of dimensions, a charged rotating black bar will radiate both electromagnetic and gravitational waves. It is easy to estimate that the radiating power into each channel is

$$P^{\mathrm{em}} \sim GQ^2\ell_\parallel^2\Omega^D \,, \tag{3.20}$$

$$P^{\mathrm{gr}} \sim GM^2\ell_\parallel^4\Omega^{D+2} \,, \tag{3.21}$$

where, note, we are measuring the charge in geometric units, hence the factor $G$ in $P^{\mathrm{em}}$.

Since we always have $\Omega \leq 1/2$, this radiation at large $D$ is exponentially small, $\sim e^{-D}$, and thus invisible in the perturbative $1/D$ expansion. This is why in our approach we can find black bars as stationary solutions: their decay time is exponentially long in $D$.

For a long black bar, with

$$\ell_\parallel^2 \sim \frac{\sqrt{1 - 2\mathfrak{q}^2}}{\Omega^2} \tag{3.22}$$

the ratio of radiation into each channel is

$$\frac{P^{\text{em}}}{P^{\text{gr}}} \sim \left( \frac{Q}{M} \right)^2 \frac{1}{\sqrt{1 - 2(Q/M)^2}} . \tag{3.23}$$

There are two different factors here that, as charge is added to the bar, enhance the power into electromagnetic radiation relative to gravitational radiation. The overall factor $(Q/M)^2$ accounts for the larger amount of charge that the bar carries. The second factor in (3.23) is due to the electromagnetic-dipolar vs. gravitational-quadrupolar nature of the emission of radiation: as we mentioned above, for a given mass and rotation velocity the bar gets shorter and fatter as charge is added, which reduces the quadrupole moment by a larger factor than the dipole moment.

## 3.4  Quasinormal modes

### 3.4.1  Co-rotating zero modes

We begin by studying co-rotating zero-mode perturbations, which keep the solution stationary. In this case we can directly adapt the results obtained in [12] for the neutral case. Note that stationarity of the charged perturbations implies that there is no charge diffusion mode.

**Kerr-Newman black hole**

By a direct map from the neutral case, we obtain the co-rotating, zero-mode perturbations in the form

$$\mathcal{R}(r) = \frac{2}{1 + a_q^2} \left( 1 - \frac{r^2}{4} \right) + \epsilon\, \delta\mathcal{R}(r) e^{im_\phi(\phi - \Omega t)} , \tag{3.24}$$

where

$$\delta\mathcal{R}(r) = r^{|m_\phi|} L_k^{|m_\phi|} \left( \frac{r^2}{2(1 + a_q^2)} \right) . \tag{3.25}$$

These modes only exist if the width parameter $a_q$ takes the values

$$a_{q,c}^2 = \ell - 1 , \tag{3.26}$$

with

$$\ell = 2k + |m_\phi| , \qquad k = 0, 1, 2, \dots , \qquad |m_\phi| = 0, 1, 2, \dots \tag{3.27}$$

which in turn implies via (3.5) a quantization condition for the angular velocities at which zero modes appear

$$\Omega = \frac{\sqrt{\ell - 1}}{\ell} \left( 1 - 2\mathfrak{q}^2 \right)^{1/4} , \tag{3.28}$$

(only $\ell \geq 2$ is meaningful) and also for the angular momenta

$$\frac{J}{M} = 2\sqrt{\ell - 1}\left(1 - 2\left(\frac{Q}{M}\right)^2\right)^{1/4}. \tag{3.29}$$

Observe that the appearance of these modes—which, we will see, mark the thresholds of instabilities—depends on the width of the profile, $a_q$, and not on the charge and rotation separately. In particular this implies that the addition of charge reduces the range where a solution of given rotation is stable. Equivalently, a mode of given $k$ and $|m_\phi|$ will appear at lower rotation the larger its charge is. Again, these are manifestations of the repulsive effect of charge.

The axisymmetric modes with $m_\phi = 0$ are expected to lead to branches of 'bumpy charged black holes'. The fundamental non-axisymmetric modes, with $k = 0$ and $\ell = |m_\phi| \geq 2$ are multipole-bar-mode deformations[5]; when $\ell = |m_\phi| = 2$ we recover the linearization of the charged black bar (3.14) solution near the maximal angular velocity (3.13). Indeed (3.29) for $\ell = 2$ correctly reproduces the bound on the existence of black bars.

**Black Bars**

The same analysis applies for charged black bars, which have zero modes for

$$\frac{\Omega}{(1 - 2\mathfrak{q}^2)^{1/4}} = \frac{\sqrt{2}}{3}, \frac{\sqrt{3}}{4}, \frac{2}{5} \ldots \tag{3.30}$$

or equivalently, for

$$\frac{J}{M} = \frac{n + 1}{\sqrt{n}}\left(1 - 2\left(\frac{Q}{M}\right)^2\right)^{1/4}, \qquad n = 2, 3, 4 \ldots \tag{3.31}$$

(the value $n = 1$ corresponds again to the bifurcation with KN black holes). As before, adding charge makes the zero modes appear at slower rotation.

These zero modes, like those found in [12], create ripples along the bar which, in the limit $\Omega \to 0$ where $\ell_\parallel \to \infty$, become Gregory-Laflamme modes of a black string. Although we have not managed to solve for non-zero modes of black bars, we expect that they are unstable for $\Omega < \frac{\sqrt{2}}{3}\left(1 - 2\mathfrak{q}^2\right)^{1/4}$, i.e., for $J/M > (3/\sqrt{2})\left(1 - 2(Q/M)^2\right)^{1/4}$. This is indicated in fig. 3.1.

---

[5]The mode with $k = 0$ and $|m_\phi| = 1$ is gauge.

### 3.4.2 Quasinormal modes of the $D \to \infty$ Kerr-Newman black hole

We now turn to the study of the quasinormal modes of the full time-dependent equations (1.35)-(1.39). We consider linear perturbations of the form

$$m = \bar{m}(r) + e^{-i\omega t + m_\phi \phi} \, \delta m(r) \,, \tag{3.32}$$

$$p_r = \bar{p}_r(r) + e^{-i\omega t + m_\phi \phi} \, \delta p_r(r) \,, \tag{3.33}$$

$$p_\phi = \bar{p}_\phi(r) + e^{-i\omega t + m_\phi \phi} \, \delta p_\phi(r) \,, \tag{3.34}$$

$$q = \bar{q}(r) + e^{-i\omega t + m_\phi \phi} \, \mathfrak{q} \, \delta q(r) \,, \tag{3.35}$$

where $\bar{m}$, $\bar{p}_r$, $\bar{p}_\phi$, $\bar{q}$ correspond to the charged, rotating black hole background in sec. 3.2, concretely,

$$\bar{m}(r) = m_0 \exp\left( \frac{2}{1+a_q^2} \left( 1 - \frac{r^2}{4} \right) \right) \,, \tag{3.36}$$

and

$$\bar{p}_r(r) = \partial_r \bar{m}, \quad \bar{p}_\phi(r) = \Omega \bar{m} r^2, \quad \bar{q}(r) = \mathfrak{q} \bar{m} \,, \tag{3.37}$$

with $\Omega$ the angular velocity in (3.5) and $m_0$ an arbitrary constant.

**Charge diffusion perturbations**

It is easy to show that the effects due to charge diffusion decouple from the dynamics. In order to see this, we introduce the variable

$$\delta Q(r) \equiv \frac{1}{\bar{m}(r)} (\delta q(r) - \delta m(r)). \tag{3.38}$$

Combining the mass and charge continuity equations, we can easily derive the following decoupled equation for $\delta Q$

$$\delta Q'' + \left( \frac{1}{r} - \frac{r}{1+a_q^2} \right) \delta Q' + \left( i(\omega - m_\phi \Omega) - \frac{m_\phi^2}{r^2} \right) \delta Q = 0, \tag{3.39}$$

This the same confluent hypergeometric equation that was found in [12] as governing the spheroidal harmonics at small polar angles. Its regular solutions can be written as

$$\delta Q = r^{|m_\phi|} L_{k-1}^{|m_\phi|} \left( \frac{r^2}{2(1+a_q^2)} \right) \tag{3.40}$$

where $k \geq 1$ is an integer related to $\omega$ as

$$\omega = |m_\phi|\Omega - i \frac{2(k-1) + |m_\phi|}{1+a_q^2} \,. \tag{3.41}$$

Solutions with $k = 1$, $m_\phi = 0$ are pure gauge. As mentioned before, there are no co-rotating charge diffusion modes.

The remaining equations are a set of three, coupled, second order ODEs, in which $\delta Q$ and $\delta Q'$ appear as sources. Once a solution for $\delta Q$ has been inserted, we can solve for the remaining profiles. The easiest way to reconstruct the profiles is to write down

an appropriate ansatz which reduces the ODEs to algebraic equations for some constant coefficients. For the axisymmetric case $m_\phi = 0$, we find

$$\delta a = e^{-\frac{r^2}{2(1+a_q^2)}} \sum_{i=0}^{k} \delta a^{(i)} r^{2i} \,, \tag{3.42}$$

$$\delta p_r = e^{-\frac{r^2}{2(1+a_q^2)}} r \sum_{i=0}^{k} \delta p_r^{(i)} r^{2i} \,, \tag{3.43}$$

$$\delta p_\phi = e^{-\frac{r^2}{2(1+a_q^2)}} r^2 \sum_{i=0}^{k} \delta p_\phi^{(i)} r^{2i} \,. \tag{3.44}$$

For non-axisymmetric modes $|m_\phi| \geq 1$, the profiles are given by

$$\delta a = e^{-\frac{r^2}{2(1+a_q^2)}} r^{|m_\phi|} \sum_{i=0}^{k} \delta a^{(i)} r^{2i} \,, \tag{3.45}$$

$$\delta p_r = e^{-\frac{r^2}{2(1+a_q^2)}} r^{|m_\phi|-1} \sum_{i=0}^{k+1} \delta p_r^{(i)} r^{2i} \,, \tag{3.46}$$

$$\delta p_\phi = e^{-\frac{r^2}{2(1+a_q^2)}} r^{|m_\phi|} \sum_{i=0}^{k+1} \delta p_\phi^{(i)} r^{2i} \,. \tag{3.47}$$

**Gravitational perturbations**

Since charge diffusion perturbations decouple henceforth we consistently set $\delta q = \delta m$ in order to study perturbations in the mass density and the velocity, which describe the truly gravitational degrees of freedom. Their structure closely resembles the neutral fluctuations discussed in [12]. In particular, they can also be fully decoupled by means of a sixth order operator which factorizes in terms of confluent hypergeometric operators. More concretely, we can derive a sixth order equation for $\delta m$ of the form

$$\mathcal{L}_1 \mathcal{L}_2 \mathcal{L}_3 \delta \mathcal{R}(r) = 0 \,, \tag{3.48}$$

where

$$\delta \mathcal{R}(r) = \frac{\delta m(r)}{\bar{m}(r)} \,, \tag{3.49}$$

and the $\mathcal{L}_i$ are three commuting differential operators of the same confluent hypergeometric type as in [12],

$$\mathcal{L}_i = \frac{d^2}{dr^2} + \left( \frac{1}{r} - \frac{r}{1+a_q^2} \right) \frac{d}{dr} + \left( \frac{2k_i + m_\phi}{1+a_q^2} - \frac{m_\phi^2}{r^2} \right) \,. \tag{3.50}$$

The constants $k_i$ are solutions of the cubic equation

$$\omega^3 + \frac{i\omega^2}{2(1+a_q^2)} P_2 + \frac{\omega}{2(1+a_q^2)^2} P_1 + \frac{i}{2(1+a_q^2)^3} P_0 = 0 \tag{3.51}$$

where

$$P_2 = (\beta^2 + 1)(3\ell - 4) + 6ia_q\beta m_\phi \tag{3.52}$$

$$P_1 = 2a_q^2\beta^2\left(\ell + 3m_\phi^2 - 4\right) - 6ia_q\beta(\beta^2 + 1)(\ell - 1)m_\phi,$$
$$- (\ell - 1)\left((\beta^2(\beta^2 + 4) + 1)\ell - 2(\beta^2 + 1)^2\right), \tag{3.53}$$

$$P_0 = a_q^2\beta^2(\beta^2 + 1)\left((2 - 3\ell)m_\phi^2 - (\ell - 2)\ell\right) - 2ia_q^3\beta^3 m_\phi\left(\ell + m_\phi^2 - 2\right)$$
$$\beta^2(\beta^2 + 1)(\ell - 2)(\ell - 1)\ell + ia_q\beta(\ell - 1)\left(\beta^4(\ell - 2) + 4\beta^2\ell + \ell - 2\right)m_\phi, \tag{3.54}$$

with $\ell$ as in (3.27) and we abbreviate

$$\beta = (1 - 2\mathfrak{q}^2)^{1/4}. \tag{3.55}$$

Note that this equation is a cubic in $\omega$ and also in $\ell$ (or $k$). Since the operators $\mathcal{L}_i$ commute, all solutions of this cubic are equivalent and can be analized separately. Moreover, solving the radial equations we learn that $k$ must be non-negative integers. Thus, (3.51) becomes a quantization condition for the frequencies, in such a way that, for a given value of $k$ and $m_\phi$, and the black hole parameters, (3.51) determines three possible frequencies associated to them.[6]

Eq. (3.51) reproduces our previous result in [12] in the neutral case $\beta = 1$. Moreover, in the static limit $a_q = 0$ with nonzero charge we can solve to find

$$\omega = -\frac{i}{2}(\ell - 2)(\beta^2 + 1), \tag{3.56}$$

$$\omega = -\frac{i}{2}(\ell - 1)(\beta^2 + 1) \pm \frac{1}{2}\left[(\ell - 1)[(\beta^2 + 1)^2 - \ell(\beta^2 - 1)^2]\right]^{1/2}. \tag{3.57}$$

These frequencies match the results obtained in [78, 29] (provided we account for the different definitions of $\ell$ for vectors and scalars), which used a different approach for the perturbations of static charged black holes at $D \to \infty$. These modes are all stable, but they illustrate a continuing theme in our analysis: the addition of charge reduces the stability of the solution, in this case by decreasing the damping rate of the perturbation.

The analysis of the solutions to the quantization condition (3.51) and the reconstruction of the full profiles proceeds in close parallel to [12]. In the remainder of this section we record such expressions and highlight the presence of some unstable modes.

**Axisymmetric modes:** $m_\phi = 0$

There are no regular solutions for $\ell = 0$. For $\ell = 2, 4, 6, \ldots$, all solutions are regular and have profiles given by

$$\delta p_r = e^{-\frac{r^2}{2(1+a_q^2)}} r \sum_{i=0}^{k} \delta p_r^{(i)} r^{2i}, \tag{3.58}$$

$$\delta p_\phi = e^{-\frac{r^2}{2(1+a_q^2)}} r^2 \sum_{i=0}^{k} \delta p_\phi^{(i)} r^{2i}. \tag{3.59}$$

---

[6]If we keep the degree of freedom $\delta q$ in the analysis, we can derive an eighth-order equation factorized into operators of the form (3.50), with a quartic equation for $\omega$ which factorizes into (3.51) and a linear piece equal to (3.41).

**Non-axisymmetric modes:** $|m_\phi| \geq 1$

- For $k = 0$, $\ell = |m_\phi|$ we find

$$\omega_0 = \frac{a_q\beta(|m_\phi| + 4) - i(\beta^2 + 1)(|m_\phi| - 2)}{2(1 + a_q^2)}, \tag{3.60}$$

$$\omega_\pm = \frac{(|m_\phi| - 1)[2a_q\beta - i(\beta^2 + 1)]}{2(1 + a_q^2)} \tag{3.61}$$

$$\pm \frac{i}{2(1 + a_q^2)} \left\{ (|m_\phi| - 1)(\beta^2 - 1)^2 |m_\phi| + \left(2a_q\beta - i(\beta^2 + 1)\right)^2 \right\}^{1/2}. \tag{3.62}$$

Modes with frequency $\omega_0$ are regular for $|m_\phi| > 2$, so they are stable. Modes with $\omega = \omega_\pm$ are regular if $|m_\phi| \geq 1$. All these solutions have profiles of the form

$$\delta p_r = e^{-\frac{r^2}{2(1+a_q^2)}} r^{|m_\phi|+1} \delta p_r^{(1)}, \tag{3.63}$$

$$\delta p_\phi = e^{-\frac{r^2}{2(1+a_q^2)}} r^{|m_\phi|+2} \delta p_\phi^{(1)}. \tag{3.64}$$

- For $k \geq 1$, all solutions are regular and have profiles given by

$$\delta p_r = e^{-\frac{r^2}{2(1+a_q^2)}} r^{|m_\phi|-1} \sum_{i=0}^{k+1} \delta p_r^{(i)} r^{2i}, \tag{3.65}$$

$$\delta p_\phi = e^{-\frac{r^2}{2(1+a_q^2)}} r^{|m_\phi|} \sum_{i=0}^{k+1} \delta p_\phi^{(i)} r^{2i}. \tag{3.66}$$

**Near-critical unstable modes**

The zero modes that signal the onset of the instability, already found in (3.26), occur at

$$a_q = a_{q,c} \equiv \sqrt{\ell - 1}, \qquad \omega = \omega_c = |m_\phi|\Omega. \tag{3.67}$$

In order to examine the solutions near this point, we perform a perturbative analysis letting

$$a_q = a_{q,c} + \delta a_q, \qquad \omega = \omega_c + \delta\omega. \tag{3.68}$$

We find

$$\mathrm{Re}\,\delta\omega = \delta a_q \frac{4\beta^3 |m_\phi| \left(-4(\beta^2 - 1)^2 - (\beta^2 + 1)^2\ell^2 + 4(\beta^2 - 1)^2\ell\right)}{\ell\left((\ell - 1)\left((\beta^2 + 1)^2\ell - 2(\beta^2 - 1)^2\right)^2 + 4\beta^2(\beta^2 + 1)^2|m_\phi|^2\right)}, \tag{3.69}$$

$$\mathrm{Im}\,\delta\omega = \delta a_q \frac{2\beta^2(\beta^2 + 1)\sqrt{\ell - 1}\left\{(\ell - 2)\ell\left((\beta^2 + 1)^2\ell - 2(\beta^2 - 1)^2\right) + 8\beta^2|m_\phi|^2\right\}}{\ell\left((\ell - 1)\left((\beta^2 + 1)^2\ell - 2(\beta^2 - 1)^2\right)^2 + 4\beta^2(\beta^2 + 1)^2|m_\phi|^2\right)}.$$
$$\tag{3.70}$$

The imaginary part of the perturbed frequency is manifestly positive for $\delta a_q > 0$, which shows that there are unstable modes for $a_q > a_{q,c}$. For $|m_\phi| = 0$, the real part of the frequency vanishes, so these modes are static. On the other hand, for

$|m_\phi| > 0$ these modes have a non-zero real part so they correspond to bar modes. Moreover, we see that for $|m_\phi| > 0$ , $\mathrm{Re}\,\delta\omega < 0$: the unstable modes rotate in the same sense but more slowly than the black hole.

As the charge increases and $\beta$ decreases from 1 to zero, the value of $\mathrm{Im}\,\delta\omega/|\delta a_q|$ decreases monotonically towards zero. This implies that in the stable side, where $\delta a_q < 0$, the damping rate decreases with increasing charge: this is the same effect as mentioned after (3.57). On the other hand, it also implies that the instability for $\delta a_q > 0$ develops more slowly when charge is present; the same behavior was observed for charged black branes in [31].

In fig. 3.1 we have only indicated the onset of the instability that appears at slowest rotation, namely the mode $k = 0$, $\ell = |m_\phi| = 2$. This perturbation is unstable for all Kerr-Newman black holes with $a_q > 1$. As $J$ increases past the thresholds (3.29) and (3.31), further unstable modes appear in the red region of the diagram.

# Chapter 4

# Black ripples and black flowers

## 4.1 Overview

Black hole solutions in higher dimensional gravity show a far richer behavior than their counterparts in four spacetime dimensions. In higher dimensions, the rotation plays a significant role to fertilize a variety of new solutions. Since in $D > 5$, the (Newtonian) gravitational potential $\sim \frac{GM}{r^{D-3}}$ falls off more rapidly than the centrifugal barrier $\sim \frac{J^2}{M^2 r^2}$, the horizon can be deformed to an extended shape at large angular momentum, and hence becomes vulnerable to a Gregory-Laflamme type instability [32, 46]. This allows a family of non-uniform stationary solutions to branch off from the zero modes of the instabilities [10].

Different to the blackfold approach, the large $D$ limit is naturally endowed with a separation of scales between gradients along and orthogonal to the horizon: the gradient orthogonal to the horizon becomes large compared to gradients along the horizon in the limit of large $D$ as a result of the steepening of the gravitational potential. This enables us to formulate an effective theory without the requirement that the gradients along the horizon have to be infinitesimal, which makes the large $D$ expansion a powerful tool to study the non-uniform 'bumpy' phases of black holes.

In this chapter, we explore the phase space of compact stationary solutions with a single spin in the large $D$ limit, specifically, we focus on the (non-)axisymmetric deformed families branching off from the Myers-Perry family. The instability of ultra-spinning MP black holes and the existence of nearby 'rippled' solution was first conjectured in [58] and later, after the proof of existence of the zero modes and the instability [60, 80, 81, 82, 83], the rippled solutions were constructed numerically and identified as solutions that connect to black rings and black Saturns [84, 62, 61, 85].

Because of the strong suppression of gravitational radiation at large $D$ [15], the effective large $D$ description also admits stationary non-axisymmetric branches such as *black bars* [12] and other multipolar solutions. Here we apply the *blob* approximation developed in [12, 13], where localized black hole solutions such as the Myers-Perry black hole are identified as stationary lumps ("blobs") on a membrane which share the same horizon topology as the black brane solution but nevertheless encode most of the physics pertaining to the localized solution.

Figure 4.1 shows the full phase space plot of solutions we obtain. The solutions correspond to Myers-Perry solutions and their axissymmetric 'bumpy' deformations leading to black rings and black Saturns. We are also including stationary solutions without axisymmetry, which only can remain stationary at large $D$ since gravitational radiation decouples. These solutions have been shown to play an important role in dynamical evolutions of the ultra-spinning instability [14, 15, 86, 54, 87]. The first solution of this kind, a dipolar solution "black bar" was found analytically in [12]. Here we study its stationary deformations and also find its multipolar generalizations "black flowers". To illustrate features of the found solutions, we show plots of the mass density of four examples in figure 4.2.[1]
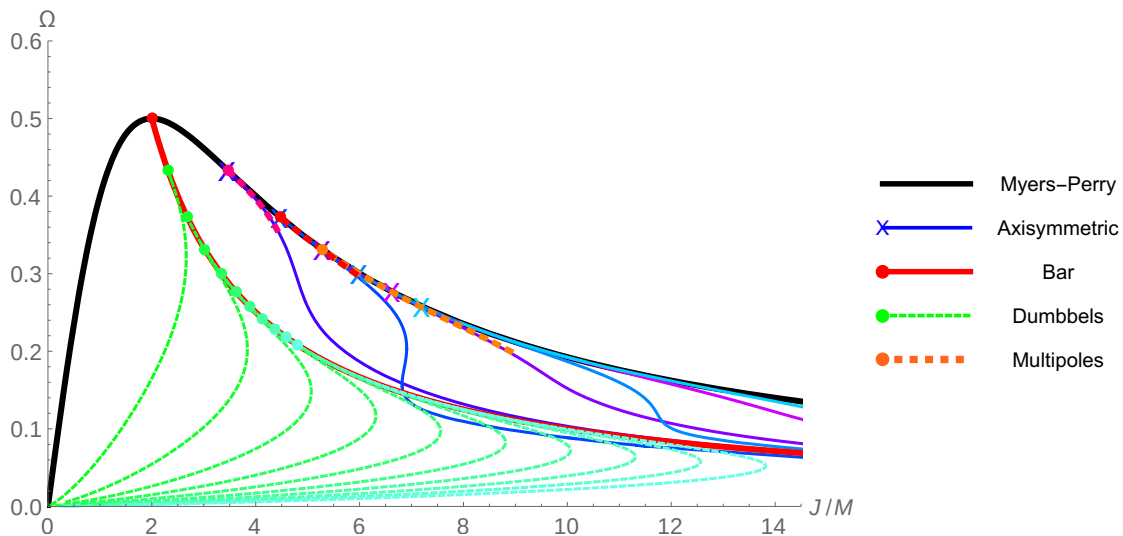


Figure 4.1: Phase space plot of the first appearing branches of solutions with a single angular momentum (per unit mass) $\mathcal{J}/\mathcal{M}$ and angular velocity $\Omega$. In the ultra-spinning regime $\mathcal{J}/\mathcal{M} > 2$ the MP-BH develops instabilities and the corresponding zero modes appear at places marked with dots or crosses. For the analytically known black bar, we also study its non-uniform deformations ('dumbbells'), whose branches are shown in different shadings of a color to make them more distinguishable.

We observe that most of bumpy deformations remain tangential to their 'parent'-branch until the deformation becomes comparable to the original solution and new blobs start to form. At some point, these blobs barely have any overlap and the branches enter a new asymptotic behavior for small $\Omega$ becoming completely separated. Some very short branches stick out non-tangentially above the parent-branch.

The chapter is structured as follows: In section 4.2, we construct perturbatively (including non-leading order results) and numerically stationary 'bumpy' deformations of the MP black hole that lead to (multiple) black rings and Saturns. In section 4.3 and 4.4, we construct stationary non-axisymmetric solutions from multipolar deformations of MP black holes and those of black bars. Section 4.5 discusses effects of adding charge to

---

[1]The flower branches are hard to to construct far away from their branching points, so figure 4.1 shows them only partially.
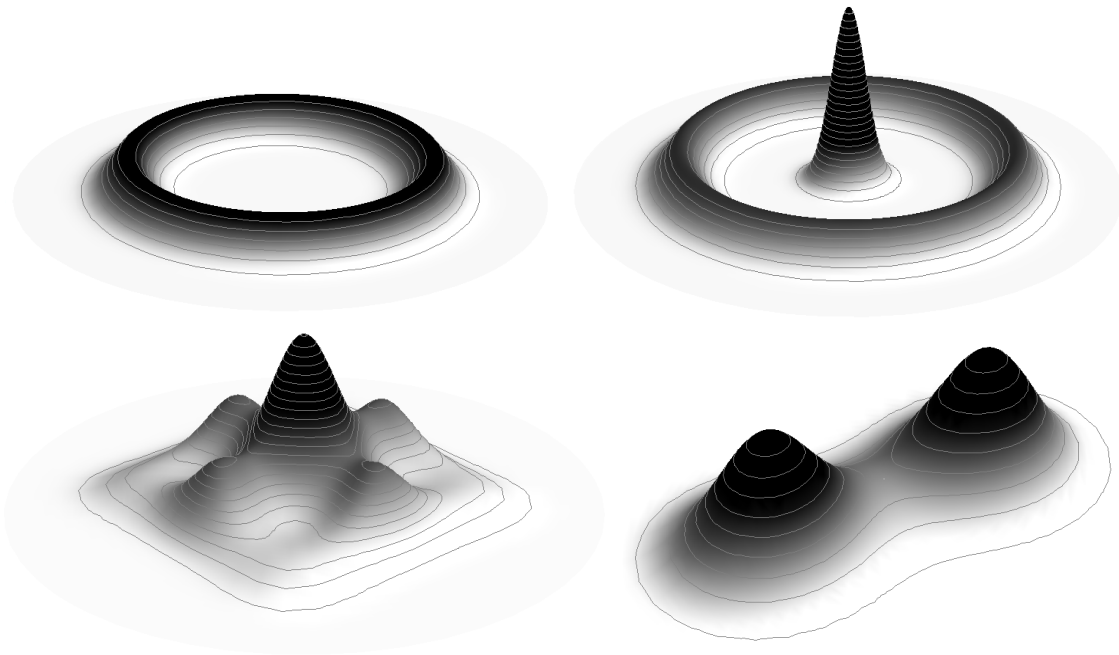
Figure 4.2: Four examples of bumpy solutions: Upper Left: Ring-like ripple. Upper Right: Saturn-like ripple Lower Left: Black flower with a quadrupolar deformation. Lower Right: Dumbbell. Plots show the mass density $m$. Coloring was chosen to highlight the important details of the solution, strictly speaking all solutions share the same horizon topology.

obtain charged (but non-extremal) solutions. Section 4.6 provides details of the numerical methods we employed, while finally 4.7 summarizes all the results giving some more detail than this overview.

## 4.2   Axisymmetric sector: Black Ripples

First, we consider the axisymmetric deformation of the Myers-Perry, which leads to an infinite number of 'bumpy' solutions, which we are going to refer to as *black ripples*.

### 4.2.1   Zero mode deformations

The MP-solution (3.1) allows axisymmetric co-rotating zero mode deformations according to[2]

$$\mathcal{R}(r) = \mathcal{R}_{\mathrm{MP}}(r) + \delta\mathcal{R}(r). \tag{4.1}$$

Plugging this into eq. (2.18), we obtain

$$\delta\mathcal{R}''(r) + \frac{1}{r}\frac{1+a^2-r^2}{1+a^2}\delta\mathcal{R}'(r) + \delta\mathcal{R}(r) = -\frac{1}{2}\delta\mathcal{R}'(r)^2. \tag{4.2}$$

---

[2]For brevity of presentation we restrict to the case of zero charge for now and drop the subscript $q$. We will discuss the effects of non-zero charge in section 4.5.

Introducing a new radial variable $z$ via

$$z := \frac{r^2}{2(1+a^2)},$$ (4.3)

the deformation equation becomes a Laguerre equation with a quadratic source term

$$\mathcal{L}_{(a^2+1)/2}\left[\delta\mathcal{R}\right] := z\delta\mathcal{R}''(z) + (1-z)\delta\mathcal{R}'(z) + \frac{a^2+1}{2}\delta\mathcal{R}(z) = -\frac{z}{2}\delta\mathcal{R}'(z)^2,$$ (4.4)

where we introduced the Laguerre operator $\mathcal{L}$. We note that, in terms of the new variable, the MP-solution is now written as

$$\mathcal{R}_{\mathrm{MP}}(z) = \frac{2}{a^2+1} - z.$$ (4.5)

Perturbations of this solution should be normalizable in the sense of eq. (4.33), which means for the perturbed profile $m = \exp(\mathcal{R}_{\mathrm{MP}} + \delta\mathcal{R})$

$$\int_0^\infty dr\, r\, m(r) \sim \int_0^\infty dz e^{-z}\exp\left(\delta\mathcal{R}(z)\right) < \infty,,$$ (4.6)

which is accomplished if the perturbation grows as a polynomial at each order, not showing exponential growth $\sim e^z$ or any divergences.

At leading order, the regular and normalizable perturbations are given by Laguerre polynomials,

$$\delta\mathcal{R}(z) = \varepsilon L_N(z) + \mathcal{O}\left(\varepsilon^2\right),$$ (4.7)

only if $a^2 + 1 = 2N$, for integer $N$. Which was first derived in [12], where a different notation is used, $i.e.,\, N$ is called $k$ instead. Please note, that this notation was also adapted in the other chapters of this thesis.

Non-trivial solutions have $N \geq 2$. $N$ has the interpretation of a 'radial overtone' number, $i.e.,$ it counts the number of oscillations along $r$. Since these zero modes correspond to 'bumpy black holes' [58, 62, 61], $N$ can also be interpreted as the number of bumps in the cross-section of the corresponding solution.

## 4.2.2   Nonlinear perturbations

In the following, we study how to include higher order perturbations for these zero-modes obtaining better control over the phase space of stationary solutions and also to support the later numerical analysis.

The general perturbative soution to eq. (4.4) is written as

$$\delta\mathcal{R}(z) = \sum_{k=0}^\infty \varepsilon^{k+1} f_k(z).$$ (4.8)

and for a leading order solution with $a^2 + 1 = 2N,\, (N = 2,3,4,\dots)$, the deformation equation (4.4) becomes

$$\mathcal{L}_N\left[f_k(z)\right] = \mathcal{S}_k(z)$$ (4.9)

at each perturbation order $k$. As usual, the source term $\mathcal{S}_k(z)$ is expressed by the solution up to $(k-1)$-th order.

A similar higher order perturbation analysis has been performed in [53, 11] for perturbations (non-uniformities) of black strings. It was found there, that the length of the black string has to be renormalized to avoid secular terms that would break the periodic boundary condition. Here, for spinning localized solutions, it turns out that we have to renormalize the angular velocity $\Omega$ or the corresponding spin parameter $a$ which changes the blob size, to avoid secular behavior that would break the normalization condition (4.6).

**Resonance and secular perturbation**

Secular behavior in perturbation theory is typically encountered when the dependence of some physical parameter on the perturbation parameter $\varepsilon$ is ignored. A common example for this is the slightly anharmonic oscillator

$$\ddot{x}(t) + {\omega_0}^2 x(t) = -\varepsilon x(t)^3, \tag{4.10}$$

Note that if we assume $x \ll 1$ the lowest order effect of the anharmonic term $\varepsilon x^3$ is to modify the frequency: $\omega_0 \to \omega_0 + \varepsilon\omega_1$. The appropriate ansatz accordingly should be $x(t) = \sin((\omega_0 + \varepsilon\omega_1)t)$, but naive perturbation theory $x(t) = x_0(t) + \varepsilon x_1(t)$ leads to the solution

$$x_0(t) = \sin(\omega_0 t), \tag{4.11}$$

$$x_1(t) = t \cdot \sin(\omega_0 t) + \dots, \tag{4.12}$$

where the first correction grows unboundedly invalidating the perturbative ansatz and violating conservation of energy. Note here that the secular term (4.12) results from a resonance phenomenon between the zeroth order solution (4.11) acting as a resonant source for the first order correction.

For our perturbative problem (4.9), a similar resonant behavior occurs. Assuming $S_k(z)$ can be decomposed into a linear combination of Laguerre polynomials $L_M(z)$, we have to distinguish two cases in

$$\mathcal{L}_N f(z) = L_M(z). \tag{4.13}$$

For $M \neq N$, the solution remains regular and normalizable,

$$f(z) = \frac{L_M(z)}{N - M}. \tag{4.14}$$

However, for $M = N$, which we are going to call the *resonant* case, the solution is

$$f(z) = -L_N(z) \log z - \sum_{I=0}^{N-1} \frac{2}{N - I} L_I(z) + B\Psi(N, 0, z) \tag{4.15}$$

with $B$ an integration constant and $\Psi(N, 0, z)$ a Laguerre function of the second kind. Since $\Psi(N, 0, z)$ has both a logarithmic divergence at $z = 0$ and exponential growth for $z \to$

$\infty$, the solution can never be regular and normalizable at the same time. This corresponds to secular behavior because the resonant term can be eliminated by a infinitesimal shift of $a$ in eq. (4.4) since,

$$\partial_\alpha L_\alpha(z)|_{\alpha=N} = \Psi(N, 0, z) + L_N(z) \log z + (\text{polynomial of } z). \tag{4.16}$$

**Recurrence formula**

The perturbative solution can be obtained systematically by removing resonant terms in the sources order by order, which leads to an algebraic recurrence relation. For this, we assume both $\delta\mathcal{R}(z)$ and $a$ are expanded in $\varepsilon$,

$$\delta\mathcal{R}(z) = \sum_{k=0}^\infty \varepsilon^k f_k(z), \quad a^2 + 1 = 2N \left( 1 + \sum_{k=1}^\infty \varepsilon^k \mu_k \right), \tag{4.17}$$

where we set

$$f_0(z) = L_N(z). \tag{4.18}$$

Plugging this into eq. (4.4) and expanding in $\varepsilon$, we obtain the perturbation equation for each order in $\varepsilon$,

$$\mathcal{L}_N f_k(z) = -\frac{1}{2} \sum_{\ell=0}^{k-1} z f'_\ell(z) f'_{k-1-\ell}(z) - N \sum_{\ell=1}^k \mu_\ell f_{k-\ell}(z) =: \mathcal{S}_k(z). \tag{4.19}$$

Assuming that $f_\ell(z)$ are polynomials for $\ell < k$, the source term also becomes a polynomial, and hence should be decomposed to the linear combination of the Laguerre polynomials,

$$\mathcal{S}_k(z) := \sum_{K=0}^M \mathcal{C}_K L_K(z) - N\mu_k L_N(z), \tag{4.20}$$

where $M$ is a finite positive integer. After eliminating $L_N(z)$ from the source by using $\mu_k$, $f_k(z)$ can be expressed as a polynomial as well. And we can decompose the solution at each order into a finite linear combination of Laguerre polynomials

$$f_k(z) = \sum_I \mathcal{C}_{k,I} L_I(z). \tag{4.21}$$

The coefficients of the resonant term $\mathcal{C}_{k,N}$ correspond to the reparametrizations of $\varepsilon$, and hence can be set to 0.

So the problem reduces to determining the coefficients $\mathcal{C}_{k,I}$ and $\mu_k$ at each order. Substituting eq. (4.21) into the source term (4.19), we obtain

$$\mathcal{S}_k(z) = \mathcal{L}_N \left[ -\sum_{M \neq N} \left( \sum_{I,J} \sum_{i=0}^{k-1} \mathcal{C}_{i,I} \mathcal{C}_{k-1-i,J} \frac{I+J-M}{4(N-M)} \mathcal{X}_{I,J}^M \right) L_M(z) \right.$$
$$\left. - \sum_{M \neq N} \sum_{i=1}^{k-1} \frac{N\mu_i C_{k-i,M}}{N-M} L_M(z) \right]$$
$$- \left[ N\mu_k + \frac{1}{4} \sum_{I,J} \sum_{i=0}^{k-1} (I+J-N) \mathcal{C}_{i,I} \mathcal{C}_{k-1-i,J} \mathcal{X}_{I,J}^N + \sum_{i=1}^{k-1} N\mu_i \mathcal{C}_{k-i,N} \right] L_N(z), \tag{4.22}$$

where $\mathcal{X}_{I,J}^K$ comes from the decomposition of the product of Laguerre polynomials [88],

$$L_I(z)L_J(z) = \sum_{K=|I-J|}^{I+J} \mathcal{X}_{I,J}^K L_K(z), \qquad (4.23)$$

which is written as

$$\mathcal{X}_{I,J}^K = \frac{(-2)^{I+J-K}K!}{(K-I)!(K-J)!(I+J-K)!} \, {}_3F_2 \left( \begin{array}{c} K+1, \frac{1}{2}(K-I-J), \frac{1}{2}(K-I-J+1) \\ K-I+1, K-J+1 \end{array} ; 1 \right). \qquad (4.24)$$

The last line in eq. (4.22) is proportional to the resonant term, and hence should be removed by setting

$$\mu_k = -\frac{1}{4N} \sum_{I,J} \sum_{i=0}^{k-1} (I+J-N)\mathcal{C}_{i,I}\mathcal{C}_{k-1-i,J}\mathcal{X}_{I,J}^N - \sum_{i=1}^{k-1} \mu_i \mathcal{C}_{k-i,N}. \qquad (4.25a)$$

For non-resonant terms, the $k$-th order coefficients are determined by

$$\mathcal{C}_{k,M\neq N} = -\sum_{I,J}\sum_{i=0}^{k-1} \mathcal{C}_{i,I}\mathcal{C}_{k-1-i,J} \frac{I+J-M}{4(N-M)} \mathcal{X}_{I,J}^M - \sum_{i=1}^{k-1} \frac{N\mu_i \mathcal{C}_{k-i,M}}{N-M}. \qquad (4.25b)$$

The coefficient of $L_N(z)$ is set to zero $\mathcal{C}_{k,N} = 0$ for $k \geq 1$. With these recurrence equations, the perturbation equation can be solved algebraically.

**Perturbation solution**

To solve the recurrence equation (4.25), we first set

$$\mathcal{C}_{0,M} = \delta_{N,M}. \qquad (4.26)$$

Then, we have the solution for $k = 1$

$$\mu_1 = -\frac{1}{4}\mathcal{X}_{N,N}^N, \quad \mathcal{C}_{1,M\neq N} = -\frac{2N-M}{4(N-M)}\mathcal{X}_{N,N}^M. \qquad (4.27)$$

Repeating the calculation, we get the result at $k = 2$,

$$\mu_2 = \sum_{I\neq N} \frac{(2N-I)I}{8N(N-I)}\mathcal{X}_{N,N}^I\mathcal{X}_{I,N}^N, \qquad (4.28)$$

and

$$\mathcal{C}_{2,M\neq N} = \sum_{I\neq N} \frac{(I+N-M)(2N-I)}{8(N-M)(N-I)}\mathcal{X}_{N,I}^M\mathcal{X}_{N,N}^I - \frac{N(2N-M)}{16(N-M)^2}\mathcal{X}_{N,N}^N\mathcal{X}_{N,N}^M. \qquad (4.29)$$

Especially, the leading order shift in $a$ is given by

$$\mu_1 = -\frac{1}{4}\mathcal{X}_{N,N}^N = -(-2)^{N-2} \, {}_3F_2 \left[ \begin{array}{c} N+1, -\frac{N}{2}, -\frac{N-1}{2} \\ 1, 1 \end{array} ; 1 \right]. \qquad (4.30)$$

Here we note that $\mu_1$ alternates in sign with $N$. For the first values of $N$, we obtain

$$\mu_1\big|_{N=2,3,4,5} = -\frac{5}{2} \ , \ 14 \ , \ -\frac{173}{2} \ , \ 563. \qquad (4.31)$$

The leading order shift can also be related to the Franel numbers and one can show that the amplitude of $\mu$ grows very rapidly with $N$,

$$\mu_1 \sim (-1)^{N+1}\frac{2^{3N}}{N}. \qquad (4.32)$$

**Phase diagram**

Given the perturbative solution we can calculate the physical quantities $\mathcal{M}$, $\mathcal{J}$ and the value at the origin $\mathcal{R}_0 = \mathcal{R}(0)$ (which is used as an initial condition in the numerical analysis) perturbatively as follows. We recall that the physical quantities in the effective theory are calculated according to[3]

$$\mathcal{M} = \int_0^{2\pi} d\phi \int_0^\infty dr\, r\, m(r, \phi), \tag{4.33}$$

$$\mathcal{J} = \int_0^{2\pi} d\phi \int_0^\infty dr\, r\, p_\phi(r, \phi)$$

$$= \int_0^{2\pi} d\phi \int_0^\infty dr\, \Omega\, r^3\, m(r, \phi). \tag{4.34}$$

**Angular velocity and center thickness** By definition, the angular velocity has the expansion

$$\Omega = \frac{a}{1 + a^2} = \frac{\sqrt{2N - 1}}{2N}\left(1 - \frac{N - 1}{2N - 1}\mu_1\varepsilon + \mathcal{O}\left(\varepsilon^2\right)\right). \tag{4.35}$$

The center thickness is given by

$$\mathcal{R}_0 = \frac{2}{1 + a^2} + \varepsilon + \mathcal{O}\left(\varepsilon^2\right) = \frac{1}{N}\left(1 + (N - \mu_1)\varepsilon + \mathcal{O}\left(\varepsilon^2\right)\right). \tag{4.36}$$

Which gives the gradient on the branching point is given by

$$\left.\frac{\partial_\varepsilon \log \Omega}{\partial_\varepsilon \log \mathcal{R}_0}\right|_{\varepsilon=0} = \frac{N - 1}{2N - 1}\frac{\mu_1}{\mu_1 - N}. \tag{4.37}$$

Since $\mu$ grows much faster than $N$, the gradient rapidly approaches to that of the Myers-Perry branch for the larger value of $N$. For the first few values of $N$, we obtain

$$\left.\frac{\partial_\varepsilon \log \Omega}{\partial_\varepsilon \log \mathcal{R}_0}\right|_{N=2,3,4,5} = \frac{5}{27}, \quad \frac{28}{55}, \quad \frac{519}{1267}, \quad \frac{1126}{2511}. \tag{4.38}$$

At higher order, the center thickness is given by

$$\mathcal{R}_0 = \frac{a}{1 + a^2} + \sum_{k=0} \varepsilon^{k+1}\left(\sum_I \mathcal{C}_{k,I}\right) \tag{4.39}$$

where $\mathcal{C}_{k,I}$ is the coefficients of the Laguerre expansion at each order in eq. (4.21). To compare with the numerical result (figure 4.3), we calculated the formula for $(\mathcal{R}_0, \Omega)$-space up to $\varepsilon^2$,

$$\Omega = \frac{\sqrt{2N - 1}}{2N}\left(1 + \omega_1\bar{\varepsilon} + \omega_2\bar{\varepsilon}^2\right), \tag{4.40}$$

where

$$\bar{\varepsilon} := N\mathcal{R}_0 - 1. \tag{4.41}$$

---

[3]Note that the quantities $\mathcal{M}$, $\mathcal{J}$ correspond to the quantities $M$, $J$ in previous chapters.

$\omega_1$ coincides with eq. (4.37). Here we do not show the explicit formula for $\omega_2$, since it no longer reduces to the simple form. The coefficients for several branches are

$$\omega_1\big|_{N=2,3,4,5} = \frac{5}{27}, \frac{28}{55}, \frac{519}{1267}, \frac{1126}{2511}, \tag{4.42}$$

$$\omega_2\big|_{N=2,3,4,5} = \frac{118}{729}, -\frac{172629}{66550}, \frac{82075592}{290557309}, -\frac{1528095425}{4691010024}. \tag{4.43}$$

**Mass and angular momentum** Provided that the perturbation is normalizable, the mass (4.33) and angular momentum (4.34) are easily obtained by

$$\mathcal{M} = \mathcal{M}_{\mathrm{MP}} \int_0^\infty e^{-z} \exp\left(\delta\mathcal{R}(z)\right) dz, \tag{4.44}$$

$$\mathcal{J} = 2a\mathcal{M} - 2a\mathcal{M}_{\mathrm{MP}} \int_0^\infty e^{-z} L_1(z) \exp\left(\delta\mathcal{R}(z)\right) dz, \tag{4.45}$$

where $\mathcal{M}_{\mathrm{MP}}$ is the mass of the Myers-Perry of the same $a$ and $z = L_0(z) - L_1(z)$ is used. Since these integrations take the form of the inner product of the Laguerre polynomials, it is convenient to use the expansion of the perturbative solution into the Laguerre polynomials,

$$\delta\mathcal{R}(z) = \sum_{k=0}^\infty \sum_M \varepsilon^{k+1} \mathcal{C}_{k,M} L_M(z), \tag{4.46}$$

where $\mathcal{C}_{0,M} = \delta_{M,N}$ for the $N$-branch and $M$ runs over some finite at each perturbative order $k$. Up to $\mathcal{O}\left(\varepsilon^2\right)$, one can expand as

$$\exp\left(\delta\mathcal{R}(z)\right) = 1 + \varepsilon L_N(z) - \varepsilon^2 \sum_{M \neq N} \frac{M \mathcal{X}_{N,N}^M}{4(N-M)} L_M(z), \tag{4.47}$$

where we made use of the second order solution (4.27). Putting this into eqs. (4.44) and (4.45), we obtain

$$\frac{\mathcal{J}}{\mathcal{M}} = 2a \left[1 - \frac{\mathcal{X}_{N,N}^1}{4(N-1)} \varepsilon^2\right], \tag{4.48}$$

in which $a$ also should be expanded according to (4.17). We see that the ratio of angular momentum to mass only differs by $\mathcal{O}\left(\varepsilon^2\right)$ from the Myers-Perry branch.

### 4.2.3 Numerical construction

To construct fully non-linear solutions we have to solve numerically the axisymmetric version of the soap bubble equation (2.18)

$$\mathcal{R}'' + \frac{\mathcal{R}'}{r} + \frac{1}{2}\mathcal{R}'^2 + \mathcal{R} + \frac{\Omega^2 r^2}{2} = 0, \tag{4.49}$$

which is a second order nonlinear differential equation for $\mathcal{R}(r)$. Since $r$ is a radial coordinate, any physical solution of eq. (4.49) must satisfy the regularity condition $\mathcal{R}'(0) = 0$. This leaves the parameter $\mathcal{R}_0 \equiv \mathcal{R}(0)$ as the initial condition that is needed to integrate the differential equation outwards radially. However, not all values of $\mathcal{R}_0$ will result in physical solutions. In general, as a consequence of the nonlinearity of eq. (4.49), $\mathcal{R}(r)$ will

become singular at a finite value of $r = r_s$ and only a discrete set of initial conditions will allow for solutions that that extend to $r \to \infty$. To find these branches our numerical procedure consists in maximizing the value $r_s$ where the singularity appears. Solutions appear as singularities/ peaks of $r_s$ as a function of the initial conditions. See sec. 4.6 for a more detailed description of the numerical method.

For fixed $\Omega \in [0, 1/2]$, the two branches (stable and unstable) of the MP black hole (3.1) correspond to two such solutions. In terms of the parameter $a$, the MP solutions describe an ellipse in the $(\mathcal{R}_0, \Omega)$ plane as

$$\mathcal{R}_0 = \frac{2}{1 + a^2}, \qquad \Omega = \frac{a}{1 + a^2}. \tag{4.50}$$

Apart from the MP black hole solutions, we find that multiple branches of bumpy solutions extend from every axisymmetric zero-mode. They can be represented in $(\mathcal{R}_0, \Omega)$ plane as curves that extend from the Myers-Perry ellipse, as shown in figure 4.3.
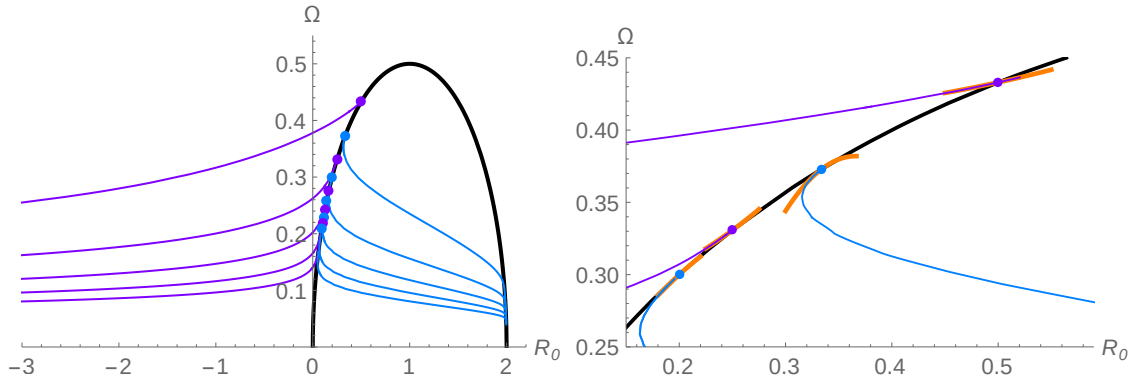


Figure 4.3: Branches of axisymmetric deformations (blue) of MP black hole (black) on the $(\mathcal{R}_0, \Omega)$ plane. Branches moving towards negative $\mathcal{R}_0$ connect to black rings. And have a decreasing mass density at the origin. While the branches moving towards positive $\mathcal{R}_0$ connect to black Saturns and $\mathcal{R}_0$ approaches a value of the stable MP black hole. The right plot is a close-up showing good agreement with the analytic expansions (orange). The right plot also shows the very short $(-)$-branches.

We observe that the bumpy branches fall in two distinct categories. Those branches that arise from even $N$ zero modes, as defined in eq. (4.7), tend to $\mathcal{R}_0 \to -\infty$ as $\Omega \to 0$ (asymptotically like $\mathcal{R}_0 \propto -\frac{1}{\Omega^2}$). This is equivalent to a rapidly decreasing mass density at the rotation axis as one moves along the branch. These bumpy branches connect the MP-branch to families of $N - 1$ concentric black rings. In figure 4.4, the mass density profiles $m = e^{\mathcal{R}}$ are shown. On the other hand, for the zero modes with odd values of $N$, we have $\mathcal{R}_0 \to 2$, which means that the mass density at the center will closely approach that of a stable MP black hole. These branches will resemble black Saturns with $N - 2$ rings, as shown in figure 4.5.

As discussed in [61, 62], every axisymmetric branch extends in both directions from the zero mode. This corresponds to the fact that linear perturbations of the Myers-Perry black hole can be added with either a positive or a negative amplitude. According to the

convention in [62], branches adding the amplitude of the sign $(-1)^{N+1}$ on the axis are called (+)-branches, which deform the MP-black hole towards the black rings or black Saturns, and the opposites, (−)-branches, which develop a singularity on the equator of the horizon. It is so far unclear if this (−)-branch connects to some singly spinning black hole solution.

Agreeing with this, we find that the negative side of the branches extends only for a very short interval, after which the allowed solutions cease to exist. This behavior is to some extent expected, since our approach can not resolve singular or conical solutions in phase space. Numerically the vanishing of a solution manifests itself as a vanishing pole in $r_s$. The (−)-branches are shown in the close-up plot of figure 4.3, as the very short blue lines extending into the opposite site of the (+)-branches. From the perturbative result (4.35), one can also see that all (−)-branches increase $\Omega$, and vice versa at the linear level.
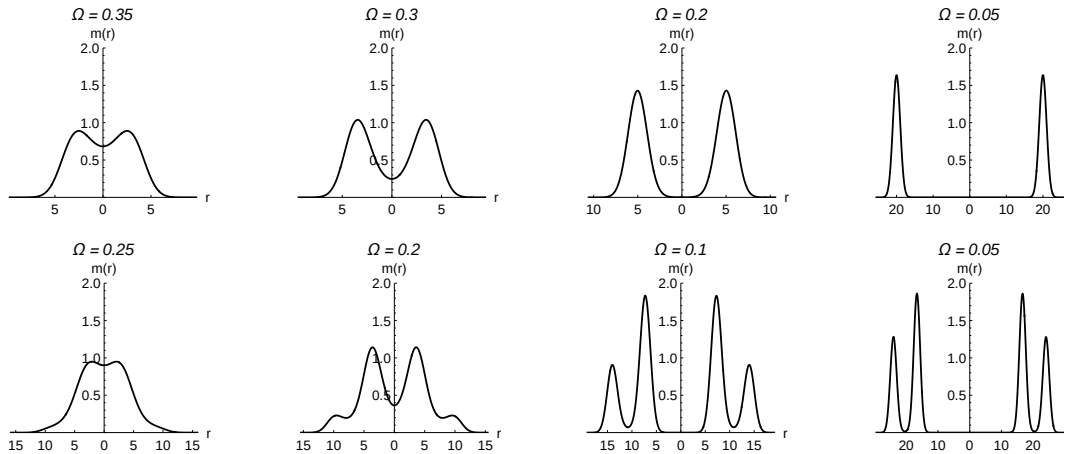


Figure 4.4: Cross-sections of the mass density $m$ for black ripples leading to black rings corresponding to the zero modes $N = 2, 4$, at different values of $\Omega$. Close to the branching points the solutions develop bumpy deformations whereas far away from it the solutions closely resemble separated black rings. The (expected) pinching of the necks as we move away from the MP-branch follows a behavior described already in [62]: For multiple rings the pinching starts at the interior necks and later on the outer ones.

The angular momentum (per unit mass) is calculated numerically according to eq. (4.34). The bumpy branches can then be represented on the usual $(\mathcal{J}/\mathcal{M}, \Omega)$ phase diagram, as depicted in figure 4.6.

Figures 4.4, 4.5, 4.6 show that the bumpy branches for black rings and black Saturns seem to extend to arbitrary angular momentum[4] without encountering any conical singularities. For a sufficiently high angular momentum, the deformation ends up as multiple lumps/rings barely connected by exponentially thin necks. Figure 4.6 also shows this in a

---

[4]Saturn type solutions become harder to construct numerically, since the different Saturn-type solutions pile up in initial condition space as can be seen in figure 4.3, but we see no evidence that the corresponding poles in $r_s$ vanish.
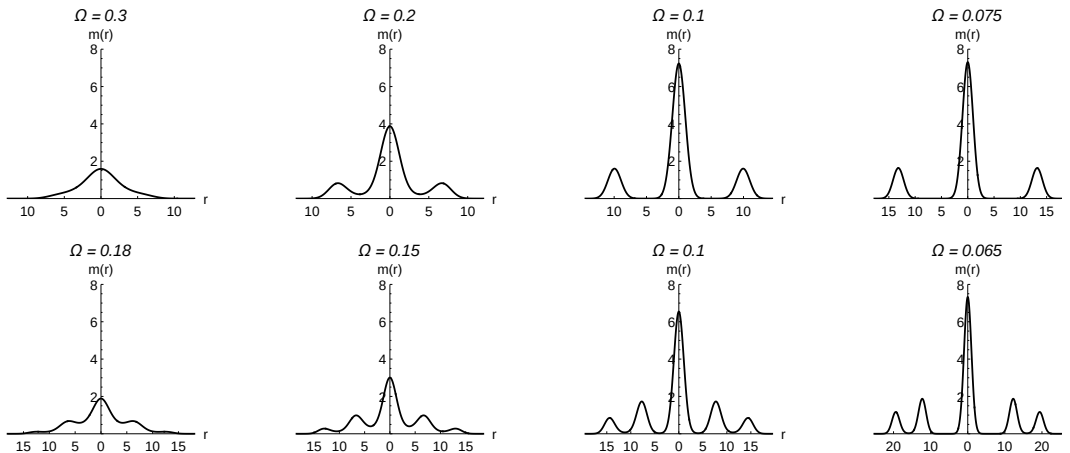
Figure 4.5: Cross-sections of the mass density $m$ for black ripples leading to black Saturns corresponding to the zero modes $N = 3, 5$, at different values of $\Omega$.

change of behavior of the curves: All branches show three phases of qualitative behaviors: In the first stage the branches are nearly tangential to the MP-branch. After that in an intermediate stage new (ringlike) blobs start to form until they reach a new asymptotic phase. In this final phase the blobs are practically separated and do barely deform further but the distance between the blobs keeps increasing, the angular momentum behaves asymptotically like $\mathcal{J}/\mathcal{M} \propto 1/\Omega$.

For solutions with multiple ripples, we find that at low $\Omega$ the radii of ringlike blobs follow two different behaviors. The innermost ring has an approximate radius growing like $\Omega^{-1}$, while the distance between the following outer rings increases slower than that and we estimate it to be $\sim \sqrt{|\log \Omega|}$. The $\Omega^{-1}$-behavior agrees with the blackfold result for multi-rings if the separations of the rings are much shorter than the ring radius [89]. These observations on the far extended branches lead us to the expectation that our ring/Saturn-like bumpy solutions will be connected via a topology changing transition to the single bumpy rings/Saturns, not directly to multi-rings or higher Saturns. This picture is consistent with the numerical result in $D = 6$ bumpy Myers-Perrys [62].

## 4.3    Multipole deformations: Black Flowers

In the large $D$ limit, the soap bubble equation (2.18) also admits non-axisymmetric stationary solutions, because gravitational waves are completely decoupled as a non-perturbative effect in $1/D$ and solutions with time-dependent multipoles do not radiate.

### 4.3.1    Multipolar zero modes

We study again perturbations of the MP-black hole, but this time allow for angular dependence of the perturbations

$$\mathcal{R}(z, \phi) = \mathcal{R}_{\mathrm{MP}}(z) + \delta\mathcal{R}(z, \phi). \tag{4.51}$$
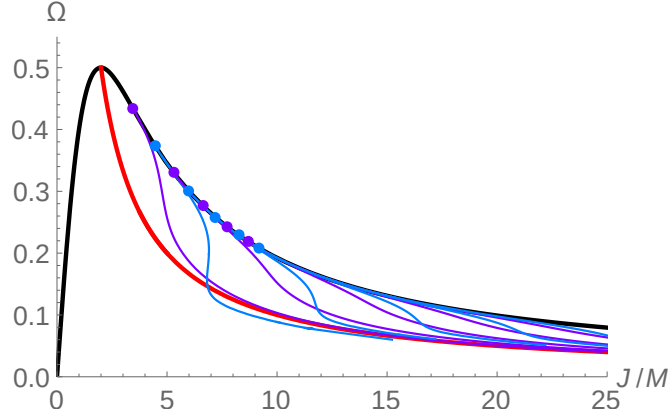
Figure 4.6: Phase diagram for axisymmetric solutions, we show the 10 first appearing branches: Ring-branches are shown in purple, and Saturn branches in light-blue. The Myers-Perry and black bar solutions are also plotted by the black and red curves. We do not expect the Saturn branches to terminate, but they become harder to construct for low $\Omega$.

Then, the deformation equation becomes

$$\mathcal{L}_{z,\phi}\delta\mathcal{R}(z,\phi) = \mathcal{S}(z,\phi), \tag{4.52}$$

where we defined

$$\mathcal{L}_{z,\phi} := z\partial_z^2 + (1-z)\partial_z + \frac{1}{4z}\partial_\phi^2 + \frac{a^2+1}{2}, \tag{4.53}$$

$$\mathcal{S}(z,\phi) := -\frac{1}{2}z(\partial_z\delta\mathcal{R}(z,\phi))^2 - \frac{1}{8z}(\partial_\phi\delta\mathcal{R}(z,\phi))^2. \tag{4.54}$$

It is convenient to expand the angular dependence as a Fourier series

$$\delta\mathcal{R}(z,\phi) = \sum_{k=0}^{\infty} z^{\frac{k}{2}} f^{(k)}(z)\cos k\phi, \tag{4.55}$$

where each radial function is expanded in $\varepsilon$,

$$f^{(k)}(z) = \sum_{p=0}^{\infty} \varepsilon^{p+1} f_p^{(k)}(z). \tag{4.56}$$

With the Fourier decomposition, the linear part reduces to the generalized Laguerre equation

$$\mathcal{L}_{z,\phi}\delta\mathcal{R}(z,\phi) = \sum_{k=0}^{\infty} z^{\frac{k}{2}}\mathcal{L}_{(a^2+1-k)/2}^{(k)}f^{(k)}(z)\cos(k\phi), \tag{4.57}$$

which admits normalizable solutions for $k = m$ when

$$a^2 + 1 - m = 2N \ (N = 0, 1, 2, \dots). \tag{4.58}$$

We also decompose the source terms into Fourier modes

$$\mathcal{S}(z,\phi) = \sum_{k=0} z^{\frac{k}{2}}\mathcal{S}^{(k)}(z)\cos k\phi, \tag{4.59}$$

where

$$\mathcal{S}^{(k)}(z) = -\frac{1}{4}\sum_{\ell=0}^{\infty} z^{\ell-1}\left(\ell(\ell+k)f^{(\ell)}(z)f^{(\ell+k)}(z) + (\ell+k)zf^{(\ell)\prime}(z)f^{(\ell+k)}(z)\right.$$

$$\left. +\ell z f^{(\ell)}(z)f^{(\ell+k)\prime}(z) + 2z^2 f^{(\ell)\prime}(z)f^{(\ell+k)\prime}(z)\right)$$

$$-\frac{1}{8}\sum_{\ell=0}^{k}\left((k-\ell)f^{(\ell)\prime}(z)f^{(k-\ell)}(z) + kf^{(\ell)}(z)f^{(k-\ell)\prime}(z) + 2zf^{(\ell)\prime}(z)f^{(k-\ell)\prime}(z)\right). \quad (4.60)$$

Here the last line exists only for $k > 0$.

### 4.3.2   Nonlinear perturbation

For higher order perturbations, we proceed in almost the same manner as for the axisymmetric sector. The generalized Laguerre operators $\mathcal{L}_N^{(m)}$ also show resonant behavior if they are sourced by the corresponding resonant term $L_N^{(m)}(z)$, provided $N$ is a nonnegative integer. Therefore, for the solution to be regular and normalizable, the resonant term has to be removed from the source for every mode by renormalizing the angular velocity as

$$a^2 + 1 = \left(N + \frac{m}{2}\right)\left(1 + \sum_{p=1}^{\infty}\mu_p\varepsilon^p\right). \quad (4.61)$$

A new phenomenon we observe, is that some modes can not independently excited at linear order, otherwise the renormalization of the angular velocity becomes impossible. To show this, let us assume to the contrary that we start at linear order only with the zero mode corresponding to $a^2 + 1 - m = 2N$,

$$f_0^{(m)}(z) = L_N^{(m)}(z). \quad (4.62)$$

Then, this mode acts as a source for the neighboring perturbations $f_1^{(0)}$ and $f_1^{(2m)}$ at next-to-leading order,

$$\mathcal{L}_{N+m/2}^{(0)}f_1^{(0)}(z) = \mathcal{S}^{(0)}(z), \quad (4.63)$$

$$\mathcal{L}_{N-m/2}^{(2m)}f_1^{(2m)}(z) = \mathcal{S}^{(2m)}(z). \quad (4.64)$$

If $m$ is a even, eqs. (4.63) and (4.64) will contain resonant sources.[5]  However, since we did not include the corresponding linear order term at leading order, the parameter renormalization cannot absorb the resonant terms. This implies that we are forced to include also the neighboring overtone modes at leading order

$$f_0^{(0)}(z) = \alpha_0 L_{N+m/2}^{(0)}, \quad f_0^{(m)}(z) = \alpha_1 L_N^{(m)}(z), \quad f_0^{(2m)}(z) = \alpha_2 L_{N-m/2}^{(2m)}(z). \quad (4.65)$$

Repeating the same argument for the new linear solution, one might be concerned that now we need an infinite tower of overtone modes to regularize the secular behavior. However, if $N - (i-1)m/2 < 0$ for the $i$-th overtone, the equation

$$\mathcal{L}_{N-(i-1)m/2}^{(im)}f_1^{(im)}(z) = S^{(im)}(z) \quad (4.66)$$

---

[5]For odd $m$, the neighboring modes would have half integer parameters, so resonant behavior only can appear starting at third order.

ceases to produce secular behavior as long as the source term is a polynomial. Therefore, given $m$ and $N$, the linear order solution should be a linear combination of its overtone modes whose overtone number does not exceed $2N/m + 1$.[6]

**Recurrence formula**

Using the expansion of the spin parameter (4.61) we can derive a recurrence formula for all orders in perturbation theory. Eq. (4.52) can be rewritten as

$$\mathcal{L}^{(k)}_{N+(m-k)/2} f^{(k)}(z) = \bar{\mathcal{S}}^{(k)}(z),\tag{4.67}$$

where

$$\bar{\mathcal{S}}^{(k)}(z) = \mathcal{S}^{(k)}(z) - \left(N + \frac{m}{2}\right)\sum_{p=1}^{\infty}\mu_p \varepsilon^p f^{(k)}(z),\tag{4.68}$$

and $\mathcal{S}^{(k)}(z)$ given through eq. (4.60). Under the perturbative expansion (4.56), we also expand the source term by

$$\bar{\mathcal{S}}^{(k)}(z) = \sum_{p=1}^{\infty}\varepsilon^p \bar{\mathcal{S}}^{(k)}_p(z).\tag{4.69}$$

Using an inductive argument, the regular normalizable perturbations are shown to be polynomials to all orders of the perturbation. Therefore, we expand the radial functions at each order by the associated Laguerre polynomials,

$$f_p^{(k)}(z) = \sum_I \mathcal{C}^{(k)}_{p,I} L_I^{(k)}(z).\tag{4.70}$$

As discussed in the previous section, the linear order solution should include all the overtone modes with $N - im/2 > 0$,

$$\mathcal{C}^{(0)}_{0,N+m/2} := \alpha_0, \quad \mathcal{C}^{(m)}_{0,N} := \alpha_1, \quad \mathcal{C}^{(2m)}_{0,N-m/2} := \alpha_2, \ \dots \ , \mathcal{C}^{(\eta m)}_{0,N-(\eta-1)m/2} := \alpha_\eta,\tag{4.71}$$

where $\eta := \lfloor 2N/m \rfloor + 1$. If $m$ is odd, the even overtones are turned off. Using the reparametrization of $\varepsilon$, we set

$$\mathcal{C}^{(m)}_{p,N} = 0 \quad (\text{if } p > 0).\tag{4.72}$$

Substituting this expansion into eq. (4.68), the source term can be decomposed into a resonant part and a normalizable part

$$\bar{\mathcal{S}}^{(k)}_p(z) = \mathcal{T}_p^{(k)} L^{(k)}_{N+(m-k)/2}(z) + \mathcal{L}^{(k)}_{N+(m-k)/2}\big[(\text{polynomial of } z)\big]\tag{4.73}$$

where $\mathcal{T}_p^{(k)} = 0$ gives the normalization condition[7]. To extract the resonant term from the source, the following decomposition formula of the product of the associated Laguerre polynomials is used

$$z^{\frac{i+j-k}{2}} L_I^{(i)}(z) L_J^{(j)}(z) = \sum_{K=0}\mathcal{Y}^{(i,j,k)}_{I,J,K} L_K^{(k)}(z),\tag{4.74}$$

---

[6]This limit is the same in the case of odd $m$, taking into account that only odd overtone modes are involved.

[7]If $N + (m - k)/2$ is not a non-negative integer, $\mathcal{T}_p^{(k)}$ becomes trivially zero.

where the coefficients are written by the integral of the triple product of the associated Laguerre polynomials

$$\mathcal{Y}_{I,J,K}^{(i,j,k)} = \frac{K!}{(K+k)!}\mathcal{I}_{I,J,K}^{(i,j,k)} \tag{4.75}$$

with

$$\mathcal{I}_{I,J,K}^{(i,j,k)} := \int_0^\infty dz e^{-z} z^{\frac{i+j+k}{2}} L_I^{(i)}(z) L_J^{(j)}(z) L_K^{(k)}(z). \tag{4.76}$$

This integration can be expressed through Lauricella's generalized hypergeometric functions [90].[8]

Since the LO-perturbation only contains the fundamental mode $m$ and its overtones, also at NLO only $m$ and its overtones are excited. To eliminate the resonant part in (4.73), we require for $i = 0, \ldots, \eta$ (again, only odd $i$ if $m$ is odd)

$$\left(N + \frac{m}{2}\right)\sum_{q=1}^{p}\mu_q \mathcal{C}_{p-q,N+(1-i)m/2}^{(im)}$$

$$= -\frac{1}{4}\sum_{j=0}^{\infty}\sum_{q=0}^{p-1}\sum_{I,J}\mathcal{C}_{q,I}^{(jm)}\mathcal{C}_{p-1-q,J}^{((i+j)m)}(I+J-N+(i+2j-1)m/2)\mathcal{Y}_{I,J,N+(1-i)m/2}^{(jm,(i+j)m,im)}$$

$$-\frac{1}{8}\sum_{j=0}^{i}\sum_{q=0}^{p-1}\sum_{I,J}\mathcal{C}_{q,I}^{(jm)}\mathcal{C}_{p-1-q,J}^{((i-j)m)}(I+J-N+(i-1)m/2)\mathcal{Y}_{I,J,N+(1-i)m/2}^{(jm,(i-j)m,im)}, \tag{4.77}$$

where the last line only exists for $i > 0$. Other than the resonant terms, we also obtain the coefficients

$$\mathcal{C}_{p,K}^{(im)} = -\sum_{q=1}^{p-1}\frac{N+m/2}{N+(1-i)m/2-K}\mu_q \mathcal{C}_{p-q,K}^{(im)}$$

$$-\sum_{j=0}^{\infty}\sum_{q=0}^{p-1}\sum_{I,J}\mathcal{C}_{q,I}^{(jm)}\mathcal{C}_{p-1-q,J}^{((i+j)m)}\frac{I+J+jm-K}{4(N+(1-i)m/2-K)}\mathcal{Y}_{I,J,K}^{(jm,(i+j)m,im)}$$

$$-\sum_{j=0}^{i}\sum_{q=0}^{p-1}\sum_{I,J}\mathcal{C}_{q,I}^{(jm)}\mathcal{C}_{p-1-q,J}^{((i-j)m)}\frac{I+J-K}{8(N+(1-i)m/2-K)}\mathcal{Y}_{I,J,K}^{(jm,(i-j)m,im)}. \tag{4.78a}$$

Again, we do not have the last line for $i = 0$.

### Comparison to the numerical results

For later comparison with the numerical result, we derive an expression for the center value of each angular Fourier mode. As in the axisymmetric sector, the center thickness is defined by

$$\mathcal{R}_0 = \frac{2}{1+a^2} + \sum_{i=0}^{\infty}\varepsilon^{i+1}\sum_I \mathcal{C}_{i,I}^{(0)}, \tag{4.79a}$$

and for the multipoles, we define[9]

$$\mathcal{R}_k = \sum_{i=0}^{\infty}\varepsilon^{i+1}\sum_I \frac{(I+k)!\mathcal{C}_{i,I}^{(k)}}{(2(1+a^2))^{k/2}I!k!}. \tag{4.79b}$$

---

[8]An English reference is found, for example, in [91].

[9]Which will serve as initial conditions in the numerical setup (4.120).

**Even multipoles**

The analysis for different fundamental modes $(N, m)$ differs in important aspects, so we are going to distinguish several cases in the following. Let us begin with the case $m$ even. As opposed to the axisymmetric modes, the normalization condition (4.77) already gives the coupled equation that determines the linear coefficients and the parameter renormalization,

$$\mu_1 \alpha_0 = -\frac{1}{4} \sum_{j=0}^{\eta} \mathcal{A}_{0,j} \alpha_j^2, \tag{4.80a}$$

$$\mu_1 \alpha_i = -\frac{1}{4} \sum_{j=0}^{\eta-i} \mathcal{A}_{i,j} \alpha_j \alpha_{i+j} - \frac{1}{8} \sum_{j=0}^{i} \mathcal{B}_{i,j} \alpha_j \alpha_{i-j} \quad (i > 0), \tag{4.80b}$$

where

$$\mathcal{A}_{i,j} = \mathcal{Y}_{N+(1-j)m/2, N+(1-i-j)m/2, N+(1-i)m/2}^{(jm, (i+j)m, im)}, \tag{4.81}$$

$$\mathcal{B}_{i,j} = \mathcal{Y}_{N+(1-j)m/2, N+(1-i+j)m/2, N+(1-i)m/2}^{(jm, (i-j)m, im)}. \tag{4.82}$$

The nonlinear eq. (4.80) is hard to solve in general and we will further distinguish different cases.

**Even multipoles with $2N < m$** Here the leading order solution consists of only two modes

$$f_0^{(0)}(z) = \alpha_0 L_{N+m/2}^{(0)}(z), \quad f_0^{(m)}(z) = \alpha_1 L_N^{(m)}(z). \tag{4.83}$$

The normalization condition (4.80) becomes

$$\mu_1 \alpha_0 = -\frac{\mathcal{I}_0}{4} \alpha_0^2 - \frac{(N+m)!}{4N!} \mathcal{I}_1 \alpha_1^2, \tag{4.84}$$

$$\mu_1 \alpha_1 = -\frac{1}{2} \mathcal{I}_1 \alpha_0 \alpha_1, \tag{4.85}$$

where

$$\mathcal{I}_0 = \mathcal{X}_{N+m/2, N+m/2}^{N+m/2}, \quad \mathcal{I}_1 = \mathcal{Y}_{N+m/2, N, N}^{(0, m, m)}. \tag{4.86}$$

Setting $\alpha_1 = 0$ immediately reproduces the axisymmetric result (4.30). Therefore assuming $\alpha_1 \neq 0$, we obtain

$$\mu_1 = -\frac{1}{2} \mathcal{I}_1 \alpha_0, \tag{4.87}$$

and

$$(2\mathcal{I}_1 - \mathcal{I}_0) \alpha_0^2 = \frac{(N+m)!}{N!} \mathcal{I}_1 \alpha_1^2. \tag{4.88}$$

Which has real solutions only if

$$\frac{\mathcal{I}_0}{\mathcal{I}_1} \leq 2. \tag{4.89}$$

This leads to an upper bound for $m$ (see figure 4.7). Since the sign of $\alpha_1$ does not matter, we obtain

$$\alpha_1 / \alpha_0 = \sqrt{\frac{N!}{(N+m)!}} \sqrt{2 - \frac{\mathcal{I}_0}{\mathcal{I}_1}}. \tag{4.90}$$
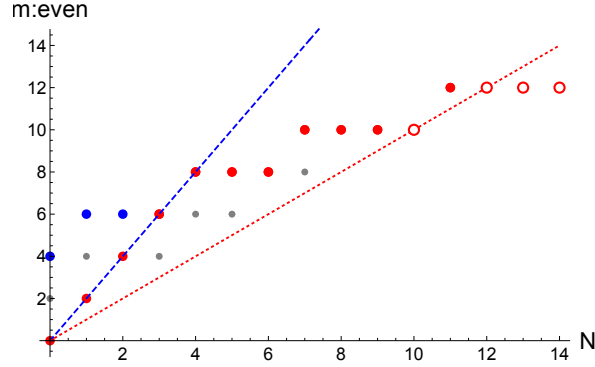
Figure 4.7: The maximum values of $m$ in the $2N < m$ sector (blue circles), defined by the constraint (4.89), and in the $N < m \leq 2N$ sector (red and red empty circles), defined by the positivity of eq. (4.104). The blue dashed and red dotted curves denote $m = 2N$ and $m = N$, respectively. Branches in each sector should be above each curve. The maximum values below $m = N$ (which can not be realized physically) are shown by red empty circles. Gray dots denote possible branches below the maxima.

The only branches satisfying $2N < m$ and the constraint (4.89) are

$$(N, m) = (0, 2): \quad \mu_1 = 1, \quad \alpha_1 = \frac{1}{\sqrt{2}} \quad \text{(black bar)}, \tag{4.91a}$$

$$(N, m) = (0, 4): \quad \mu_1 = -3, \quad \alpha_1 = \frac{1}{6\sqrt{2}}, \tag{4.91b}$$

$$(N, m) = (1, 4): \quad \mu_1 = 20, \quad \alpha_1 = \frac{1}{10\sqrt{2}}, \tag{4.91c}$$

$$(N, m) = (1, 6): \quad \mu_1 = -\frac{175}{2}, \quad \alpha_1 = \frac{1}{210\sqrt{5}}, \tag{4.91d}$$

$$(N, m) = (2, 6): \quad \mu_1 = 658, \quad \alpha_1 = \frac{1}{168}\sqrt{\frac{19}{47}}, \tag{4.91e}$$

where we set $\alpha_0 = 1$.

The right hand side in eq. (4.89) monotonically grows in $N$, and for $N \geq 3$, the bound (4.89) finally starts to exclude all of $m > 2N$. We will see that a similar bound appears also in the sector $N < m \leq 2N$ for $N \geq 3$. This upper bound does not mean the absence of the higher multipole deformation, but rather implies such deformation should be coupled with the lower companions even in the linear order. For example, $(N, m) = (0, 6)$ can be coupled with $(N, m) = (2, 2)$ (together with $(3, 0)$ and $(1, 4)$), which is in $\frac{2}{3}N < m \leq N$ sector.

Lastly, we evaluate the center values and angular velocity in eq. (4.79) up to $\mathcal{O}(\varepsilon)$,

$$\mathcal{R}_0 = \frac{2}{1 + a^2} + \alpha_0 \varepsilon = \frac{1}{N + m/2}\left(1 - (\mu_1 - (N + m/2)\alpha_0)\varepsilon\right), \tag{4.92}$$

and

$$\mathcal{R}_m = \frac{(N + m)!\alpha_1}{(4n + 2m)^{m/2}N!m!}\varepsilon. \tag{4.93}$$

By defining $\bar{\varepsilon} := (N + m/2)\mathcal{R}_0 - 1$ we obtain

$$\Omega = \frac{\sqrt{2N + m - 1}}{2N + m}(1 + \omega_1\bar{\varepsilon}), \quad \mathcal{R}_m = r_1\bar{\varepsilon}. \tag{4.94}$$

with the expansion coefficients

$$(N, m) = (0, 4): \quad \omega_1 = \frac{1}{5}, \quad r_1 = \frac{1}{1920\sqrt{2}}, \tag{4.95a}$$

$$(N, m) = (1, 4): \quad \omega_1 = \frac{8}{17}, \quad r_1 = -\frac{1}{4896\sqrt{2}}, \tag{4.95b}$$

$$(N, m) = (1, 6): \quad \omega_1 = \frac{25}{61}, \quad r_1 = \frac{1}{11243520\sqrt{5}}, \tag{4.95c}$$

$$(N, m) = (2, 6): \quad \omega_1 = \frac{2632}{5877}, \quad r_1 = -\frac{1}{31344000}\sqrt{\frac{19}{47}}. \tag{4.95d}$$

Some of these results are compared with the numerical analysis in figure 4.8.

**Even multipoles with $N < m \le 2N$** Here three modes have to be excited at leading order

$$f_0^{(0)}(z) = \alpha_0 L_{N+m/2}^{(0)}(z), \quad f_0^{(m)}(z) = \alpha_1 L_N^{(m)}(z), \quad f_0^{(2m)}(z) = \alpha_2 L_{N-m/2}^{(2m)}(z). \tag{4.96}$$

The normalization condition (4.80) leads to a quadratic constraint for the relative amplitudes

$$\mu_1\alpha_0 = -\frac{1}{4}\mathcal{I}_0\alpha_0^2 - \frac{1}{4}\mathcal{I}_1'\alpha_1^2 - \frac{1}{4}\mathcal{I}_2'\alpha_2^2, \tag{4.97a}$$

$$\mu_1\alpha_1 = -\frac{1}{2}\mathcal{I}_1\alpha_0\alpha_1 - \frac{1}{4}\mathcal{I}_3\alpha_2\alpha_1, \tag{4.97b}$$

$$\mu_1\alpha_2 = -\frac{1}{2}\mathcal{I}_2\alpha_0\alpha_2 - \frac{1}{8}\mathcal{I}_3'\alpha_1^2, \tag{4.97c}$$

where the coefficients are given by

$$\mathcal{I}_0 = \mathcal{X}_{N+m/2,N+m/2}^{N+m/2}, \qquad\qquad \mathcal{I}_1 = \mathcal{Y}_{N+m/2,N,N}^{(0,m,m)}, \tag{4.98}$$

$$\mathcal{I}_2 = \mathcal{Y}_{N-m/2,N-m/2,N+m/2}^{(2m,2m,0)}, \qquad \mathcal{I}_3 = \mathcal{Y}_{N,N-m/2,N}^{(m,2m,m)}, \tag{4.99}$$

and

$$\mathcal{I}_1' = \frac{(N+m)!}{N!}\mathcal{I}_1, \quad \mathcal{I}_2' = \frac{(N+3m/2)!}{(N-m/2)!}\mathcal{I}_2, \quad \mathcal{I}_3' = \frac{(N-m/2)!}{(N+3m/2)!}\frac{(N+m)!}{N!}\mathcal{I}_3. \tag{4.100}$$

Setting $\alpha_1 = 0$ immediately reproduces the previous analysis in which $m$ is replaced by $2m$. Therefore, we consider $\alpha_1 \neq 0$ and (4.97b) reduces to

$$\mu_1 = -\frac{1}{2}\mathcal{I}_1\alpha_0 - \frac{1}{4}\mathcal{I}_3\alpha_2. \tag{4.101}$$

Substituting this to the rest of eq. (4.97), we obtain two quadratic equations

$$(2\mathcal{I}_1 - \mathcal{I}_0)\alpha_0^2 + \mathcal{I}_3\alpha_2\alpha_0 - \mathcal{I}_2'\alpha_2^2 = \mathcal{I}_1'\alpha_1^2, \tag{4.102}$$

$$4(\mathcal{I}_1 - \mathcal{I}_2)\alpha_0\alpha_2 + 2\mathcal{I}_3\alpha_2^2 = \mathcal{I}_3'\alpha_1^2. \tag{4.103}$$

$\mathcal{I}_1$ and $\mathcal{I}_2$ (and accordingly $\mathcal{I}_1'$ and $\mathcal{I}_2'$) have to have the same sign for fixed $N$ and $m$. Thus eq. (4.102) and eq. (4.103) describe an ellipse and a hyperbola in the $(\alpha_1/\alpha_0, \alpha_2/\alpha_0)$ plane. The curves always have two (or no) intersections, which are shown to be identical by a constant shift in the angular coordinate $\phi \to \phi + \pi/m$. Therefore, we have at most one branch for each $(N, m)$ with $N < m \leq 2N$.

The radii of the ellipse from eq. (4.102) are proportional to

$$2 - \frac{\mathcal{I}_0}{\mathcal{I}_1} + \frac{\mathcal{I}_3^2}{4\mathcal{I}_0\mathcal{I}_2'} . \tag{4.104}$$

The positivity of this value is the necessary condition for the existence of the branch, which gives the upper bound for $m$ (figure 4.7). Since the last term in eq. (4.104) decays very quickly in $N$, the upper bound coincides with that from eq. (4.89) for $N \geq 3$. And for $N > 11$ the upper and the lower bound can not be satisfied at the same time. Accordingly this sector only contains a finite finite number of branches, like the $m > 2N$ sector.

We show the result for the lower branches

$$(N, m) = (1, 2): \quad \mu_1 = -4.48, \quad \alpha_1 = 0.382, \quad \alpha_2 = 0.00243, \tag{4.105a}$$

$$(N, m) = (2, 4): \quad \mu_1 = -132.5, \quad \alpha_1 = 0.0439, \quad \alpha_2 = -3.84 \times 10^{-8}, \tag{4.105b}$$

$$(N, m) = (3, 4): \quad \mu_1 = 903.0, \quad \alpha_1 = 0.0299, \quad \alpha_2 = -1.20 \times 10^{-9}, \tag{4.105c}$$

$$(N, m) = (3, 6): \quad \mu_1 = -4851.0, \quad \alpha_1 = 0.00268, \quad \alpha_2 = -2.87 \times 10^{-13}, \tag{4.105d}$$

where we set $\alpha_0 = 1$. One can observe that the amplitude of the overtone mode will be strongly suppressed for larger $N$ and $m$. The gradient of the angular velocity and the center values (4.94) are also evaluated for the same branches as

$$(N, m) = (1, 2): \quad \omega_1 = 0.230, \quad r_1 = 0.0221, \quad r_2 = -4.89 \times 10^{-7}, \tag{4.106a}$$

$$(N, m) = (2, 4): \quad \omega_1 = 0.416, \quad r_1 = 0.0000189, \quad r_2 = -2.56 \times 10^{-18}, \tag{4.106b}$$

$$(N, m) = (3, 4): \quad \omega_1 = 0.447, \quad r_1 = -2.92 \times 10^{-6}, \quad r_2 = 2.49 \times 10^{-20}, \tag{4.106c}$$

$$(N, m) = (3, 6): \quad \omega_1 = 0.454, \quad r_1 = 3.36 \times 10^{-9}, \quad r_2 = -4.64 \times 10^{-32}, \tag{4.106d}$$

where we also evaluated the amplitude of the overtone $r_2$ defined via

$$\mathcal{R}_{2m} = \frac{(N + m/2)! \alpha_2}{(4n + 2m)^m (N - m/2)! (2m)!} \varepsilon =: r_2 \bar{\varepsilon} . \tag{4.107}$$

**Odd multipoles with $2N < m$**

For odd $m$ the leading order modes do not produce secular behavior at second order, but starting from third order it will also appear in this case. Here the LO-solution consists of a single mode,

$$f_0^{(m)}(z) = L_N^{(m)}(z). \tag{4.108}$$

At second order the even $m$ modes have to be excited

$$\mathcal{C}_{1,K}^{(0)} = -\frac{2N + m - K}{4(N + m/2 - K)} \mathcal{Y}_{N,N,K}^{(m,m,0)}, \tag{4.109}$$

$$\mathcal{C}_{1,K}^{(2m)} = -\frac{2N - K}{8(N - m/2 - K)} \mathcal{Y}_{N,N,K}^{(m,m,2m)}, \tag{4.110}$$

without any renormalization,

$$\mu_1 = 0. \tag{4.111}$$

Iterating eq. (4.78) reveals that there are only even $m$ modes for every odd order in $\varepsilon$, and vice versa. Which results in $\mu_k = 0$ for odd $k$. At third order, the normalization condition (4.77) becomes

$$
\begin{aligned}
\mu_2 &= -\sum_K \left[ \mathcal{C}_{1,K}^{(0)} \frac{K}{2N+m} \mathcal{Y}_{K,N,N}^{(0,m,m)} + \mathcal{C}_{1,K}^{(2m)} \frac{K+m}{2(2N+m)} \mathcal{Y}_{K,N,N}^{(2m,m,m)} \right] \\
&= \frac{N!}{(N+m)!} \left[ \sum_{K=0}^{2N+m} \frac{K(2N+m-K)}{4(2N+m)(N+m/2-K)} \left( \mathcal{I}_{K,N,N}^{(0,m,m)} \right)^2 \right. \\
&\qquad\qquad \left. + \sum_{K=0}^{2N} \frac{(K+m)(2N-K)}{16(2N+m)(N-m/2-K)} \frac{K!}{(K+2m)!} \left( \mathcal{I}_{K,N,N}^{(2m,m,m)} \right)^2 \right].
\end{aligned}
\tag{4.112}
$$

Different from the even cases, the normalization condition for the simplest odd multipoles does not lead to a bound for $m$. For the lower sector $m \leq 2N$, we will have multiple overtones at linear order, which leads to coupled equations at third order as in the even modes. This may bound $m$ as in the even modes.

In contrast to the case of $m$ even, $\Omega$ and $\mathcal{R}_0$ only have even powers of $\varepsilon$ appearing in their expansion

$$\Omega = \frac{\sqrt{2N+m-1}}{2N+m} \left( 1 - \frac{N+m/2-1}{2N+m-1} \mu_2 \varepsilon^2 \right), \tag{4.113}$$

$$\mathcal{R}_0 = \frac{1}{N+m/2} \left[ 1 + \varepsilon^2 \left( (N+m/2) \sum_{K=0}^{2N+m} \mathcal{C}_{1,K}^{(0)} - \mu_2 \right) \right], \tag{4.114}$$

while $\mathcal{R}_m$ is odd in $\varepsilon$,

$$\mathcal{R}_m = \frac{(N+m)!}{(4N+2m)^{m/2} N! m!} \varepsilon. \tag{4.115}$$

This means that odd branches go out from the Myers-Perry branch only in one direction.[10] The leading order corrections can be written as

$$\Omega = \frac{\sqrt{2N+m-1}}{2N+m} \left( 1 + \omega_2 \varepsilon^2 \right), \quad \mathcal{R}_0 = \frac{1}{N+m/2} \left( 1 + \rho_0 \varepsilon^2 \right), \quad \mathcal{R}_m = \rho_m \varepsilon. \tag{4.116}$$

And the first few branches satisfy,

$$(N,m) = (0,3): \mu_2 = 0, \ \omega_2 = 0, \quad \rho_0 = 36, \quad \rho_m = \frac{1}{6\sqrt{6}}, \tag{4.117a}$$

$$(N,m) = (0,5): \mu_2 = 0, \ \omega_2 = 0, \quad \rho_0 = -6400, \quad \rho_m = \frac{1}{100\sqrt{10}}, \tag{4.117b}$$

$$(N,m) = (1,3): \mu_2 = -6592, \ \omega_2 = 2472, \quad \rho_0 = 4352, \quad \rho_m = \frac{1}{5}\sqrt{\frac{2}{5}}. \tag{4.117c}$$

---

[10]Changing the sign of $\varepsilon$ in $\mathcal{R}_m$ is equivalent to the constant rotation $\phi \to \phi + \pi/m$, and hence does not lead to another branch.
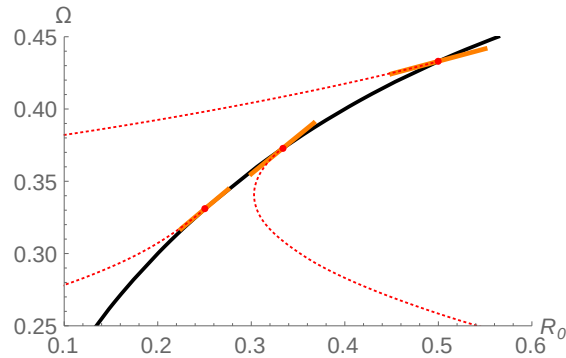
Figure 4.8: Beginning of the branches for $(N, m) = (0, 4)$, $(1, 4)$ and $(1, 6)$ on the $(\mathcal{R}_0, \Omega)$ plane.

For $N = 0$ branches, eq. (4.112) gives $\mu_2 = 0$ for any odd $m$,

$$\Omega|_{N=0} = \frac{\sqrt{m-1}}{m} \left(1 + \mathcal{O}\left(\varepsilon^4\right)\right). \tag{4.118}$$

For $N > 0$, for example, we have

$$\frac{d \ln \Omega}{d \ln \mathcal{R}_0}\bigg|_{(N,m)=(1,3)} = \frac{309}{544}. \tag{4.119}$$

### 4.3.3   Numerical construction

To obtain the fully non-linear multipole solutions numerically, we use a Fourier decomposition corresponding to overtones of a fundamental mode $m$

$$\mathcal{R}_m(r, \phi) = \sum_{n=0}^{\infty} \mathcal{R}^{(nm)}(r)\, r^{nm} \cos(nm\phi). \tag{4.120}$$

Plugging this into the stationary master equation (2.18), we obtain a countable set of coupled equations for the fundamental Fourier mode $\mathcal{R}^{(m)}(r)$ and its overtones $\mathcal{R}^{(n \cdot m)}(r)$ ($n = 2, 3, \dots$). From the perturbative analysis, we know that close to the MP-branch higher overtones will only be weakly excited. So we truncate the Fourier series for some $n_{\max}$ to obtain a finite dimensional problem. The resulting coupled ODEs can be now solved using the shooting method described in section 4.6, where now the space of initial conditions is spanned by the amplitudes of the Fourier modes $\mathcal{R}^{(nm)}(r)$ close to the origin, which we will denote as $\mathcal{R}_0, \mathcal{R}_m, \mathcal{R}_{2m}, \dots, \mathcal{R}_{n_{\max}m}$.

In figure 4.8, we show examples of branches extracted numerically with only the fundamental Fourier mode, i.e., $n_{max} = 1$, and compare them to the perturbative result. We checked that the truncation $n_{max} = 1$ is consistent for the beginning of the branch we show by comparing the results to a higher truncation with $n_{max} = 2$ and finding good agreement of the results. To extend the branches further overtones should be included.

The inclusion of overtones however makes our numerical procedure much less efficient (see section 4.6.3 for details), s.t. at this point we do not find conclusive results for odd multipole branches and even multipole branches corresponding to the opposite sign of the perturbation.
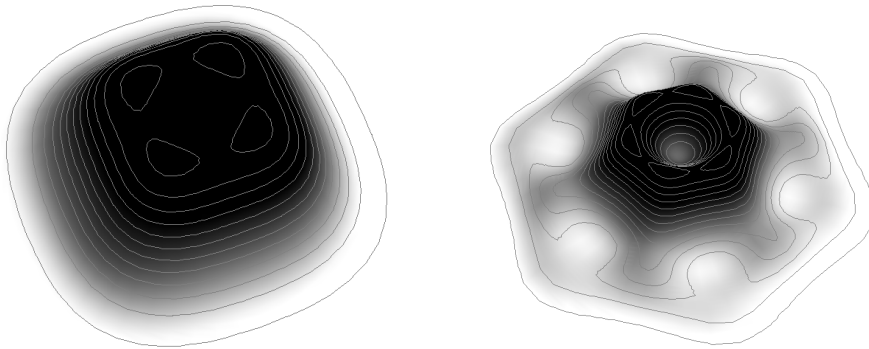
Figure 4.9: Mass profiles for branches with $(N, m) = (0, 4)$ (left) and $(N, m) = (1, 6)$ (right).
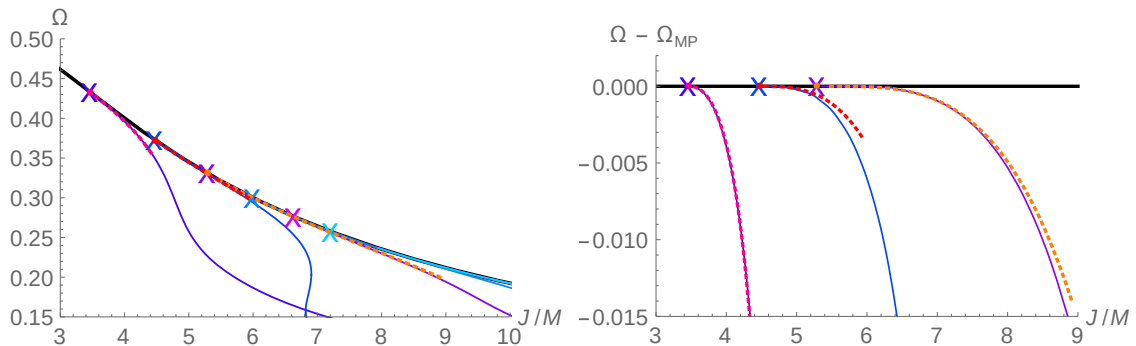


Figure 4.10: Dashed lines: Branches for $(N, m) = (0, 4)$, $(1, 4)$ and $(1, 6)$ in the $(\mathcal{J}/\mathcal{M}, \Omega)$ plane. Solid lines: Branches of axisymmetric solutions. It can be observed that black flower curves take a similar path to the ripple branches originating from the same zero modes.

In figure 4.9, we show representative plots of mass densities for some of the branches. The profiles for even multipoles show a behavior that can be related to the perturbative result that modes of different $N$ and $m$ couple to each other: The black flower branches show mass profiles, which when averaged over the angular direction resemble the corresponding axisymmetric branch that starts at the same branching point, which results in a similar $(\mathcal{J}/\mathcal{M}, \Omega)$-curve see figure 4.10.

## 4.4 Deformed black bars: Dumbbells and Spindles

As already studied in the previous section the large $D$ effective equations allow for stationary solutions without axisymmetry around the rotation axis, the first (and so far only) analytically known solution is the dipolar black bar [12]. Like the other multipolar solutions, the black bar plays an important role in the decay of the ultra-spinning instability of MP-black holes [14, 15, 87]. At high enough angular momentum the bar gets very elongated and develops a Gregory-Laflamme type instability. In this section, we are going to study the zero mode configurations corresponding to this instability.

The black bar is best studied in Cartesian coordinates in the co-rotating frame

$$x = r\cos(\phi - \Omega t), \quad y = r\sin(\phi - \Omega t), \tag{4.121}$$

where it can be written as

$$\mathcal{R}_{\mathrm{bar}}(x, y) = 1 - \frac{x^2}{2\ell_\perp^2} - \frac{y^2}{2\ell_\parallel^2} \tag{4.122}$$

where

$$\ell_\perp^2 = \frac{2}{1 + \sqrt{1 - 4\Omega^2}}, \quad \ell_\parallel^2 = \frac{2}{1 - \sqrt{1 - 4\Omega^2}}. \tag{4.123}$$

Note that for small $\Omega$ the bar becomes very elongated and in the limit $\Omega \to 0$ the solution connects to a non-rotating black string along the $y$-direction.

### 4.4.1   Co-rotating zero modes

We deform the bar perturbatively via $\mathcal{R} = \mathcal{R}_{\mathrm{bar}}(x, y) + \delta\mathcal{R}(x, y)$, where the deformation $\delta\mathcal{R}(x, y)$ satisfies

$$\left[\partial_x^2 - \frac{x}{\ell_\perp^2}\partial_x + \partial_y^2 - \frac{y}{\ell_\parallel^2}\partial_y + 1\right]\delta\mathcal{R} = -\frac{1}{2}((\partial_x\delta\mathcal{R})^2 + (\partial_y\delta\mathcal{R})^2) \tag{4.124}$$

At linear order, the regular solutions are given by Hermite polynomials

$$\delta\mathcal{R}(x, y) = \varepsilon H_{n_x}\left(\frac{x}{\sqrt{2}\ell_\perp}\right) H_{n_y}\left(\frac{y}{\sqrt{2}\ell_\parallel}\right) + \mathcal{O}\left(\varepsilon^2\right), \tag{4.125}$$

where $n_x, n_y$ are non-negative integers with

$$\frac{n_x}{\ell_\perp^2} + \frac{n_y}{\ell_\parallel^2} = 1. \tag{4.126}$$

Together with the constraint $\ell_\perp^{-2} + \ell_\parallel^{-2} = 1$, the regular and non-trivial perturbations are available only for

$$n_x = 0, \quad n_y = \ell_\parallel^2 \geq 2. \tag{4.127}$$

### 4.4.2   Nonlinear perturbations

Considering the linear result, we can assume only $y$-dependence even in the non-linear regime. Then, by rescaling

$$z = \frac{y}{\sqrt{2}\ell_\parallel}, \tag{4.128}$$

the deformation equation reduces to

$$\mathcal{H}_{\ell_\parallel^2}\delta\mathcal{R}(z) = -\frac{1}{2}\delta\mathcal{R}'(z)^2, \tag{4.129}$$

where $\mathcal{H}_N$ is the Hermite operator defined by

$$\mathcal{H}_N := \frac{d^2}{dz^2} - 2z\frac{d}{dz} + 2N. \tag{4.130}$$

Given the value of $\ell_\parallel$, $\Omega$ and $\ell_\perp$ is written by

$$\Omega = \frac{\sqrt{\ell_\parallel^2 - 1}}{\ell_\parallel^2}, \quad \ell_\perp = \frac{\ell_\parallel}{\sqrt{\ell_\parallel^2 - 1}} = \frac{1}{\ell_\parallel \Omega}. \tag{4.131}$$

The corrections beyond the linear order can be derived in the same manner as the bumpy deformation of the Myers-Perry. First, we expand the deformation function by $\varepsilon$

$$\delta\mathcal{R}(z) = \sum_{k=0}^{\infty} \varepsilon^{k+1} f_k(z). \tag{4.132}$$

If we consider a branch bifurcating from the zero mode $\ell_\parallel^2 = N$ on the black bar branch, one can set

$$f_0(z) = H_N(z). \tag{4.133}$$

The length of the bar $\ell_\parallel$ for the deformed branch should be expanded by $\varepsilon$,

$$\ell_\parallel^2 = N\left(1 + \sum_{k=1}^{\infty} \mu_k \varepsilon^k\right), \tag{4.134}$$

where the running coefficient $\mu_k$ is determined so that $f_k(z)$ remains to be normalizable at each order. Expanding eq. (4.130) by $\varepsilon$, we obtain

$$\mathcal{H}_N f_k(z) = -\frac{1}{2}\sum_{i=0}^{k-1} f_i'(z) f_{k-1-i}'(z) - 2N\sum_{i=0}^{k-1} \mu_{k-i} f_i(z) =: \mathcal{S}_k(z). \tag{4.135}$$

Similar to the bumpy solutions, the higher order corrections can be solved algebraically. Assuming $f_k(z)$ is a polynomial, each order solution can be expanded by the Hermite polynomials,

$$f_k(z) = \sum_{M=0} \mathcal{C}_{k,M} H_M(z), \tag{4.136}$$

where the linear order solution is supposed to be $\mathcal{C}_{0,M} = \delta_{M,N}$. Substituting this, the source term of each order becomes

$$\mathcal{S}_k(z) = -\frac{1}{2}\sum_{i=0}^{k-1}\sum_{I,J} \mathcal{C}_{i,I}\mathcal{C}_{k-1-i,J} H_I'(z) H_J'(z) - 2N\sum_{i=0}^{k-1}\sum_{I} \mu_{k-i}\mathcal{C}_{i,I} H_I(z). \tag{4.137}$$

Using the properties of the Hermite polynomials, the source term can be decomposed to the resonant and non-resonant terms,

$$S_k(z) = \mathcal{H}_N\left[-\frac{1}{4}\sum_{K\neq N}\sum_{I,J}\sum_{i=0}^{k-1} \mathcal{C}_{i,I}\mathcal{C}_{k-1-i,J}\frac{I+J-K}{N-K}\mathcal{Q}_{I,J}^K H_K(z) - \sum_{K\neq N}\sum_{i=1}^{k-1}\frac{N\mu_{k-i}\mathcal{C}_{i,K}}{N-K} H_K(z)\right]$$
$$-\left[\frac{1}{2}\sum_{I,J}\sum_{i=0}^{k-1}(I+J-N)\mathcal{C}_{i,I}\mathcal{C}_{k-1-i,J}\mathcal{Q}_{I,J}^N + 2N\sum_{i=0}^{k-1}\mu_{k-i}\mathcal{C}_{i,N}\right] H_N(z), \tag{4.138}$$

where $Q_{I,J}^K$ is defined by $H_I(z)H_J(z) = \sum_{K=|I-J|}^{I+J} Q_{I,J}^K H_K(z)$. Using $\mathcal{C}_{0,M} = \delta_{M,N}$, the regularizing condition is given by

$$\mu_k = -\sum_{I,J}\sum_{i=0}^{k-1}\frac{I+J-N}{4N}\mathcal{C}_{i,I}\mathcal{C}_{k-1-i,J}Q_{I,J}^N - \sum_{i=1}^{k-1}\mu_{k-i}\mathcal{C}_{i,N}\,, \tag{4.139a}$$

and the non-resonant coefficients,

$$\mathcal{C}_{k,M\neq N} = -\frac{1}{4}\sum_{I,J}\sum_{i=0}^{k-1}\mathcal{C}_{i,I}\mathcal{C}_{k-1-i,J}\frac{I+J-M}{N-M}Q_{I,J}^M - \sum_{i=1}^{k-1}\frac{N\mu_{k-i}\mathcal{C}_{i,M}}{N-M}. \tag{4.139b}$$

For the resonant term, we simply set

$$\mathcal{C}_{k,N} = 0 \quad (k > 0). \tag{4.140}$$

Using induction one can show for odd branches that $f_k(z)$ has only odd (even) power for the even (odd) order, and $\mu_k$ vanishes for every odd order. Similarly, for even $N$, it can be shown that at each order only even powers appear.

**Perturbative solution**

By solving the recurrence equation with $\mathcal{C}_{0,M} = \delta_{M,N}$, one can obtain the solution to arbitrary order. The result for $\mathcal{O}\left(\varepsilon^2\right)$ is

$$\mu_1 = -\frac{1}{4}Q_{N,N}^N, \quad \mathcal{C}_{1,M\neq N} = -\frac{2N-M}{4(N-M)}Q_{N,N}^M, \tag{4.141}$$

and for $\mathcal{O}\left(\varepsilon^3\right)$,

$$\mu_2 = \frac{1}{8}\sum_I \frac{I(2N-I)}{N(N-M)}Q_{N,N}^I Q_{N,I}^N, \tag{4.142}$$

$$\mathcal{C}_{2,M\neq N} = \frac{1}{8}\sum_{I\neq N}\frac{(N+I-M)(2N-I)}{(N-M)(N-I)}Q_{I,N}^M Q_{N,N}^I - \frac{N(2N-M)}{16(N-M)^2}Q_{N,N}^N Q_{N,N}^M, \tag{4.143}$$

where $Q_{N,N}^N = 0$ for the odd $N$, giving $\mu_1 = 0$ for the odd dumbbells.

**Physical quantities**

Once, given the deformation $\delta\mathcal{R}(z)$ as

$$\delta\mathcal{R}(z) = \sum_{i=0}^{\infty}\sum_I \varepsilon^{i+1}\mathcal{C}_{i,I}H_I(z), \tag{4.144}$$

the physical quantities are calculated using properties of the Hermite polynomials.

**Value at the origin** Here we evaluate the center values $\mathcal{R}_0 = \mathcal{R}(0)$ and $\bar{\mathcal{R}}_0 = \mathcal{R}'(0)$, which are also used as the boundary condition for the numerical analysis. Due to the mirror symmetry in the even case, $\bar{\mathcal{R}}_0$ only exists for the odd branches. The center thickness $\mathcal{R}_0$ of the deformed bar is given by

$$\mathcal{R}_0 = 1 + \sum_{i=0}^{\infty} \sum_I \varepsilon^{i+1} \mathcal{C}_{i,I} H_I(0), \tag{4.145}$$

where

$$H_M(0) = \begin{cases} (-2)^{M/2}(M-1)!! & (M : \text{even}) \\ 0 & (M : \text{odd}) \end{cases}. \tag{4.146}$$

For the odd branch, only odd Hermite polynomials appear at every odd order in $\varepsilon$, so $\mathcal{R}_0$ becomes the function of $\varepsilon^2$. Using $H_I'(0) = -H_{I+1}(0)$, $\bar{\mathcal{R}}_0$ is similarly evaluated to

$$\bar{\mathcal{R}}_0 = -\sum_{i=0}^{\infty} \sum_I \varepsilon^{i+1} \mathcal{C}_{i,I} H_{I+1}(0). \tag{4.147}$$

With eq. (4.141), we obtain

$$\mathcal{R}_0 = 1 + \varepsilon H_N(0) - \varepsilon^2 \sum_{I \neq N} \frac{4N-I}{2(N-I)} \mathcal{Q}_{N,N}^I H_I(0) + \mathcal{O}\left(\varepsilon^3\right), \tag{4.148}$$

$$\bar{\mathcal{R}}_0 = -\varepsilon H_{N+1}(0) + \mathcal{O}\left(\varepsilon^3\right), \tag{4.149}$$

where $\bar{\mathcal{R}}_0$ does not have $\mathcal{O}\left(\varepsilon^2\right)$ term, because $\mathcal{Q}_{N,N}^I$ vanishes for odd $I$. For comparison with the numerical analysis (figure 4.11), we obtain,

$$\Omega = \frac{\sqrt{N-1}}{N}\left(1 + \omega_1\bar{\varepsilon} + \omega_2\bar{\varepsilon}^2\right), \quad \bar{R}_0 = \bar{\rho}_0\bar{\varepsilon} \tag{4.150}$$

where

$$\bar{\varepsilon} := \begin{cases} \mathcal{R}_0 - 1 & (\text{even}) \\ \sqrt{|\mathcal{R}_0 - 1|} & (\text{odd}) \end{cases} \tag{4.151}$$

For odd branches with $N = 2n+3$, $\mathcal{R}_0$ is given by $\mathcal{R}_0 = 1 + (-1)^n\bar{\varepsilon}^2$. The even branches have

$$\omega_1|_{N=4,6,8,10} = 2, \quad -16, \quad 129, \quad -896 \tag{4.152}$$

$$\omega_2|_{N=4,6,8,10} = 52, \quad 8088, \quad \frac{4178816}{5}, \quad \frac{529505120}{7}, \tag{4.153}$$

and the odd branches have $\omega_1 = 0$ and

$$\omega_2|_{N=3,5,7,9} = \frac{12}{19}, \quad \frac{19200}{1969}, \quad \frac{5480160}{53939}, \quad \frac{23886707712}{24551641}, \tag{4.154}$$

$$\bar{\rho}_0|_{N=3,5,7,9} = -2\sqrt{\frac{3}{19}}, \quad 6\sqrt{\frac{5}{1969}}, \quad -10\sqrt{\frac{7}{53939}}, \quad \frac{210}{\sqrt{24551641}}. \tag{4.155}$$

This shows that one always need to spin up the black hole for the transition to an odd branch.

**Mass and angular momentum**    The mass (4.33) and angular momentum (4.34) can be calculated by

$$\mathcal{M} = \mathcal{M}_{\text{bar}} \int_{-\infty}^{\infty} \frac{dz}{\sqrt{\pi}} e^{-z^2} \exp(\delta\mathcal{R}(z)), \tag{4.156}$$

and

$$\mathcal{J} = \frac{\mathcal{M}}{\Omega} + 4\mathcal{M}_{\text{bar}} \ell_{\parallel}^2 \Omega \int_{-\infty}^{\infty} \frac{dz}{8\sqrt{\pi}} e^{-z^2} H_2(z) \exp(\delta\mathcal{R}(z)), \tag{4.157}$$

where $\mathcal{M}_{\text{bar}} = 2\pi e/\Omega$ is the mass of the bar solution for the given $\Omega$. Due to the orthogonal property of the Hermite polynomials, the integrals in $\mathcal{M}$ and $\mathcal{J}$ pick up $H_0(z)$ and $H_2(z)$ components in $\exp(\delta\mathcal{R}(z))$, respectively.

Using the result in the previous section, the ratio of the angular momentum to the mass is given by

$$\frac{\mathcal{J}}{\mathcal{M}} = \frac{1}{\Omega}\left(1 - \frac{2(N-1)}{N(N-2)}\mathcal{Q}_{N,N}^2 \varepsilon^2 + \mathcal{O}\left(\varepsilon^3\right)\right), \tag{4.158}$$

where we note that $\Omega$ should also varies in $\varepsilon$. For the odd branch, both $\mathcal{J}/\mathcal{M}$ and $\Omega$ become a function of $\varepsilon^2$.

### 4.4.3    Numerical construction

In order to find fully nonlinear deformations of the black bar, we begin by considering equation (1.48) with the ansatz

$$\mathcal{R}(x,y) = -\frac{x^2}{2\ell_{\perp}^2} + \mathcal{R}(y), \tag{4.159}$$

where we imply that $\mathcal{R}(y) \equiv \mathcal{R}(0,y)$, and $\ell_{\perp}^2$ is defined by eq. (4.123). With this substitution, we are left with

$$\mathcal{R}'' + \frac{1}{2}\mathcal{R}'^2 + \mathcal{R} + \frac{\Omega^2 y^2}{2} = \ell_{\perp}^{-2}. \tag{4.160}$$

Since $y$ is no longer a radial coordinate, the condition $\mathcal{R}'(0) = 0$ is no longer required. We can define $\mathcal{R}'(0) \equiv \bar{\mathcal{R}}_0$ instead. Allowed solutions must extend regularly both to $y \to -\infty$ and $y \to \infty$ simultaneously. If we start the integration from $y = 0$, the initial conditions are given by $\mathcal{R}_0 \equiv \mathcal{R}(0)$ and $\bar{\mathcal{R}}_0 \equiv \mathcal{R}'(0)$, which have to be tuned in order to get allowed solutions.

The branches arising from even $N$ zero modes have a $y \to -y$ symmetry, so $\bar{\mathcal{R}}_0 = 0$. These bars only require $\mathcal{R}_0$ to be tuned, so they can be found in the same way as the axisymmetric solutions. Nonzero values of $\bar{\mathcal{R}}_0$ give rise to the branches originating in odd $N$ zero modes. This requires a slightly more involved numerical algorithm, which is described in sec. 4.6.

In figure 4.11, the first branches of deformed black bars are shown in the $(\mathcal{R}_0, \Omega)$ plane. In this case, there is a strong qualitative difference between even and odd $N$. Odd branches extend only in one direction. This is to be expected, since in this case, reversing the sign of linear perturbations is equivalent to the gauge change $\phi \to \phi + \pi$. Surprisingly, for odd
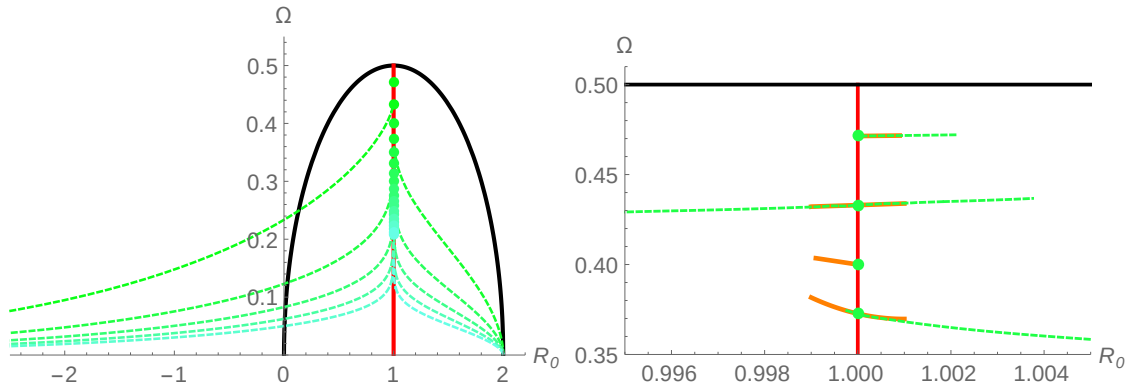
Figure 4.11: Branches of black bar deformations on the $(\mathcal{R}_0, \Omega)$ plane. The right plot is a close-up showing good agreement with the analytic expansions (orange) and also zooms in on the short branches. Different tones of green are being used for different branches for the sake of clarity.

$N$ branches, $\Omega$ increases as we move away from the zero modes, and these branches are also very short.

Even $N$ branches result in the bar breaking apart in $N/2$ separated blobs. In $(\mathcal{R}_0, \Omega)$ plane, they behave in a way that is qualitatively similar to the axisymmetric case, and can therefore be classified in two types. If $N$ is a multiple of 4, $\mathcal{R}_0 \to 0$ and the mass density approaches zero at the origin. If $N$ is even but not a multiple of 4, then one of the blobs stays at the origin, with $\mathcal{R}_0 \to 2$. The profiles of the first two symmetric bars ($N = 4, 6$) are depicted in figure 4.12.

Similar to the axisymmetric branches, even $N$ branches can be extended far away from the black bar to the arbitrarily small $\Omega$, in which the mass profile approaches to the multiple blobs located in the almost equal interval. Again, we observe these intervals grow very slowly at the same logarithmic rate as that of ring-like blobs in the axisymmetric branches. Therefore, one can expect these branches finally would pinch off to the array of binary black holes.

The angular momentum per unit mass is calculated using eqs. (4.33) and (4.34)

$$\frac{\mathcal{J}}{\mathcal{M}} = \frac{\int dx \, dy \, p_\phi}{\int dx \, dy \, m} \,, \tag{4.161}$$

with

$$m(x, y) = \exp\left(\mathcal{R}(y) - \frac{x^2}{2\ell_\perp^2}\right), \tag{4.162}$$

$$p_\phi(x, y) = \left[(x^2 + y^2)\,\Omega + \frac{xy}{\ell_\perp^2} + x\mathcal{R}'(y)\right] m(x, y) \tag{4.163}$$

The phase diagram for the deformed bars is shown in figure 4.13.
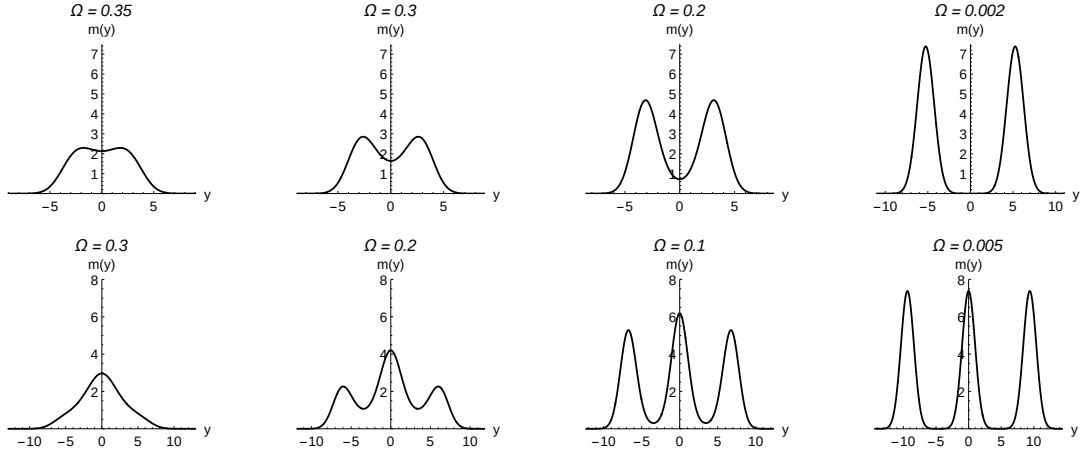
Figure 4.12: Deformed black bars corresponding to $N = 4, 6$ (dumbbells) for different values of $\Omega$. The deformation only shows $y$-dependence and the dumbbells remain Gaussian in $x$-direction.
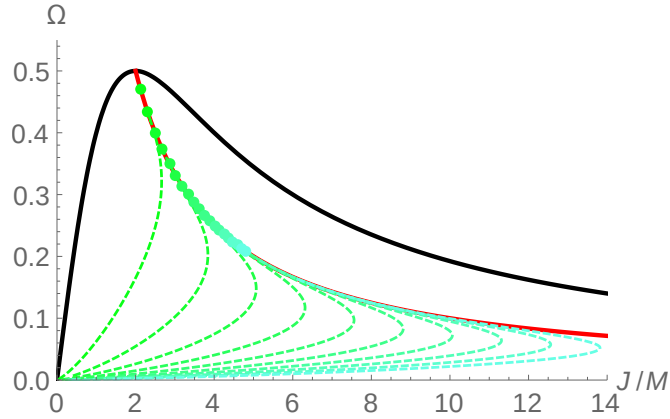


Figure 4.13: The 10 first dumbbell branches, we also plot the branching points of the odd bar perturbations marked by points that only give rise to short 'spindle' branches. The Myers-Perry solutions are represented by the thick black curve, and the (non-deformed) black bars by the thick red curve. Different tones of green are being used for different branches for the sake of clarity.

## 4.5 Effects of adding charge

Following the approach of [13] and as already described in section 1.4.1 we can easily construct the (non-extremal) charged solution corresponding to every uncharged solution. According to eq. (1.47) for a given charge parameter $\mathfrak{q} = \frac{Q}{M}$ and given $\Omega$, the charged solution has the profile of an uncharged solution with rotation parameter

$$\Omega_q = \frac{\Omega}{(1 - 2\mathfrak{q}^2)^{1/4}} \, . \tag{4.164}$$

The $(\mathcal{J}/\mathcal{M}, \Omega)$ phase diagrams for $|Q| > 0$ are thus the same diagrams as in the uncharged case with a rescaling of the $\Omega$-axis by the factor $\left(1 - 2\mathfrak{q}^2\right)^{-1/4}$. Accordingly the bumpy branches will appear at the same $\mathcal{J}/\mathcal{M}$ but at a lower $\Omega$. As shown in the

previous sections lower values of $\Omega$ correspond to more elongated/ further separated blobs, *i.e.,* adding charge to the black holes leads to stronger deformations. This intuitively can be understood as charge repulsion deforming the horizon.

## 4.6 Numerical methods

### 4.6.1 Axisymmetric sector

Stationary axisymmetric black holes are regular solutions of eq. (4.49) that extend from 0 to $r \to \infty$. Due to singular point at $r = \infty$ from the rotation term it is particularly difficult to use of spectral and relaxation methods. For this reason, the approach used in this paper is essentially a shooting method. By regularity at the origin the ODE can be generally integrated radially outwards with the initial conditions $\mathcal{R}(0) = \mathcal{R}_0$ and $\mathcal{R}'(0) = 0$. The numerical solution will generally become singular at some finite $r = r_s$. In figure 4.14, the values of $r_s$ are shown as a function of the initial condition parameter $\mathcal{R}_0$, interestingly the appearance of singularities is (semi-) continuous in the space of initial conditions which makes it possible to look for singularities/ peaks where the solution extends to infinity. These peaks correspond to (approximate) locations of the allowed solutions.
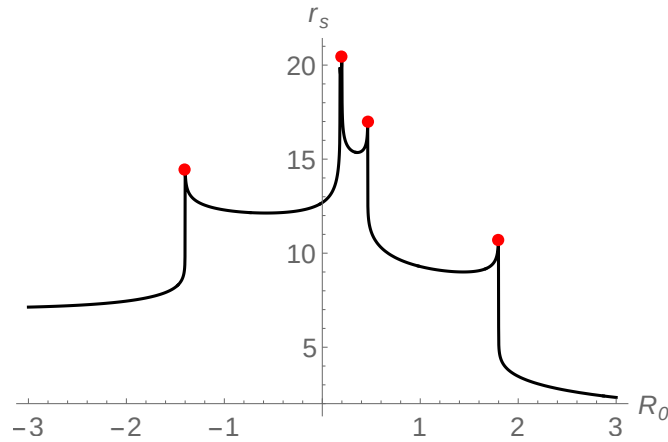


Figure 4.14: Values of $r_s$ (radius where the solution becomes singular) for $\Omega = 0.3$. The solutions that have to be free of such singularities and extend to infinity appear as sharp peaks, which we marked here with red dots.

When a branch ends, as for the negative amplitude modes, the peak that represents it becomes a local maximum, with no divergence whatsoever. This requires us to define a criterion for a local maximum to be considered a proper peak, or a *vanishing peak*. The criterion that has been taken for a peak to be valid is

### 4.6.2 Black bar deformations

Deformations with even values of $N$ are found in a way which is completely analogous to the axisymmetric case.

Odd deformations of bars are described by solutions of eq. (4.160) that have a nonzero value of $\bar{\mathcal{R}}_0 = \mathcal{R}'(0)$. This increases the complexity of the problem, since it now requires to tune both $\mathcal{R}_0$ and $\bar{\mathcal{R}}_0$ in order to get a solution that extends to infinity both for the negative and positive sides of the $y$ axis. This complication can be partially circumvented by noticing that, for the deformed black bars, the change $y \to -y$ is equivalent to $\bar{\mathcal{R}}_0 \to -\bar{\mathcal{R}}_0$. This means that, if $(\Omega, \mathcal{R}_0, \bar{\mathcal{R}}_0)$ gives an allowed solution, then so does $(\Omega, \mathcal{R}_0, -\bar{\mathcal{R}}_0)$. This fact allows the right values of $\mathcal{R}_0$ to be found by requiring the peaks in $r_s(\Omega, \mathcal{R}_0, \bar{\mathcal{R}}_0)$ to be located at opposite values of $\bar{\mathcal{R}}_0$. This is done by the secant root-finding method in a few iterations. Again, *vanishing peaks* and *fake blobs* are discarded in a similar way as in the axisymmetric case.

### 4.6.3   Multipole deformations

By using the ansatz (4.120) truncated at some Fourier mode $\cos(n_{\max}m\phi)$, we obtain a set of $n_{\max} + 1$ coupled equations for the functions $\mathcal{R}^{(nm)}(r)$. These equations, by imposing the regularity condition $\mathcal{R}^{(nm)'}(0) = 0 \,\forall n$, can be solved by specifying the values of the radial functions at the origin. The problem reduces then to finding peaks in the singular radius $r_s(\Omega, \mathcal{R}_0, \mathcal{R}_m, \mathcal{R}_{2m}, \ldots, \mathcal{R}_{n_{\max}m})$.

Identifying peaks on a function with more than one variable is in general not an easy task, especially if there is no straightforward way of reducing the problem to one variable (as in the case of odd deformations of the black bar). For this reason, here we restrict ourselves to the fundamental Fourier mode, *i.e.,* we maximize $r_s(\Omega, \mathcal{R}_0, \mathcal{R}_m)$. We use the *Mathematica* function **NMaximize** to identify the peak by incrementing $\Omega$ in small steps, and constraining the search in a small region around the result of the previous step.

Even with this method, the values of the $\mathcal{R}_0, \mathcal{R}_m$ still are affected by small fluctuations (which are likely due to numerical error) around the branch. We correct this by subsampling the data points.

## 4.7   Summary of results

In this chapter we have demonstrated that the hydro-elastic equations [31] contain a whole new class of 'rippled' stationary solutions, besides the already known black branes, their non-uniform deformations [11] and the non-deformed spinning localized black holes [12].

We have constructed solutions that branch off from the singly spinning Myers-Perry solution directly or indirectly via the black bar branch, which has been already identified in [12]. We found both axisymmetric and non-axisymmetric solutions, and only the former ones can remain stationary at finite $D$, since non-axisymmetric solutions will radiate gravitational waves. However, with increasing number of dimension the emission of gravitational waves becomes weaker, which will allow the non-axisymmetric solutions to be long-lived.

The axisymmetric solutions described in this paper, we have identified as *ring-like* and *Saturn-like* bumpy black holes, or *black ripples* in short. They bifurcate from the

axisymmetric zero modes of Myers-Perry in the ultra-spinning regime. As in the numerical studies in finite dimensions [61, 62], we found that all branches extend in two directions: either with a positive or a negative amplitude of the deformation. The direction that increases the angular velocity leads to a very short branch, the other direction extends indefinitely at large $D$. This suggests that the former directions lead to singular solutions, as observed in previous numerical constructions [61, 62].

Multipolar deformations can not be stationary in a fixed number of dimensions, but are indicative of ultraspinning instabilities of the Myers-Perry black hole. In high enough dimension they correspond to long-lived transient objects. We generically call them *black flowers*, the simplest case among them is the black bar and it has an analytic solution.

The black bar also has an infinite number of co-rotating zero modes, from which deformed branches develop: the *dumbbells* and the *spindles*. We classify the deformed bars by the parity of their zero mode as odd and even. Similarly to the ripples, the even branches go out in two directions. In the spin-down direction, the deformation grows a dumbbell-like profile with a distinct number of blobs for each branch, and hence we call them *dumbbells*. In the opposite direction, we could find only very short branches which we call *spindles*. Odd branches turned out very short as well. Odd branches and spindles correspond to solutions with increased angular velocity. One might expect that both the spindles and the odd branches end up forming a singularity.

It is very suggestive that the spindle branches correspond to the solutions that develop sharp pointy endings, as observed dynamically in [87, 15]. These sharp endings of the deformed bar would be possibly affected by the Gregory-Laflamme instability, presenting a large number of zero modes close to the end of the short branch. The sharpened tips could, in principle, pinch off producing detached small black holes.

This process of a black hole developing long arms that end up pinching off has indeed been observed in [87, 15], not only for the spindles but also for higher multipole deformations. We find it likely that these dynamical solutions would correspond to the short branches described above, *i.e.,* those resulting from exciting the zero modes in the direction with increasing $\Omega$. This would apply both to the spindle solutions and to multipolar deformations leading to multiple arms. This conjecture is supported by the fact that short branches go in the direction of decreasing $\mathcal{J}/\mathcal{M}$, which should be favored in finite $D$ simulations since gravitational radiation tends to decrease the angular momentum to mass ratio of the evolving object.

The method used to identify axisymmetric solutions should be exhaustive, and thus we do not expect the ripple branches to have their own secondary axisymmetric zero modes. We expect, on the other hand, that the axisymmetric solutions will become unstable to multipolar deformations. An indication of a ring-like ripple breaking apart into four black holes via an $m = 4$ deformation was already found at large $D$ in [15]. Interestingly, black rings share the same kind of instabilities and subsequent pinch-offs [92, 93, 94, 95]. Such instabilities would begin at zero modes along the branches of ripples. This fact leaves open the possibility of the 'long' multipolar branches actually merging with the ripple branches at these zero modes. No conclusive results have been obtained about this

intriguing possibility so far.

We have found no evidence that the long multipolar branches have bifurcations. This possibility could be analyzed in future work, possibly with an improved numerical setup. The dumbbell branches end as an array of separated black holes and thus seem unlikely to have further zero modes.

In the formalism employed here, the effect of the charge is simply incorporated in the effective angular velocity $\Omega_q = \Omega/(1 - 2\mathfrak{q}^2)^{1/4}$ as in [13]. Therefore, with a given value of charge and $\Omega$, the corresponding charged solution is immediately obtained from the uncharged one. Due to the factor $\left(1 - 2\mathfrak{q}^2\right)^{-1/4}$, the charged deformed branches will appear for the same $\mathcal{J}/\mathcal{M}$ but for a lower $\Omega$, which corresponds to more elongated/further separated blobs. This can be interpreted as the effect of the charge repulsion. Since all the analysis is written in terms of $\Omega_q$, one can take the extremal limit $\mathfrak{q}^2 \to 1/2$ of all branches, keeping $\Omega_q$ finite, resulting in a smooth limit, that leads to rather strange deformed 'extremal' branches, both with and without rotation. The proper large $D$ limit of extremal horizons is however yet unclear, and a more careful analysis seems appropriate.

**Fate of far extended branches**   All 'long' branches (corresponding to bulging deformations) extend far away from the original bifurcating points in the phase space, where they develop broad thin regions. Currently, very little is known about how to interpret these nearly zero thickness regions in the large $D$ effective theory. In the case of spherical black holes the thickness falls off towards infinity as a Gaussian profile, which might be interpreted as the round tip of the black hole. Therefore, if the deformation develops a thin neck between blobs, and its size grows infinitely large, one can expect such deformation to end up as a pinch off of the horizon at finite $D$. This would correspond to a topology-changing transition.

We found that the ripple branches develop such long thin necks connecting Gaussian-shaped ring blobs (with a central blob in the case of Saturns) at their final stages of deformation. Particularly, we observed that the separation process involves two distinct length scales. From the numerical solutions, we could easily estimate that the radii of ring blobs grow like $\Omega^{-1}$ as $\Omega \to 0$. The same behavior has been derived in the blackfold approach [84, 89], which might imply that the blackfold approximation becomes already accurate in the pinch off phase, due to the localization of gravity at large $D$. Another scaling is that of the intervals between ring blobs, which are estimated as $\sim \sqrt{|\log \Omega|}$. Due to the hierarchy in these two scales, we expect the first pinch off to occur always on the axis, indicating a first topology change to a bumpy black ring/Saturn, before transitioning to the multi-rings/Saturns, as observed in the $(+)_3$-branch of $D = 6$ bumpy black holes [62].

Dumbbell branches also extend far away from the black bar to arbitrarily small $\Omega$, where the mass profile approaches that of multiple evenly spaced blobs. As opposed to the ripples, dumbbells show only a single scaling, which has the same logarithmic growth as the intervals between the ring blobs in the case of ripples. Therefore, one can expect that these branches would finally pinch off to multiple black holes[11].

---

[11]Or one might say 'rotating black hole array'.

**Finite $D$ effects**   The blob coordinate is supposed to be identified as the small patch of the $\sqrt{D}$-amplified entire coordinate.[12] Therefore, the blob approximation will break down if the length of the thin neck reaches $\sim \sqrt{D}$, when the $1/D$ corrections are included. This breakdown will give some information on the transition in phase space. For example, the pinch off from the ripples to black rings or Saturns will take place at $\Omega \sim 1/\sqrt{D}$. Actually, black rings are already constructed by using the large D effective theory approach in the same scaling [28, 78]. This implies that one can use the effective theory result as the global setup to solve the local topology-change. For other logarithmic scalings $\sim \sqrt{|\log \Omega|}$, the break down will occur at much smaller spin $\Omega \sim e^{-D}$. In the black string analysis, a similar type of breakdown is already seen after including $1/D$ corrections [11]. The black hole entropy is another important quantity to evaluate the stability of the solutions. Since the mass and entropy become degenerate at $D \to \infty$, we would need to know the next-to-leading order terms in $1/D$ expansion to calculate the entropy difference for a given mass.

**Blob-Blob interactions**   For the ripples and dumbbells, we observed a universal scaling of the blob distance as $\sqrt{|\log \Omega|}$ at $\Omega \to 0$, implying an effective interaction between the blobs (or ring-like blobs). This indicates the possibility to reconstruct the large $D$ effective theory as a particle-like (or soliton-like) effective description of blobs weakly interacting via very thin necks. This possibility will be pursued elsewhere.

The origin of this logarithmic dependence, though very naively, might be understood as a force balance between the centrifugal force and the attraction between the blobs at large $D$. Assuming a black hole of radius $r_{\mathrm{H}}$ and an orbiting particle, the gravitational force is approximated as $(r_{\mathrm{H}}/r)^D$ and the centrifugal force as $\Omega^2 r$. The equilibrium is accomplished by $r/r_{\mathrm{H}} \sim 1 - 2D^{-1}\log \Omega$. Therefore, the particle orbit exists very close to the horizon $\sim |\log \Omega|/D$. This introduces the $|\log \Omega|$ scaling in the near horizon region. Curiously, if we assume two adjacent black holes with the same mass, the equilibrium condition would be modified to $r/r_H \sim 2 - 2D^{-1}\log(e^{D/2}\Omega)$ with $e^{D/2}\Omega = \mathcal{O}(1)$ or $|\log \Omega| \sim D$. This coincides with the value at which the neck length between blobs reaches $\sqrt{|\log \Omega|} \sim \sqrt{D}$ and the blob approximation breaks down.

**Towards the topology change**   The topology-changing transition at large $D$ is described by the conifold metric which solves the Ricci flow equation [96]. Especially, the black string/black hole transition is completely solved by the King-Rosenau (KR) solution for the $2D$ Ricci flow. Some of the topology-changing transitions (Saturn-like ripples, dumbbells) can be reduced to the $2D$ Ricci flow problem in the co-rotating frame, since the transition occurs in a very narrow region. Hence, they should also be solved by the KR solution, due to the rigidity in $2D$ compact ancient flow [97]. For the transition between ring-like ripples and black rings, we need a better understanding of the $3D$ Ricci flow.

Here we should note that, in the case of the black string/black hole transition, one just has to give the global configuration (such as the black hole (blob) radius and the

---

[12]This is only an estimate from the Myers-Perry solution, in which the exact coordinate match is known.

compactification scale) as boundary conditions for the conifold metric, without considering the force balance condition. Now, for example, if we consider the transition between a dumbbell and binary black hole, we also have the rotation $\Omega$, which will not appear in the large $D$ conifold analysis after switching to the co-rotating frame. To relate $\Omega$ with the mass and separation, one needs to find the proper force balance condition at large $D$, as roughly estimated in the previous paragraph.

In the current formalism, we could only follow the $(-)$-ripple branches for a very short range. These $(-)$-branches are shown to develop a single-sided conical horizon on the equator when they approach the end of their branch [62]. Therefore, it should also be possible to study the ending phase of $(-)$-branches using the large $D$ conifold metric and Ricci flow methods. Different from the usual pinch off problem, one may have to find the non-compact Ricci flow solution, in which only one side is the horizon.

# Chapter 5

# Black hole collisions and instabilities

## 5.1 Overview

The cosmic censorship (CC) conjecture [98] roughly asserts that, if one starts with physical or 'good' initial conditions GR never produces any observable singularities. Nowadays it is distinguished between the *strong cosmic censorship conjecture* and the *weak cosmic censorship conjecture.*

Strong CC is concerned with the predictivity of GR and asserts that in generic circumstances GR will not produce any Cauchy horizons, *i.e.,* that there are situations in GR where an observer could pass into a part of spacetime that is not predicted by GR starting from a complete Cauchy slice. In most cases the discussion focuses on the charged or rotating black holes, which have (when unperturbed) Cauchy horizons in their interior, which when crossed would allow an observer to receive signals from the timelike singularity present in the analytical extension of the solution. As such strong CC is often just taken in a looser sense as a hypothesis about the interior of black holes.

On the contrary weak CC asserts that in GR singularities do not form outside an horizon. So if they appear, they have to be unobservable to an observer who is often taken to be in asymptotically flat region outside of the black hole. We will be mostly concerned with this formulation of CC in this chapter.

It is expected that if classical GR predicts a singularity to form, in an actual physical situation previous to the formation of the singularity effects of quantum gravity would grow so large that the classical description ceases to apply. In this sense CC is the assertion that no low energy configuration evolves into a quantum gravity regime (in a classical time scale[1]).

By now there is some evidence that CC is violated: In 4 spacetime dimensions Choptuik found the (fine-tuned) example of critical scalar collapse [99]. In higher dimensions transitions between different black hole solutions provide a prominent candidate for viola-

---

[1]Otherwise the formation and subsequent evaporation of a blackhole could be taken as a counterexample. It is however important that the evaporation process is not governed by classical GR only.

tions of weak CC [51, 85]. In these examples higher dimensional black holes with instable, elongated horizons evolve towards stable spherical black holes. These evolutions resembles the breakup of fluid jets or bigger drops into smaller drops.

In this chapter we are going to present our claim [14, 15], that CC is violated in black hole collisions in higher dimensions. The basic process can be easily understood as follows and is depicted in figure 5.1: In dimensions $D \geq 6$ black holes can form an elongated horizon after a collision if the total angular momentum is high enough. These states resemble black bars [54, 12] or black dumbbells [16]. These are elongated rotating black holes which can exist as stationary objects when $D \to \infty$, and which are expected to be long-lived (quasi-stationary) at large but finite $D$, since the gravitational emission from the rotating bar is suppressed like $\sim D^{-D}$. Because these black holes have elongated horizons they are susceptible to Greggory-Laflamme type instabilities [32, 51] akin to the instabilities of Myers-Perry black holes first conjectured in [58].
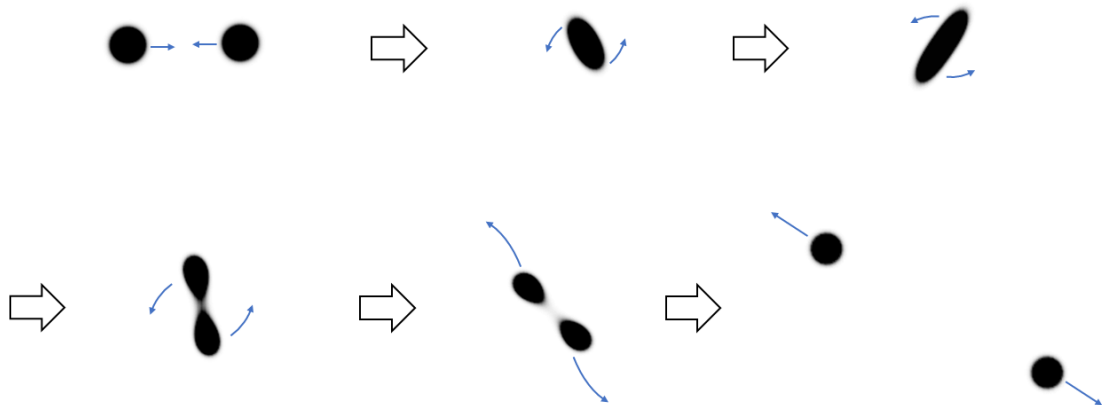


Figure 5.1: Two spinning black holes collide and form a rotating black bar, which then breaks up into two outgoing black holes different than the initial ones (the figures are high-contrast density plots of the mass density obtained from the numerical simulation of a collision in the large-$D$ effective theory).

Here we will show that black bars do form in black holes collisions when $D \geq 6$, and are dynamically unstable in a manner qualitatively and even quantitatively similar to the Gregory-Laflamme (GL) instability of a black string [32, 51]. This is the mechanism that drives the system to the violation of CC in the black hole collision.

As we will discuss below, the presence of an intermediate quasi-stationary bar is cleanest when the total angular momentum in the merger is dominated by the initial intrinsic spin of the black holes, rather than the orbital angular momentum in the collision. In that case, the intermediate state can be closely matched to a stationary rotating black bar during several rotation cycles. In contrast, in collisions where the orbital angular momen-

tum dominates (through sizable impact parameter or collision velocities), the intermediate state resembles less closely a stationary bar, and more a dumbbell, which pinches down more quickly than a black bar. We may think of the dumbbell as a bar at a later stage of pinching, so we regard all these collisions and decays as proceeding within the same qualitative dynamics.

Our evolutions are performed in the limit $D \to \infty$ where gravitational radiation is completely absent. One may wonder whether at finite $D$ the radiative spin-down of the bar can avert the development of the GL-like instability. To investigate this, we estimate the radiation rate using the quadrupole formula in $D$ dimensions (the emission rate of energy was obtained in [100], while the emission rate of angular momentum is presented here for the first time). We find that the radiation is suppressed not only by high dimensionality; also the spin-down rate is small for long black bars with high spin, since their rotation velocity is slow. As a consequence, it must be possible to violate CC in a collision of two black holes if large enough total angular momentum is achieved in the intermediate, merged phase, to form a long enough black bar. In the terminology of [58], these results mean that at high spins 'death by fragmentation' can occur more quickly than 'death by radiation'. However, we have not managed to get reliable estimates for the minimum dimension in which such long, high-spin bars can form in a black hole collision. This is due to the current uncertainties in the values of the capture impact parameter and, more importantly, of the initial emission of radiation in the collision. Therefore, while CC violation is certainly possible in collisions at large enough $D$, our estimates do not allow to be equally sure about the outcome at relatively low $D$ (e.g., $D = 6$ or 7).

In addition, we present results for the non-linear evolution of instabilities of ultraspinning black holes. These exhibit remarkably rich structures, see e.g., figure 5.2, which are strikingly similar to the shapes recently observed in numerical simulations in $D = 6, 7$ in [87]. As mentioned in that article, the dynamics of these configurations is expected to lead to novel violations of CC.



Figure 5.2: Late-time horizon shape of unstable ultraspinning Myers-Perry black holes when perturbed with a tripolar and a quadrupolar mode, and then evolved with the large-$D$ effective theory. Further evolution of the black hole suggests that the arms pinch, violating CC through 'death by fragmentation' [58]. The quadrupolar 'star' and its evolution to singular pinches has been recently observed in numerical simulations in $D = 6, 7$ in [87].

The outline of this chapter is the following. Section 5.2 contains a detailed description of the ideas, methods, and results in our simulations of black hole collisions, including a final discussion of the violation of CC. In section 5.3 we perform non-linear evolutions of the ultraspinning instabilities of MP black holes, which appear to lead to novel violations of CC. In section 5.4 we study the GL-like instabilities of black bars. Our numerical results are in agreement with a model that approximates the black bar as a segment of black string. To estimate how much angular momentum and mass is lost to gravitational radiation, we compute in 5.5 the quadrupolar angular momentum emission rate and prove that, for bodies rigidly rotating with angular velocity $\Omega$, the emission rates of energy $E$ and angular momentum $\mathcal{J}$ satisfy

$$\frac{dE}{dt} = \Omega \, \frac{d\mathcal{J}}{dt} \tag{5.1}$$

in all $D$.[2] Section 5.6 then estimates the radiative spin-down of black bars at finite $D$, and compares its timescale with that of the GL-like instability that drives the evolution towards CC violation. We find that the spin-down of sufficiently long bars is very inefficient in all dimensions where they exist ($D \geq 6$, and possibly $D = 5$), and also for shorter bars in large enough $D$ ($D \gtrsim 8$ or possibly lower).

## 5.2 Collision, merger, and break up

Our main tool are the effective equations for the dynamics of neutral, asymptotically flat black $p$-branes in the large $D$ limit as presented in chapter 1. It is worth pausing to note what the effective equations (1.6), (1.7) achieve for solving the fully non-linear, time-dependent evolution in a black hole merger and other similarly complex phenomena. The problem is straightforward: we can specify initial data corresponding to black holes (*i.e.,* blobs) moving towards each other with by giving them a Galilean boost, and simply follow the time evolution by numerically solving (1.6), (1.7). Since the equations are first order in time, we only need to supply the field configuration $(m, p_i)|_{t=0}$ in an initial time slice. There are no constraint equations to solve or keep track of, nor gauge issues: the analysis that led to the effective equations disposed of them already. We can directly read off the gauge-invariant, physical quantities of interest from the outcome of the time integration. Perhaps even more importantly, the effective dimensionality of the problem has been reduced by one, since the dependence on the radial variable $\rho$ away from the horizon has been explicitly integrated in the effective theory. Then, our simulations in the $2 + 1$ dimensions of the effective theory correspond to $3 + 1$ evolutions in the complete spacetime (plus the $n + 1 = D - 4$ dimensions of the "passive" $S^{n+1}$).

Interestingly, the effective equations are almost linear, with all the non-linearities confined to the last term in (1.7). That is, this term alone is responsible for the interaction between the two colliding black holes: without it, they would pass through each other undisturbed. Both (1.6) and (1.7) resemble diffusion equations,[3] and they produce very

---

[2]This result was quoted, without derivation, in [58].

[3]So the system evolves irreversibly even though the total entropy remains constant.

stable numerical evolution. Since there is no gravitational radiation at $D \to \infty$, no wave extraction is required (nor possible!) and the asymptotic behavior needs no special consideration. We simply impose periodic boundary conditions in a square domain in the spatial directions.

With all these simplifications, black hole collisions can be numerically simulated in not more than a few minutes in a conventional computer.

### 5.2.1 Black brane as 'regulator'

An unavoidable feature of our effective theory of black holes is the presence of a black brane horizon at all points. The Gaussian profiles (2.25) and (2.66) extend all the way to infinity on the brane, and so the black holes are never completely localized—indeed, the presence of a non-vanishing mass and area density everywhere is a requisite for the validity of the effective theory.

Notice, though, that the mass density asymptotes to zero at infinity with exponential fall-off, so the infinite brane background is not a problem for the computation of extensive physical magnitudes of black holes (their total mass, area and spin), which never diverge. The Gaussian localization on the horizon is indeed a very basic feature of the large $D$ limit of spherical (or ellipsoidal) black holes [12]. Observe also that, even if infinitely extended black branes of constant mass density are GL-unstable, this instability does not afflict the Gaussian blobs; actually, the blobs naturally appear as stable end states of the GL instability. We may say that the exponential fall-off leaves too little mass density at large distances to clump into smaller blobs.

Nevertheless, the ever- and omni-present horizon introduces peculiarities in configurations with more than one black hole. In an initial configuration with two blobs, the brane continuously connects them, and we cannot unambiguously say where one black hole ends and the other begins—at least not without introducing an arbitrary cutoff, *e.g.,* where the mass density becomes $10^{-2}$ of the peak density. And we cannot exactly determine either the moment when two black holes merge, since they are always part of one and the same continuous horizon.

More relevant to our purposes, the black brane horizon in (1.2) is always regular and there never appears a singularity in it. Then, strictly speaking, within this approach we can never observe a violation of CC—an important point that we will return to in section 5.2.4. In our simulations, as we will see, two blobs approach and merge into a single one, which then splits into two different blobs that fly away from each other. But at all moments the horizon is smooth and continuous; we cannot ascribe a splitting instant without introducing an arbitrary cutoff at low mass densities on the brane.[4]

---

[4]A Gaussian blob can be matched to the pole region of a stationary black hole [12], and the initial configuration in the effective black brane theory with two blobs would correspond to the transient, dumbbell-like black hole formed when two separate black holes touch and quickly merge in a timescale $\sim 1/D$. The results of [96] (although in stationary configurations) suggest that the 'neck' where this merger starts (or where the eventual break up occurs) affects only non-perturbatively in $1/D$ the physics in the pole region that is captured by the black brane effective theory. A more precise characterization of the separation

Given the smoothness of all the evolutions in the effective theory, we may regard the 'black brane background' as a kind of regulator in the system, which prevents the appearance of curvature singularities, and which allows the black holes to separate after a collision without the evolution ever breaking down. In this respect, the black brane may look similar to the apparent horizon regulator introduced in numerical holographic collisions in AdS [101]. A distinction between the two is that in our effective theory the mass density asymptotes to zero, while [101] introduce a small energy density everywhere. A more significant difference is that in [101], the regulator size can be parametrically separated from other scales, and therefore it is in principle possible to continuously remove it from the system, reducing its effects in a controllable manner. This is not possible in our set up. Therefore, although the 'brane regulator' does not impose any serious difficulty for the initial and intermediate stages in our black hole collisions, it does imply an inability to follow the evolution through to the putative horizon break up. This is a limitation inherent to the use of the black brane effective theory, and not merely a practical convenience for numerical solution, as it is in [101] (and in our own handling of numerics, see section 4.6).

The position we take is that our simulations do show that certain horizons (in collisions, and in the evolution of unstable black holes) develop instabilities that lead them towards localized pinch-offs—the evidence we present for this is clean and clear. For the further evolution of these horizons, we rely on what is known about the evolution of qualitatively related systems, in particular the development of black string instabilities. We will avail ourselves of all the current information about these in order to construct a strong, convincing case for the violation of CC. These conclusions should then be tested in future dedicated numerical simulations of collisions and black hole instabilities at finite $D$.

Now we can proceed to the results of our numerical simulations.

### 5.2.2   Initial states

As stated above, in order to supply initial data for our simulations, we only need to specify an initial configuration $(m, p_i)|_{t=0}$. In the case at hand, we consider the superposition of two configurations of the form (2.30) centered at positions $\mathbf{x}_1$, $\mathbf{x}_2$, with initial velocities $\mathbf{u}_1$, $\mathbf{u}_2$, mass parameters $m_{0,1}$, $m_{0,2}$ and rotational parameters $a_1$, $a_2$. Due to translational, boost and scale invariance of the effective equations, we can always set, say $\mathbf{x}_1 = \mathbf{u}_1 = 0, m_{0,1} = 1$, without loss of generality, which shows that the space of parameters has dimension 7.

For numerical simplicity, we require our configurations to be reflection symmetric, which guarantees that the intermediate state will form and evolve at the center of our computational domain. We thus restrict ourselves to configurations of the form

$$m_{0,1} = m_{0,2} = m_0, \qquad a_1 = a = \sigma a_2 \tag{5.2}$$

$$u_{x,1} = -u_{x,2} = u, \qquad u_{y,1} = u_{y,2} = 0, \tag{5.3}$$

$$x_1 = -x_2 = -x_0 \qquad y_1 = -y_2 = -b/2. \tag{5.4}$$

---

between the two black holes would require going beyond the leading large-$D$ theory.

Here, $\sigma = \pm 1$ controls whether the spins are aligned or anti-aligned. The parameter $x_0$ does not play any significant physical role, and it is chosen such that the Gaussian profiles do not overlap significantly at $t = 0$. The initial states of our simulations are then characterized by three physical parameters: the relative velocity $u$, the impact parameter $b$ and the intrinsic spin controlled by $a$. In [14] we focused on configurations within this class with $a = 0$. We now expand our exploration of the space of parameters by considering $a \geq 0$. We show examples of our initial conditions in figure 5.3.
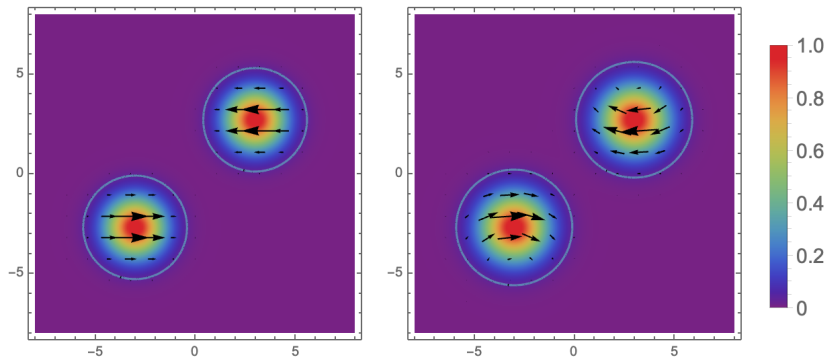


Figure 5.3: Initial data for $u = 1$, $b = 2.5$, $x_0 = 3$, and $a = 0$ (left) and $a = 0.5$, $\sigma = 1$ (right). Here we have chosen units $m_0 = 1$.

### 5.2.3 Black hole collision

Having set up the initial conditions as described above, we follow the evolution of the system by numerically solving (1.6), (1.7). We use a numerical procedure that we describe briefly here.

#### Numerical Methods

We have used two independent codes, with equivalent results: one is written in the *Julia* language [102] and the other one in *Mathematica*. The *Julia* code uses a two-dimensional Fourier grid with FFT differentiation in the spatial directions, and the *DifferentialEquations.jl* package [103] for time integration. The *Mathematica* code uses finite differences in the spatial directions and a fourth-order Runge-Kutta method in the time direction.

#### Collision tomography

Before describing our results, we discuss a convenient way to characterize our final and intermediate state configurations. In this discussion, we will make heavy use of the symmetry assumptions described in section 5.2.2, so our methods are only valid for simulations resulting from initial conditions within this class.

A necessary condition for a configuration to be at equilibrium is that the maxima of $m(t, \mathbf{x})$ and $p_i(t, \mathbf{x})$ are constant in time. We use this simple criterion as a first check of the settling-down of a given time-evolving configuration. Moreover, in order to check whether

a configuration evolves as a connected or disconnected object, we find it convenient to check for the value of energy density at the origin $m_{origin} := m(t, \mathbf{0})$. In all our initial states $m_{origin}$ is very close to zero, and this is clearly also the case for two black holes flying apart from each other.

In order to gain extra information about the spatial distribution of the energy density, we introduce the *tensor of inertia*[5]

$$I_{ij}(t) = \int d^2x\, m(t, \mathbf{x})\, x^i x^j \,. \tag{5.5}$$

We can obtain the principal axes of rotation and effective lengths as eigenvectors and eigenvalues $\lambda_1 \leq \lambda_2$ of the inertia tensor. Going to this frame of reference allows us to easily identify final states corresponding to MP black holes or bars by comparing the one-dimensional profiles along the axes with Gaussians.

**Final states**

Let us now discuss the final states obtained in our collisions. First, note that when $b$ is sufficiently large, the black holes almost do not interact. This appropriately reflects the fact that at large $D$ the interaction between two massive objects decreases very quickly with the distance.[6] All the interesting cases thus lie in a region in parameter space where $0 < b < b_{crit}$, with $b_{crit}$ being a complicated function of $a$ and $u$. While it may be interesting to determine the shape of this function, we do not attempt it here. We will assume below that we are always in the regime in which a non-trivial intermediate state forms, *i.e.,* in which a non-trivial interaction of the black holes takes place.

A very important finding of [14] is that, at least for $a = 0$ in our highly symmetric configurations, the type of final state that we arrive at does not depend separately on $u$ and $b$, but *only on $J/M$, the total angular momentum per unit mass of the system.*

Although we have found that this result holds for a large fraction of the parameter space, an extensive exploration reveals that, for sufficiently high initial speeds, there are more exotic intermediate configurations in which additional lumps of energy emerge along the line that connects the two drifting black holes. This indicates that the scattering of black holes may not be only of the types

$$2 \to 1 \,,$$
$$2 \to 2 \,,$$

that were considered in [14], but more generally

$$2 \to N = 1, 2, 3, 4 \ldots \tag{5.6}$$

---

[5]This differs from the conventional definition by a trace term, but it is equally good for our purposes.

[6]This is a little too glib. The range of the gravitational interaction between two separate black holes is $\sim 1/D$ (in units of the horizon radius), while the distances along the brane in the effective theory are much larger, $\sim 1/\sqrt{D}$. In the effective theory the direct gravitational attraction does not play any role, instead it captures well the elastic-type interaction between two black holes that have merged into a single horizon—see footnote 4.

Such scatterings may be of interest, but their casuistics seems fairly complex. Henceforth we will assume that our initial speeds are small enough that the scattering is always $2 \rightarrow 1$ or $2 \rightarrow 2$.

For relatively small initial speeds—with our without initial intrinsic spins—, the available final states for a given value of $J/M$ can be predicted simply from the stability properties of the black holes and bars in the phase diagram in figure 2.4. More concretely, for $J/M < 2$ the final states are MP black holes, while for $2 < J/M < (J/M)_{crit} = 4/\sqrt{3}$ the collisions form bars. This critical value of $J/M$ corresponds to the first parity-even marginal mode of the bars in (2.143): the dumbbell deformation of the bar. For $J/M$ above $(J/M)_{crit}$, the intermediate state formed in the collision breaks up. As we elaborate later, this is the signal of evolution towards a violation of CC.

We have checked that introducing spin $a > 0$ opens a new channel for violation of CC. Most notably, we will show that the intermediate state of collisions of spinning black holes can be quantitatively accurately approximated as almost stationary black bars. This confirms that the mechanism responsible for their break up is the GL instability.

We have not made a detailed analysis of what is the precise final state after the horizon break up, *i.e.,* what is the outgoing impact parameter and the spins and velocities of the outgoing black holes, and how strongly these depend on initial state properties other than the total $J/M$. But it is possible to extract some generic features. In particular, we expect that the spin of the final black holes is smaller than that of the initial black holes, since when the horizon breaks up, it does so from a fairly long black bar, and therefore the outgoing impact parameter is larger than the initial one. Then, the final orbital angular momentum is larger than the initial one, and so the intrinsic spin must be smaller. For instance, this is visible in figure 5.1, where the initial black holes look larger than the final ones, even though they necessarily have the same mass, but the size of the blobs, for a given mass, is larger for larger spin. With larger initial impact parameter or velocities the situation is less clear, and probably the initial and final spins are more comparable.

In Figure 5.4 we show the final states of simulations with parameters in the following range:

- Varying Initial Velocity: $u \in [0.1, 1.7]$, $b = 3$, $x_0 = 3$, $a = 0$

- Varying Impact Parameter: $u = 1.7$, $b \in [0, 3]$, $x_0 = 3$, $a = 0$

- Varying Spins: $u = 0.5$, $b = 0$, $x_0 = 5$, $a \in [0, 1.25]$, $\sigma = 1$

Within this domain in parameter space, whether the collision is $2 \rightarrow 1$ or $2 \rightarrow 2$ can be predicted from the sole knowledge of the initial value of the total $J/M$ (which is conserved along the evolution).

**Intermediate black bars**

As discussed above, the intermediate states of the collisions that yield CC violation have the form of bar-like objects. This, combined with the fact that no stable bars are observed
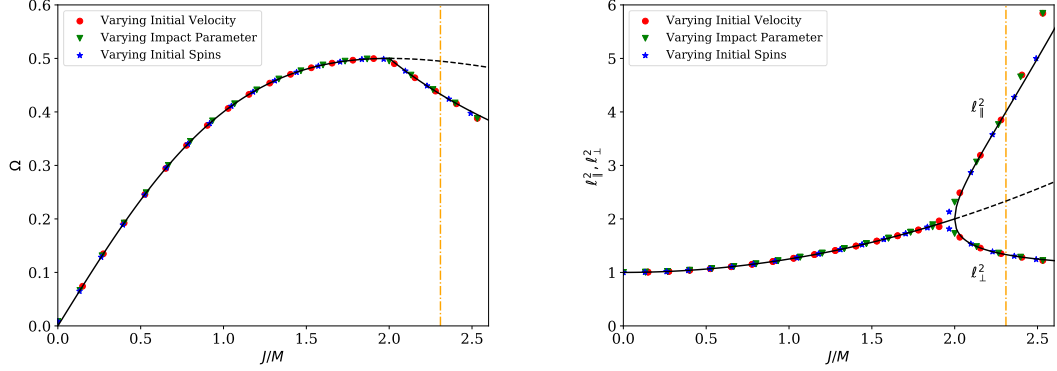
Figure 5.4: Final states of collisions for varying impact parameter, initial velocities and spins. The dashed and continuous lines correspond to stationary MP black holes and black bars. The left plot is superimposed on the phase diagram of figure 2.4. The right plot shows the (squared) longitudinal and transverse axial lengths $\ell_\parallel^2$ and $\ell_\perp^2$ described in (2.69) of the final states, and provides more detailed evidence that the collision forms a rotating black bar. The values of $\ell_\parallel^2$ and $\ell_\perp^2$ are obtained by linear regression of $\log m$ with respect to $r^2$ along the longitudinal and transverse directions, respectively. We see that the initial value of $J/M$ (conserved along the evolution) predicts the end state. The vertical dash-dotted orange line shows the onset of the fundamental symmetric mode of the black bar. We observe certain configurations lying beyond this line, but these are not stable: their appearance is an artifact of running the simulation for a finite amount of time.

to form above the threshold predicted by the marginal mode computation, suggests that the mechanism for the pinching off is the GL instability present in the black bars. However, there is a possible caveat: in the $a = 0$ simulations the intermediate states are highly distorted elongated objects, which makes the comparison with actual bars rather indirect. It turns out that this argument can be put on a quantitative basis in the case of initial spinning black holes, as we now show in detail.

Let us consider for concreteness the case of a collision with $a = 0.99$, $b = 1.2$, $u = 1.2$. The energy density of the black holes is such that $m_0 = 1$. For these parameters, $J/M = 2.69$, so we expect the formation of a bar-like object which should then break apart since we are in the region of unstable bars. This is indeed the case, as we show in Fig. 5.5, where we depict the time evolution of the maximum of the mass density and its value at the origin. We see that $m_{max} = m_{(0,0)}$ for a long part of the evolution, which corresponds to the interval in which a metastable bar exists. At later times, $m_{max} > m_{(0,0)}$, indicating that the break up has taken place.

We show the profiles of the energy and momentum at a time in which there is rigid rotation in Fig. 5.6. To ease visualization, we only show these at the principal axes, as defined by the inertia tensor (5.5). We compare these to the values of an analytic bar, with $\Omega$ given by the initial data $\Omega = M/J \approx 0.37$ and $m_{max}$ extracted from the numerics. We observe that there is excellent agreement between the configuration and that of an analytic black bar.
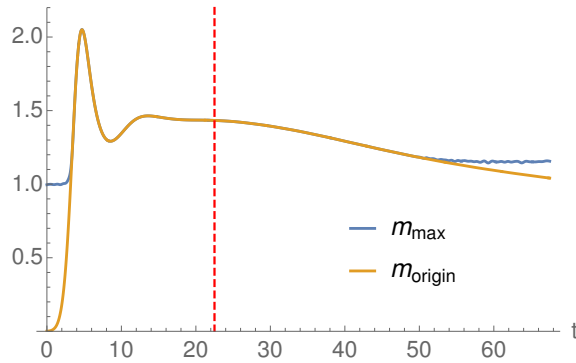
Figure 5.5: Time evolution of the maximum of the energy density $m_{max}$ and its value at the origin $m_{(0,0)}$. After a short period, these two values become equal, signaling rigid rotation. At late times, their values begin to differ, as a consequence of the break up of the bar. We extract the profiles at a time $t \approx 22$, shown in red, and plot them in Fig. 5.6 below.
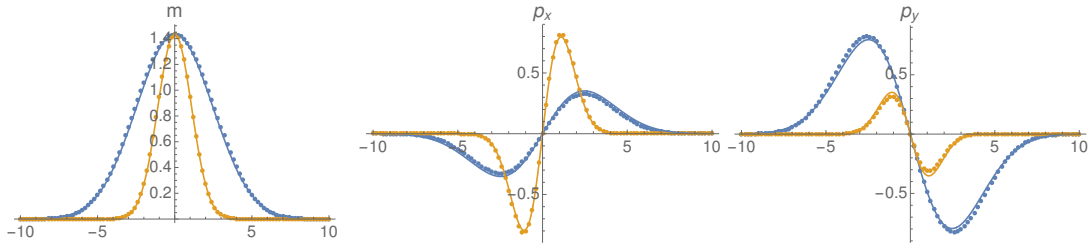


Figure 5.6: Values of the profiles at $t \approx 22$ along the principal axes, in blue and yellow. The data points correspond to the numerical data, while the solid lines show the analityc profiles in (2.66), (2.20). The value of $\Omega$ is obtained from our initial data, while $m_{max}$ is extracted from the numerics.

### 5.2.4  Violation of Cosmic Censorship and subsequent evolution

**Singularity formation**

We now have proven that the collision of two black holes at very large $D$, and with high enough total angular momentum, forms an intermediate, elongated, bar-like horizon that then pinches at its middle. However, as we discussed above, in the effective theory at $D \to \infty$ the pinch never shrinks to zero size, since at any finite distance on the brane there is always a non-zero thickness of the horizon. If $1/D$ corrections to the effective theory were included, their effects would grow large as the pinch becomes thinner, rendering the large-$D$ expansion inappropriate as an approximation to finite values of $D$. In other words, the large-$D$ approach employed here does not by itself allow to reveal the formation of a naked curvature singularity.

Nevertheless, as argued in [12] and further elaborated here, the instability of the intermediate bar state is, at least at its onset, of the same kind as the GL instability of black strings, even quantitatively (see section 5.4.2) . We can then draw upon the numerical simulations at finite $D$ of the non-linear evolution of the GL instability of black strings in [51] (and of related higher-dimensional black holes in [85, 95]), which convincingly show-

sthe formation of a naked singularity at a horizon pinch in a finite time. The only effect that we envisage as possibly preventing a similar evolution of the black bar is a spin-down back to stability through gravitational radiation emission. This will be the subject of detailed study in section 5.6, where we show that this emission is very strongly suppressed for long bars, and also as $D$ grows. Thus, the conclusion seems to us inescapable that at large enough $D$ the merger with an intermediate long bar will end up producing a naked singularity.

The point may be raised that the numerical simulations in [51] were performed in $D = 5$ (and other relatively low $D$ in [85, 95]), while it is known that above a critical dimension $D_* \simeq 13.6$, an unstable black string may evolve into a stable non-uniform black string, instead of proceeding to a singular pinch [49, 11]. This, however, is not relevant to our analysis, since it is a consequence of the confining effect of the compact circle that the black string lives in. In any finite $D$, if the circle is long enough—compared to the thickness of the black string—the non-uniform strings are unstable and the evolution will not stop at them but proceed to pinch off [11]. In the case of a rotating black bar in asymptotically flat space, there is no limit to the distance to which it can spread, and thus there is nothing to stop its unstable evolution towards pinch-off. Furthermore, we expect that the centrifugal repulsion will accelerate the pinching faster than in the case of a black string. Indeed, it may well proceed quickly enough as to prevent the formation of the small 'droplets' that were observed in [51].[7]

So we see no plausible alternative to the conclusion that, at high enough $D$, if the unstable bar forms, a pinch in the horizon will develop where the curvature grows arbitrarily large in a finite time: a violation of CC.

**Proposal for resolution: Neck evaporation**

In our simulations, the 'brane regulator' allows us to follow the evolution of the pinching bar and observe two blobs flying apart. However, as we argued, this regulator cannot be removed in a parametrically controlled manner from the theory. As a consequence, this part of our simulations of the system cannot be regarded as 'proof' of how the process unfolds after the singular pinch-off. When General Relativity breaks down, the further evolution requires new laws of physics, arguably a quantum theory of gravity.[8] Here we want to propose a plausible resolution of the singularity such that the input from quantum gravity is minimal and affects very little the subsequent evolution of the system.

The neck that forms in the horizon has very high curvature, and may be regarded as a small, 'Planck-size black hole', with very high effective temperature. It seems natural to expect that such an object, without any conserved charges that could prevent its decay,

---

[7]A small central droplet at the rotation axis may appear, as we have observed in collisions with high enough velocities.

[8]It may well happen that, if string theory is valid and the string coupling constant is small, General Relativity is replaced by classical string theory that resolves the singularity before reaching the Planck scale. The picture that we propose does not substantially change: the neck would evaporate at the Hagedorn scale instead of the Planck scale.

must indeed quantum-mechanically decay by emitting a few Planck-energy quanta, in a few Planck times. That is, we propose that the neck evaporates in much the same manner as the neck that forms in a fluid-jet evaporates (literally) and breaks the jet into a number of droplets. This break-up is not described by classical hydrodynamics, but rather by molecular dynamics; however, hydrodynamics quickly resumes control of droplet evolution after the brief episode of evaporation. Similarly, classical General Relativity resumes after the horizon breaks up, and controls how the two resulting black holes fly apart.

Note also that, although the evaporation of the neck is reminiscent of the expected endpoint of Hawking evaporation, in the case of a black string the evolution towards the Planck-size object is governed by classical dynamics and therefore is unaffected by the unitarity paradox.

If this picture is correct, then the evolution of the black hole collision and merger will result in a horizon pinch, which then quickly evaporates through quantum-gravity effects (just a little 'pixie dust') and yields two outgoing black holes. The loss of classical predictivity is very small: the horizon bifurcates with a variation of the horizon area (increase or decrease) of only Planckian-size, and the uncertainty in the outgoing scattering angle will be proportional to at most a power of $(M_{\text{Planck}}/M)$, where $M$ is the total mass of the system. Hence, the indeterminacy is a parametrically very small number for any macroscopic initial mass. Predictivity of the entire evolution using General Relativity will be maintained to great accuracy. Except for the details of the break up, the picture we have presented in figure 5.1 will then be essentially correct.

## 5.3 Non-linear evolution of ultraspinning black hole instabilities

Our setup also allows the efficient simulation of the non-linear evolution of instabilities, such as those of ultra-spinning MP black holes [58]. We will not attempt a detailed quantitative study, but rather a preliminary qualitative investigation of which intermediate and end states appear in the evolutions.

The development of the instabilities is quite different depending on whether they are triggered by axisymmetric or non-axisymmetric perturbations. In generic cases, the latter will dominate the evolution of an unstable black hole (see figure 5.7). We find that the unstable black hole sheds off its 'excess' angular momentum (*i.e.,* the spin above the stability limit of MP black holes) by breaking off smaller black holes. In the terminology of [58], this is 'death by fragmentation', since 'death by radiation' is outlawed in $D \to \infty$. We expect (see section 5.6) that at large enough $D$ and large enough spin this violent, CC-violating chastisement of overspeeding black holes also prevails over the milder, CC-preserving radiative correction to stable, lower spin states. As $D$ increases, the value of the spin for which the CC-violating evolution occurs becomes smaller.

As a first case of interest we study non-axisymmetric perturbations of an ultraspinning black hole with $a = 3$ . For each multipole $m_\phi$ we consider the fundamental mode (with
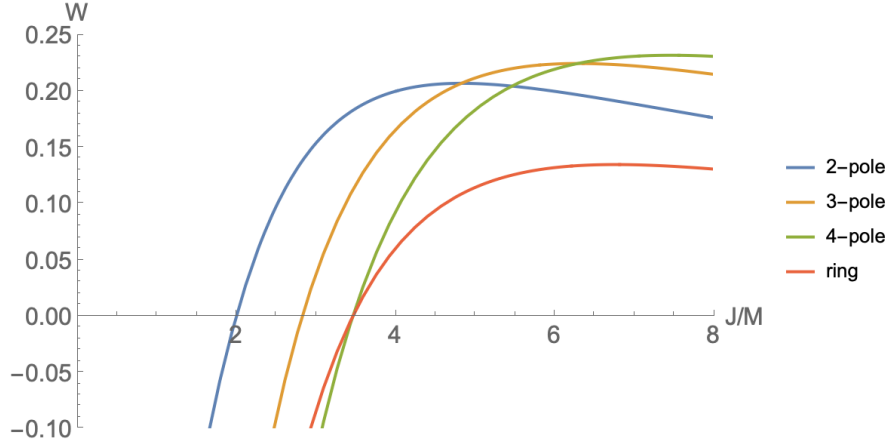
Figure 5.7: Growth rates $W$ of unstable modes of MP black holes at $D \to \infty$, as a function of the spin per unit mass $J/M$ of the black hole (as calculated in [26, 12]). Higher non-axisymmetric modes ('$m_\phi$-poles') become successively dominant as the spin grows, and generically overwhelm the development of axisymmetric 'ring' deformations.

the least nodes in the polar direction $r$, *i.e.*, $m_\phi \neq 0$ and $k = 0$ in [12], which first appear as marginal modes at the values (2.88)). The first one is the dipole $m_\phi = 2$ mode, with similar dynamics as for the collision process, but in this example at a very large spin $J/M = 6$. The dipolar perturbation leads to the formation of an elongated horizon that resembles closely a stationary black bar. It then quickly decays into two smaller black holes after a formation of a dip in its middle.



Figure 5.8: Intermediate states of the evolution of the MP black hole with $a = 3$, after perturbations with $m_\phi = 2, 3, 4, 5$ (from left to right). These are again high-contrast density plots, where this time the minimal value that appears as black was chosen low enough to highlight the full structure, *i.e.*, these plots do not represent well that the relative mass density, which is higher in all places where blobs form.

For perturbations with $m_\phi \geq 3$, a novel set of intermediate states appear, which grow 'arms' as shown in figure 5.8. While growing longer and thinner during evolution, these arms develop a GL-like instability on their own and pinch off, leaving behind a number $m_\phi$ of small black holes that get slung away from the central MP black hole, which now has a spin within the stability bounds.

Figure 5.9 shows snapshots of the evolution in the case of a perturbation with $m_\phi = 4$. These are strikingly similar to the images presented in [87] for the evolution of MP black

holes at spins high enough to excite the unstable quadrupole mode (see their figure 6).



Figure 5.9: Snapshots of time evolution for the MP black hole with $a = 3$, perturbed by the fundamental $m_\phi = 4$ mode

Next we examine the first axisymmetric perturbation (which appears as a marginal mode at $a = \sqrt{3}$ (2.87), *i.e.*, $m_\phi = 0$ and $k = 2$ in [12]) for the same MP black hole with $a = 3$ added with a positive amplitude. Figure 5.10 shows snapshots of the evolution. We find that the instability leads to the formation of a black ring. This was observed in the axisymmetric numerical evolutions in $D = 6$ of [85]. However, the axial symmetry of these rings is expected to break down by non-axisymmetric GL-like instabilities along the ring, and we do see this phenomenon: the black ring decays following a quadrupole perturbation that is triggered by numerical noise. Again, this agrees with the instability of thin black rings observed in [95]. Since our method allows us to evolve past the pinch-off we can observe four spherical black holes flying apart as the end state of the process.



Figure 5.10: Snapshots of time evolution of a ring-like axisymmetric perturbation of the MP black hole with $a = 3$. The eventual breakdown of axial symmetry is triggered by any generic perturbation, such as numerical noise.

Lastly, we consider the possibility of adding the above marginal mode, $m_\phi = 0$ and $k = 2$, again for a MP black hole with $a = 3$, now added with an opposite (negative) amplitude, *i.e.*, a $(-)$-branch evolution. We observe, that instead of forming a dip in the middle of the MP black hole, one or more ringlike objects are emitted that move rapidly outwards and do not break up for the duration of our simulation.

## 5.4 Black bar instabilities

As for MP black holes, we can follow the non-linear evolution of the instabilities of black bars.

Figure 5.11: Snapshots of time evolution of a 'negative' ring-like axisymmetric perturbation of the MP black hole (with rotation parameter $a = 3$). The initial perturbation has amplitude opposite to the one in figure 5.10, *i.e.,* a bulge at the center, instead of a pinch.

## 5.4.1   Spindles and Dumbbells

Fo reflection invariant initial conditions like in the symmetric collisions considered here, the fundamental symmetric mode of black bars is of most relevance to us. It gives rise to two branches of solutions in phase space, depending on the sign of the amplitude with which the perturbation is added. Let us first consider the negative sign, which (by our conventions) leads to a spindle-like deformation. Figure 5.12 shows snapshots of the evolution. These spindles resemble horizon shapes observed in [87] in the numerical evolution of dipolar MP instabilities in $D = 6, 7$. The formation of pointy tips is followed by the development of arms, similar to the ones observed above for MP black holes. The arms subsequently pinch off, sending away two small black holes.



Figure 5.12: Snapshots of time evolution of the fundamental $n_y = 4$ mode added with negative amplitude (i.e., creating a bulge in the middle, instead of a pinch).

Since the qualitative evolution of the fundamental symmetric mode has already been described in earlier sections, here we will only estimate instability rates for this mode and the total duration of break-up.

## 5.4.2   Black bar decay rates

We expect the unstable modes of the black bars to behave as

$$\delta \Phi_A = e^{Wt} \delta \hat{\Phi}_A(r, \phi - \Omega t) \,, \tag{5.7}$$

where $\Phi_A = m, p_r, p_\phi$, and $W$ is the purely real instability rate. It is possible to estimate $W$ close to the onset of the zero modes that appear when $\Omega = \Omega_{n_y}$, (2.143), by comparing to the analytic solution for the GL growth rate for a black string of length $L$ and radius $r_0 = 1$ at large $D$ [56],

$$W_s = \frac{2\pi}{L} \left( 1 - \frac{2\pi}{L} \right) . \tag{5.8}$$

Close to the marginal mode at $L_0 = 2\pi$, this behaves as

$$W_s \approx \frac{L}{2\pi} - 1 . \tag{5.9}$$

Since the length of a black bar is inversely proportional to its angular velocity, (2.72), we relate the relative deviation from the zero modes of the black bar and the string as

$$\frac{L}{L_0} \approx \frac{\Omega_{n_y}}{\Omega} . \tag{5.10}$$

This leads to the estimate

$$W \approx \frac{\Omega_{n_y}}{\Omega} - 1 = \frac{1}{\Omega} \frac{\sqrt{n_y - 1}}{n_y} - 1 = \frac{J}{M} \frac{\sqrt{n_y - 1}}{n_y} - 1 . \tag{5.11}$$

This estimate turns out to be in remarkable agreement with the growth rate of the fundamental symmetric mode $n_y = 4$, as measured from numerical solutions. We extract it from the quantity

$$\Delta_0 \equiv |m_{\text{origin}}(t) - m_{\text{origin}}(t = 0)| \tag{5.12}$$

*i.e.,* the deviation of the central mass density from its initial value. In figure 5.13, $\Delta_0$ is plotted as a function of time for several values of $J/M$.
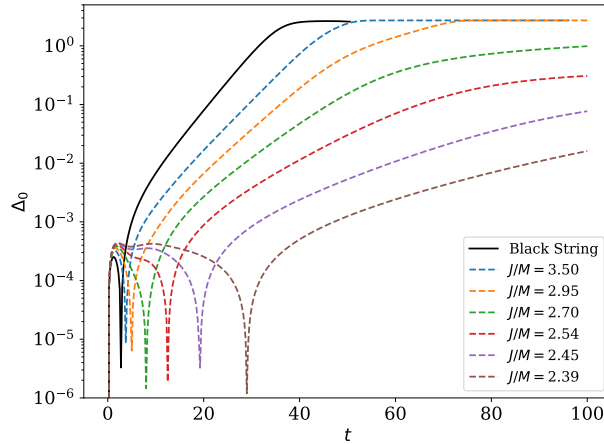


Figure 5.13: Deformation of the black bars at their center, as a function of time, for several values of $J/M$. Perturbations of all unstable bars $(J/M > 4/\sqrt{3})$ present a phase of exponential growth given by the linear growth rate $W$ of the dominant mode. The zero mode with $n_y = 4$ is recovered as the growth rate vanishes at the threshold of the instability, $W(J/M = 4/\sqrt{3}) = 0$. Also, for very long bars, $W(J/M \to \infty) \to 1/4$, recovering the dominant growth rate of a black string.

By numerically evaluating the growth rate of the $\Delta_0(t)$ curves in their phase of exponential growth (in our case, when $\Delta_0 \approx 10^{-2}$), we can obtain an estimate for the instability rate $W$ of the fundamental mode. This is depicted in figure 5.14, where it is manifest that the black-string-like relation (5.11) is satisfied with remarkable accuracy for values of $J/M$ close to the threshold value for the $n_y = 4$ mode. At large values of $J/M$, $W$ asymptotes to the infinite black string value of $1/4$ as expected.
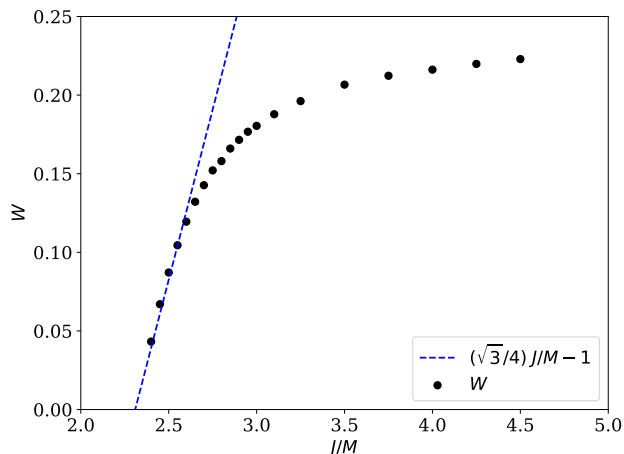


Figure 5.14: Growth rate $W$ of the dominant unstable mode of the black bars as a function of $J/M$. The rates are computed by linear regression of the curves in Figure 5.13 at a value of the deformation of $10^{-2}$. The blue dashed line is the black string approximation to a black bar.

We conclude that, at least at its onset, the instability of black bars is of the same qualitative and quantitative nature as the GL instability of black strings. This lends further support to the overall picture we presented here.

## 5.5   Gravitational radiation in $D$ dimensions

We intend to estimate the energy and angular momentum radiated into gravitational waves by a rotating black bar using the quadrupole formula in $D$ dimensions. For this purpose, we begin in sec. 5.5.1 by modelling a black bar as a rigidly rotating ellipsoid. In sec. 5.5.2 we apply to this model the result of [100] for the energy radiation rate. The general formula for angular momentum radiation was not derived in that reference, so we obtain it anew in sec. 5.5.3. Then, in sec. 5.5.4 we use it to prove that the radiation rates of energy and angular momentum for uniform, rigidly rotating objects (such as the rotating ellipsoidal bar) are related in a simple manner, eq. (5.77).

### 5.5.1   Black bar as a rotating ellipsoid in $D$ dimensions

We model the black bar by a $D-1$-dimensional spheroid with long axis $\ell_\parallel$, short axis $\ell_\perp$, and radius $r_+$ for the remaining round sphere factor $S^{D-3}$. This is a rigid body described

in co-rotating coordinates $y_1(t)$, $y_2(t)$, as

$$\mathfrak{B} = \left\{ y^i \in \mathbb{R}^{D-1} \ \middle| \ \frac{y_1^2}{\ell_{||}^2} + \frac{y_2^2}{\ell_\perp^2} + \frac{1}{r_+^2} \sum_{i=3}^{D-1} y_i^2 \leq 1 \right\} , \tag{5.13}$$

where $y_1(t)$, $y_2(t)$ are related to the inertial coordinates as in (3.15).

Given a mass distribution $T^{00}(t,x)$, we introduce the tensor

$$M^{ij} = \int_{\mathfrak{B}} d^{D-1}x \, T^{00}(t,x) x^i x^j , \tag{5.14}$$

from which we subtract the trace to obtain the quadrupole moment tensor

$$Q^{ij} = M^{ij} - \frac{1}{D-1} \delta^{ij} M_{kk} . \tag{5.15}$$

In order to compute (5.14) we shall use the integrals,

$$\int d\Omega_{D-2} \, n_i n_j = \frac{\Omega_{D-2}}{D-1} \delta_{ij} , \tag{5.16}$$

$$\int d\Omega_{D-2} \, n_i n_j n_l n_m = \frac{\Omega_{D-2}}{D^2-1} \left( \delta_{ij}\delta_{lm} + \delta_{il}\delta_{jm} + \delta_{im}\delta_{jl} \right) , \tag{5.17}$$

where $n^i = x^i/|\mathbf{x}|$ is the unit vector, and $\Omega_{D-2}$ is the volume of $S^{D-2}$,

$$\Omega_{D-2} = \frac{2\pi^{(D-1)/2}}{\Gamma[(D-1)/2]} . \tag{5.18}$$

Then, assuming a constant mass density $\rho$ for the black bar,

$$M^{11} = \int_{\mathfrak{B}} d^{D-1}y \, T^{00}(0,y) \left( y^1 \cos(\Omega t) - y^2 \sin(\Omega t) \right)^2$$
$$= \ell_{||} \ell_\perp^3 \rho \frac{r_+^{D-3}}{D+1} \frac{\Omega_{D-2}}{D-1} \left( \left(\frac{\ell_{||}}{\ell_\perp}\right)^2 \cos^2(\Omega t) + \sin^2(\Omega t) \right) ,$$

$$M^{22} = \int_{\mathfrak{B}} d^{D-1}y \, T^{00}(0,y) \left( y^1 \sin(\Omega t) + y^2 \cos(\Omega t) \right)^2$$
$$= \ell_{||} \ell_\perp^3 \rho \frac{r_+^{D-3}}{D+1} \frac{\Omega_{D-2}}{D-1} \left( \left(\frac{\ell_{||}}{\ell_\perp}\right)^2 \sin^2(\Omega t) + \cos^2(\Omega t) \right) , \tag{5.19}$$

$$M^{12} = \int_{\mathfrak{B}} d^{D-1}y \, T^{00}(0,y) \left( y^1 \cos(\Omega t) - y^2 \sin(\Omega t) \right) \left( y^1 \sin(\Omega t) + y^2 \cos(\Omega t) \right)$$
$$= \ell_{||} \ell_\perp^3 \rho \frac{r_+^{D-3}}{D+1} \frac{\Omega_{D-2}}{D-1} \left( \left( \left(\frac{\ell_{||}}{\ell_\perp}\right)^2 - 1 \right) \sin(\Omega t) \cos(\Omega t) \right) . \tag{5.20}$$

Note that these are the only components that can be time-dependent for our setup.

The mass of the bar is[9]

$$M = \int d^{D-1}x T^{00}(t,x) = \int_{\mathfrak{B}} dy^{D-1} \rho = \ell_{||} \ell_\perp \rho \frac{r_+^{D-3}}{D-1} \Omega_{D-2} . \tag{5.21}$$

---

[9]In order to unclutter the notation, in this section we denote the physical mass and angular velocity by $M$ and $\Omega$, instead of $\mathbf{M}$ and $\mathbf{\Omega}$ as in the main text.

So we have

$$M^{11} = \frac{M\ell_\perp^2}{D+1}\left(\left(\frac{\ell_{||}}{\ell_\perp}\right)^2\cos^2(\Omega t) + \sin^2(\Omega t)\right),\tag{5.22}$$

$$M^{22} = \frac{M\ell_\perp^2}{D+1}\left(\left(\frac{\ell_{||}}{\ell_\perp}\right)^2\sin^2(\Omega t) + \cos^2(\Omega t)\right),\tag{5.23}$$

$$M^{12} = \frac{M\ell_\perp^2}{D+1},\left(\left(\left(\frac{\ell_{||}}{\ell_\perp}\right)^2 - 1\right)\sin(\Omega t)\cos(\Omega t)\right).\tag{5.24}$$

Noting that the trace $M^{ii}$ is time-independent, we can obtain

$$(\partial_t)^p Q^{ij} = (\partial_t)^p M^{ij}.\tag{5.25}$$

### 5.5.2   Radiative power of a black bar

Ref. [100] obtained the radiative power of a slowly moving distribution of matter in $D$ dimensions, characterized by the tensor $M_{ij}$ (5.14), as

$$\frac{dE}{dt} = \frac{2^{2-D}G(D-3)D}{\pi^{\frac{D-5}{2}}\Gamma\left[\frac{D-1}{2}\right](D^2-1)(D-2)}\left[(D-1)\partial_t^{\frac{D+2}{2}}M_{ij}(t)\partial_t^{\frac{D+2}{2}}M_{ij}(t) - \left|\partial_t^{\frac{D+2}{2}}M_{ii}(t)\right|^2\right].\tag{5.26}$$

The last term does not contribute for a rotating ellipsoidal bar since we have shown in appendix 5.5.1 that in this case the trace $M_{ii}$ is time-independent. Inserting the results for the tensor components we obtain (5.67).

### 5.5.3   Angular momentum radiated by slowly moving objects in $D$ dimensions

Ref. [100] did not compute the quadrupolar radiation rate of angular momentum in $D$ dimensions, so we derive it here from the start.

The angular momentum is given by

$$\mathcal{J}^{ij} = \frac{1}{16\pi G}\int d^{D-1}x\left[-\delta^{[i}{}_k\delta^{j]}{}_l\dot{h}_{ab}^{\text{TT}}x^k\partial^l h_{ab}^{\text{TT}} + 2\delta^{[i}{}_k\delta^{j]}{}_l h_{ak}^{\text{TT}}\dot{h}_{al}^{\text{TT}}\right],\tag{5.27}$$

with $h_{ab}^{\text{TT}}$ the gravitational perturbation in transverse traceless gauge. The first summand corresponds to an angular part and the second to the spin part of the spin 2 perturbation. Since we can interpret the integrand of equation (5.27) as the averaged angular momentum density $\langle j^{ij}\rangle$, this implies that the rate of radiated momentum is

$$\frac{d\mathcal{J}^{ij}}{dt} = \frac{1}{16\pi G}\int d^{D-2}\Omega\, r^{D-2}\left[-\delta^{[i}{}_k\delta^{j]}{}_l h_{ab}^{\text{TT}}x^k\partial^l h_{ab}^{\text{TT}} + 2\delta^{[i}{}_k\delta^{j]}{}_l h_{ak}^{\text{TT}}\dot{h}_{al}^{\text{TT}}\right].\tag{5.28}$$

Define $\bar{h}_{\mu\nu}$ via $\bar{h}_{\mu\nu} = h_{\mu\nu} - \frac{1}{2}h\eta_{\mu\nu}$. In Lorenz gauge $\partial^\mu\bar{h}_{\mu\nu} = 0$ it satisfies

$$\Box\bar{h}_{\mu\nu} = -16\pi G T_{\mu\nu}.\tag{5.29}$$

Then we have the solution [100]

$$\bar{h}_{\mu\nu}(t, \mathbf{x}) = -16\pi G \int dt' \int d^{D-1}\mathbf{x}' T_{\mu\nu}\left(t', \mathbf{x}'\right) \mathcal{G}\left(t - t', \mathbf{x} - \mathbf{x}'\right) + \text{ homogeneous solutions }, \tag{5.30}$$

where we are interested in the retarded Green's function

$$\mathcal{G}^{\text{ret}}(t, \mathbf{x}) = \frac{1}{4\pi}\left[-\frac{\partial}{2\pi r \partial r}\right]^{(D-4)/2}\left[\frac{\delta(t-r)}{r}\right], \tag{5.31}$$

as long as $D$ is even. It is convenient to introduce the transverse traceless projector constructed via $P_{ij}(\hat{\mathbf{k}}) = \delta_{ij} - k_i k_j$,

$$\Lambda_{ij,kl}(\hat{\mathbf{k}}) = P_{ik}P_{jl} - \frac{1}{D-2}P_{ij}P_{kl}. \tag{5.32}$$

Explicitly,

$$\Lambda_{ij,lm}(\hat{k}) = \delta_{il}\delta_{jm} - \hat{k}_j\hat{k}_m\delta_{il} - \hat{k}_i\hat{k}_l\delta_{jm} + \frac{1}{D-2}\left(-\delta_{ij}\delta_{lm} + \hat{k}_l\hat{k}_m\delta_{ij} + \hat{k}_i\hat{k}_j\delta_{lm}\right)$$
$$+ \frac{D-3}{D-2}\hat{k}_i\hat{k}_j\hat{k}_l\hat{k}_m. \tag{5.33}$$

With this, we can extract the transverse traceless (TT) part of $h_{kl}$ in harmonic gauge

$$h_{ij}^{\text{TT}} = \Lambda_{ij,kl}h_{kl} = \Lambda_{ij,kl}\bar{h}_{kl}, \tag{5.34}$$

so outside the source we can put the field in TT-gauge

$$h_{ij}^{\text{TT}}(t, \mathbf{x}) = 4G\Lambda_{ij,kl}(\hat{\mathbf{n}}) \iint dt' d^{D-1}x'\left[-\frac{\partial}{2\pi r \partial r}\right]^{(D-4)/2}\left[\frac{\delta(t-t'-|\mathbf{x}-\mathbf{x}'|)}{|\mathbf{x}-\mathbf{x}'|}\right] T_{kl}\left(t', \mathbf{x}'\right). \tag{5.35}$$

We consider only the part of Green's function with the weakest fall-off since we are interested in an expansion in the wave-zone, which gives

$$h_{ij}^{\text{TT}}(t, \mathbf{x}) = -8\pi G\Lambda_{ij,kl}(\hat{\mathbf{n}})\frac{1}{(2\pi r)^{(D-2)/2}}\partial_t^{\frac{D-4}{2}}\left[\int d^{D-1}\mathbf{x}' T_{kl}\left(t - |\mathbf{x}-\mathbf{x}'|, \mathbf{x}'\right)\right]. \tag{5.36}$$

Now we expand using the small extent $d$ of the source, defining $r = |\mathbf{x}|, \hat{\mathbf{n}} = \frac{\mathbf{x}}{r}$

$$|\mathbf{x} - \mathbf{x}'| = r - \mathbf{x}' \cdot \hat{\mathbf{n}} + O\left(\frac{d^2}{r}\right), \tag{5.37}$$

which gives

$$h_{ij}^{\text{TT}}(t, \mathbf{x}) = -8\pi G\Lambda_{ij,kl}(\hat{\mathbf{n}})\frac{1}{(2\pi r)^{(D-2)/2}}\partial_t^{\frac{D-4}{2}}\left[\int d^{D-1}\mathbf{x}' T_{kl}\left(t - r - \mathbf{x}' \cdot \hat{\mathbf{n}}, \mathbf{x}'\right)\right]. \tag{5.38}$$

The next approximation is the Newtonian approximation for slow internal velocities of the source: For this consider the Fourier transform of the stress-energy tensor

$$T_{kl}\left(t - \frac{r}{c} + \frac{\mathbf{x}' \cdot \hat{\mathbf{n}}}{c}, \mathbf{x}'\right) = \int \frac{d^D k}{(2\pi)^D}\tilde{T}_{kl}(\omega, \mathbf{k})e^{-i\omega(t-r/c+\mathbf{x}'\cdot\hat{\mathbf{n}}/c)+i\mathbf{k}\cdot\mathbf{x}'}, \tag{5.39}$$

which we can expand in $\omega d$

$$e^{-i\omega(t-r+\mathbf{x}'\cdot\hat{\mathbf{n}})} = e^{-i\omega(t-r)}\left[1 - i\omega x'n^i + \frac{1}{2}(-i\omega)^2 x'^i x'^j n^i n^j + \dots\right], \tag{5.40}$$

which corresponds to the expansion in $\mathbf{x}' \cdot \hat{\mathbf{n}}$ ,

$$T_{kl}\left(t - r + \mathbf{x}' \cdot \hat{\mathbf{n}}, \mathbf{x}'\right) \simeq T_{kl}\left(t - r, \mathbf{x}'\right) + x'^i n^i \partial_0 T_{kl} + \frac{1}{2}x'^i x'^j n^i n^j \partial_0^2 T_{kl} + \dots. \tag{5.41}$$

Define the momenta of the stress-energy tensor

$$S^{ij}(t) = \int d^{D-1}x T^{ij}(t, \mathbf{x}), \tag{5.42}$$

$$S^{ij,k}(t) = \int d^{D-1}x T^{ij}(t, \mathbf{x})x^k, \tag{5.43}$$

$$S^{ij,kl}(t) = \int d^{D-1}x T^{ij}(t, \mathbf{x})x^k x^l. \tag{5.44}$$

With this, eq. (5.38) becomes

$$h_{ij}^{\mathrm{TT}}(t, \mathbf{x}) = 8\pi G\Lambda_{ij,kl}(\hat{\mathbf{n}})\frac{1}{(2\pi r)^{(D-2)/2}}\partial_t^{\frac{D-4}{2}}\int d^{D-1}\mathbf{x}'\int\frac{d^D k}{(2\pi)^D}\tilde{T}_{kl}(\omega, \mathbf{k})e^{-i\omega(t-r/c+\mathbf{x}'\cdot\hat{\mathbf{n}}/c)+i\mathbf{k}\cdot\mathbf{x}'}$$

$$= 8\pi G\Lambda_{ij,kl}(\hat{\mathbf{n}})\frac{(-i\omega)^{\frac{D-4}{2}}}{(2\pi r)^{(D-2)/2}}\int d^{D-1}\mathbf{x}'\int\frac{d^D k}{(2\pi)^D}\tilde{T}_{kl}(\omega, \mathbf{k})e^{-i\omega(t-r/c+\mathbf{x}'\cdot\hat{\mathbf{n}}/c)+i\mathbf{k}\cdot\mathbf{x}'}, \tag{5.45}$$

which we can approximate as

$$h_{ij}^{\mathrm{TT}}(\omega, \mathbf{x}) \simeq 8\pi G\Lambda_{ij,kl}(\hat{\mathbf{n}})\frac{(-i\omega)^{\frac{D-4}{2}}}{(2\pi r)^{(D-2)/2}}\tilde{S}_{kl}(\omega). \tag{5.46}$$

Now using conservation of the stress-energy tensor and using (5.14) we can show that

$$S^{ij} = \frac{1}{2}\ddot{M}^{ij}. \tag{5.47}$$

We can write equation (5.46), using (5.47), (5.15), and the properties of the $\Lambda$-tensor

$$h_{ij}^{\mathrm{TT}}(\omega, \mathbf{x}) \simeq 4\pi G\Lambda_{ij,kl}(\hat{\mathbf{n}})\frac{(-i\omega)^{\frac{D-4}{2}}}{(2\pi r)^{(D-2)/2}}(-i\omega)^2\tilde{M}_{kl}(\omega)$$

$$= 4\pi G\Lambda_{ij,kl}(\hat{\mathbf{n}})\frac{(-i\omega)^{\frac{D}{2}}}{(2\pi r)^{(D-2)/2}}\tilde{Q}^{kl}(\omega)$$

$$= 4\pi G\frac{(-i\omega)^{\frac{D}{2}}}{(2\pi r)^{(D-2)/2}}\tilde{Q}_{kl}^{\mathrm{TT}}(\omega), \tag{5.48}$$

or equivalently, in position space,

$$h_{ij}^{\mathrm{TT}}(t, \mathbf{x}) = 4\pi G\frac{1}{(2\pi r)^{(D-2)/2}}\partial_t^{\frac{D}{2}}Q_{kl}^{\mathrm{TT}}(t - r). \tag{5.49}$$

Now consider the orbital part of equation (5.28) and use (5.49)

$$\frac{d\mathcal{J}^{ij}}{dt} = \frac{1}{16\pi G}\int d^{D-2}\Omega\, r^{D-2}\left[-\delta^{[i}_{\ k}\delta^{j]}_{\ l}\dot{h}_{ab}^{\mathrm{TT}}x^k\partial^l h_{ab}^{\mathrm{TT}}\right]$$

$$= \frac{\pi G}{(2\pi)^{D-2}}\int d^{D-2}\Omega\left[-\delta^{[i}_{\ k}\delta^{j]}_{\ l}\partial_t^{\frac{D+2}{2}}Q_{ab}^{\mathrm{TT}}x^k\partial^l\partial_t^{\frac{D}{2}}Q_{ab}^{\mathrm{TT}}\right]. \tag{5.50}$$

When calculating $\partial_l Q_{ab}^{\mathrm{TT}}(t-r) = \partial_l \left( \Lambda_{ab,cd} \left( \frac{\mathbf{x}}{r} \right) Q_{cd}(t-r) \right)$ all contributions from derivatives acting on $Q_{cd}$ vanish since $\partial_l Q_{cd}(t-r) = -\frac{x_l}{r} Q_{cd}(t-r)$ which after antisymmetrization does not give any contributions to (5.50). Thus

$$\frac{d\mathcal{J}_{\mathrm{orbit}}^{ij}}{dt} = \frac{\pi G}{(2\pi)^{D-2}} \left\langle \partial_t^{\frac{D+2}{2}} Q_{cd} \, \partial_t^{\frac{D}{2}} Q_{fg} \right\rangle \int d^{D-2}\Omega \, \Lambda_{ab,cd} x^{[i} \partial^{j]} \Lambda_{ab,fg} \,. \tag{5.51}$$

After some algebra we obtain

$$\frac{d\mathcal{J}_{\mathrm{orbit}}^{ij}}{dt} = \frac{\pi G}{(2\pi)^{D-2}} \left\langle \partial_t^{\frac{D+2}{2}} Q_{cd} \, \partial_t^{\frac{D}{2}} Q_{fg} \right\rangle \int d^{D-2}\Omega \, \delta^{[i}{}_k \delta^{j]}{}_l n_k \left( n_f \Lambda_{cd,lg} + n_g \Lambda_{cd,lf} \right) \,, \tag{5.52}$$

which can be calculated using (5.33) and (5.16). These integrals are everything we need since the term containing a product of 4 $n_i$ vanishes due to antisymmetrization. With this we obtain

$$\begin{aligned}
\frac{d\mathcal{J}_{\mathrm{orbit}}^{ij}}{dt} &= \frac{\pi G}{(2\pi)^{D-2}} \left\langle \partial_t^{\frac{D+2}{2}} Q^{[i}{}_d \, \partial_t^{\frac{D}{2}} Q^{j]}{}_d \right\rangle \frac{2(D-3)D}{(D-2)(D-1)(D+1)} \frac{2\pi^{(D-1)/2}}{\Gamma[(D-1)/2]} \\
&= \frac{G(D-3)D}{2^{D-4}\pi^{\frac{D-5}{2}}(D-2)(D-1)(D+1)\Gamma[(D-1)/2]} \left\langle \partial_t^{\frac{D+2}{2}} Q^{[i}{}_d \, \partial_t^{\frac{D}{2}} Q^{j]}{}_d \right\rangle \,. \tag{5.53}
\end{aligned}$$

The calculation of the spin part gives

$$\begin{aligned}
\frac{d\mathcal{J}_{\mathrm{spin}}^{ij}}{dt} &= \frac{1}{16\pi G} \int d^{D-2}\Omega \, r^{D-2} \left[ 2\delta^{[i}{}_k \delta^{j]}{}_l h_{ak}^{\mathrm{TT}} \dot{h}_{al}^{\mathrm{TT}} \right] \\
&= \frac{\pi G}{(2\pi)^{D-2}} \left\langle \partial_t^{\frac{D+2}{2}} Q_{mn} \, \partial_t^{\frac{D}{2}} Q_{cd} \right\rangle \int d^{D-2}\Omega \, 2\delta^{[i}{}_k \delta^{j]}{}_l \Lambda_{al,mn} \Lambda_{ak,cd} \,. \tag{5.54}
\end{aligned}$$

Using the identity

$$\Lambda_{al,mn} \Lambda_{ak,cd} = P_{ln} \Lambda_{mk,cd} - \frac{1}{D-2} P_{mn} \Lambda_{kl,cd} \,, \tag{5.55}$$

and antisymmetry we find

$$\begin{aligned}
\frac{d\mathcal{J}_{\mathrm{spin}}^{ij}}{dt} &= \frac{2\pi G}{(2\pi)^{D-2}} \left\langle \partial_t^{\frac{D+2}{2}} Q_{mn} \, \partial_t^{\frac{D}{2}} Q_{cd} \right\rangle \int d^{D-2}\Omega \, \delta^{[i}{}_k \delta^{j]}{}_l P_{ln} \Lambda_{mk,cd} \\
&= \frac{2\pi G}{(2\pi)^{D-2}} \left\langle \partial_t^{\frac{D+2}{2}} Q^{[i}{}_d \, \partial_t^{\frac{D}{2}} Q^{j]}{}_d \right\rangle \frac{(D-3)D}{D^2-1} \frac{2\pi^{(D-1)/2}}{\Gamma[(D-1)/2]} \\
&= \frac{G(D-3)D}{2^{D-4}\pi^{\frac{D-5}{2}}(D^2-1)\Gamma[(D-1)/2]} \left\langle \partial_t^{\frac{D+2}{2}} Q^{[i}{}_d \, \partial_t^{\frac{D}{2}} Q^{j]}{}_d \right\rangle \,. \tag{5.56}
\end{aligned}$$

Adding both contributions we obtain the final result

$$\frac{d\mathcal{J}^{ij}}{dt} = G \frac{(D-3)D}{2^{D-4}\pi^{\frac{D-5}{2}}(D-2)(D+1)\Gamma[(D-1)/2]} \left\langle \partial_t^{\frac{D+2}{2}} Q^{[i}{}_d \, \partial_t^{\frac{D}{2}} Q^{j]}{}_d \right\rangle \,. \tag{5.57}$$

### 5.5.4  Radiation rates of energy and angular momentum for rigidly rotating objects

A body rotating rigidly in the $(1,2)$-plane with an angular velocity $\Omega$, such as the rotating ellipsoidal bar of section 5.5.1, is described by a mass distribution that will appear static

in its inertial frame defined by (3.15). To simplify calculations it will be convenient to introduce polar coordinates $(\tilde{r}, \tilde{\phi})$ for the rotation plane of the inertial frame. These are related to the static coordinates $x^i$ according to

$$
\begin{aligned}
x^1 &= y^1 \cos(\Omega t) - y^2 \sin(\Omega t) = \tilde{r} \cos(\tilde{\phi} + \Omega t)\,, \\
x^2 &= y^1 \sin(\Omega t) + y^2 \cos(\Omega t) = \tilde{r} \sin(\tilde{\phi} + \Omega t)\,.
\end{aligned}
\tag{5.58}
$$

In these coordinates we calculate the momenta of its mass distribution

$$
\begin{aligned}
M^{11} &= \int d^{D-1}y\, T^{00}(0,y) \left( \tilde{r} \cos(\tilde{\phi} + \Omega t) \right)^2 \\
&= \int d^{D-1}y\, T^{00}(0,y) \frac{\tilde{r}^2}{2} \left( 1 + \cos(2\tilde{\phi}) \cos(2\Omega t) - \sin(2\tilde{\phi}) \sin(2\Omega t) \right) \\
&= \widetilde{M}^{11} \cos(2\Omega t) - \widetilde{M}^{22} \sin(2\Omega t) + \text{const.}\,,
\end{aligned}
\tag{5.59}
$$

$$
\begin{aligned}
M^{22} &= \int d^{D-1}y\, T^{00}(0,y) \left( \tilde{r} \sin(\tilde{\phi} + \Omega t) \right)^2 \\
&= -\widetilde{M}^{11} \cos(2\Omega t) + \widetilde{M}^{22} \sin(2\Omega t) + \text{const.}\,,
\end{aligned}
\tag{5.60}
$$

$$
\begin{aligned}
M^{12} &= \int d^{D-1}y\, T^{00}(0,y) \left( \tilde{r}^2 \cos(\tilde{\phi} + \Omega t) \sin(\tilde{\phi} + \Omega t) \right) \\
&= \widetilde{M}^{11} \sin(2\Omega t) + \widetilde{M}^{22} \cos(2\Omega t) + \text{const.}\,,
\end{aligned}
\tag{5.61}
$$

where we defined

$$
\begin{aligned}
\widetilde{M}^{11} &= \frac{1}{2} \int d^{D-1}y\, T^{00}(0,y) y^1 y^1\,, \\
\widetilde{M}^{22} &= \frac{1}{2} \int d^{D-1}y\, T^{00}(0,y) y^2 y^2\,,
\end{aligned}
\tag{5.62}
$$

as the momenta of the mass distribution in the co-rotating frame.

   With this we can evaluate the tensor structures appearing in eq. (5.26), (5.57). Noting again that the trace does not show time dependence we calculate

$$
\partial_t^{\frac{D+2}{2}} M_{ij}(t) \partial_t^{\frac{D+2}{2}} M_{ij}(t) = 2(2\Omega)^D \left( (\widetilde{M}^{11})^2 + (\widetilde{M}^{22})^2 \right)\,,
\tag{5.63}
$$

and

$$
\partial_t^{\frac{D+2}{2}} M^{[1}{}_d \partial_t^{\frac{D}{2}} M^{2]}{}_d = \frac{1}{2\Omega} (2\Omega)^D \left( (\widetilde{M}^{11})^2 + (\widetilde{M}^{22})^2 \right)\,.
\tag{5.64}
$$

Inserting these into eq. (5.26) and (5.57), and comparing the results, we obtain (5.77).

## 5.6   Spin-down from gravitational radiation

A rotating black bar has a varying quadrupole mass moment and will necessarily emit gravitational radiation in any finite $D$. This radiation will carry away both energy and angular momentum, so the ratio $J/M$ will change over time, possibly decreasing quickly enough that the bar enters a regime of lower $J/M$ where it is stable. If this were the case, instead of proceeding to pinch-off, the bar would spin itself down through gravitational

radiation to a stable MP black hole, thus thwarting the evolution towards CC-violation. Already in [56] generic arguments were given that at very large $D$ the emission of radiation is very strongly suppressed; here we attempt to be much more precise about the effect.

Ref. [54], and more recently [87], have followed numerically the evolution of the transient black bars that form from the ultraspinning instability of MP black holes in $D = 6, 7, 8$. Both references find that the black bars return back to MP black holes after radiating their excess spin. Indeed, ref. [87] reports huge emissions of the initial mass (31%) and angular momentum (50%) into gravitational waves in $D = 6$.

These results may seem to go against—or at least not provide support for—our claim that black bars become GL-unstable. The simplest interpretation is that in the relatively low dimensions considered in [54, 87] the emission is not suppressed enough to let the GL instability grow, but in higher dimensions the latter should dominate. While our arguments make this almost certainly true, we also believe that a stronger case can be made, since we can argue that down to $D = 6$, long black bars with large enough spin, if they form, radiate too slowly to prevent the development of the GL instability towards a naked singularity.

At first this sounds bizarre: shouldn't a long bar with large angular momentum radiate more copiously than one that is shorter and has smaller spin? This reasoning misses the property, seen in (2.71) and (2.72), that black bars with large $J/M$, although very long, rotate very slowly, and this is enough to suppress their wave emission. As we shall show below, the characteristic time for radiative spin-down of a bar of length $\ell_\parallel$ and angular velocity $\Omega$ is (in units of mass)

$$\tau_{\rm rad} \sim \frac{1}{\ell_\parallel^4 \Omega^{D+2}} . \tag{5.65}$$

So, although lengthening the bar accelerates the radiative spin-down, reducing the angular velocity suppresses it—and with a stronger power. For a black bar it is the latter effect that dominates, since $\ell_\parallel \simeq 1/\Omega$, so

$$\tau_{\rm rad} \sim \frac{1}{\Omega^{D-2}} . \tag{5.66}$$

Hence we expect that slowly rotating, long black bars in any $D \geq 6$ are almost stable to gravitational wave emission. Since they are also GL-unstable, and (as we show below) the growth rate of this instability depends weakly on $D$, we conclude that long black bars die by fragmentation and not by radiation.[10] However, since shorter bars have been observed to die by radiation in $D = 6, 7, 8$, there must be a critical value of the spin per unit mass which separates the two behaviors. This critical value (which currently we cannot compute) will decrease as $D$ grows.

Then, the question of whether cosmic censorship is violated in a black hole collision in a given dimension $D$ hinges on whether high-spin, supercritical long black bars can

---

[10]Ref. [87] observes lower wave emission at higher spins in four-armed configurations (figure 5.9), but attributes the effect to the smaller mass in the arms, rather than to slower angular velocity. In view of our arguments, the radiative spin down of the black bars observed in [54, 87] is the consequence of having too low an initial spin.

form in the merger. To this end, the total spin that can be achieved in the collision is enhanced by having intrinsic spin in the initial MP black holes. This helps, but is limited if we require that these black holes are stable. On the other hand, the initial orbital angular momentum can be increased by enlarging the impact parameter and by increasing the collision velocity. The former is limited by the maximum value for capture. The latter is only limited by the speed of light, but the initial state radiation can grow large as ultrarrelativistic speeds are approached and may lead to considerable loss of angular momentum. Recall that at large $D$ this radiation is emitted very quickly, in a short burst of duration $\sim 1/D$, and high frequency $\omega \sim D/r_+$.

While we have tried to estimate these effects with all the presently available evidence (including [104, 105, 106, 107, 108, 109]), we have not been able to reach a definite conclusion for how high a spin can the intermediate state reach in a collision in $D = 6, 7$. It seems plausible, though, that in all dimensions $D \gtrsim 8$ collisions can be achieved with high enough total angular momentum such that the intermediate deformed horizon triggers a GL-instability more quickly than radiation spins it down, in accord with the picture that the large-$D$ effective theory has given us.[11] The determination of the actual lower value of $D$ where this is possible will have to await for dedicated numerical simulations in full General Relativity.

### 5.6.1   Radiative spin-down

Let us now present our estimates of gravitational wave emission from black bars at finite $D$.

We shall model the gravitational wave emission and spin-down of a black bar by assimilating it to a rotating ellipsoid (see section 5.5) which radiates according to the $D$-dimensional quadrupole formula. The quadrupolar energy radiation rate in arbitrary (even) $D$ was obtained in [100]. The emission of energy $E$ reduces the mass of the radiating system $\mathbf{M}$ according to $dE = -d\mathbf{M}$. Then (see section 5.5), for the ellipsoidal bar the relative mass loss rate is

$$\frac{\dot{\mathbf{M}}}{\mathbf{M}} = -\frac{8(D-3)D}{\pi^{\frac{D-5}{2}}(D-2)(D+1)^3\Gamma\left[\frac{D-1}{2}\right]}G\mathbf{M}\mathbf{\Omega}^{D+2}\left(\ell_\parallel^2 - \ell_\perp^2\right)^2$$

$$= -\frac{\pi D(D-3)^2}{(D-2)(D+1)^3}\frac{1}{\Gamma\left(\frac{D-1}{2}\right)^2}\left(\frac{8G\mathbf{M}}{\Omega_{D-4}}\right)\mathbf{\Omega}^{D+2}\left(\ell_\parallel^2 - \ell_\perp^2\right)^2. \qquad (5.67)$$

Here $\mathbf{\Omega}$ is the physical (dimensionful) rotation velocity of the bar. The radiation rate is proportional to $G$ and thus depends on the choice of units. We find convenient to bundle $G\mathbf{M}$ in the term $8G\mathbf{M}/\Omega_{D-4}$, which is typically proportional (with a coefficient that is weakly dependent on $D$, *i.e.,* not exponential nor factorial) to the characteristic horizon

---

[11]We are not invoking decay through four-armed horizons: although at high spins these may grow more quickly than dipole deformations, the structure of the collision strongly favors the development of dipolar bar-like horizons. Nevertheless, four-armed configurations dominate the ultraspinning instability of MP black holes at high spins [87]. Also, we do not expect spindle bars to drive the evolution: dumbbell bars appear more natural in a collision, and indeed they are the ones we observe in our simulations.

radius of the black hole to the power $D - 3$. When making comparisons, we will keep this quantity fixed.[12]

We have also split the numerical $D$-dependent factor in (5.67) into two terms. The first one is a rational function that depends weakly on $D$, while the second one yields a factorially suppressed radiation rate at large $D$,

$$\frac{\dot{\mathbf{M}}}{\mathbf{M}} \propto -D^{-D} . \tag{5.68}$$

The remaining terms in (5.67) refer to physical properties of the black bar, namely, its rotation velocity and its shape. They are not independent: for a black bar, in the limit of $D \to \infty$ where it exists as a stationary object, we have

$$\left(\ell_\parallel^2 - \ell_\perp^2\right)^2 = \frac{1 - 4\left(r_+\mathbf{\Omega}\right)^2}{\mathbf{\Omega}^4} \tag{5.69}$$

(this follows from (2.69) after restoring units, with $r_+$ the horizon radius of the $S^{D-4}$ at the rotation axis). Then

$$\frac{\dot{\mathbf{M}}}{\mathbf{M}} = -\frac{\pi D(D - 3)^2}{(D - 2)(D + 1)^3} \frac{1}{\Gamma\left(\frac{D-1}{2}\right)^2} \left(\frac{8G\mathbf{M}}{\Omega_{D-4}}\right) \mathbf{\Omega}^{D-2} \left(1 - 4\left(r_+\mathbf{\Omega}\right)^2\right) . \tag{5.70}$$

When the bar is long, $\ell_\parallel \gg \ell_\perp, r_+$, we find

$$\frac{\dot{\mathbf{M}}}{\mathbf{M}} \propto -\ell_\parallel^4 \mathbf{\Omega}^{D+2} \tag{5.71}$$

$$\propto -\mathbf{\Omega}^{D-2} . \tag{5.72}$$

These results are the basis for the estimate (5.65), which is valid in any $D$, and for (5.66), which applies to black bars insofar as (5.69) approximately holds.

In order to obtain the emission rate for a black bar of a given mass and angular velocity, we need $r_+$ in terms of these parameters. Using the leading large-$D$ expression for black bars,

$$\mathbf{M} = \frac{\Omega_{D-4}}{8G} \frac{r_+^{D-4}}{\mathbf{\Omega}} , \tag{5.73}$$

we get

$$r_+\mathbf{\Omega} = \left(\frac{8G\mathbf{M}}{\Omega_{D-4}}\right)^{\frac{1}{D-4}} \mathbf{\Omega}^{\frac{D-3}{D-4}} . \tag{5.74}$$

Notice that at large $D$ and for fixed mass, this is linear in $\mathbf{\Omega}$.

Let us now analyze the dependence on $\mathbf{\Omega}$ in (5.70). It vanishes when $r_+\mathbf{\Omega} = 1/2$, which is the bifurcation point with MP black holes; this solution is axisymmetric so it does not radiate. It also vanishes when $\mathbf{\Omega} \to 0$, which is when the bar becomes infinitely long and static. It is maximized at a value of $\mathbf{\Omega}$ slightly below the bifurcation point,

$$r_+\mathbf{\Omega}_{\max} = \frac{1}{2}\left(1 - \frac{c}{D}\right) , \tag{5.75}$$

---

[12]For reference, recall that $\Omega_{D-4} = \frac{D-3}{2\pi}\Omega_{D-2} = 2\pi^{(D-3)/2}/\Gamma\left(\frac{D-3}{2}\right)$.

where $c$ is a $D$-independent positive number, which we cannot accurately determine without further knowledge of black bars beyond the leading large-$D$ limit.

The maximum radiation rate for a bar of mass $\mathbf{M}$ is then

$$\left(\frac{\dot{\mathbf{M}}}{\mathbf{M}}\right)_{\max} = -\frac{\pi c}{2^D D} \frac{1}{\Gamma\left(\frac{D-1}{2}\right)^2} \left(\frac{\Omega_{D-4}}{8G\mathbf{M}}\right)^{\frac{1}{D-3}} \left(1 + \mathcal{O}\left(\ln D/D\right)\right) . \tag{5.76}$$

We have not expanded the $\Gamma$ functions here since their $D$-dependence even at subleading orders seems robust enough. In any case it is clear that they dominate the large-$D$ behavior.

The radiation rate of angular momentum $\mathcal{J}$ into gravitational waves in arbitrary (even) $D$ has not been calculated in previous literature. In section 5.5.3 we derive the general quadrupole formula for it. If we then apply it to an object rigidly rotating with angular velocity $\mathbf{\Omega}$ we find the simple relation

$$\dot{E} = \Omega\dot{\mathcal{J}} , \tag{5.77}$$

in any dimension $D$. The spin of the radiating object diminishes as $\dot{\mathbf{J}} = -\dot{\mathcal{J}}$, and we find

$$\dot{\mathbf{M}} = \mathbf{\Omega}\,\dot{\mathbf{J}} . \tag{5.78}$$

Our derivation has been made for a rigid, slowly rotating, material solid, but let us apply it to a black hole, and assume that the evolution is slow enough as to proceed along quasistationary configurations. Then the first law of black holes implies that

$$\frac{\kappa}{8\pi}\dot{\mathbf{A}}_H = \dot{\mathbf{M}} - \mathbf{\Omega}\dot{\mathbf{J}} = 0 , \tag{5.79}$$

namely, the radiation emission is such that entropy production (area increase) is strictly minimized. We stress that this result is independent of $D$, and relies only on the application of the quadrupole emission formula.

For black bars, to leading order at $D \to \infty$, the mass, spin, and angular velocity are related by (2.71). In physical magnitudes, using (2.57) and (2.60), this is

$$\mathbf{J} = \frac{\mathbf{M}}{(D-2)\mathbf{\Omega}} , \tag{5.80}$$

so (5.78) gives us

$$\frac{\dot{\mathbf{J}}}{\mathbf{J}} = D\frac{\dot{\mathbf{M}}}{\mathbf{M}}\left(1 + \mathcal{O}\left(\frac{1}{D}\right)\right) . \tag{5.81}$$

We see that the relative loss of spin is $D$ times faster than the relative loss of mass, so radiation emission does lead the bar towards smaller values of the spin per unit mass.

We define the characteristic spin-down time as the inverse decay rate of the dimensionless spin per unit mass,

$$\tau_{\mathrm{rad}}^{-1} = -\left(\frac{\mathbf{J}}{\mathbf{M}^{\frac{D-2}{D-3}}}\right)^{-1}\frac{d}{dt}\left(\frac{\mathbf{J}}{\mathbf{M}^{\frac{D-2}{D-3}}}\right) \tag{5.82}$$

$$= -\frac{\dot{\mathbf{J}}}{\mathbf{J}} + \frac{D-2}{D-3}\frac{\dot{\mathbf{M}}}{\mathbf{M}} . \tag{5.83}$$

For black bars and when $D$ is large, (5.81) applies, so

$$\tau_{\text{rad}}^{-1} = -D\frac{\dot{\mathbf{M}}}{\mathbf{M}}\left(1 + \mathcal{O}\left(\frac{1}{D}\right)\right).$$

(5.84)

Plugging in (5.76) we obtain our estimate for the fastest radiative spin-down time

$$\tau_{\text{rad}} = \frac{2^D}{\pi c}\Gamma\left(\frac{D-1}{2}\right)^2\left(\frac{8G\mathbf{M}}{\Omega_{D-4}}\right)^{\frac{1}{D-3}}\left(1 + \mathcal{O}\left(\frac{\ln D}{D}\right)\right).$$

(5.85)

The number $c$ is a stand-in for $\mathcal{O}(1)$ uncertainties from different sources—not only (5.75), but also, $e.g.,\mathcal{O}(1)$ corrections to the exponent in $2^D$. These are more important than other uncertainties in our estimates, $e.g.,$ from properties of black bars at finite $D$ such as (5.69) and (5.73), which enter only as subleading corrections in $1/D$.

### 5.6.2   Break-up time for the GL-instability

We estimate the growth rate of the GL instability of the black bar using the results for a black string in $D$ dimensions obtained in the blackfold approach [110]. This seems to be a very reasonable approximation, given the excellent agreement that we have found in section 5.4 for the unstable growth rates of black bars and black strings. The growth time is

$$\tau_{\text{inst}}^{-1} = \frac{k}{\sqrt{D-3}}\left(1 - \frac{D-2}{(D-4)\sqrt{D-3}}kr_s\right),$$

(5.86)

where $k$ is the wavenumber of the perturbation and $r_s$ the radius of the black string. This result is valid for all $D$ in an expansion for small $kr_s$. It does not estimate very well the threshold $k$ (where $\tau \to \infty$) at low $D$, but it is close at all $D$ to the known values for the minimum of $\tau_{\text{inst}}$, where the instability is fastest. Since (5.86) is a parabolic profile, the minimum of $\tau_{\text{inst}}$ is at the midpoint

$$k_{\text{inst}}r_s = \frac{(D-4)\sqrt{D-3}}{2(D-2)},$$

(5.87)

which gives

$$\tau_{\text{inst}} = 4\frac{D-2}{D-4}r_s.$$

(5.88)

Observe crucially that *this does not grow with $D$*, in fact its dependence on $D$ is very weak. It is written in units of $r_s$, but the latter has also a weak dependence on $D$ in units of $8G\mathbf{M}/\Omega_{D-4}$. Indeed, let us translate to mass units. The length of the string that fits this fastest unstable mode is

$$L_{\text{inst}} = \frac{2\pi}{k_{\text{inst}}}$$

(5.89)

and the mass of the black string of this length is

$$\mathbf{M} = \frac{(D-3)\Omega_{D-3}}{16\pi G}Lr_s^{D-4}.$$

(5.90)

Using now that

$$\Omega_{D-3} = \sqrt{\pi}\frac{\Gamma\left(\frac{D-3}{2}\right)}{\Gamma\left(\frac{D-2}{2}\right)}\Omega_{D-4},$$

(5.91)

we find that, for the fastest unstable black string,

$$r_s = \left( \frac{8G\mathbf{M}}{\Omega_{D-4}} \frac{D-4}{2\sqrt{\pi}(D-2)\sqrt{D-3}} \frac{\Gamma\left(\frac{D-2}{2}\right)}{\Gamma\left(\frac{D-3}{2}\right)} \right)^{\frac{1}{D-3}} . \tag{5.92}$$

Plugging this into (5.88), we get the GL growth rate for a given mass. When $8G\mathbf{M}/\Omega_{D-4}$ is fixed, this rate does depend weakly on $D$,

$$\tau_{\text{inst}} = 4 \left( \frac{8G\mathbf{M}}{\Omega_{D-4}} \right)^{\frac{1}{D-3}} \left( 1 + \mathcal{O}\left( \frac{\ln D}{D} \right) \right) . \tag{5.93}$$

One possible weak link in this estimate is the identification of the instability time $\tau_{\text{inst}}$ with the perturbative result for the growth of the GL instability of a black string. In numerical simulations of the latter, the linear instability starts only after transients that may last for a few $\tau_{\text{inst}}$, and the time to develop a very large pinch can be significantly larger than $\tau_{\text{inst}}$, possibly even two orders of magnitude larger. Although this would seem to increase the actual value of $\tau_{\text{inst}}$, on the other hand, as we mentioned earlier, we can expect that the instability of the intermediate black bar formed in a collision proceeds more quickly than the black string instability, mostly because the centrifugal repulsion and the absence of a 'box' (the compact Kaluza-Klein direction of the string) will accelerate the development of the instability and push the dumbbell blobs apart. Although we refrain from attempting to estimate these effects, in our simulations at infinite $D$ we do see that the black bars formed in a collision pinch-off more quickly than black strings.

### 5.6.3   Comparing the time scales

We now have the fastest radiative spin-down time (5.85) and GL-instability time (5.93), both for a given mass in units of $(8G\mathbf{M}/\Omega_{D-4})^{\frac{1}{D-3}}$. The main finding is almost self-explanatory:

$$\tau_{\text{inst}} = \mathcal{O}\left( 1 \right) \ll \tau_{\text{rad}} = \mathcal{O}\left( D^D \right) . \tag{5.94}$$

So, for large enough $D$, the radiative spin-down will be so slow as to be negligible. The overall prefactor in (5.85) is in fact larger than the factor 4 in (5.93) for all $D \geq 6$ unless $c > 9$. Of course these numbers cannot be fully trusted since, $e.g.,$ the exponent in $2^D$ may easily be, say, $2^{D-3}$, which would make the radiative time faster than the unstable time in $D \approx 6$ with only moderate values of $c$. However, even in this case, having $\tau_{\text{inst}} > \tau_{\text{rad}}$ in $D \gtrsim 8$ would require seemingly unnaturally large values $c \gtrsim 30$, due to the factorial suppression terms.

In conclusion, our estimates suggest that the gravitational emission spin-down will be inefficient to quench the pinch-down instability whenever $D$ is larger than $\approx 8$, and possibly, but much more uncertainly, even down to $D = 6$, the lowest dimension where we expect black bars (or similar elongated horizons) to form.

# Chapter 6

# Entropy production in fission and fusion

## 6.1 Overview

The area theorem, or second law of black holes, has pervasive implications in all of black hole physics. It puts absolute bounds on gravitational wave emission in collisions (Hawking's original motivation in [111]) and limits other classical black hole evolutions, but also, through the identification of horizon area as entropy [112], it gives an entry into quantum gravity, holography, and applications of the latter to strongly coupled systems.

Investigating the growth of black hole entropy should throw interesting light into complex dynamical black hole processes. How does the second law constrain the possible final states? Are there phenomena where it can provide more than bounds on allowed outcomes, for instance, indicating their likelihood, according to how much entropy they generate? Since the area of the event horizon can be computed outside stationary equilibrium, one may even study the mechanisms that drive its growth at different stages.

Unfortunately, computing this entropy during a highly dynamical process, such as a black hole merger, is in general very complicated and requires sophisticated numerical calculations. In this article we resort to an approach that simplifies enormously the task: the effective theory of black holes in the limit of a large number of dimensions, $D \to \infty$ [56, 21], developed in [24, 25, 27, 29]. We use the equations of [27, 31] for the study of asymptotically flat black holes, their stability, and collisions between them [12, 14, 15].

We examine in detail the production of entropy—its total increase, but also its generation localized in time and in space on the horizon—in processes where an unstable black hole (a black string [32, 51] or an ultraspinning black hole [57, 58]) decays and fissions, and in collisions where two black holes fuse into a single horizon. If the total angular momentum in the collision is not too large, the fusion ends on a stable rotating black hole. However, as shown in [14, 15], when $D$ is large and if the total angular momentum is also large enough, the merger does not end in the fusion, but proceeds to fission: the intermediate merged horizon is unstable, pinches at a neck—in a mild violation of cosmic censorship [15, 113]—and arguably breaks up into two (or possibly more) black holes that

then fly apart. The phenomenon, up until the formation of the singular pinch, has been verified to occur in $D = 6, 7$ through numerical analysis in [114]. The importance of the intermediate phase in the evolution of the system was noticed in the earlier studies [14, 15], but here we will go significantly further in revealing how it controls the outcome.

Before we present our main results, we shall discuss general issues related to area growth, its identification with entropy, and its computation in the large $D$ effective theory.

**Black hole entropy and its growth.**   In General Relativity the horizon area increases through two effects: the addition of new generators to the horizon (at caustics or crossover points, on spacelike crease sets), and the expansion of pencils of existing generators. In this article, the methods and approximations that we employ allow to study the latter, *i.e.,* how the area expands smoothly. The effective theory of large $D$ black brane dynamics provides explicit entropy production formulas for viscous dissipation on the horizon [31, 40, 59, 115], which we apply to the evolution of unstable asymptotically flat black holes, and to the fusion and fission in black hole collisions. The addition of generators through caustics is actually suppressed when $D$ is large[1]. We expect that, at finite $D$, the entropy growth through this addition in the merger of two black holes is important only during the first instants of the fusion, and much less so during the relaxation. In fission, the break-up of the horizon across a naked but mild singularity involves a region of very small horizon area[2] and therefore loses only a few generators in any dimension, and even fewer as $D$ grows large. This process is controlled by quantum gravity, but we have argued elsewhere that the effects upon the classical evolution should be negligibly small [113].

The notions of entropy and entropy current that we use are associated to the area of the event horizon, and in this respect they are closely related to the ones in the Fluid/Gravity correspondence in [117, 118]. Indeed, we expect that the discussion in that context carries over to the large $D$ formulation: it is possible that other currents with non-negative divergence can be constructed. A related concern is whether one should identify the entropy with the area of the apparent horizon, as there are general arguments in favor of this [119], and it has been possible to identify corresponding currents in Fluid/Gravity [120]. While it would be interesting to further investigate this in the large $D$ effective theory, we will not be concerned with it here. The divergence of the entropy current that we use is as expected for a physical fluid (from viscous dissipation of shear and expansion of the fluid), so at the very least our results will not be unreasonable. Moreover, we expect that the growth properties of different entropy notions will be very similar. Within the large $D$ effective theory, the system evolves smoothly and continuously and so we expect the entropy to do that too. With these methods one does not capture the less smooth features (*e.g.,* caustics) of the event horizon in the first stages of the merger, and large discontinuous jumps in the area of the apparent horizon are not expected; these should be suppressed when $D \gg 1$. So, despite the ambiguities in the definition of out-of-equilibrium entropy, we expect that our conclusions remain qualitatively valid for other viable notions

---

[1]This can be seen, for instance, in extreme-mass-ratio mergers with the methods of [116].

[2]A Planckian area, which vanishes in the classical limit.

of it.

The other main aspect of finite $D$ physics that is not captured by our methods is the production of gravitational waves, which implies that in our calculations the total energy and angular momentum of the black holes are conserved, making it easier for us to characterize the evolutions. Again, we expect that this radiation is stronger during the initial instants when the black holes first come together. Radiation effects should quickly become less relevant as the number of dimensions grows [100, 56, 59, 15].

The upshot is that we expect that the patterns of entropy production that we find are broadly applicable in $D \geq 6$, and possibly even qualitatively valid for fusion in $D = 4$. We will return to this last point near the end.

**Main conclusions.**   All the collisions we study are symmetric, *i.e.,* between black holes of equal mass and spin.[3] This is mostly for simplicity; our methods allow to collide black holes with generic parameters.

Our analysis shows that:

- Black hole fusion generates comparatively much more entropy, and at faster rates, than black hole fission.

- Unstable black strings decay with a simple pattern of entropy production which is reproduced in other fission processes.

- Merger collisions of two black holes have a critical value of the total angular momentum per unit total mass[4]
$$\left(\frac{J}{M}\right)_c \approx 2.66 \tag{6.1}$$
that divides low $J/M$ collisions $2 \to 1$ that end in fusion, from higher $J/M$ collisions $2 \to 1 \to N \geq 2$ that evolve to fission. The bound holds except for 'grazing' mergers with large initial impact parameters.

- $2 \to 1 \to 2$ collisions are dominated by the formation of intermediate, long-lived, quasi-stationary, bar-like entropic attractors (fig. 6.1):

    - The intermediate quasi-thermalization largely erases the memory of the initial state, so the final outgoing states are almost independent of the initial parameters, other than the total conserved $J/M$.

    - This attractor effect is stronger the closer $J/M$ is to the critical value (6.1).

    - The attractor can be approximately (but not exactly) predicted by maximizing the entropy generation among possible outgoing black holes.

---

[3]In $2 \to 1 \to 2$ collisions, the two outgoing black holes will both have the same mass and spin, but the initial and final spins will in general be different. Mass conservation to leading order in $1/D$ implies that the final masses are the same as the initial ones.

[4]These $J$ and $M$ are defined in the effective theory; the corresponding physical quantities are given in sec 2.4.2.
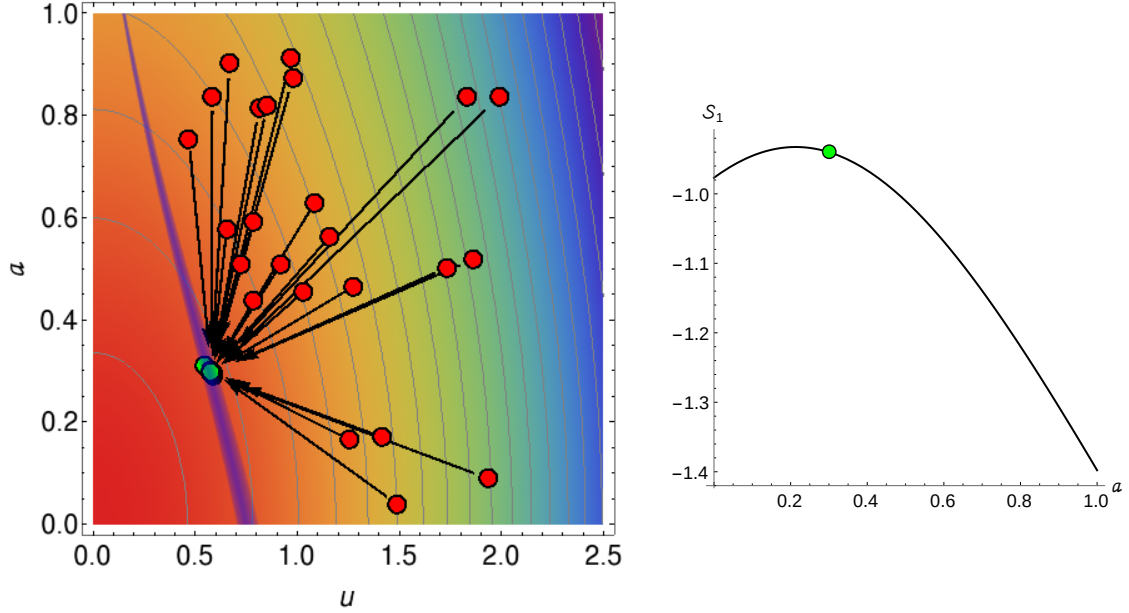
Figure 6.1: Entropic attractor in black hole collisions $2 \rightarrow 1 \rightarrow 2$. *Left*: red dots represent initial states, connected by an arrow line to the corresponding final states (green) after dynamical evolution. The initial and final pairs of black holes are characterized by their rotation (spin) parameter $a$ and their linear velocity $u$ (ingoing or outgoing). The (conserved) total angular momentum per unit mass in these collisions is fixed to $J/M = 2.8$. We see that, independently of the initial states, the final states cluster on $(a, u) \approx (0.3, 0.6)$. This is due to the formation of an intermediate, long-lived, quasi-thermalized phase. The contour colors correspond to the (NLO) entropy $\mathcal{S}_1$ of the configuration. Entropy would be maximized at the lower-left corner, but this would correspond to infinite impact parameter $b$, which is unphysical since $b$ is constrained by the geometric size of the collision. The thin purple strip is the region where $b$ takes on geometrically-allowed values for final states. *Right*: entropy along the central value of the purple strip. The attractor is close to the maximum possible final entropy; larger values of $a$ (smaller values of $u$) would be entropically disfavoured, while in the opposite direction the entropy gain would be very small.

- Entropy is produced through viscous dissipation of shear and expansion of the effective velocity field. In fusion generically, and in fission always, both enter in almost equal proportion. The formation of the intermediate bar phase can be dominated by shearing depending on initial conditions.

The reason the attractor effect is stronger when $J/M$ is near criticality is that the intermediate state is closer to a marginally stable solution. When $J/M$ is higher, the intermediate black hole is shorter-lived and its features are less precisely defined, so its decay outcomes show larger spread. We emphasize that the attractor is a feature of $2 \rightarrow 1 \rightarrow 2$ collisions with intermediate fusion; this requires that the initial impact parameter and initial velocities are not too large, otherwise the two black holes fly by each other. Fusionless $2 \rightarrow 2$ collisions are not included in fig. 6.1, and are little studied in this article.

Let us elaborate on the near-maximization of entropy in collisions $2 \rightarrow 1 \rightarrow 2$. After fixing an overall scale by setting the total mass to one, the outgoing black holes are char-

acterized by their spin parameter $a$, outgoing velocity $u$, and outgoing impact parameter $b$.[5] We argue that these can be well predicted by considering three different constraints:

(i) Kinematic: the total final angular momentum must be the same as the initial one, which imposes a relation between $a$, $b$ and $u$.

(ii) Geometric: the outgoing impact parameter is limited by the geometrical size of the collision. This yields a constraint between $b$ and $a$.

(iii) Entropic: after imposing (i) and (ii), near-maximization of the final entropy gives a good approximation to the final values of $a$, $b$, and $u$.

In fig. 6.1, (i) is included by considering states with given total $J/M = 2.8$, while (ii) restricts final states to the lie along the purple band; the graph on the right then makes (iii) apparent.

The most remarkable of these constraints is entropy maximization: it provides a simple proxy for the complex dynamics that drives the system to its final state. We do not have an answer to why it is not a perfect predictor—other than there is no reason that it should be—but given our results it is natural to wonder how accurate it becomes as $J/M$ approaches from above the critical value (6.1).

The principle of entropy maximization actually holds quite well in four-dimensional black hole collisions: in the merger, the final entropy would be maximal (consistent with conservation of energy and angular momentum) if no gravitational waves were emitted. The fact that the radiated energy is typically only a few-percent fraction of the total energy means that the final entropy is only a few percent off the maximum. In the limit $D \to \infty$, the $2 \to 1$ fusion trivially maximizes the entropy since radiation is absent. The fission of an unstable black object, instead, has a range of possible outcomes. For instance, black strings can split up into several blobs, and the final entropy is larger for fewer blobs. The decay of ultraspinning black holes (MP, bars, and dumbbells) is more similar to the fission stage in $2 \to 1 \to 2$ collisions, but the evolution of the instability is sensitive to the specific perturbation that triggers it. The process starts with an unstable system and looks more contrived and less natural than a collision, so in our study we have focused mostly on the latter. Note, however, that the decay of the critical, marginally stable solution at (6.1) may illuminate the question of how closely can entropy be maximized. This deserves closer examination.

**Entropy generation and irreversibility in the leading order (LO) large $D$ effective theory** Readers familiar with the large $D$ effective theory of black holes and branes may be surprised that the entropy growth can be computed with its equations to leading order in the $1/D$ expansion. This theory is known to exactly conserve the entropy of the system: the LO entropy current is divergence-free, and entropy generation is suppressed

---

[5]There is one more outgoing parameter: the scattering angle. However, this is not affected by conservation laws nor by entropic considerations, and we shall have little to say about it.

by a factor $1/D$ [27, 59]. A simple illustration of this property is the fusion of two equal mass Schwarzschild black holes [34, 56], each with entropy

$$S(M) \propto M^{\frac{D-2}{D-3}} \,, \tag{6.2}$$

which merge into a single one, so that (since losses into radiation are suppressed non-perturbatively in $1/D$)

$$\frac{S_{\text{final}}}{S_{\text{initial}}} = \frac{S(2M)}{2S(M)} = 1 + \frac{\ln 2}{D} + \mathcal{O}\left(\frac{1}{D^2}\right) \,, \tag{6.3}$$

*i.e.,* the entropy increase is $\propto 1/D$. This feature extends to all of the dynamics of black branes at large $D$ described by the LO effective theories of [27, 59].

This seems to make it impossible to see entropy growth unless one employs the next-to-leading order (NLO) theory. It also raises a puzzle: if the LO entropy does not grow, how can we characterize the irreversibility of the evolution in the LO theory?

We will argue that there exists a quantity $S_1(t)$ in the LO theory such that the evolution equations imply $\partial_t S_1(t) \geq 0$, and hence characterizes the irreversibility of this theory. This $S_1$ is actually the NLO ($1/D$ suppressed) entropy density, but we might not (indeed, need not) have known this, since $S_1$ and its variations are all given by LO magnitudes.

The argument of (6.3) is still valid when the black holes rotate, since rotation effects in the entropy are supresed by $1/D$ [27, 12]. However, it ceases to apply if the black holes carry charge. Correspondingly, the effective theory of large $D$ charged black branes [31, 13] allows entropy production, through charge diffusion (resistive Joule heating), at leading order in $1/D$.[6] The study of entropy production in charged collisions is much simpler than in the neutral case, since it is largely dictated by conservation laws, but it is still illustrative and confirms the conclusions above. We will discuss it after our analysis of neutral collisions.

**Outline.**   In section 6.2 we elucidate how entropy generation can be studied within the context of the LO theory. In sec. 6.3 we discuss localized black hole solutions in this effective theory and how their stability properties influence the outcome of collisions. In sec. 6.4 we perform numerical simulations of evolutions of instabilities and collisions. We investigate in detail the generation of entropy, in time and in space, and use it to characterize the different stages in the collision. The study in sec. 6.5 of the scattering of black holes reveals the role as an attractor of the intermediate state which nearly maximizes entropy production. Sec. 6.6 describes how entropy is produced through charge diffusion in collisions between charged black holes. We conclude in sec. 6.7.

## 6.2   Entropy production in the large $D$ effective theory

We begin with a discussion of the large $D$ effective theory of black branes, with a focus on entropy and its generation. The extension of the results in this section to the large $D$

---

[6]However, entropy production in the theory of charged membranes in [29] is zero at LO.

effective theory of AdS black branes is straightforward (and can be found in the appendix of [17]).

For asymptotically flat branes the entropy density and the temperature can be obtained from the area density and surface gravity of the black brane. They are

$$s = 4\pi m\,, \qquad T = \frac{1}{4\pi}\,, \tag{6.4}$$

and they satisfy the expected thermodynamic relations for the system,

$$m = Ts\,, \qquad dm = Tds\,. \tag{6.5}$$

### 6.2.1  Irreversibility in the effective theory

Let us now address in detail an elementary puzzle of this effective theory that we alluded to in the introduction. The effective equations of motion at leading order (1.6), (1.7) contain viscous dissipation, which is expected to render the evolution irreversible.[7] This is further confirmed by the spectrum of linearized perturbations, which has quasinormal frequencies with imaginary parts. After all, these equations describe horizons, which are dissipative systems par excellence, but for the moment let us forget black holes and regard by itself the system that these effective equations describe.

On very general grounds, we expect that dissipation in a thermodynamic system creates entropy, reflecting the irreversibility of the evolution. However, in the theory described by (1.6) and (1.7) the total entropy

$$S(t) = \int d^p x\, s(t,x) \tag{6.6}$$

remains constant in time, since (6.4) implies that it is exactly proportional to the total mass and this is conserved by (1.6). So, if the entropy is not growing, what, then, characterizes the irreversibility?

Remarkably, we can identify a quantity in this theory that is strictly non-decreasing under time evolution. Define the density[8]

$$s_1 = 4\pi \left( -\frac{1}{2}mv_i v^i - \frac{1}{2m}\partial_i m\, \partial^i m + m \ln m \right)\,. \tag{6.7}$$

We will justify the choice presently, but for now note that using the field equations (1.6) and (1.7) it follows that

$$\partial_t s_1 + \partial_i j_1{}^i = 8\pi m \left( \partial_{(i} v_{j)} \right) \left( \partial^{(i} v^{j)} \right)\,, \tag{6.8}$$

where

$$j_1{}^i = s_1 v^i - 4\pi \left( v^j \tau^{ij} + (\partial_j m)(\partial^j v^i) \right)\,. \tag{6.9}$$

---

[7]This is also apparent using the variable $p_i = mv_i + \partial_i m$, in which (1.6) and (1.7) take the form of inhomogeneous heat equations [27].

[8]The factors $4\pi$ that we carry over have their origin in $T$ in (6.4).

Since the right hand side of (6.8) is non-negative, we conclude that

$$S_1(t) = \int d^p x \, s_1(t, x) \tag{6.10}$$

is a non-decreasing function in time,

$$\partial_t S_1(t) \geq 0 \, . \tag{6.11}$$

This characterizes the irreversibility of the evolution in the effective theory.

Observe that the growth rate

$$\partial_t S_1(t) = 8\pi \int d^p x \, m \left( \partial_{(i} v_{j)} \right) \left( \partial^{(i} v^{j)} \right)$$
$$= \int d^p x \left( \frac{2\eta}{T} \sigma_{ij} \sigma^{ij} + \frac{\zeta}{T} \left( \partial_i v^i \right)^2 \right) \tag{6.12}$$

is that of a hydrodynamic entropy generated by viscous heating, with contributions from dissipation of shear

$$\sigma_{ij} = \partial_{(i} v_{j)} - \frac{1}{p} \delta_{ij} \, \partial_k v^k \tag{6.13}$$

and dissipation of expansion $\partial_i v^i$. This is also a feature of the entropy in the Fluid/Gravity correspondence [118, 115] (see [21] for further discussion in these contexts).

### 6.2.2   Entropy at next-to-leading order

The explanation for these properties of $S_1$ is that it is actually the leading $1/D$ contribution to the black brane entropy. Namely, the entropy density obtained from the event horizon area of the black brane is, up to a total divergence (see section 6.2.3)

$$s(t, x) = 4\pi \bar{m}(t, x) \left( 1 + \frac{c_s}{D} \right) + \frac{1}{D} s_1(t, x) \, , \tag{6.14}$$

where $\bar{m}$ is the energy density including NLO corrections, and $c_s$ is a constant (which we determine in section 6.2.4) that accounts for the fact that, in order to simplify the form of $s_1$, we have subtracted a term $\propto m$ without changing the right-hand side of (6.8). The total entropy is

$$S(t) = 4\pi M \left( 1 + \frac{c_s}{D} \right) + \frac{1}{D} S_1(t) \, . \tag{6.15}$$

Eq. (6.12) then gives the production rate of entropy to NLO in the $1/D$ expansion. The point to notice is that, since the LO entropy is proportional to the energy, which is constant to all orders, the time derivative of the entropy at NLO can be computed using only quantities of the LO effective theory. This is what allows us to identify within this theory the quantities $s_1$ and $S_1$ which behave irreversibly.

Observe that we can write (6.14) as

$$s(t, x) = 4\pi \left( \bar{m} - \frac{1}{D} \left( \frac{1}{2} m v^2 + \frac{1}{2m} (\partial m)^2 - c_s \right) \right)^{1 + 1/D} \, , \tag{6.16}$$

which we can understand as follows. The dependence of entropy on mass (6.2) for a Schwarzschild black hole at finite $D$ is $S \propto M^{1 + 1/(D-3)}$, which is like (6.14) at large $D$.

The term $-\frac{1}{2}mv^2$ is a kinetic energy[9]. It appears here because, out of the total energy of the black hole, only its rest (irreducible) mass contributes to entropy. Observe that this motion could be linear, as in a boosted black hole, or circular, as in a rotating black hole: both reduce the 'heat' fraction of the total energy. The last term in (6.16) is (likely) a correction from curvature of the horizon due to the difference between the radial position measured by $m$ and the actual area density.

The entropy density (6.7) simplifies for stationary solutions which rotate rigidly, such that [31]

$$\partial_t m + v^i \partial_i m = 0, \qquad \partial_t v^i = 0, \qquad \partial_{(i} v_{j)} = 0. \tag{6.17}$$

In this case the effective equations reduce to the 'soap bubble equation'

$$\frac{1}{2} m v^i v_i + m \ln m + \partial_i \partial^i m - \frac{1}{2m} \partial_i m \, \partial^i m = c\, m, \tag{6.18}$$

where $c$ is an integration constant that corresponds to a choice of scale for the total mass. We set it to zero, since in the end we will work with scale-invariant quantities where $c$ would disappear. Using this equation we obtain, after dropping a boundary term from a total derivative,

$$S_1(t) = -4\pi \int d^p x \, m v_i v^i. \tag{6.19}$$

For a solution that rotates along independent angles $\phi_a$ with velocities $v^{\phi_a} = \Omega^a$, this gives

$$TS_1 = -\Omega^a J_a, \tag{6.20}$$

where $T$ is the LO temperature (6.4). It is easy to verify that, when added to the LO entropy, this reproduces the Smarr relation for black holes at NLO in $1/D$.

### 6.2.3 Stress-energy and entropy in the effective theory to $1/D$

Let us assume the $D = n+p+3$ spacetime is written in Eddington-Finkelstein coordinates

$$ds^2 = -A dt^2 + 2u_t dt dr - 2C_I dt dZ^I + H_{IJ} dZ^I dZ^J. \tag{6.21}$$

For the spatial metric, we assume a rescaling in the 'active' dimensions and spherical symmetry in the 'passive' ones,

$$H_{IJ} dZ^I dZ^J = \frac{1}{n} G_{ij} dz^i dz^j + r^2 d\Omega_{n+1}^2, \tag{6.22}$$

where $G_{ij}$ is the $p$-dimensional metric.

The metric is expanded in $1/n$,

$$A = \sum_{k=0} \frac{A_{[k]}}{n^k}, \quad u_t = 1 + \sum_{k=0} \frac{u_{t,[k]}}{n^{k+1}}, \quad C_i = \sum_{k=0} \frac{C_{i,[k]}}{n^{k+1/2}}, \quad G_{ij} = \delta_{ij} + \sum_{k=0} \frac{G_{ij,[k]}}{n^{k+1}}, \tag{6.23}$$

---

[9]Physical velocities in the effective theory are rescaled by a factor $1/\sqrt{D}$ [27], which explains why the term is $1/D$ suppressed.

where we introduce a radial coordinate $\mathsf{R} = r^n$. At leading order, we obtain

$$A_{[0]} = 1 - \frac{m}{\mathsf{R}}, \quad C_{i,[0]} = \frac{p_i}{\mathsf{R}}, \quad G_{ij,[0]} = \frac{p_i p_j}{m\mathsf{R}}, \quad u_{t,[0]} = -\frac{p_i p^i}{2m\mathsf{R}^2}, \tag{6.24}$$

where $m = m(t, z)$ and $p_i = p_i(t, z)$ are integration functions. To avoid ambiguity in the definition of the integration functions at higher order, we fix $m$ and $p_i$ by

$$A(\mathsf{R} = m) = 0, \quad C_i(\mathsf{R} = m) = \frac{p_i}{m}. \tag{6.25}$$

Note that in general $\mathsf{R} = m$ differs from the horizon position, which will be relevant below.

**Quasi-local stress tensor**

The quasi-local stress tensor is defined at the asymptotic boundary of the near-horizon region,

$$\mathbf{T}_{\mu\nu} = \lim_{r \to \infty} \frac{\Omega_{n+1} r^{n+1}}{8\pi G} (K\gamma_{\mu\nu} - K_{\mu\nu}) + (\text{regulator}), \tag{6.26}$$

where $(\gamma_{\mu\nu}, K_{\mu\nu})$ are the metric and extrinsic curvature on a surface at constant $r$. The regulator terms are chosen to eliminate the divergent terms at $r \to \infty$. The boundary metric is given by

$$ds^2 = -dt^2 + \frac{1}{n} dz^i dz_i. \tag{6.27}$$

For convenience, we use the dimensionless tensor,

$$\mathbf{T}_{\mu\nu} = \frac{(n+1)\Omega_{n+1}}{16\pi G} T_{\mu\nu}. \tag{6.28}$$

The result up to NLO in the $1/n$ expansion is given by[10]

$$T^{tt} = m - \frac{1}{n}(2 + \ln m)\partial_i p^i, \tag{6.29}$$

$$T^{ti} = p_i - \partial_i m - \frac{1}{2nm^2}\Big[2m(m + \partial_i p^i)(p^i - \partial^i m) + 2p^i p^j \partial_j m - p_j p^j \partial^i m + 4mp_j \partial^{[j} p^{i]}$$
$$+ \big(2m\partial_j(p^i p^j) - 2p^i p^j \partial_j m - 2m^2 \partial^i \partial_j p^j\big) \ln m\Big], \tag{6.30}$$

$$T^{ij} = \alpha\delta^{ij} + \beta_{ij}, \tag{6.31}$$

where

$$\alpha = \left(1 - \frac{1}{n}\right)(-m + \partial_t m + \partial_k p^k)$$
$$+ \frac{1}{n}\left[-\frac{1}{2m}\partial^2(p^2) - \partial_k p^k\left(1 - \frac{2p^2}{m^2} + \frac{3p^k \partial_k m}{m^2}\right) - \frac{p^k - \partial^k m}{m}\partial_k(p^2) + \frac{p^k}{m^2}\partial^\ell m \partial_k p_\ell\right.$$
$$\left. + \frac{p^2}{m}\left(1 + \frac{\partial^2 m}{2m}\right) - \partial^2\left(\frac{p^2}{m}\right)\ln m + \partial_k p^k \ln m - \partial_t(\partial_k p^k \ln m)\right], \tag{6.32}$$

---

[10] Here the indices of $T_{\mu\nu}$ are raised with the boundary metric (6.27), while $p_i$ and $\partial_i$ with $\delta^{ij}$.

and

$$
\begin{aligned}
\beta_{ij} = {} & \left(1 - \frac{1}{n}\right)\left(-2\partial_{(i}p_{j)} + \frac{p_i p_j}{m}\right) \\
& + \frac{1}{n}\left[-\frac{p^2}{m^3}\partial_i m \partial_j m + \left(\frac{2p^k \partial_k m}{m^2} - \frac{(\partial m)^2}{m^2} - \frac{3\partial_k p^k}{m}\right)\frac{p_i p_j}{m}\right. \\
& + \frac{2}{m^3}(-p^2 + 2m\partial_k p^k)p_{(i}\partial_{j)}m + \left(\frac{2p^k \partial_k m}{m^2} - \frac{p^2}{m^2} - 2\ln m\right)\partial_{(i}p_{j)} \\
& + \frac{2}{m^2}\left(p_{(i}\partial_{j)}(p^2) - \partial_k m p_{(i}\partial_{j)}p^k\right) + \partial_i \partial_j\left(\frac{p^2}{m}\right)\ln m + \left.(-1 + \ln m)\partial_t\left(\frac{p_i p_j}{m}\right)\right]. \quad (6.33)
\end{aligned}
$$

Here we have written $p^2 = p_i p^i$ and $\partial^2 = \partial_k \partial^k$.

**Entropy density and entropy current**

The position of the event horizon $\Phi = r - r_h(t, Z^I) = 0$ is given by the null condition for the normal vector $d\Phi = dr - \partial_t r_h dt - \partial_I r_h dZ^J$,

$$
d\Phi^2 = \frac{1}{u_t^2}\left[A - 2u_t \partial_t r_h + H^{IJ}(C_I - u_t \partial_J r_h)(C_J - u_t \partial_J r_h)\right] = 0. \quad (6.34)
$$

In the dynamical case, this condition does not give the actual event horizon but rather the local one. However, as in [118], this is useful to define the entropy current on the black brane. Expanding up to NLO in $1/n$ we obtain

$$
\mathsf{R}_h = r_h^n = m - \frac{1}{n}\left(\frac{p^i p_i}{m} - 2p^i \partial_i \ln m + \frac{1}{m}\partial_i m \partial^i m - 2\partial_t m\right). \quad (6.35)
$$

One can see that $\mathcal{R} = m$ also gives the event horizon for the static solution. With a rigid rotation, however, we have $\mathsf{R}_h \neq m$ beyond LO. Using eq. (6.34), the geometry on the horizon becomes

$$
ds^2\big|_{\mathcal{H}} = h_{IJ}(dZ^I - V^I dt)(dZ^J - V^J dt), \quad (6.36)
$$

where $h_{IJ} = H_{IJ}|_{\mathcal{H}}$ and $V^I = h^{IJ}(C_J - u_t \partial_J r_h|_{\mathcal{H}})$. Following [118], the entropy $(D-2)$-form is defined from the area-form of this surface,

$$
\mathcal{A} = \frac{1}{4G}\sqrt{h}(dZ^1 - V^1 dt) \wedge \cdots \wedge (dZ^{D-2} - V^{D-2} dt), \quad (6.37)
$$

which determines the entropy current to be

$$
\mathcal{A} = \frac{\epsilon_{\bar\mu \bar\mu_1 \dots \bar\mu_{D-2}}}{(D-2)!}\bar{\mathcal{J}}_s^{\bar\mu} dX^{\bar\mu_1} \wedge \cdots \wedge dX^{\bar\mu_{D-2}}, \quad (6.38)
$$

where $X^{\bar\mu} = (t, Z^I)$. By comparison, one obtains

$$
\bar{\mathcal{J}}_s^{\bar\mu}\partial_{\bar\mu} = \frac{1}{4G}\left(\sqrt{h}\partial_t + \sqrt{h}V^I \partial_I\right). \quad (6.39)
$$

Recalling the spatial setup (6.22), the entropy current reduces to

$$
\mathcal{J}_s^\mu \partial_\mu = \frac{\Omega_{n+1} r_h^{n+1}}{4Gn^{p/2}}\left(\sqrt{\mathcal{G}}\partial_t + \sqrt{\mathcal{G}}V^i \partial_i\right), \quad (6.40)
$$

where $x^\mu = (t, z^i)$ and $\mathcal{G}_{ij} = G_{ij}|_{\mathcal{H}}$. The dimensionless version is

$$\mathcal{J}_s^\mu = \frac{\Omega_{n+1}}{4Gn^{p/2}} J_s^\mu. \tag{6.41}$$

For the black brane, the result up to NLO in $1/n$ expansion is

$$J^t = m + \frac{1}{2nm}\left(2m^2 \ln m - p^2 + 4p^i \partial_i m - 2(\partial m)^2 + 4m\partial_t m\right), \tag{6.42}$$

$$J^i = p^i - \partial^i m + \frac{1}{2nm^2}\left(-p^2 p^i + 4m(p_j - \partial_j m)(\partial^i p^j - \partial^i \partial^j m) - 4m^2 \partial_t \partial^i m \right.$$
$$\left. + 2m^2 \ln m (p^i - 2\partial^i m)\right). \tag{6.43}$$

We can use the LO equations (1.6) and (1.7) to find that in the effective theory the entropy density is

$$s = 4\pi J^t$$
$$= 4\pi\bar{m} + \frac{4\pi}{n}\left((m + \partial_i p^i) \ln m + 2\partial^2 m - \frac{1}{2m}(p^2 - 4p^i \partial_i m + 2\partial_i m \partial^i m)\right), \tag{6.44}$$

where we have defined the mass density to NLO from (6.29)

$$\bar{m} = m - \frac{1}{n}\left(2 + \ln m\right)\partial_i p^i. \tag{6.45}$$

Using again the LO equations with

$$p_i = mv_i + \partial_i m, \tag{6.46}$$

we can rewrite (6.44) as

$$s = 4\pi\bar{m} + \frac{4\pi}{n}\left(-\frac{1}{2}mv_i v^i - \frac{1}{2m}(\partial m)^2 + m \ln m\right) + \text{total divergence}. \tag{6.47}$$

Dropping the total divergence term, which does not contribute to the integrated entropy, we obtain (6.7) and (6.14).

### 6.2.4   Measuring the entropy

#### Scale invariant entropy

When we compare the entropy of different solutions—*e.g.,* ingoing and outgoing black holes—we will do it between configurations with the same total mass. For this purpose, if **S** and **M** are the physical entropy and mass of the black hole in $D$ dimensions, one works with a mass-normalized, scale-invariant, dimensionless entropy of the form

$$\mathcal{S} = C\frac{\mathbf{S}}{\mathbf{M}^{\frac{D-2}{D-3}}}. \tag{6.48}$$

Here

$$C = \left(\frac{(D-2)\Omega_{D-2}}{16\pi G}\right)^{1/(D-3)}\frac{D-2}{4\pi} \tag{6.49}$$

is a suitable convention to simplify later expressions; it could be set to one by adequately choosing Newton's constant $G$.

Similarly, in the effective theory we define a mass-normalized, scale-invariant entropy,

$$\mathcal{S}_1(t) = \frac{S_1(t)}{4\pi M} - \ln \frac{M}{2\pi e^2} . \tag{6.50}$$

Subtraction of the term $\ln M$ makes this quantity independent of the choice of mass scale, in particular of the value of $c$ in (6.18). We have also added a constant $\ln(2\pi e^2)$ to simplify later expressions. One can then verify (section 6.2.4) that the physical mass-normalized entropy (6.48) is given in terms of the effective theory one (6.50) by

$$\mathcal{S} = 1 + \frac{1}{D}\mathcal{S}_1(t) + \mathcal{O}\left(\frac{1}{D^2}\right) . \tag{6.51}$$

**Relation to physical entropy**

Using the relations of the conserved charges of the effective field theory to the proper physical quantities given in section 2.4.2 and defining an physical entropy according to

$$\mathbf{S} = \frac{\mathbf{A}}{16\pi G} , \tag{6.52}$$

we obtain the mass-normalized, dimensionless entropy (6.48) as

$$\begin{aligned} \mathcal{S} &= \frac{S}{4\pi M}\left(1 - \frac{1}{D}\ln\frac{M}{2\pi m_0}\right) \\ &= 1 + \frac{1}{D}\left(c_s + \ln 2\pi m_0 + \mathcal{S}_1\right) , \end{aligned} \tag{6.53}$$

where in the last expression we have used (6.15) and (6.50).

In order to determine the constant $c_s$ we apply these formulas to the MP blob solution (2.25) so that we recover the known results for the exact MP black hole solution. These are

$$\mathbf{M} = \frac{\Omega_{D-2}}{16\pi G}(D-2)r_m^{D-3} , \tag{6.54}$$

$$\mathbf{S} = \frac{\Omega_{D-2}}{4G}r_m^{D-3}r_+ , \tag{6.55}$$

where the mass-radius $r_m$ and the horizon radius $r_+$ are related by

$$\frac{r_+}{r_m} = \left(1 + \frac{a^2}{r_+^2}\right)^{-1/(D-3)} \simeq 1 - \frac{1}{D}\ln\left(1 + \frac{a^2}{r_+^2}\right) . \tag{6.56}$$

Then, for this black hole, the mass-normalized, dimensionless entropy defined in (6.48) is

$$\mathcal{S} = 1 - \frac{1}{D}\ln(1 + a^2) , \tag{6.57}$$

where, henceforth, since we work with scale-invariant quantities, we can set $r_+ = 1$.

For the MP blob solution (2.25), the effective theory NLO entropy (6.10) is

$$\frac{S_1}{4\pi M} = -\frac{2a^2}{1+a^2} , \tag{6.58}$$

and then the mass-normalized one, $\mathcal{S}_1$ in (6.50), is given in (6.61). Plugging the latter into (6.53) and setting

$$c_s = 2 - \ln m_0 , \tag{6.59}$$

we recover correctly the physical value (6.57). Using this now in the general formula (6.53), we obtain (6.51).

## 6.3    General features of black hole collisions

In the following we restrict to black holes with rotation on a single plane, which will also be the plane on which the black holes move and collide. Then, in the effective theory we study configurations with non-trivial dependence in only $2 + 1$ dimensions, *i.e.,* on a 2-brane. Accordingly we can use the formulation of the effective theory also adapted in previous chapters.

### 6.3.1    Entropy evaluated on blobs

Remember that the effective field theory mass $M$ depends on the choice of scale of normalization $m_0$ in (2.25). Accordingly more relevant are scale-invariant quantities, namely the spin per unit mass

$$\frac{J}{M} = 2a \tag{6.60}$$

and the NLO mass-normalized entropy

$$\mathcal{S}_1 = -\ln(1 + a^2). \tag{6.61}$$

The fact that $\mathcal{S}_1$ becomes more negative with larger $a$ is the familiar decrease of the black hole entropy as the spin grows, in the large $D$ limit.

Another exact solution describes rotating black bars,

$$m = \exp\left(1 - \frac{x_c^2}{4}\left(1 + \sqrt{1 - 4\Omega^2}\right) - \frac{y_c^2}{4}\left(1 - \sqrt{1 - 4\Omega^2}\right)\right), \tag{6.62}$$

where $x_c$, $y_c$ are corotating coordinates given by (3.15). And our scale normalization is again consistent with $c = 0$ in (6.18). This solution has

$$M = \frac{2\pi}{\Omega}, \tag{6.63}$$

and

$$\frac{J}{M} = \Omega^{-1}, \qquad \mathcal{S}_1 = \ln \Omega. \tag{6.64}$$

For $\Omega = 1/2$ this branch of solutions joins the MP family.

Ref. [16] constructed numerically large classes of other stationary solutions. The most relevant for us are rotating dumbbells. They can be regarded as black bars with a pinch in their middle, see fig. 6.2.

### 6.3.2    Phase diagrams and the outcomes of collisions

Fig. 6.3 is a phase diagram that summarizes the main properties of these solutions, and the implications for the possible initial and, more importantly, final states of a collision. Depending on the value of $J/M$ (distinguished by band-colouring in the figure) the stable phases of stationary single blobs are:
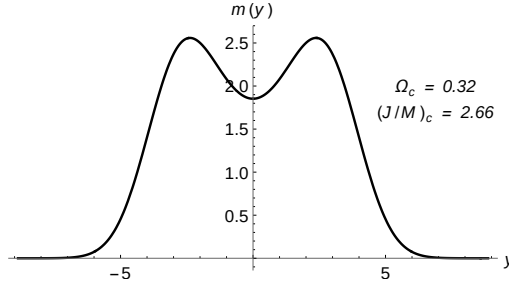
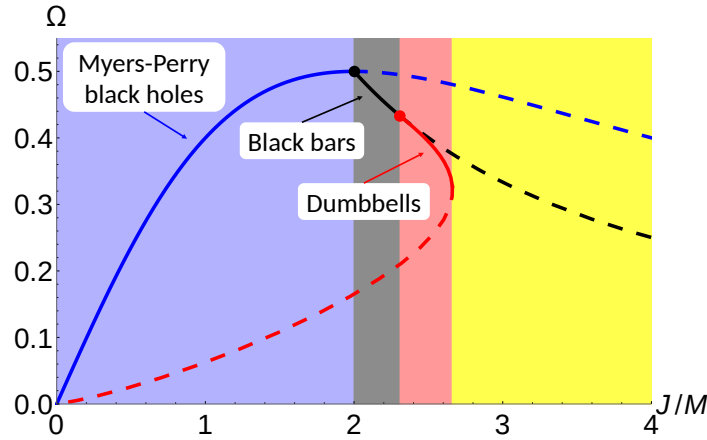Figure 6.2: Profile along the long axis of the 'critical' dumbbell solution with $J/M$ equal to (6.1).



Figure 6.3: Phases of blobs and their stability as relevant to outcomes of mergers. Solid/dashed lines are stable/unstable stationary blobs. Blue: Myers-Perry black holes, stable up to $J/M = 2$. Black: black bars, stable up to $J/M = 4/\sqrt{3} \approx 2.31$. Red: black dumbbells, stable up to $J/M = (J/M)_c \approx 2.66$ (dumbbells along the dashed line are unstable binaries of blobs). The background shading indicates the expected outcome of a merger for an initial value of $J/M$. No stable stationary blobs exist for $J/M > (J/M)_c$ (yellow), so, if a merger occurs in this region, it can only evolve to a multi-blob state. The numerical solutions for dumbbells are from [16]. The same color coding is used in the next figures.

$$0 \leq J/M < 2: \quad \text{MP black holes}$$
$$2 \leq J/M < \frac{4}{\sqrt{3}} \approx 2.31: \quad \text{Black bars}$$
$$\frac{4}{\sqrt{3}} \leq J/M < (J/M)_c: \quad \text{Black dumbbells}$$
$$(J/M)_c \leq J/M: \quad \text{No stable single black hole}$$

where the numerically determined upper limit $(J/M)_c$ for the existence of stable phases is (6.1).

Let us clarify an aspect of the stability of phases in this diagram that was not discussed in [16]. In that article a second branch of dumbbells (lower in $\Omega$, shown dashed in fig. 6.3) was found to exist, starting from $J/M = 0$ until it joins the first, upper branch at $(J/M)_c$. In this second branch, the dumbbells are more like slowly rotating black hole binaries, consisting of two gaussian blobs joined by a thin, long tube between them. All these

solutions have the same LO entropy, but the NLO entropy $\mathcal{S}_1$ (6.50) distinguishes between them. In fig. 6.4 we show that lower-branch dumbbells have less entropy than the upper branch. They are therefore thermodynamically unstable. Moreover, a Poincaré turning point argument tells us they must have one more negative mode than the upper-branch, and hence be dynamically unstable. This is indeed consistent with two other observations: (i) in our numerical collisions, we never observe a lower-branch dumbbell forming (while upper-branch dumbbells do form); (ii) stationary Keplerian binaries in $D \geq 6$ exist but are unstable.
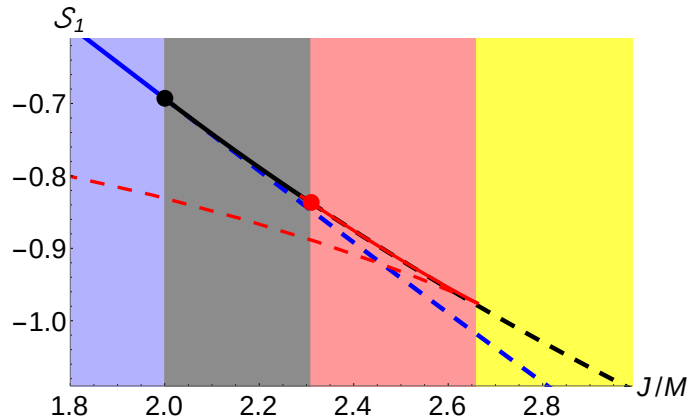


Figure 6.4: Phase diagram depicting the entropy $\mathcal{S}_1$ of the different configurations close to the first black bar zero-mode, as a function of angular momentum. For $J/M > 2$ the black bar (black) is entropically favored over the MP black hole (blue). At the zero-mode $J/M = 4/\sqrt{3}$, a branch of stable dumbbells (red) appears with $\mathcal{S}_{\text{inv}}$ slightly higher that that of unperturbed black bars. This phase dominates entropically up to the turning point at $(J/M)_c \approx 2.66$, where stable dumbbells cease to exist, and the system typically evolves to a fission.

In contrast, upper-branch dumbbells resemble (segments of) stable non-uniform black strings (fig. 6.2). Although other more non-uniform phases were found in [16], by generic turning-point/bifurcation arguments they are expected to have more negative modes and hence be dynamically unstable. Therefore, no other stable solutions are expected to exist besides those shown in fig. 6.3.

Fig. 6.3 is then a major guide to predicting the outcome of a collision between two blobs, based only on the total angular momentum $J$ and total mass $M$ of the system, which are conserved. If $J/M < 2.66$, two blobs that merge can relax into a stable single blob, namely the only one that is stable for the corresponding value of $J/M$. Bear in mind that they will not necessarily do so, since the dynamical evolution may avoid that endpoint.

If $J/M > (J/M)_c$ the final state must consist of more than a single blob. That is, if there is fusion it will be followed by fission. If $J/M$ is less than $\approx 4$, we observe that the end state is always two outgoing black holes, i.e., $2 \rightarrow 1 \rightarrow 2$. At higher $J/M$, a third, smaller black hole can appear between them, the apparent reason being that at these angular momenta there exists an unstable branch of three-bumped bars. End states with more than two blobs are entropically disfavored but nevertheless are dynamically possible.
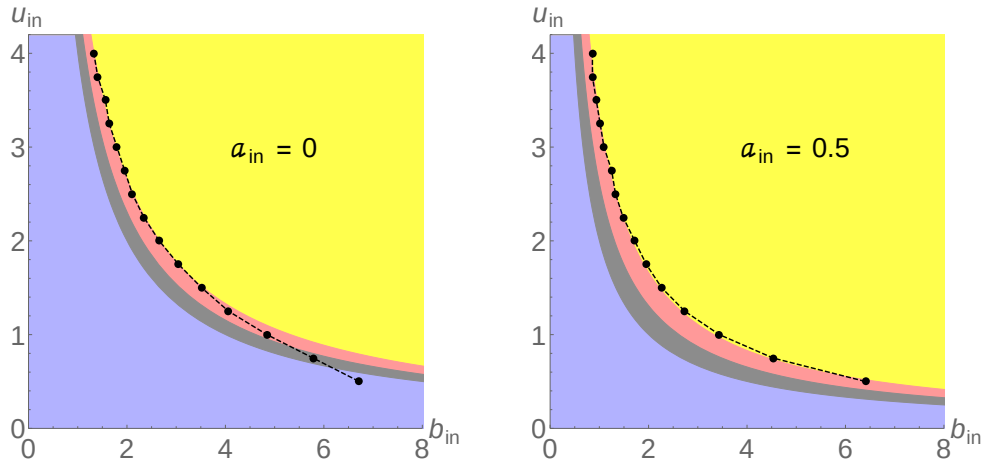
Figure 6.5: Outcome of symmetric collisions of two black holes with initial spin, velocity, and impact parameter $(a_{in}, u_{in}, b_{in})$. The dots (joined by dashed lines) separate between initial conditions that lead to $2 \to 1$ fusion events (below the dots) and $2 \to 1 \to N$ cosmic-censorship-violating fission events (above the dots). The colors distinguish between the stable phases available (same color coding as in fig. 6.3). For small enough $b_{in}$ the system always settles down into the available stable single blob, but for very large $b_{in}$ the dynamical evolution passes too far from the stable phase and proceeds to fission.

In particular, in collisions at large $J$ with large initial orbital angular momentum the evolution can exhibit complicated patterns. Their investigation would take us beyond the scope of this article.

### 6.3.3 $2 \to 1$ vs. $2 \to 1 \to N$

In the next sections we will study collisions between two initial MP black holes, of equal mass and equal initial spins, with initial rotation parameter $a_{in}$ within the stability range of MP black holes $0 \le a_{in} < 1$.[11] Their initial velocities will be $\pm u_{in}$ and the impact parameter $b_{in}$. We select the collisions where there is fusion; the cases where the two black holes scatter without ever merging may also be of interest but their physics is different than we intend to explore here and we will barely discuss them[12].

For some values of the initial parameters $(a_{in}, u_{in}, b_{in})$ the system fissions. Figure 6.5 shows the numerically determined boundary (dots joined by dashed lines) between initial conditions that lead to a $2 \to 1$ collision, leaving a rotating central object, and initial conditions that produce more than one outgoing object, usually two but possibly more.

As already noted in previous papers [14, 15], the boundary follows a curve of constant $J/M = (J/M)_c$, as long as the impact parameter is below some threshold (which depends on $a_{in}$). This means that for these values of $b_{in}$ the merger always settles down into the unique stable solution that is available. However, if $b_{in}$ is large enough, this possible end

---

[11]We do not consider initial black bars and dumbbells. They are expected to exist at finite $D \ge 6$ but not be completely stable, not even stationary, since they must radiate gravitational waves.

[12]Since the effective theory describes a continuous horizon, the distinction is not perfectly clear-cut and involves discretionary choices. However, the more ambiguous cases are only marginal to our analysis.

state is avoided: the two colliding black holes form a horizon that is too elongated to find its path to the stable blob. In these cases, the colliding black holes attract each other deflecting their trajectories,[13] and then they either fly apart or suddenly fall onto each other to form a stable central object. It is suggestive that this $2 \to 2$ scattering might be understood as the formation of an unstable, long dumbbell (two gaussian blobs joined by a long tube), which then either collapses or breaks apart.

### 6.3.4   Kinematics, entropy and geometry of the collisions

Let us now be more specific about the collisions we study. The two initial black holes are MP blobs on a 2-brane like (2.30) that start in the $(x, y)$ plane at

$$(x, y) = \left( \pm \infty, \pm \frac{b_{\mathrm{in}}}{2} \right) , \tag{6.65}$$

with velocities

$$(v_x, v_y) = (\mp u_{\mathrm{in}}, 0) . \tag{6.66}$$

The latter are achieved by applying a Galilean boost to each blob. The entropy of each individual boosted black hole, normalized by its own mass, is

$$\mathcal{S}_1 = -\frac{1}{2} u^2 - \ln(1 + a^2) \tag{6.67}$$

(see eq. (6.88)). The presence of the term $\propto u^2$ is due to the fact, already mentioned, that the kinetic energy must be subtracted from the total energy of the black hole, since only the rest (irreducible) mass contributes to entropy. It is directly related to the fact that the horizon area of a black hole does not change through Lorentz contraction [121], which is also a property of entropy in the effective theory, as proved in section 6.3.5.

The entropy of a system of two equal MP black holes, now normalized by their combined mass $M$, is

$$\mathcal{S}_1 = -\frac{1}{2} u^2 - \ln 2(1 + a^2) . \tag{6.68}$$

and, using (6.60), their total angular momentum is[14]

$$\frac{J}{M} = 2a + \frac{bu}{2} . \tag{6.69}$$

The conservation of mass-energy (which includes kinetic energy to NLO) and angular momentum imposes restrictions on the possible outgoing final states, and on how much entropy can be produced. The analysis can be made entirely within the large $D$ effective theory, but since we are only considering initial and final states that are MP black holes, we could also consider the properties of the known solutions exactly in $D$. That is, we could work at finite $D$ using physical magnitudes, expand in $1/D$ and translate into effective theory magnitudes. The two methods of calculation are easily seen to agree.[15]

---

[13]Despite the absence of stable Keplerian orbits in $D \geq 5$, we find that the two blobs can perform more than one revolution around each other before either flying apart or merging. In this respect, these collisions resemble four-dimensional ones more than one might have expected.

[14]Each black hole has spin $2(M/2)a$ and orbital angular momentum $(M/2)u(b/2)$.

[15]Similar considerations were made in [58].

$2 \to 1$: **fusion.** If the black holes fuse and then relax into a single, stable blob, this final state can be read from fig. 6.3 as the unique stable solution with the value

$$\frac{J}{M} = 2a_{\text{in}} + \frac{b_{\text{in}}u_{\text{in}}}{2} \, . \tag{6.70}$$

If this end state is an MP black hole or a black bar, the final entropy will be

$$\mathcal{S}_1^{(\text{MP})} = -\ln \left( 1 + \frac{1}{4} \left( \frac{J}{M} \right)^2 \right)^2 \, , \tag{6.71}$$

$$\mathcal{S}_1^{(\text{bar})} = -\ln \left( \frac{J}{M} \right) \, . \tag{6.72}$$

The total entropy production in the fusion will be the difference between these and (6.68). We do not have analytical expressions for the entropy of black dumbbells.

$2 \to 1 \to 2$: **fusion $\Rightarrow$ fission.** The final states of the $2 \to 1 \to 2$ collision are always two equal MP black holes[16] with outgoing parameters $0 \leq a_{\text{out}} < 1$ and

$$(x, y) = R(\theta) \left( \pm\infty, \pm\frac{b_{\text{out}}}{2} \right) \, , \tag{6.73}$$

$$(v_x, v_y) = R(\theta)(\pm u_{\text{out}}, 0) \, , \tag{6.74}$$

where $R(\theta)$ is a rotation matrix with angle $\theta$. Conservation of mass and angular momentum implies

$$\frac{J}{M} = 2a_{\text{in}} + \frac{b_{\text{in}}u_{\text{in}}}{2} = 2a_{\text{out}} + \frac{b_{\text{out}}u_{\text{out}}}{2} \, . \tag{6.75}$$

The collision is characterized by seven parameters: $(a, u, b)_{\text{in/out}}$ plus the scattering angle $\theta$. The latter is not affected by conservation laws and it does not enter into entropic arguments, so we will leave it aside in the following discussion.

Of the six parameters $(a, u, b)_{\text{in/out}}$, only five are independent once (6.75) is imposed. We can regard the three initial parameters as given, and then two outgoing parameters, say, $u_{\text{out}}$ and $a_{\text{out}}$, are unconstrained by conservation laws, that is they will be determined by the dynamical evolution of the system.

The difference in the entropy between the initial and final states is

$$\Delta\mathcal{S}_1 = \frac{u_{\text{in}}^2 - u_{\text{out}}^2}{2} + \ln \frac{1 + a_{\text{in}}^2}{1 + a_{\text{out}}^2} \, . \tag{6.76}$$

The entropy of the final state will be larger if the outgoing velocities and spins are as small as possible, since both $a$ and $u$ tend to reduce the entropy of a MP black hole with fixed mass. However, they cannot be made arbitrarily small. The total angular momentum must be conserved, and even though (6.75) seems to allow for two unconstrained outgoing parameters, we cannot expect to have $a_{\text{out}}, u_{\text{out}} \to 0$. For any $J \neq 0$ this would require that the outgoing impact parameter diverges, $b_{\text{out}} \to \infty$, which is unreasonable: if the

---

[16]In principle, these could also be stable bars and dumbbells. However, the spin of the outgoing states that we observe is always below the range of their existence.

two initial black holes do indeed collide and merge, the outgoing impact parameter will be comparable to the size of an intermediate (unstable) state with the same $J$ and $M$. From the distance between the two peaks in the critical dumbbell, fig. 6.2, we can expect that

$$b_{\text{out}} \approx 7 \, , \tag{6.77}$$

and probably a little larger after the fission. This is indeed a good predictor for the actual values we find below. Another well-motivated and better defined geometric estimate is obtained by demanding that $b_{\text{out}}$ is approximately equal to twice the radius of the two outgoing black holes. In the appendix of [17] we find that this gives

$$b_{\text{out}} \approx 2\sqrt{2(1 + a_{\text{out}}^2)\ln \epsilon_b^{-1}} \, . \tag{6.78}$$

It depends on a small number (which can be thought of as the brane-cutoff described in section 5.2.1) that we estimate to be $\epsilon_b \approx 10^{-3}$. If entropy is to be maximized, then $b$ will be close to this upper bound.

Eqs. (6.75) and (6.78) leave one unconstrained degree of freedom: an equation between $u_{\text{out}}$ and $a_{\text{out}}$. The last constraint that fixes them will be discussed in sec. 6.5.

### 6.3.5   Boost invariance of the entropy

The effective theory is invariant under Galilean symmetry. Therefore a Galilean transformation acting on a blob solution $m(t,x)$, $v_i(t,x)$ yields another solution

$$m'(t,x) = m(t, x - X(t)), \qquad v_i'(t,x) = v_i(t, x - X(t)) + u_i \tag{6.79}$$

where $X_i(t) = u_i t + b_i$. The mass and the linear and angular momenta transform as

$$M' = M, \qquad P_i' = P_i + M u_i \qquad J_{ij}' = J_{ij} + (b_i u_j - b_j u_i)M \, . \tag{6.80}$$

The first two are actually the Lorentz transformation (setting for simplicity $u_i = (u, 0, \ldots, 0)$)

$$\begin{pmatrix} M' \\ \frac{1}{\sqrt{D}}P_x' \\ \frac{1}{\sqrt{D}}P_{i\neq x}' \end{pmatrix} = \begin{pmatrix} \cosh\alpha & \sinh\alpha & 0 \\ \sinh\alpha & \cosh\alpha & 0 \\ 0 & 0 & \delta_{ij} \end{pmatrix} \begin{pmatrix} M \\ \frac{1}{\sqrt{D}}P_x \\ \frac{1}{\sqrt{D}}P_{j\neq x} \end{pmatrix}, \tag{6.81}$$

up to leading order in the large-$D$ limit of non-relativistic velocities,

$$\alpha = \text{arctanh}\frac{u}{\sqrt{D}} = \frac{u}{\sqrt{D}} + \mathcal{O}\left(\frac{1}{D^{3/2}}\right). \tag{6.82}$$

Although the masses remain invariant in the LO effective theory, the Lorentz transformation generates terms at NLO

$$\begin{pmatrix} M' \\ \frac{1}{\sqrt{D}}P_x' \\ \frac{1}{\sqrt{D}}P_{i\neq x}' \end{pmatrix} = \begin{pmatrix} 1 + \frac{u^2}{2D} & \frac{u}{\sqrt{D}} & 0 \\ \frac{u}{\sqrt{D}} & 1 + \frac{u^2}{2D} & 0 \\ 0 & 0 & \delta_{ij} \end{pmatrix} \begin{pmatrix} M \\ \frac{1}{\sqrt{D}}P_x \\ \frac{1}{\sqrt{D}}P_{j\neq x} \end{pmatrix}, \tag{6.83}$$

whose effect we must take into account when computing the Lorentz transformation of the entropy.

The NLO entropy (6.10) transforms as

$$
\begin{aligned}
S_1' &= 4\pi \int_{\mathbb{R}^p} d^p x \left( -\frac{1}{2} m' v'^2 - \frac{1}{2m'} (\partial m')^2 + m' \log m' \right) \\
&= 4\pi \int_{\mathbb{R}^p} d^p x \left( -\frac{1}{2} m v^2 - \frac{1}{2m} (\partial m)^2 + m \log m - m v_i u^i - \frac{1}{2} m u^2 \right) \\
&= S_1 - 4\pi \left( u^i P_i + \frac{1}{2} u^2 M \right) ,
\end{aligned}
\tag{6.84}
$$

which implies that the mass-normalized entropy (6.50) transforms as

$$
\mathcal{S}_1' = \mathcal{S}_1 - \frac{1}{2} u^2 - \frac{u^i P_i}{M} .
\tag{6.85}
$$

We see that the NLO entropies are not boost invariant. However, it is straightforward to verify that under (6.83) the total entropy

$$
S = 4\pi M + \frac{1}{D} S_1 = 4\pi M' + \frac{1}{D} S_1' = S'
\tag{6.86}
$$

is invariant. The mass-normalized total entropy (6.51) is not, since the mass (energy) is not boost invariant.

If the 'unprimed' frame is at rest, so that $P_i = 0$ and $M$ is the rest mass, then

$$
M' = \frac{M}{\sqrt{1 - \frac{u^2}{D}}} = M + \frac{1}{D} \frac{M u^2}{2} + \mathcal{O} \left( \frac{1}{D^2} \right)
\tag{6.87}
$$

and

$$
\mathcal{S}_1' = \mathcal{S}_1 - \frac{1}{2} u^2 .
\tag{6.88}
$$

This directly yields (6.67) from (6.61).

## 6.4 Entropy production

With our methods we can easily track the entropy production, in space and in time, during the evolution of three different kinds of phenomena:

- $1 \rightarrow N$: decay and fission of unstable black holes

- $2 \rightarrow 1$: fusion of two black holes

- $2 \rightarrow 1 \rightarrow 2$: fusion of two black holes followed by fission

Understanding entropy production in the first two will give us insight into the third.

We evolve the equations numerically, using two different codes (the same as in [14, 15], now using finite differences instead of FFT differentiation), until the system either settles into a stable single blob, or breaks up into blobs that fly apart. By keeping track of $m(t, \mathbf{x})$ and $v^i(t, \mathbf{x})$ we can then compute all physical magnitudes.

### 6.4.1   $1 \to N$: decay and fission of unstable black strings and black holes

Here we follow the non-linear evolution of the decay of an unstable, fissile blob. We have chosen three important examples which most clearly exhibit the physics relevant for other more complex evolutions, see fig. 6.6: the black string; an ultraspinning MP black hole with $a = 2$ decaying through an intermediate black bar; and an MP black hole with $a = 3$ decaying through an intermediate black ring. The latter evolutions are triggered by choosing different inital perturbations, which excite different unstable modes of the ultraspinning black hole.

Let us emphasize that our simulations of the decay of unstable black strings are not expected to reproduce the details of the late-time evolution in the (much more expensive) numerical evolutions in [51], nor of the related and more complex simulations in [95, 85, 87]. This has been discussed in detail in [11]. In particular, the large $D$ effective theory does not reveal the cascading formation of small 'satellites'. However, our concern here is with how entropy is produced in this decay, and this appears to occur mostly in the intermediate stages of the evolution. At late times, most of the mass and area reside in the large, black-hole-like blobs, and little on the satellites and thin tubes inbetween them. Therefore, we expect that our study accounts for the main contributions to entropy production.

The analysis of black string decay reveals generic aspects of entropy production in fission. The pattern we see in fig. 6.6 (top) will be present in all subsequent fission phenomena: a single peak in the entropy production rate, midway along the fission, with dissipation equally shared into shear and expansion.

The two decays of the ultraspinning MP black hole in fig. 6.6 show qualitative similarities between themselves: first, a long-lived but ultimately unstable configuration forms—a black bar, or a black ring.[17] Entropy is generated mostly through shear dissipation. In fact, it is clear that a dominant shearing motion must be driving the evolution to a bar, while the formation of the ring should also involve some compression. Both features are visible in the entropy production curves. Afterwards, this intermediate state decays following the pattern of black string fission.

The second peak in entropy production appears to have universal features. This confirms that the physics of black string decay also controls the fission of the blob. Observe, however, that in the MP decay the peak is a little higher—hence more irreversible—than in the black string. This could be expected since the latter is a more symmetric configuration.

Finally, we see that the duration of the string break up is on the order of

$$(\Delta t)_{\text{fission}} \approx 20M \,. \tag{6.89}$$

This will be a characteristic of other fissions.

---

[17]When $D$ is not large enough this bar radiates away its excess spin fast enough to return to stability [54].
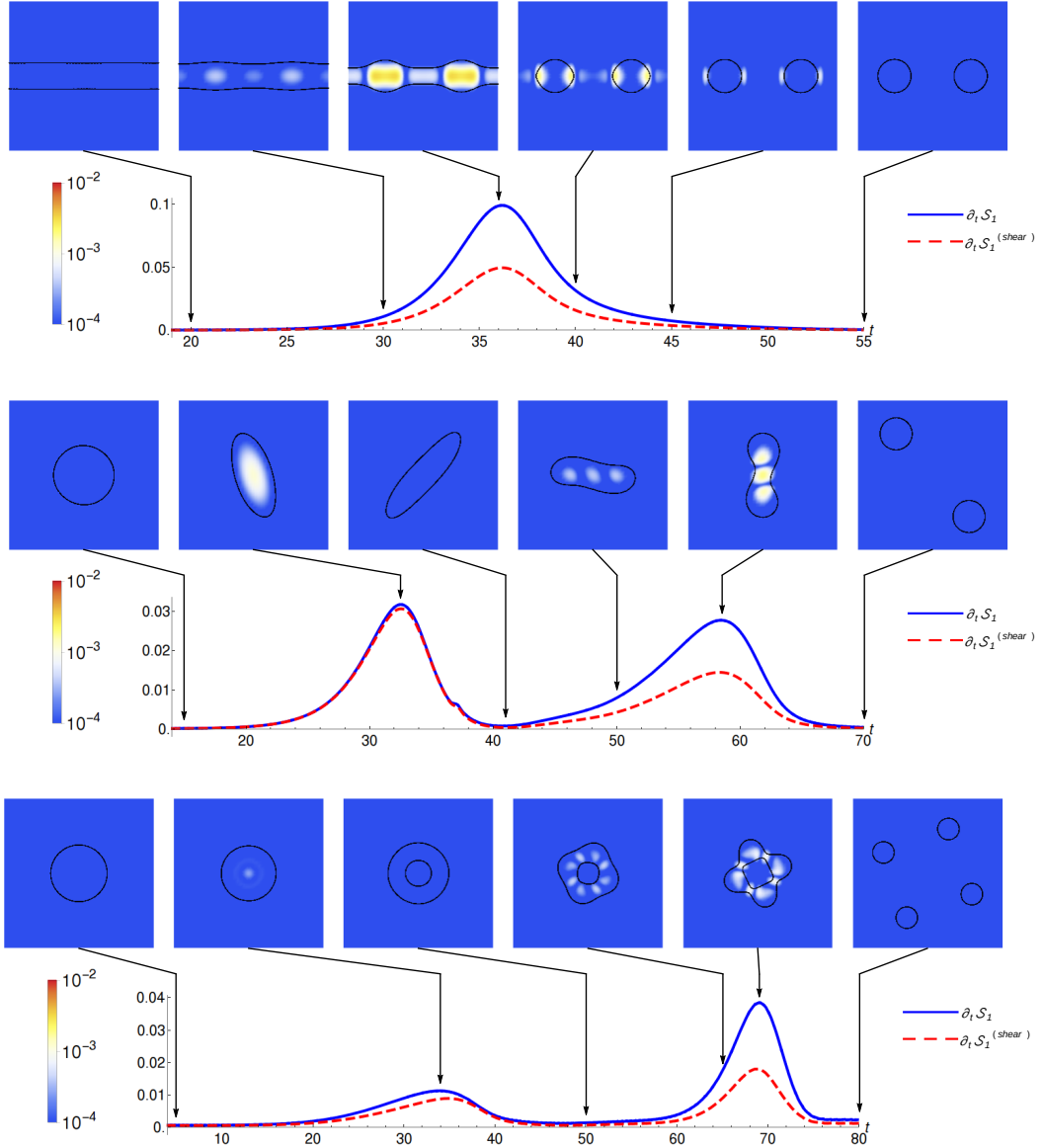
Figure 6.6: Entropy production, as a function of time and space, during the decay of: unstable black string (top); ultraspinning MP black hole through intermediate black bar (middle); ultraspinning MP black hole through intermediate black ring (bottom). The blue curves give the production rate of the NLO entropy, $\partial_t \mathcal{S}_1$ (integrated in space); the dashed red curves are the production rate through dissipation of shear (and not of expansion), $\partial_t \mathcal{S}_1^{(\text{shear})}$. The density plots show the time derivative of the entropy density (colors in log scale). The thin black contours serve to guide the eye to where the black hole blobs are, and correspond to $m(x, y) = 0.001M$. We can see that the pattern of entropy production in the black string decay is reproduced in the second peak of the decays of the MP black hole. The first peak is mostly due to shearing when the intermediate black bar or black ring forms.

## 6.4.2 $2 \to 1$: fusion $\Rightarrow$ thermalization

In a $2 \to 1$ collision the final state is completely determined by the conserved initial value of $J/M$: the system settles into the only stable stationary black hole with that value: an
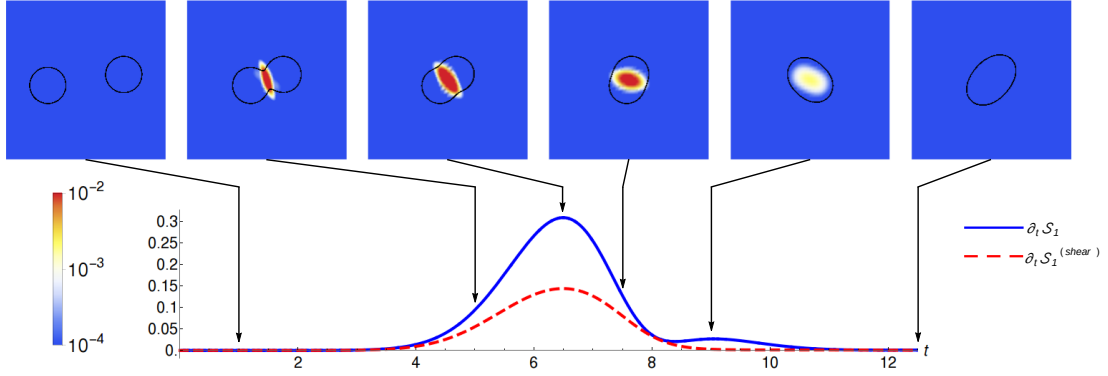
Figure 6.7: Entropy production during a collision with fusion into a stable black bar. The first, large fusion peak is followed by a smaller peak for the thermalization to the black bar. The height of this second peak is comparable to that in fig. 6.6 (middle).

MP black hole, a black bar, or a black dumbbell.

In fig. 6.7 we present an illustrative example: a symmetric collision of two black holes with $(b_{\text{in}}, u_{\text{in}}, a_{\text{in}}) = (2, 1.0, 0.6)$, so $J/M = 2.2$, resulting in the formation of a stable black bar. The figure shows that when the two black holes first meet and fuse there is a large production of entropy. There follows a phase in which the system equilibrates (thermalizes) into the final stable black bar. This second phase is similar to the formation of the (unstable) bar in the decay of the ultraspinning MP black hole in fig. 6.6 (middle), with both peaks having similar height ($\approx 0.03$, in mass-normalized entropy rate). The duration of this phase in the decay of the MP black hole is much longer, since the system there starts in stationary, but unstable, equilibrium, while the merged horizon is farther from equilibrium.

The contributions to dissipation from shear and expansion vary at different stages in the evolution. During the initial fusion phase, one or the other may dominate depending on the initial parameters, but generically we observe both expansion (and compression) and shearing motion of the blob, which contribute roughly equally to entropy production. During the formation of the intermediate quasi-thermalized bar, the proportions of shear and expansion can vary, depending on how much the preceding blob is already bar-like or not. In the simulation shown in fig. 6.7, from $t \approx 9$ to 1 the blob has to undergo less shearing to acquire the bar shape than in fig. 6.6 (middle) from $t \approx 20$ to 40. Presumably this explains the lower presence of shear dissipation.

### 6.4.3   $2 \to 1 \to 2$: fusion $\Rightarrow$ quasi-thermalization $\Rightarrow$ fission

With large enough total angular momentum, the fusion results in a fissile intermediate state.

**Stages in the evolution.**   In fig. 6.8 we present the evolution of entropy production in a collision with initial parameters $(b_{\text{in}}, u_{\text{in}}, a_{\text{in}}) = (3.4, 1.0, 0.8)$, so $J/M = 3.3$. It can be interpreted by combining what we have learned so far:
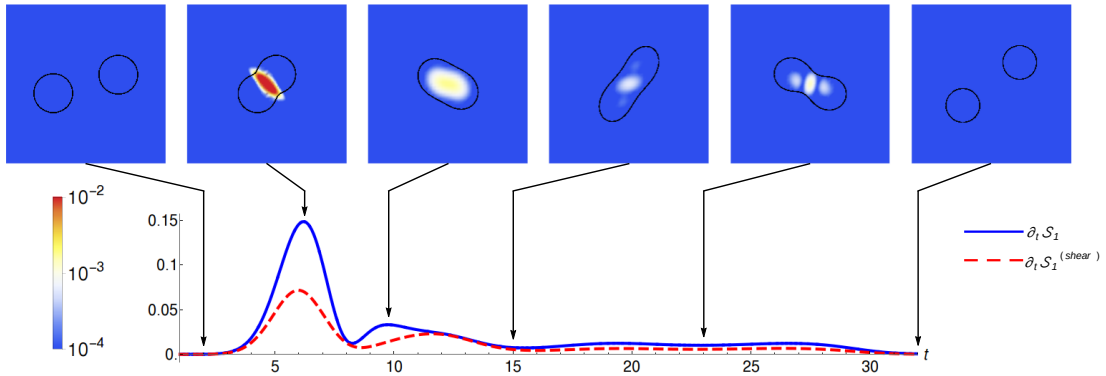
Figure 6.8: Entropy production during a collision with fusion followed by fission. The entire process can be divided in three stages: $t \approx 4$ to $8$, fusion; $t \approx 9$ to $14$, quasi-thermalization into a bar; $t \approx 15$ to $30$, fission of the bar, similar to black string decay.

1. *Fusion:* $t \approx 4$ to $8$. This is a strongly irreversible phase, very similar to the first peak in $2 \to 1$ fusion, fig. 6.7.

2. *Quasi-thermalization:* $t \approx 9$ to $14$. The fused blob follows qualitatively the evolution of unstable MP black holes in fig. 6.6 (middle): a quasi-thermalization phase with the (faster) formation of a long-lived bar.

3. *Fission:* $t \approx 15$ to $30$. The intermediate bar fissions into two outgoing black holes, in a manner similar to fig. 6.6 (middle), ultimately patterned after the decay of black strings, fig. 6.6 (top). It lasts for a time comparable to (6.89).

Observe that not only the qualitative features of the decay of the MP bhs are reproduced in the $2 \to 1 \to 2$ collision: also the height of the peaks in the mass-normalized entropy production rates, after the fusion peak in fig. 6.8, are quantitatively similar.

The proportions of viscous dissipation from shear and expansion also follow what we have seen before.

## 6.5 Scattering of black holes and entropic attractors

We now turn to a more complete investigation of collisions, in particular those that result in fission, and the role that the entropy increase plays in them. For this purpose we have performed an extensive, although not exhaustive, study of symmetric collisions of black holes for wide ranges of the initial parameters $(a_{\text{in}}, u_{\text{in}}, b_{\text{in}})$.

In our simulations we verify that the final blobs can be identified with known stable stationary blobs. In $2 \to 1$ and $2 \to 1 \to 2$ events, the final spin parameter, $a_{\text{out}}$, is extracted from the width of the gaussian blobs by linear regression of $\ln m$ as a function of $r^2$, where $r$ is the distance to the center of the blob (see (2.25)). In fission, we extract the parameters $u_{\text{out}}$ and $b_{\text{out}}$ of the outgoing blobs from the velocity field at their centers,

As we have seen, fusion into a single stable black hole is fully determined by the conservation of mass and angular momentum. In our simulations we have been able to
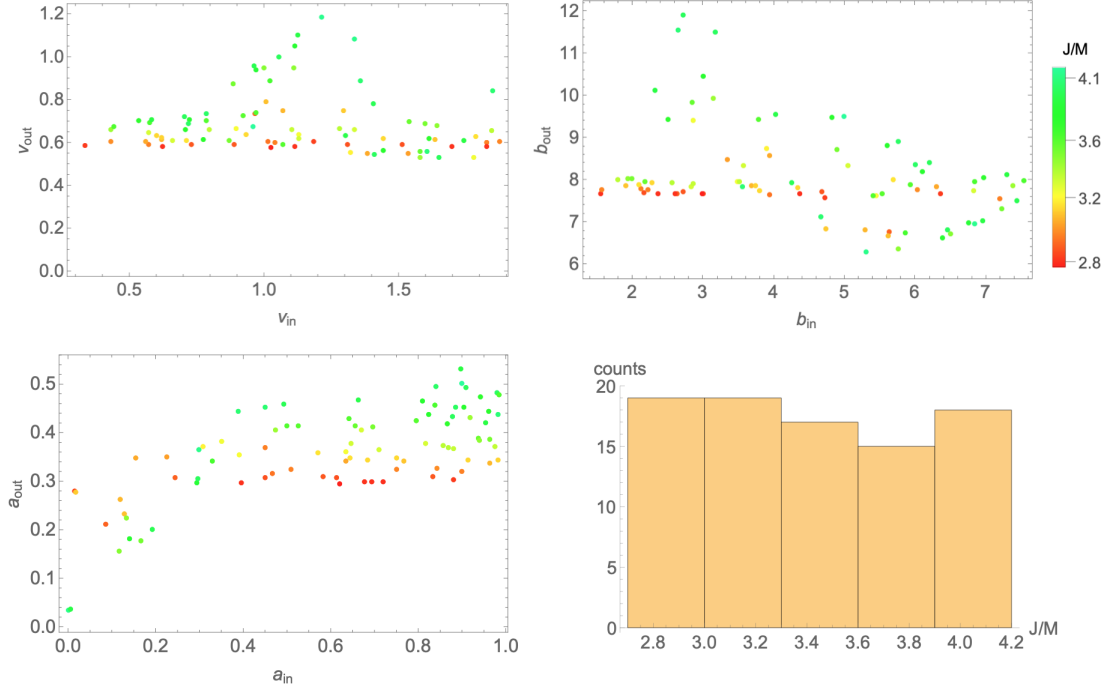
Figure 6.9:  $2 \to 1 \to 2$  collisions: in 100 simulations, the outgoing parameters  $(a_{\text{out}}, u_{\text{out}}, b_{\text{out}})$  show little correlation with initial ingoing parameters  $(a_{\text{in}}, u_{\text{in}}, b_{\text{in}})$ . This is a consequence of quasi-thermalization in an intermediate stage in the collision. Outgoing parameters cluster in a relatively narrow range, the more so the lower the total  $J/M$ , for which the intermediate phase lasts longer.

verify that the integration over space and time of the entropy density reproduces correctly the exact predictions from sec. 6.3.4. This is a good check on the accuracy of our methods.

### 6.5.1    $2 \to 1 \to 2$ : In & Out

In contrast to  $2 \to 1$  fusion, here there is a continuous two-dimensional range of out states that are allowed by the conservation laws. In figs. 6.9 we present the results for the outgoing parameters  $(a_{\text{out}}, u_{\text{out}}, b_{\text{out}})$  of 100 simulations with randomly chosen values of the ingoing parameters  $(a_{\text{in}}, u_{\text{in}}, b_{\text{in}})$ .[18] We also present, as color shading, the value of the the conserved  $J/M$  for each event. Since our sampling is not exhaustive, we have not attempted to perform detailed statistical analyses, but nevertheless there are several discernible patterns in these plots that are worth remarking on.

First, there is a clear clustering of the out parameters. It is stronger the lower  $J/M$  is, with  $(u_{\text{out}}, a_{\text{out}}, b_{\text{out}})$  being essentially unique for the lowest  $J/M$  (slightly above  $(J/M)_c = 2.66$ ). The latter are the cases where an unstable but very long-lived intermediate state

---

[18]We discard events where the intermediate interaction is too weak to involve fusion. We implement this by removing from our analysis events for which the initial impact parameter is large ( $b_{\text{in}} > 7$ ) and the outgoing parameters change less than 5% relative to the initial ones. In these cases the spin  $a$  changes very little, while  $u$  and  $b$  can change more, as expected if the process is one of direct (fusionless)  $2 \to 2$  scattering.

forms in the collision. The dissipation that happens in this intermediate phase effectively erases the memory of the initial state parameters, other than the conserved $J/M$. As $J/M$ grows larger, the intermediate state is less long-lived and less precisely defined, and the system retains more memory of the initial configuration (for instance, there is some correlation between the values of $a_{\text{in}}$ and $a_{\text{out}}$), resulting in more dispersion in the plots.

More generally, the plots show that the out parameters lie approximately in the following ranges:[19]

Spin:

$$a_{\text{out}} \approx 0.3 \,^{+0.2}_{-0.1}, \tag{6.90}$$

with the upper bound being fairly robust.

Velocity:

$$u_{\text{out}} \approx 0.6 \,^{+0.4}_{-0.1}, \tag{6.91}$$

with a strong bias towards the lower value, which is never below $\approx 0.5$.

Impact parameter:

$$b_{\text{out}} \approx 8 \,^{+2}_{-1}. \tag{6.92}$$

The scant correlation of these results with the initial values other than the conserved $J/M$ is indicative of intermediate thermalization.

The clustering values might possibly be compared with those in the decay states of unstable blobs in the yellow regions close to $(J/M)_c$ in fig. 6.3. An indication in this direction is (6.77), but we have not attempted to go further since this requires additional extensive numerical studies.

Regarding the scattering angle in the final states (6.73), (6.74), we have observed that $\theta$ can be robustly obtained from the numerical simulations. In particular, it is independent of the scheme implementing a regulator at small $m$, and of the values of the regulator as this is decreased. We expect, therefore, that in collisions at finite $D$ this scattering angle can also be obtained from the classical evolution before the naked singularity forms. However, this angle does not play any role in our study in this paper.

### 6.5.2 Entropy increase

Recall that the initial and final states are characterized by the values of $(a, u, b)$, one of which can be traded for the value of $J$, which is common for the initial and final states (we always set the total mass $M = 1$). We find convenient to eliminate $b$, so in fig. 6.10, for a given value of $J$, we represent the initial and final states each one as a point (red and green, respectively) in the plane $(u, a)$. On this plane, we also show colour contours for the value of the mass-normalized entropy $\mathcal{S}_1$. We exclude the region of ultraspins $a > 1$ since these MP black holes are unstable.

We already mentioned that the entropy cannot be fully maximized, since this happens at $(u, a, b) = (0, 0, \infty)$. The geometric constraint (6.78) (particularly good for low $J/M$) selects a set of possible final states, which we mark as a purple band in the $(u, a)$ plane.

---

[19]These central values and variances are indicative and should not be taken literally; the dispersion is strongly correlated with $J/M$, and it is very low near the critical value.
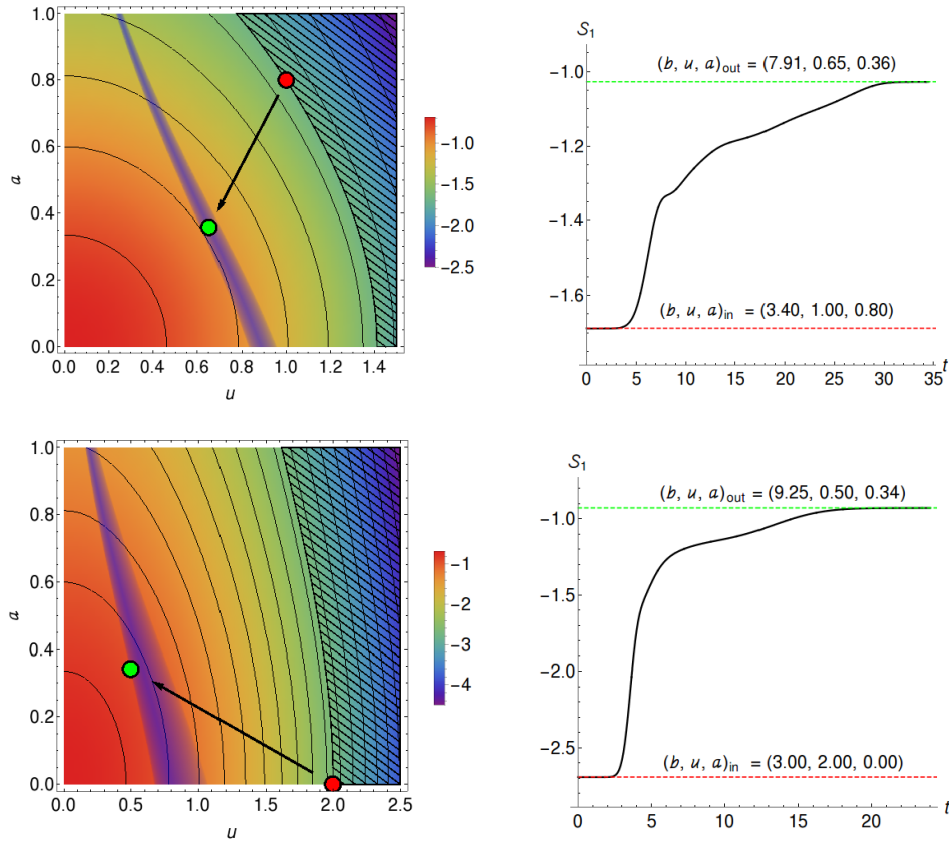
Figure 6.10: Total entropy growth in symmetric $2 \to 1 \to 2$ collisions. *Left*: coloured-contour plot for the total entropy of configurations with velocity and spin $(u, a)$, with a given value of $J/M$. Red and green dots indicate the initial and actual final states in the dynamical evolution. The hashed part marks final states forbidden by the second law. The purple band are states with impact parameter in the geometric range (6.78). We see that the actual final states lie very close to (although not exactly at) the maximum entropy with $b$ in this range. In particular, larger values of $a_{\text{out}}$ and smaller of $u_{\text{out}}$ would be entropically very disfavoured. *Right*: evolution in time of $\mathcal{S}_1$ along the simulation. The initial and final parameters are (top) $(b, u, a)_{\text{in}} = (3.4, 1.0, 0.8)$, $(b, u, a)_{\text{out}} = (7.9, 0.65, 0.36)$ and (bottom) $(b, u, a)_{\text{in}} = (3.0, 2.0, 0.0)$, $(b, u, a)_{\text{out}} = (9.25, 0.5, 0.34)$.

In fig. 6.10 the entropy changes between initial and final states are shown in two illustrative cases.[20]

The salient aspects of these plots are:

- Final states in the hashed region are excluded by the second law. High final velocities are then excluded. In particular, if the initial black holes are spinless, then the outgoing velocity cannot be higher than the ingoing one.

- The entropy increases significantly, an in particular it is close to being maximized (but not fully maximized) among the possible outgoing states with geometrically-

---

[20]The top right curve for $\mathcal{S}_1(t)$ is the integral of the blue curve in fig. 6.8.
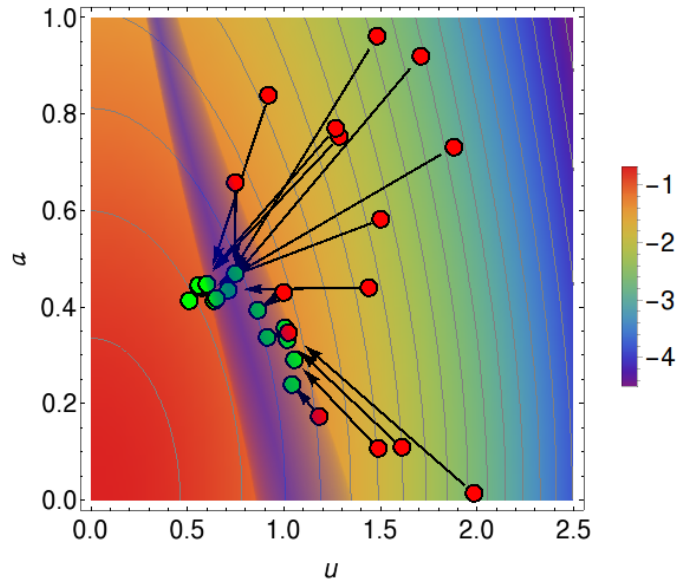
Figure 6.11: Entropic attractor in collisions $2 \to 1 \to 2$ with $J/M = 3.8$. See fig. 6.1 for the explanation. The attractor is less strong as $J/M$ grows larger. Note that initial states to the left of the purple band have large initial impact parameters and the black holes do not merge, so we do not include them.

constrained impact parameter (6.78).[21]

In fig. 6.10 (right) we show the time evolution of the entropy. In the first one (top) the total entropy change is approximately equally subdivided between the sharp production at the beginning of the collision and the slower subsequent production rate. In the second one (bottom), which starts with very high initial velocity, most of the entropy is quickly produced in the initial stages.

### 6.5.3   Entropic attractors

We can now combine the analyses of sec. 6.5.1 and sec. 6.5.2 to obtain a global perspective on the role of total entropy production in the evolution of the system.

In figs. 6.1 and 6.11 we show the results of sampling a large number of collisions $2 \to 1 \to 2$ with two specific values of $J/M$: a low value close to $(J/M)_c$ in fig. 6.1, and a quite higher one in fig. 6.11. The clustering of the final states seen in sec. 6.5.1 is even more clearly visible here, and also the near-maximization of the entropy that we discovered in sec. 6.5.2. The attractor that funnels the evolution is stronger the closer to the critical value of the conserved $J/M$, but fig. 6.11 shows that it, and the near-maximization of the entropy, are present even when $J/M$ is quite far from criticality.

We conclude that the dynamical outcome of the collision can be approximately predicted, after imposing kinematic and geometric constraints, by near-maximization of en-

---

[21]All purple bands are centered at $\epsilon_b = 0.001$, which we take as the fraction to which the mass has to have fallen off to be considered the 'end' of the blob. The bands in figs. 6.1 and 6.10 (up) span the range $\ln(\epsilon_b) = \ln(0.001) \pm 0.5$. In figs. 6.10 (down) and 6.11 the range is wider, $\ln(\epsilon_b) = \ln(0.001) \pm 1.5$.

tropy generation. The maximization is not exact, but this principle is a powerful guide to the end result of a complex dynamical process.

## 6.6   Charge diffusion in black holes

Since the entropy of neutral black holes is proportional to their mass in the limit $D \to \infty$, it can only be generated at NLO in the $1/D$ expansion—although, as we have argued, this production can be computed using the LO effective theory. However, when charge is present, the entropy of a black hole when $D \to \infty$ is no longer proportional to the mass. Instead of (6.2), we have

$$
S(M,Q) \propto \left( M + M\sqrt{1 - 2\left(\frac{Q}{M}\right)^2} \right)^{\frac{D-2}{D-3}}
$$
$$
= M + M\sqrt{1 - 2\left(\frac{Q}{M}\right)^2} + \mathcal{O}\left(\frac{1}{D}\right) . \tag{6.93}
$$

This is easily seen to imply that in the fusion between two black holes with different charge-to-mass ratios, $Q_1/M_1 \neq Q_2/M_2$ (including the charge sign), the charge redistribution that occurs gives rise to entropy production, even when $D \to \infty$. The mechanism that drives it is not viscous dissipation, but Joule heating through charge diffusion.

This gives us the opportunity to explore a different mechanism for entropy production, and also provides a simpler set up where we can confirm the general picture that we have developed in the previous sections. It will be easy, and interesting, to consider asymmetric collisions, where the two initial black holes have different parameters, in particular different charge-to-mass ratios.

### 6.6.1   Entropy generation in charged fusion and fission

Our discussion will be succint, and for more details we refer to [31] and [13]. The effective theory for a charged black brane has as its variables, besides the mass density and the velocity, the charge density $q(t, \mathbf{x})$. In terms of these, the entropy density is

$$
s = 2\pi \left( m + \sqrt{m^2 - 2q^2} \right) . \tag{6.94}
$$

The chemical potential, conjugate to the charge, and the temperature are

$$
\mu = \frac{2q}{m + \sqrt{m^2 - 2q^2}} , \qquad T = \frac{1}{2\pi} \frac{\sqrt{m^2 - 2q^2}}{m + \sqrt{m^2 - 2q^2}} . \tag{6.95}
$$

The effective equations then imply that

$$
\partial_t s + \partial_i j_s^i = \kappa_q \partial_i \left(\frac{\mu}{T}\right) \partial^i \left(\frac{\mu}{T}\right) , \tag{6.96}
$$

where the expressions for the entropy current $j_s^i$ and the charge diffusion coefficient $\kappa_q$ can be found in [31]. The term on the right generates entropy when there is a gradient of

$$
\frac{\mu}{T} = 4\pi \frac{q/m}{\sqrt{1 - 2(q/m)^2}} , \tag{6.97}
$$

that is, when $q/m$ is not homogeneous so there can be charge diffusion. Observe that, unlike in the neutral case, the temperature need not be uniform: it is smaller where $|q/m|$ is larger.

The effective equations admit exact solutions for charged blobs that are easy extensions of the neutral ones, in particular charged rotating black holes and black bars [13]. The former are the large $D$ limit of the Kerr-Newman (KN) black hole.

The entropy of a KN black hole or black bar at large $D$ is (cf. (6.93))

$$S = 2\pi M \left(1 + \sqrt{1 - 2\mathfrak{q}^2}\right),$$

(6.98)

where we introduce the charge-to-mass ratio of the black hole,

$$\mathfrak{q} = \frac{Q}{M}.$$

(6.99)

Observe that, in this limit of $D \to \infty$, the entropy is independent of the spin. The KN black hole and the charged black bar differ in how the spin is related to the mass and charge, but are entropically equivalent.

Consider now a configuration of two KN black holes, labelled 1 and 2, with masses $M_{1,2}$ and charges $Q_{1,2}$. We want to study the total entropy of the system for fixed total mass $M = M_1 + M_2 = 1$ and fixed total charge $Q = Q_1 + Q_2$. For the two remaining free parameters in the system, we use $\Delta M$ and $\Delta \mathfrak{q}$, such that

$$M_{1,2} = \frac{1}{2} \pm \Delta M,$$

(6.100)

$$\mathfrak{q}_{1,2} = Q - \left(\Delta M \mp \frac{1}{2}\right)\Delta\mathfrak{q},$$

(6.101)

i.e.,

$$\mathfrak{q}_1 - \mathfrak{q}_2 = \Delta\mathfrak{q}$$

(6.102)

where

$$\mathfrak{q}_{1,2} = \frac{Q_{1,2}}{M_{1,2}}.$$

(6.103)

The entropy of the two-black hole system is

$$\frac{S_{(2)}}{2\pi} = \left(\frac{1}{2} + \Delta M\right)\left(1 + \sqrt{1 - 2\mathfrak{q}_1^2}\right) + \left(\frac{1}{2} - \Delta M\right)\left(1 + \sqrt{1 - 2\mathfrak{q}_2^2}\right).$$

(6.104)

We now ask what values of $\Delta M$ and $\Delta\mathfrak{q}$ maximize this entropy for fixed total $Q$ and total $M = 1$. The answer is that the maximum is reached for

$$\Delta\mathfrak{q} = 0$$

(6.105)

for any value of $\Delta M$, and this maximum is equal to

$$\frac{S_{(0)}}{2\pi} = 1 + \sqrt{1 - 2Q^2},$$

(6.106)

which is the entropy of a single black hole or black bar with mass $M = 1$ and charge $Q$ (so $\mathfrak{q} = Q$). That is, a system of two black holes, with possibly different masses and charges

but both of them having the same charge-to-mass ratio $\mathfrak{q}$, has the same entropy as a single black hole or black bar with that same value of $\mathfrak{q}$; and a system of two black holes with different charge-to-mass ratios has lower entropy than a single black hole or black bar of the same total mass and charge.

The consequences of this for processes of black hole fusion and fission are then clear:

- Fission processes where an unstable black hole or black bar decays into two black holes are isentropic (adiabatic), and the final black holes will have the same charge-to-mass ratios $\mathfrak{q}$ as the initial one.

- When two black holes with the same values of $\mathfrak{q}$ (but possibly different masses and charges) collide and merge, the subsequent process will necessarily be isentropic, regardless of whether a long-lived intermediate state forms or not, and (if there is fission) regardless of what the final outgoing black holes are.

- When two black holes with different values of $\mathfrak{q}$ collide and merge, entropy is produced. If a stable black hole forms, then it will definitely have more entropy than the initial states. The entropy production will be given by $S_{(0)} - S_{(2)}$ above.

- If the final state consists of two outgoing black holes, then more entropy will be produced the closer the intermediate state is to a single stationary black hole or black bar (*i.e.,* the longer-lived the intermediate state is, so there is time to diffuse charge uniformly to maximize the entropy). In that case, entropy will reach a value close to saturation during the intermediate phase, with little entropy production in the subsequent fission stage.

- If there is no long-lived, almost stationary intermediate state, then entropy production will be less than maximal, but we still expect that it will happen mostly during the fusion process (where the charge-to-mass-ratios are more different) and less so in the fission.

These features (to LO at large $D$) are similar to what we have found in the neutral case (at NLO), but with stronger suppression of entropy generation in fission compared to fusion. It is easy to run numerical simulations of collisions that confirm this picture, but since conservation laws constrain much more the phenomena, they are less illustrative than in the neutral case. Therefore we only show one example of the fusion of two oppositely charged black holes, fig. 6.12. It is qualitatively similar to fig. 6.8, even in its duration.

## 6.7   Final comments

Our study has produced a consistent picture of the phenomena of fusion and fission of black holes, including the entropy generation mechanisms at different stages. One of the main results has been to highlight the attractor role that the intermediate, long-lived, quasi-thermalized black bar phase plays in a $2 \to 1 \to 2$ collision with fission, and how it is connected to a principle of total entropy maximization.
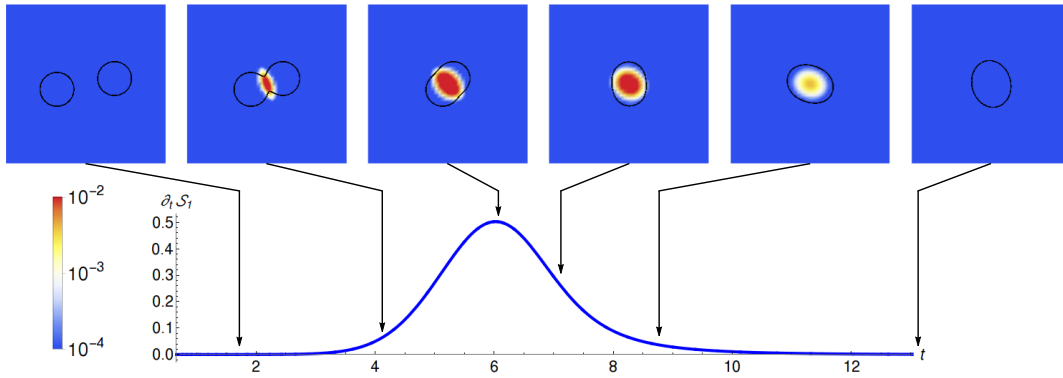
Figure 6.12: Entropy production during a charged collision with fusion into a stable black bar. At LO in the effective theory, entropy is generated through charge diffusion only. The initial parameters are $q_1 = -q_2 = -0.6$, $a_1 = a_2 = 0.4$, $u_1 = -u_2 = 1$, $b = 2$, with total mass $M = 1$.

It is surprising that entropy maximization is somehow driving the dynamics. The system obeys time-irreversible equations that imply that, if at some moment in the evolution entropy is generated, then there is no coming back. But, in principle, the dynamics does not force the system, at least not in any manifest way, to evolve in a direction where entropy grows—it only forbids it to decrease—and even less so that entropy should grow as much as possible compatibly with conservation laws. The surprise that we find is that the evolution does lead to an end state very close to maximum entropy among a continuum of kinematically and geometrically allowed states. In statistical and quantum mechanics systems evolve stochastically sampling nearby configurations—and then, final thermodynamic equilibrium is achieved when entropy reaches a maximum. Here, however, we have a completely deterministic classical system whose equations seem to drive it in a direction that almost maximizes the rather non-obvious quantity $S_1$. The time scale involved is much shorter than, say, the scrambling time for a black hole (which, in the strict classical limit, is an infinite time). And moreover, for all we can see, entropy is in general almost, but not quite, maximized among possible final states. Indeed, by adjusting the initial conditions (e.g., to make a black string break up into multiple static black holes, or colliding black holes with very large $J/M$) the difference to the maximum can be made larger. Maximal entropy provides only an approximate criterion, but a remarkably accurate and powerful one.

In addition, we have also produced a detailed temporal and spatial tomography of entropy generation. Fusion, as might be expected, is highly irreversible. The production of entropy during fusion is relatively featureless, characterized by an initial peak in the production rate, where both shear and bulk viscosity contribute. If the system then settles down to a (long-lived) bar, a second stage with smaller entropy production can appear. Fission of unstable configurations follows the pattern of the decay of unstable black strings, with a duration of the order of (6.89), and approximately equal amounts of dissipation of shear and expansion.

Our results are expected to be most applicable for black hole evolution in $D \geq 6$, but we

would like to elaborate more on their possible qualitative relevance in four dimensions. The most important differences between $D = 4$ and $D \geq 6$ refer to the dynamics of rotation[22]: (i) quasi-stable Keplerian orbits (in General Relativity they are not fully stable due to gravitational wave emission), which are important in the evolution towards a merger, are possible in $D = 4$ but not in $D \geq 6$; (ii) the properties of rotating black holes differ markedly in the two cases: in $D = 4$ their spin is bounded above, while in $D \geq 6$ it is unbounded. Moreover, in $D = 4$ the Kerr black hole (and not, *e.g.,* a black bar) will always be the endpoint of fusion, without any instability that would lead to its fission. If the total angular momentum in the system is above the Kerr bound for the final black hole, then the excess will be shed off into radiation, possibly involving an 'orbital hang up' stage that delays the merger [122, 123]. In $D \geq 6$ instead, the upper bound on the angular momentum is not absolute but dynamical and set by an instability, so the excess angular momentum does not result in hang up but triggers fission.

We do not expect our studies of fission, nor of the relaxation to a stable black bar, to have application to collisions between Kerr black holes. But when studying fusion into a stable rotating MP black hole, the differences we have mentioned are less important than they may appear. The reason is that in $D = 4$ the final plunge before two black holes merge occurs when their orbit becomes unstable. And when the spin of MP black holes is below the ultraspinning bound, their properties are similar to the Kerr black hole. It is interesting that in our simulations of collisions with relatively large impact parameters, we have observed that, prior to coalescence, the black hole trajectories are deflected into what looks like an approximately circular orbit (unstable dumbbells appear to describe such configurations), until the two black holes finally plunge towards each other. Qualitatively at least, this resembles the four-dimensional evolution.

So, as long as the angular momenta involved are moderate, the dynamics of black hole collisions and mergers in $D \geq 6$ are qualitatively similar to $D = 4$, and our study of how entropy is produced (with the caveats that concern gravitational wave emission) should provide at least a guide to what to expect in that case.

---

[22]The case $D = 5$ is in some respects closer to $D = 4$ and in others to $D \geq 6$. We will not refer to its peculiarities here.

# Chapter 7

# Summary

The large $D$ expansion of general relativity in recent years has proven to be a very useful tool for understanding the dynamics of higher dimensional black holes. The limit of a large number of dimensions effectively localizes the dynamics of higher dimensional black objects on a thin membrane situated at the black hole horizon. The dynamics of black objects then can be rephrased as a set of conservation equations of stress-energy (and potentially further charges the black hole carries). In the dynamical regime, *i.e.,* for solutions with time dependence the equations take the form of hydrodynamic type equations, resembling the other effective theories for black holes, like the fluid gravity correspondence or the blackfold approach. The large $D$ effective theory however also contains relevant differences to theses other effective theories. Maybe most importantly the theory simplifies in the static/ stationary limit to the so-called soap bubble equation which states that the mean curvature (times a red-shift factor) has to be a constant along the horizon. In this sense the large $D$ limit also captures an elastic behavior of black holes and allows for non-uniform equilibrium solutions that usually cannot be described in the fluid-gravity picture.

In this thesis we have presented a new aspect pertaining to the effective field theory of large $D$ general relativity. We have demonstrated that the theory initially developed to capture the physics of asymptotically flat branes also contains a new family of localized solutions that can be identified with higher dimensional black holes such as the Schwarzschild-Thangerlini or the Myers-Perry black holes in the limit of a large number of spacetime dimensions. Using this technique we have explored several new aspects of these black hole solutions. In this final chapter we are going to provide a short summary of all the results contained in this thesis.

**Black holes and black bars as blobs on a membrane**  We show that the effective large $D$ equations for the asymptotically flat brane also contain an analytic solution that is a gaussian blob (with the same topology as the flat membrane), and it very closely resembles the very non-uniform black strings that can appear as end states of the Greggory Laflamme instability in higher dimensions. These blobs can be given a Galilean boost, so that they travel along the membrane, additionally these solutions can be spun up such that they correspond to rotating black hole solutions. We demonstrate that these blobs capture

the main properties of Schwarzschild and Myers-Perry black holes at large $D$. It can be shown that the blob actually corresponds to a magnification of the geometry near the cap (north-pole) of the black hole. We calculate their (slow) quasi-normal spectrum, which captures the stability of Schwarzschild black holes and also the instability of ultraspinning Myers-Perry black holes.

Additionally we find novel class of rotating black bar solutions, that appear as stationary objects in the effective theory since they can not radiate gravitational waves. This is because from the perspective of the effective theory emission of gravitational waves is a non-perturbative effect in $1/D$. At finite $D$ this solution can still be a long-lived object due to the suppression of gravitational wave emission in a large number of spacetime dimensions. The slower the rotation $\Omega$ of the bar the more elongated its horizon becomes, s.t. in the limit of $\Omega \to 0$ they connect to the static string. This suggests that these solutions are subject to Gregory-Laflamme type instabilities in which the bar develops inhomogeneities along its elongated direction. And indeed we can describe zero mode deformations of the black bar that signal the onset of such an instability.

**Charged rotating black holes**   We describe a method that allows to construct (Maxwell) charged solutions form every non-charged solution that the large $D$ theory contains. Using this method we construct charged and rotating black holes in the Einstein-Maxwell theory. It can be seen that rotating black holes that carry charge typically are less stable than uncharged solutions which can be attributed to charge repulsion of the charge on the horizon. This effect can expand the ultraspinning regime of black holes to the very low angular momentum as long as the charge of the black hole is large enough.

**Black ripples and black flowers**   We explore the solutions that branch of from the (ultra-spinning) Myers-Perry (MP) black hole and the non-linear extensions of the zero-modes of the analytically known black bar. We do so by going to higher order in perturbation theory and by constructing the solutions numerically. The axisymmetric solutions branching off from the MP-branch correspond to 'bumpy' black holes that connect the MP-branch to multiple (concentric) black rings and black Saturns. These solutions strongly resemble ripples on a fluid surface and for low rotation become nearly gaussian lumps. The non-axisymmetric solutions branching off the MP-branch are similar to the black bar and only stationary in the limit of $D \to \infty$.

Further we also construct the non-linear extensions to the zero modes of the bar that give rise to dumbbell and spindle like solutions.

**Black hole collisions and instabilities**   We study the evolution of higher dimensional black hole collisions by solving numerically the effective equations of motion. We demonstrate that in these collisions it is possible to form black holes with elongated horizons such as black bars and dumbbells. At high enough angular momentum the black bars and dumbbells can be so elongated that they are susceptible to a Greggory-Laflamme type instability, that leads to the a pinch off of the horizon towards a naked singularity.

Accordingly this demonstrates a novel example of a violation of weak cosmic censorship in the quintessential process of general relativity: the collision of black holes.

Furthermore we study the evolution and decay of ultraspinning MP black holes, and observe remarkably rich structure in the intermediate states of the decay.

**Entropy production in fission and fusion**  We study how entropy production and irreversibility appear in the large $D$ effective theory. With this tool we study how black hole entropy is generated in several highly dynamical processes, such as the fusion of black holes and the fission of unstable solutions into multiple black holes. We find the black hole fusion is highly irreversible, while fission which follows the decay of unstable black strings generates much less entropy. Additionally we describe how in processes that contain fusion and fission the intermediate state is quasi-thermalized. This intermediate state erases much of the memory of the initial state and acts as an attractor that leads to a small subset of the possible parameters in the outgoing parameter space. We show that in most processes entropy tends to be maximized and how it can be taken as a guide for predicting the final states.

# Chapter 8

# Resumen en Castellano

En los últimos años la expansión de la teoría de relatividad general en el límite de un gran número $D$ de dimensiones ha demostrado ser una herramienta muy útil para comprender la dinámica de los agujeros negros de dimensiones superiores. El límite de un gran número de dimensiones localiza de forma efective la dinámica de los objetos negros en una fina membrana situada en el horizonte del agujero negro. La dinámica de los objetos negros puede entonces reformularse como un conjunto de ecuaciones de conservación de la energía y del momento (y potencialmente otras cargas que el agujero negro lleve). En el régimen dinámico, las ecuaciones toman la forma de ecuaciones de tipo hidrodinámico, parecidas a otras teorías efectivas para los agujeros negros, como la correspondencia de 'fluid-gravity' o el enfoque de los 'blackfolds'. Sin embargo, la teoría efectiva del límite de gran $D$ también contiene diferencias relevantes respecto a estas otras teorías efectivas. Tal vez lo más importante es que la teoría se simplifica en el límite estático/estacionario a una ecuación llamada 'soap bubble equation' (refiriéndose a las pompas de jabón) que establece que la curvatura media (multiplicadaz por un factor de corrimiento al rojo) tiene que ser una constante en todo el horizonte. En este sentido, el límite de gran $D$ también captura un comportamiento elástico de los agujeros negros y permite soluciones de equilibrio no uniformes que normalmente no pueden ser descritas en la correspondencia de 'fluid-gravity'.

En esta tesis hemos presentado un nuevo aspecto perteneciente a la teoría efectiva de la relatividad general en el límite de un gran número de dimensiones. Hemos demostrado que la teoría desarrollada inicialmente para capturar la física de las branas asintóticamente planas también contiene una nueva familia de soluciones localizadas que pueden ser identificadas con agujeros negros de dimensiones más altas como los agujeros negros de Schwarzschild-Thangerlini o de Myers-Perry en el límite de $D \to \infty$. Usando esta técnica hemos explorado varios aspectos nuevos de dichos agujeros negros. En este capítulo final vamos a proporcionar un breve resumen de todos los resultados contenidos en esta tesis.

**Los agujeros negros y las barras negras como un blob en una membrana**
Mostramos que las ecuaciones efectivas del limíte de gran $D$ para las branas asintóticamente

planas también contienen una solución analítica que es un blob gaussiano (con la misma
topología que la membrana plana), y se asemeja mucho a las cuerdas negras muy no uni-
formes que pueden aparecer como estados finales de la inestabilidad de Gregory Laflamme
en dimensiones más altas. Estos blobs pueden viajar a lo largo de la membrana, y se
les puede dar rotación de tal manera que correspondan a soluciones de agujeros negros
giratorios. Demostramos que estos blobs capturan las principales propiedades de los agu-
jeros negros de Schwarzschild y Myers-Perry en el limíte de dimensiones muy altas. Se
puede demostrar que dichos blobs corresponden a una ampliación de la geometría cerca
del polo norte del agujero negro. Calculamos su espectro cuasinormal lento, que capta
la estabilidad de los agujeros negros de Schwarzschild y también la inestabilidad de los
agujeros negros de Myers-Perry.

Además encontramos una nueva clase de soluciones de barras negras giratorias, que
aparecen como objetos estacionarios en la teoría efectiva ya que no pueden radiar ondas
gravitacionales. Esto se debe a que desde la perspectiva de la teoría efectiva la emisión
de ondas gravitacionales es un efecto no perturbativo en $1/D$. En el caso de $D$ finito esta
solución puede ser todavía un objeto de larga vida debido a la supresión de la emisión de
ondas gravitatorias en un gran número de dimensiones del espacio tiempo. Cuanto más
lenta es la rotación $\Omega$ de la barra más alargado se vuelve su horizonte, de tal manera que
en el límite de $\Omega \to 0$ se transforman en la cuerda estática. Esto sugiere que estos agujeros
negros están sujetos a inestabilidades de tipo Gregory-Laflamme en las que la barra desar-
rolla inhomogeneidades a lo largo de su dirección alargada. Y de hecho podemos describir
deformaciones de modo cero de la barra negra que señalan el inicio de tal inestabilidad.

**Los agujeros negros giratorios cargados**   Describimos un método que permite con-
struir soluciones cargadas a partir de cada solución no cargada. Usando este método
construimos agujeros negros cargados y giratorios en la teoría de Einstein-Maxwell. Se
puede ver que los agujeros negros giratorios que llevan carga son típicamente menos esta-
bles que las soluciones no cargadas, lo que puede atribuirse a la repulsión de la carga en
el horizonte. Este efecto puede extender el régimen de ultraspinning hasta un momento
angular muy bajo, siempre que la carga del agujero negro sea lo suficientemente grande.

**Agujeros negros ondulados y flores negras**   Exploramos las soluciones que se derivan
del agujero negro de Myers-Perry (MP) y las extensiones no lineales de los modos cero de
la barra negra. Lo hacemos yendo a un orden más alto en la teoría de perturbaciones y
construyendo las soluciones numéricamente. Las soluciones axisimétricas que se ramifican
de la rama MP corresponden a agujeros negros 'bumpy' (abultados) que conectan la rama
MP con múltiples anillos negros (concéntricos) y Saturnos negros. Estas soluciones se
asemejan fuertemente a las ondulaciones de una superficie fluida y para una baja rotación
se convierten casi en blobs gaussianos. Las soluciones no axisimétricas que se ramifican
de la rama MP son similares a la barra negra y sólo estacionarias en el límite de $D \to \infty$.

Además, también construimos las extensiones no lineales de los modos cero de la barra
que dan lugar a agujeros negros de formas perecidas a mancuernas o husos.

**Colisiones de agujeros negros e inestabilidades** Estudiamos la evolución de las colisiones de agujeros negros en dimensiones superiores usando las ecuaciones efectivas. Demostramos que en estas colisiones es posible formar agujeros negros con horizontes alargados como barras negras o con forma de mancuernas. Con un momento angular lo suficientemente alto, las barras negras pueden ser tan alargadas que son susceptibles a una inestabilidad tipo Greggory-Laflamme, que lleva a una rotura del horizonte y a una singularidad desnuda. Por consiguiente, esto demuestra un ejemplo novedoso de una violación de la hipótesis de 'cosmic censorship' (censura cósmica).

Además estudiamos la evolución y el decaimiento de los agujeros negros MP ultra-spinning, y observamos una estructura notablemente rica en los estados intermedios del decaimiento.

**Producción de entropía en fisión y fusión** Estudiamos cómo la producción de entropía y la irreversibilidad aparecen en la teoría de la gran $D$. Con esta herramienta estudiamos cómo se genera la entropía de los agujeros negros en varios procesos altamente dinámicos, como la fusión de los agujeros negros y la fisión de soluciones inestables en múltiples agujeros negros. Encontramos que la fusión de los agujeros negros es altamente irreversible, mientras que la fisión que sigue al decaimiento de las cuerdas negras inestables genera mucha menos entropía. Además, describimos cómo en los procesos que contienen fusión y fisión el estado intermedio está casi termalizado. Este estado intermedio borra gran parte de la memoria del estado inicial y actúa como un atractor que conduce los posibles parámetros a un pequeño subconjunto de parámetros de salida. Mostramos que en la mayoría de los procesos la entropía tiende a maximizarse y cómo puede tomarse como guía para predecir los estados finales.

# Bibliography

[1] A. M. Ghez, S. Salim, N. Weinberg, J. Lu, T. Do, J. Dunn et al., *Measuring distance and properties of the milky way's central supermassive black hole with stellar orbits*, *The Astrophysical Journal* **689** (2008) 1044.

[2] A. Eckart, R. Genzel, T. Ott and R. Schödel, *Stellar orbits near sagittarius a*, *Monthly Notices of the Royal Astronomical Society* **331** (2002) 917.

[3] E. H. T. Collaboration et al., *First m87 event horizon telescope results. i. the shadow of the supermassive black hole*, *arXiv preprint arXiv:1906.11238* (2019) .

[4] LIGO SCIENTIFIC, VIRGO collaboration, *Observation of Gravitational Waves from a Binary Black Hole Merger*, *Phys. Rev. Lett.* **116** (2016) 061102 [1602.03837].

[5] R. A. Hulse and J. H. Taylor, *Discovery of a pulsar in a binary system*, *The Astrophysical Journal* **195** (1975) L51.

[6] D. Walsh, R. F. Carswell and R. J. Weymann, *0957+ 561 a, b: twin quasistellar objects or gravitational lens?*, *Nature* **279** (1979) 381.

[7] F. W. Dyson, A. S. Eddington and C. Davidson, *Ix. a determination of the deflection of light by the sun's gravitational field, from observations made at the total eclipse of may 29, 1919*, *Philosophical Transactions of the Royal Society of London. Series A, Containing Papers of a Mathematical or Physical Character* **220** (1920) 291.

[8] R. V. Pound and J. Snider, *Effect of gravity on nuclear resonance*, *Physical Review Letters* **13** (1964) 539.

[9] R. Emparan and H. S. Reall, *A Rotating black ring solution in five-dimensions*, *Phys. Rev. Lett.* **88** (2002) 101101 [hep-th/0110260].

[10] R. Emparan and H. S. Reall, *Black Holes in Higher Dimensions*, *Living Rev. Rel.* **11** (2008) 6 [0801.3471].

[11] R. Emparan, R. Luna, M. Martínez, R. Suzuki and K. Tanabe, *Phases and Stability of Non-Uniform Black Strings*, *JHEP* **05** (2018) 104 [1802.08191].

[12] T. Andrade, R. Emparan and D. Licht, *Rotating black holes and black bars at large D*, *JHEP* **09** (2018) 107 [1807.01131].

[13] T. Andrade, R. Emparan and D. Licht, *Charged rotating black holes in higher dimensions*, *JHEP* **02** (2019) 076 [1810.06993].

[14] T. Andrade, R. Emparan, D. Licht and R. Luna, *Cosmic censorship violation in black hole collisions in higher dimensions*, *JHEP* **04** (2019) 121 [1812.05017].

[15] T. Andrade, R. Emparan, D. Licht and R. Luna, *Black hole collisions, instabilities, and cosmic censorship violation at large D*, *JHEP* **09** (2019) 099 [1908.03424].

[16] D. Licht, R. Luna and R. Suzuki, *Black Ripples, Flowers and Dumbbells at large D*, *JHEP* **04** (2020) 108 [2002.07813].

[17] T. Andrade, R. Emparan, A. Jansen, D. Licht, R. Luna and R. Suzuki, *Entropy production and entropic attractors in black hole fusion and fission*, *JHEP* **08** (2020) 098 [2005.14498].

[18] G. 't Hooft, *A Planar Diagram Theory for Strong Interactions*, *Nucl. Phys. B* **72** (1974) 461.

[19] J. M. Maldacena, *The Large N limit of superconformal field theories and supergravity*, *Int. J. Theor. Phys.* **38** (1999) 1113 [hep-th/9711200].

[20] E. Witten, *Anti-de Sitter space and holography*, *Adv. Theor. Math. Phys.* **2** (1998) 253 [hep-th/9802150].

[21] R. Emparan and C. P. Herzog, *The Large D Limit of Einstein's Equations*, 2003.11394.

[22] R. Emparan, R. Suzuki and K. Tanabe, *Decoupling and non-decoupling dynamics of large D black holes*, *JHEP* **07** (2014) 113 [1406.1258].

[23] O. J. Dias, G. S. Hartnett and J. E. Santos, *Quasinormal modes of asymptotically flat rotating black holes*, *Class. Quant. Grav.* **31** (2014) 245011 [1402.7047].

[24] R. Emparan, T. Shiromizu, R. Suzuki, K. Tanabe and T. Tanaka, *Effective theory of Black Holes in the 1/D expansion*, *JHEP* **06** (2015) 159 [1504.06489].

[25] S. Bhattacharyya, A. De, S. Minwalla, R. Mohan and A. Saha, *A membrane paradigm at large D*, *JHEP* **04** (2016) 076 [1504.06613].

[26] R. Suzuki and K. Tanabe, *Stationary black holes: Large D analysis*, *JHEP* **09** (2015) 193 [1505.01282].

[27] R. Emparan, R. Suzuki and K. Tanabe, *Evolution and End Point of the Black String Instability: Large D Solution*, *Phys. Rev. Lett.* **115** (2015) 091102 [1506.06772].

[28] K. Tanabe, *Black rings at large D*, *JHEP* **02** (2016) 151 [1510.02200].

[29] S. Bhattacharyya, M. Mandlik, S. Minwalla and S. Thakur, *A Charged Membrane Paradigm at Large D*, *JHEP* **04** (2016) 128 [`1511.03432`].

[30] Y. Dandekar, S. Mazumdar, S. Minwalla and A. Saha, *Unstable 'black branes' from scaled membranes at large D*, *JHEP* **12** (2016) 140 [`1609.02912`].

[31] R. Emparan, K. Izumi, R. Luna, R. Suzuki and K. Tanabe, *Hydro-elastic Complementarity in Black Branes at large D*, *JHEP* **06** (2016) 117 [`1602.05752`].

[32] R. Gregory and R. Laflamme, *Black strings and p-branes are unstable*, *Phys. Rev. Lett.* **70** (1993) 2837 [`hep-th/9301052`].

[33] T. Andrade, C. Pantelidou and B. Withers, *Large D holography with metric deformations*, *JHEP* **09** (2018) 138 [`1806.00306`].

[34] M. M. Caldarelli, O. J. Dias, R. Emparan and D. Klemm, *Black Holes as Lumps of Fluid*, *JHEP* **04** (2009) 024 [`0811.2381`].

[35] R. Emparan, T. Harmark, V. Niarchos and N. A. Obers, *Essentials of Blackfold Dynamics*, *JHEP* **03** (2010) 063 [`0910.1601`].

[36] B. Chen, P.-C. Li and C.-Y. Zhang, *Einstein-Gauss-Bonnet Black Strings at Large D*, *JHEP* **10** (2017) 123 [`1707.09766`].

[37] B. Chen, P.-C. Li, Y. Tian and C.-Y. Zhang, *Holographic Turbulence in Einstein-Gauss-Bonnet Gravity at Large D*, *JHEP* **01** (2019) 156 [`1804.05182`].

[38] B. Chen, P.-C. Li and C.-Y. Zhang, *Einstein-Gauss-Bonnet Black Rings at Large D*, *JHEP* **07** (2018) 067 [`1805.03345`].

[39] N. Iizuka, A. Ishibashi and K. Maeda, *Cosmic Censorship at Large D: Stability analysis in polarized AdS black branes (holes)*, *JHEP* **03** (2018) 177 [`1801.07268`].

[40] C. P. Herzog, M. Spillane and A. Yarom, *The holographic dual of a Riemann problem in a large number of dimensions*, *JHEP* **08** (2016) 120 [`1605.01404`].

[41] M. Rozali and A. Vincart-Emard, *On Brane Instabilities in the Large D Limit*, *JHEP* **08** (2016) 166 [`1607.01747`].

[42] K. Tanabe, *Instability of the de Sitter Reissner–Nordstrom black hole in the 1/D expansion*, *Class. Quant. Grav.* **33** (2016) 125016 [`1511.06059`].

[43] K. Tanabe, *Elastic instability of black rings at large D*, `1605.08116`.

[44] B. Chen, P.-C. Li and Z.-z. Wang, *Charged Black Rings at large D*, *JHEP* **04** (2017) 167 [`1702.00886`].

[45] C. P. Herzog and Y. Kim, *The Large Dimension Limit of a Small Black Hole Instability in Anti-de Sitter Space*, *JHEP* **02** (2018) 167 [`1711.04865`].

[46] R. Gregory and R. Laflamme, *The Instability of charged black strings and p-branes*, *Nucl. Phys. B* **428** (1994) 399 [`hep-th/9404071`].

[47] V. Asnin, D. Gorbonos, S. Hadar, B. Kol, M. Levi and U. Miyamoto, *High and Low Dimensions in The Black Hole Negative Mode*, *Class. Quant. Grav.* **24** (2007) 5527 [`0706.1555`].

[48] R. Emparan, R. Suzuki and K. Tanabe, *Quasinormal modes of (Anti-)de Sitter black holes in the 1/D expansion*, *JHEP* **04** (2015) 085 [`1502.02820`].

[49] E. Sorkin, *A Critical dimension in the black string phase transition*, *Phys. Rev. Lett.* **93** (2004) 031601 [`hep-th/0402216`].

[50] U. Miyamoto, *Non-linear perturbation of black branes at large D*, *JHEP* **06** (2017) 033 [`1705.00486`].

[51] L. Lehner and F. Pretorius, *Black Strings, Low Viscosity Fluids, and Violation of Cosmic Censorship*, *Phys. Rev. Lett.* **105** (2010) 101102 [`1006.5960`].

[52] T. Harmark, V. Niarchos and N. A. Obers, *Instabilities of black strings and branes*, *Class. Quant. Grav.* **24** (2007) R1 [`hep-th/0701022`].

[53] R. Suzuki and K. Tanabe, *Non-uniform black strings and the critical dimension in the 1/D expansion*, *JHEP* **10** (2015) 107 [`1506.01890`].

[54] M. Shibata and H. Yoshino, *Bar-mode instability of rapidly spinning black hole in higher dimensions: Numerical simulation in general relativity*, *Phys. Rev. D* **81** (2010) 104035 [`1004.4970`].

[55] M. Mandlik and S. Thakur, *Stationary Solutions from the Large D Membrane Paradigm*, *JHEP* **11** (2018) 026 [`1806.04637`].

[56] R. Emparan, R. Suzuki and K. Tanabe, *The large D limit of General Relativity*, *JHEP* **06** (2013) 009 [`1302.6382`].

[57] R. C. Myers and M. Perry, *Black Holes in Higher Dimensional Space-Times*, *Annals Phys.* **172** (1986) 304.

[58] R. Emparan and R. C. Myers, *Instability of ultra-spinning black holes*, *JHEP* **09** (2003) 025 [`hep-th/0308056`].

[59] S. Bhattacharyya, A. K. Mandal, M. Mandlik, U. Mehta, S. Minwalla, U. Sharma et al., *Currents and Radiation from the large D Black Hole Membrane*, *JHEP* **05** (2017) 098 [`1611.09310`].

[60] O. J. Dias, P. Figueras, R. Monteiro, J. E. Santos and R. Emparan, *Instability and new phases of higher-dimensional rotating black holes*, *Phys. Rev. D* **80** (2009) 111701 [`0907.2248`].

[61] O. J. Dias, J. E. Santos and B. Way, *Rings, Ripples, and Rotation: Connecting Black Holes to Black Rings*, *JHEP* **07** (2014) 045 [1402.6345].

[62] R. Emparan, P. Figueras and M. Martinez, *Bumpy black holes*, *JHEP* **12** (2014) 072 [1410.4764].

[63] A. Ishibashi and H. Kodama, *Stability of higher dimensional Schwarzschild black holes*, *Prog. Theor. Phys.* **110** (2003) 901 [hep-th/0305185].

[64] S. Chandrasekhar, *Solutions of two problems in the theory of gravitational radiation*, *Phys. Rev. Lett.* **24** (1970) 611.

[65] J. Friedman and B. F. Schutz, *Secular instability of rotating Newtonian stars*, *Astrophys. J.* **222** (1978) 281.

[66] E. T. Newman, R. Couch, K. Chinnapared, A. Exton, A. Prakash and R. Torrence, *Metric of a Rotating, Charged Mass*, *J. Math. Phys.* **6** (1965) 918.

[67] F. Tangherlini, *Schwarzschild field in n dimensions and the dimensionality of space problem*, *Nuovo Cim.* **27** (1963) 636.

[68] F. Navarro-Lerida, *Perturbative Charged Rotating 5D Einstein-Maxwell Black Holes*, *Gen. Rel. Grav.* **42** (2010) 2891 [0706.0591].

[69] M. Allahverdizadeh, J. Kunz and F. Navarro-Lerida, *Extremal Charged Rotating Black Holes in Odd Dimensions*, *Phys. Rev. D* **82** (2010) 024030 [1004.5050].

[70] M. Allahverdizadeh, J. Kunz and F. Navarro-Lerida, *Extremal Charged Rotating Dilaton Black Holes in Odd Dimensions*, *Phys. Rev. D* **82** (2010) 064034 [1007.4250].

[71] M. Ortaggio and V. Pravda, *Black rings with a small electric charge: Gyromagnetic ratios and algebraic alignment*, *JHEP* **12** (2006) 054 [gr-qc/0609049].

[72] J. H. Horne and G. T. Horowitz, *Rotating dilaton black holes*, *Phys. Rev. D* **46** (1992) 1340 [hep-th/9203083].

[73] A. Aliev, *A Slowly rotating charged black hole in five dimensions*, *Mod. Phys. Lett. A* **21** (2006) 751 [gr-qc/0505003].

[74] A. Aliev, *Rotating black holes in higher dimensional Einstein-Maxwell gravity*, *Phys. Rev. D* **74** (2006) 024011 [hep-th/0604207].

[75] M. M. Caldarelli, R. Emparan and B. Van Pol, *Higher-dimensional Rotating Charged Black Holes*, *JHEP* **04** (2011) 013 [1012.4517].

[76] R. Emparan, T. Harmark, V. Niarchos and N. A. Obers, *Blackfolds in Supergravity and String Theory*, *JHEP* **08** (2011) 154 [1106.4428].

[77] J. Armas, J. Gath and N. A. Obers, *Electroelasticity of Charged Black Branes*, *JHEP* **10** (2013) 035 [1307.0504].

[78] K. Tanabe, *Charged rotating black holes at large D*, 1605.08854.

[79] S. Kundu and P. Nandi, *Large D gravity and charged membrane dynamics with nonzero cosmological constant*, *JHEP* **12** (2018) 034 [1806.08515].

[80] O. J. Dias, P. Figueras, R. Monteiro, H. S. Reall and J. E. Santos, *An instability of higher-dimensional rotating black holes*, *JHEP* **05** (2010) 076 [1001.4527].

[81] O. J. Dias, P. Figueras, R. Monteiro and J. E. Santos, *Ultraspinning instability of rotating black holes*, *Phys. Rev. D* **82** (2010) 104025 [1006.1904].

[82] O. J. Dias, R. Monteiro and J. E. Santos, *Ultraspinning instability: the missing link*, *JHEP* **08** (2011) 139 [1106.4554].

[83] G. S. Hartnett and J. E. Santos, *Non-Axisymmetric Instability of Rotating Black Holes in Higher Dimensions*, *Phys. Rev. D* **88** (2013) 041505 [1306.4318].

[84] R. Emparan, T. Harmark, V. Niarchos, N. A. Obers and M. J. Rodriguez, *The Phase Structure of Higher-Dimensional Black Rings and Black Holes*, *JHEP* **10** (2007) 110 [0708.2181].

[85] P. Figueras, M. Kunesch, L. Lehner and S. Tunyasuvunakool, *End Point of the Ultraspinning Instability and Violation of Cosmic Censorship*, *Phys. Rev. Lett.* **118** (2017) 151103 [1702.01755].

[86] M. Shibata and H. Yoshino, *Nonaxisymmetric instability of rapidly rotating black hole in five dimensions*, *Phys. Rev. D* **81** (2010) 021501 [0912.3606].

[87] H. Bantilan, P. Figueras, M. Kunesch and R. Panosso Macedo, *End point of nonaxisymmetric black hole instabilities in higher dimensions*, *Phys. Rev. D* **100** (2019) 086014 [1906.10696].

[88] G. Watson, *A note on the polynomials of hermite and laguerre*, *Journal of the London Mathematical Society* **1** (1938) 204.

[89] R. Emparan and P. Figueras, *Multi-black rings and the phase diagram of higher-dimensional black holes*, *JHEP* **11** (2010) 022 [1008.3243].

[90] A. Erdélyi, *Über einige bestimmte integrale, in denen die whittakerschenm k, m-funktionen auftreten*, *Mathematische Zeitschrift* **40** (1936) 693.

[91] P. Lee, H. Srivastava and S. Ong, *Some integrals of the products of laguerre polynomials*, *International journal of computer mathematics* **78** (2001) 303.

[92] G. Arcioni and E. Lozano-Tellechea, *Stability and critical phenomena of black holes and black rings*, *Phys. Rev. D* **72** (2005) 104021 [hep-th/0412118].

[93] H. Elvang, R. Emparan and A. Virmani, *Dynamics and stability of black rings*, *JHEP* **12** (2006) 074 [`hep-th/0608076`].

[94] J. E. Santos and B. Way, *Neutral Black Rings in Five Dimensions are Unstable*, *Phys. Rev. Lett.* **114** (2015) 221101 [`1503.00721`].

[95] P. Figueras, M. Kunesch and S. Tunyasuvunakool, *End Point of Black Ring Instabilities and the Weak Cosmic Censorship Conjecture*, *Phys. Rev. Lett.* **116** (2016) 071102 [`1512.04532`].

[96] R. Emparan and R. Suzuki, *Topology-changing horizons at large D as Ricci flows*, *JHEP* **07** (2019) 094 [`1905.01062`].

[97] P. Daskalopoulos, R. Hamilton and N. Sesum, *Classification of compact ancient solutions to the ricci flow on surfaces*, *arXiv preprint arXiv:0902.1158* (2009) .

[98] R. Penrose, *Gravitational collapse: The role of general relativity*, *Riv. Nuovo Cim.* **1** (1969) 252.

[99] M. W. Choptuik, *Universality and scaling in gravitational collapse of a massless scalar field*, *Phys. Rev. Lett.* **70** (1993) 9.

[100] V. Cardoso, O. J. Dias and J. P. Lemos, *Gravitational radiation in D-dimensional space-times*, *Phys. Rev. D* **67** (2003) 064026 [`hep-th/0212168`].

[101] P. M. Chesler and L. G. Yaffe, *Horizon formation and far-from-equilibrium isotropization in supersymmetric Yang-Mills plasma*, *Phys. Rev. Lett.* **102** (2009) 211601 [`0812.2053`].

[102] J. Bezanson, A. Edelman, S. Karpinski and V. B. Shah, *Julia - A Fresh Approach to Numerical Computing*, *SIAM review* **59** (2017) 65.

[103] C. Rackauckas and Q. Nie, *DifferentialEquations.jl - A Performant and Feature-Rich Ecosystem for Solving Differential Equations in Julia*, *JORS* **5(1)** (2017) .

[104] H. Yoshino and Y. Nambu, *Black hole formation in the grazing collision of high-energy particles*, *Phys. Rev. D* **67** (2003) 024009 [`gr-qc/0209003`].

[105] H. Yoshino and V. S. Rychkov, *Improved analysis of black hole formation in high-energy particle collisions*, *Phys. Rev. D* **71** (2005) 104028 [`hep-th/0503171`].

[106] M. Shibata, H. Okawa and T. Yamamoto, *High-velocity collision of two black holes*, *Phys. Rev. D* **78** (2008) 101501 [`0810.4735`].

[107] U. Sperhake, V. Cardoso, F. Pretorius, E. Berti and J. A. Gonzalez, *The High-energy collision of two black holes*, *Phys. Rev. Lett.* **101** (2008) 161101 [`0806.1738`].

[108] F. S. Coelho, C. Herdeiro and M. O. Sampaio, *Radiation from a D-dimensional collision of shock waves: a remarkably simple fit formula*, *Phys. Rev. Lett.* **108** (2012) 181102 [1203.5355].

[109] W. E. East and F. Pretorius, *Ultrarelativistic black hole formation*, *Phys. Rev. Lett.* **110** (2013) 101101 [1210.0443].

[110] J. Camps, R. Emparan and N. Haddad, *Black Brane Viscosity and the Gregory-Laflamme Instability*, *JHEP* **05** (2010) 042 [1003.3636].

[111] S. Hawking, *Gravitational radiation from colliding black holes*, *Phys. Rev. Lett.* **26** (1971) 1344.

[112] J. D. Bekenstein, *Generalized second law of thermodynamics in black hole physics*, *Phys. Rev. D* **9** (1974) 3292.

[113] R. Emparan, *Predictivity lost, predictivity regained: a Miltonian cosmic censorship conjecture*, 2005.07389.

[114] T. Andrade, P. Figueras and U. Sperhake, *Violations of Weak Cosmic Censorship in Black Hole collisions*, 2011.03049.

[115] Y. Dandekar, S. Kundu, S. Mazumdar, S. Minwalla, A. Mishra and A. Saha, *An Action for and Hydrodynamics from the improved Large D membrane*, *JHEP* **09** (2018) 137 [1712.09400].

[116] R. Emparan and M. Martinez, *Exact Event Horizon of a Black Hole Merger*, *Class. Quant. Grav.* **33** (2016) 155003 [1603.00712].

[117] S. Bhattacharyya, V. E. Hubeny, S. Minwalla and M. Rangamani, *Nonlinear Fluid Dynamics from Gravity*, *JHEP* **02** (2008) 045 [0712.2456].

[118] S. Bhattacharyya, V. E. Hubeny, R. Loganayagam, G. Mandal, S. Minwalla, T. Morita et al., *Local Fluid Dynamical Entropy from Gravity*, *JHEP* **06** (2008) 055 [0803.2526].

[119] N. Engelhardt and A. C. Wall, *Decoding the Apparent Horizon: Coarse-Grained Holographic Entropy*, *Phys. Rev. Lett.* **121** (2018) 211301 [1706.02038].

[120] I. Booth, M. P. Heller, G. Plewa and M. Spalinski, *On the apparent horizon in fluid-gravity duality*, *Phys. Rev. D* **83** (2011) 106005 [1102.2885].

[121] G. T. Horowitz and E. J. Martinec, *Comments on black holes in matrix theory*, *Phys. Rev. D* **57** (1998) 4935 [hep-th/9710217].

[122] M. Campanelli, C. Lousto and Y. Zlochower, *Spinning-black-hole binaries: The orbital hang up*, *Phys. Rev. D* **74** (2006) 041501 [gr-qc/0604012].

[123] T. W. Baumgarte and S. L. Shapiro, *Numerical Relativity: Solving Einstein's Equations on the Computer.* Cambridge University Press, 2010, 10.1017/CBO9781139193344.

[124] R. Emparan, D. Grumiller and K. Tanabe, *Large-D gravity and low-D strings*, *Phys. Rev. Lett.* **110** (2013) 251102 [1303.1995].

[125] R. Emparan and K. Tanabe, *Holographic superconductivity in the large D expansion*, *JHEP* **01** (2014) 145 [1312.1108].

[126] R. Emparan and K. Tanabe, *Universal quasinormal modes of large D black holes*, *Phys. Rev. D* **89** (2014) 064028 [1401.1957].

[127] R. Emparan, R. Suzuki and K. Tanabe, *Instability of rotating black holes: large D analysis*, *JHEP* **06** (2014) 106 [1402.6215].

[128] A. M. García-García and A. Romero-Bermúdez, *Conductivity and entanglement entropy of high dimensional holographic superconductors*, *JHEP* **09** (2015) 033 [1502.03616].

[129] B. Chen, Z.-Y. Fan, P. Li and W. Ye, *Quasinormal modes of Gauss-Bonnet black holes at large D*, *JHEP* **01** (2016) 085 [1511.08706].

[130] T. Andrade, S. A. Gentle and B. Withers, *Drude in D major*, *JHEP* **06** (2016) 134 [1512.06263].

[131] E.-D. Guo, M. Li and J.-R. Sun, *CFT dual of charged AdS black hole in the large dimension limit*, *Int. J. Mod. Phys. D* **25** (2016) 1650085 [1512.08349].

[132] B. Chen and P.-C. Li, *Instability of Charged Gauss-Bonnet Black Hole in de Sitter Spacetime at Large D*, 1607.04713.

[133] Y. Dandekar, A. De, S. Mazumdar, S. Minwalla and A. Saha, *The large D black hole Membrane Paradigm at first subleading order*, *JHEP* **12** (2016) 113 [1607.06475].

[134] F. Ferrari, *The Large D Limit of Planar Diagrams*, 1701.01171.

[135] B. Chen and P.-C. Li, *Static Gauss-Bonnet Black Holes at Large D*, *JHEP* **05** (2017) 025 [1703.06381].

[136] S. Bhattacharyya, P. Biswas, B. Chakrabarty, Y. Dandekar and A. Dinda, *The large D black hole dynamics in AdS/dS backgrounds*, *JHEP* **10** (2018) 033 [1704.06076].

[137] M. Rozali, E. Sabag and A. Yarom, *Holographic Turbulence in a Large Number of Dimensions*, *JHEP* **04** (2018) 065 [1707.08973].

[138] S. Bhattacharyya, P. Biswas and Y. Dandekar, *Black holes in presence of cosmological constant: second order in $\frac{1}{D}$*, *JHEP* **10** (2018) 171 [1805.00284].

[139] A. Saha, *The large D Membrane Paradigm For Einstein-Gauss-Bonnet Gravity*, *JHEP* **01** (2019) 028 [1806.05201].

[140] R. Emparan, S. Ohashi and T. Shiromizu, *No-dipole-hair theorem for higher-dimensional static black holes*, *Phys. Rev. D* **82** (2010) 084032 [1007.3847].

[141] M. M. Caldarelli, J. Camps, B. Goutéraux and K. Skenderis, *AdS/Ricci-flat correspondence and the Gregory-Laflamme instability*, *Phys. Rev. D* **87** (2013) 061502 [1211.2815].

[142] P.-C. Li, C.-Y. Zhang and B. Chen, *The Fate of Instability of de Sitter Black Holes at Large D*, *JHEP* **11** (2019) 042 [1909.02685].

[143] J. Casalderrey-Solana, C. P. Herzog and B. Meiring, *Holographic Bjorken Flow at Large-D*, *JHEP* **01** (2019) 181 [1810.02314].

[144] M. Guo, P.-C. Li and B. Chen, *Photon Emission Near Myers-Perry Black Holes in the Large Dimension Limit*, *Phys. Rev. D* **101** (2020) 024054 [1911.08814].

[145] W. C. Parke and L. C. Maximon, *Closed-form second solution to the confluent hypergeometric difference equation in the degenerate case*, *Int. J. Diff. Eq* **11** (2016) 203.

[146] W. C. Parke and L. C. Maximon, *On second solutions to second-order difference equations*, *arXiv preprint arXiv:1601.04412* (2016) .

[147] R. Suzuki, *Brane blobology in the large D effective theory*, 2009.11823.